Università degli Studi di Ferrara

DOCTORAL COURSE IN ENGINEERING SCIENCE

CYCLE XXXV

COORDINATOR Prof. Stefano Trillo

A multiscale strategy for fouling prediction and mitigation in gas turbines

Scientific/Disciplinary Sector (SDS) ING-IND/08

Candidate
Riccardo Friso

Supervisor
Prof. Michele Pinelli

Co-Supervisor
Prof. Francesco Montomoli

Year 2019/2022

Abstract

Gas turbines are one of the primary sources of power for both aerospace and land-based applications. Precisely for this reason, they are often forced to operate in harsh environmental conditions, which involve the occurrence of particle ingestion by the engine. The main implications of this problem are often underestimated. The particulate in the airflow ingested by the machine can deposit or erode its internal surfaces, and lead to the variation of their aerodynamic geometry, entailing performance degradation and, possibly, a reduction in engine life. This issue affects the compressor and the turbine section and can occur for either land-based or aeronautical turbines. For the former, the problem can be mitigated (but not eliminated) by installing filtration systems. For what concern the aerospace field, filtration systems cannot be used. Volcanic eruptions and sand dust storms can send particulate to aircraft cruising altitudes. Also, aircraft operating in remote locations or low altitudes can be subjected to particle ingestion, especially in desert environments.

The aim of this work is to propose different methodologies capable to mitigate the effects of fouling or predicting the performance degradation that it generates. For this purpose, both hot and cold engine sections are considered. Concerning the turbine section, new design guidelines are presented. This is because, for this specific component, the time scales of failure events due to hot deposition can be of the order of minutes, which makes any predictive model inapplicable. In this respect, design optimization techniques were applied to find the best HPT vane geometry that is less sensitive to the fouling phenomena. After that, machine learning methods were adopted to obtain a design map that can be useful in the first steps of the design phase. Moreover, after a numerical uncertainty quantification analysis, it was demonstrated that a deterministic optimization is not sufficient to face highly aleatory phenomena such as fouling. This suggests the use of robust or aggressive design techniques to front this issue.

On the other hand, with respect to the compressor section, the research was mainly focused on the building of a predictive maintenance tool. This is because the time scales of failure events due to cold deposition are longer than the ones for the hot section, hence the main challenge for this component is the optimization of the washing schedule. As reported in the previous sections, there are several studies in the literature focused on this issue, but almost all of them are data-based instead of physics-based. The innovative strategy proposed here is a mixture between physics-based and data-based methodologies. In particular, a reduced-order model has been developed to predict the behaviour of the whole engine as the degradation proceeds. For this purpose, a gas path code that uses the components' characteristic maps has been created to simulate the gas turbine. A map variation technique has been used to take into account the fouling effects on each engine component. Particularly, fouling coefficients as a function of the engine architecture, its operating conditions, and the

contaminant characteristics have been created. For this purpose, both experimental and computational results have been used. Specifically for the latter, efforts have been done to develop a new numerical deposition/detachment model.

Keywords: Gas Turbine Fouling, Particle-Laden Flow, Machine Learning, Digital Twin, Computational Fluid Dynamics

Italian Abstract

Le turbine a gas sono una delle pricipali fonti di energia, sia per applicazioni aeronautiche che terrestri. Proprio per questa ragione, esse sono spesso costrette ad operare in ambienti non propriamente puliti, il che comporta l'ingestione di contaminanti solidi da parte del motore. Le principali implicazioni di questo problema sono spesso sottovalutate. Le particelle solide presenti nel flusso d'aria che il motore ingerisce durante il suo funzionamento possono depositarsi o erodere le superfici interne della macchina, e portare a variazioni alla sua aerodinamica, quindi a degrado di performance e, molto probabilmente, alla diminuzione della sua vita utile. Questo problema affligge sia la parte del compressore che la parte della turbina, e si manifesta sia in applicazioni terrestri che aeronautiche. Per quanto riguarda la prima, la questione può essere mitigata (ma non eliminata) dall'installazione di sistemi di filtraggio all'ingresso della macchina. Per le applicazioni aeronautiche invece, i sistemi di filtraggio non possono essere utilizzati. Questo implica che il particolato presente ad alte quote, magari grazie ad eventi catastrofici quali eruzioni vulcaniche, o a basse quote, quindi ambienti deseritic, entra liberamente nella turbina a gas.

Lo scopo principale di questo lavoro di tesi, è quello di proporre differenti metodologie allo scopo di mitigare gli effetti dello sporcamento o predirre il degrado che esso comporta nelle turbine a gas. Per questo scopo, sia la parte del compressore che quella della turbina sono state prese in considerazione. Per quanto riguarda la parte turbina, saranno presentate nuove guide progettuali volte al trovare la geometria che sia meno sensibile possibile al problema dello sporcamento. Dopo di ciò, i risultati ottenuti verranno trattati tramite tecniche di machine learning, ottenendo una mappa di progetto che potrà essere utile nelle prime fasi della progettazione di questi componenti. Inoltre, essendo l'analisi fin qui condotta di tipo deterministico, un'analisi delle principali fonti di incertezza verrà eseguita con l'utilizzo di tecniche derivanti dall'uncertainty quantification. Questo dimostrerà che l'analisi deterministica è troppo semplificativa, e che sarebbe opportuno spingersi verso una progettazione robusta per affrontare questa tipologia di problemi.

D'altro canto, per quanto concerne la parte compressore, la ricerca è stata incentrata principalmente sulla costruzione di uno strumento predittivo, questo perchè la scala temporale del degrado dovuto alla deposizione a "freddo" è molto più dilatata rispetto a quella della sezione "calda". La trategia proposta in questo lavoro di tesi è un'insieme di modelli fisici e data-driven. In particolare, si è sviluppato un modello ad ordine ridotto per la previsione del comportamento del motore soggetto a degrado dovuto all'ingestione di particolato, durante un'intera missione aerea. Per farlo, si è generato un codice cosiddetto gas-path, che modella i singoli componenti della macchina attraverso le loro mappe caratteristiche. Quest'ultime vengono modificate, a seguito della deposizione, attraverso opportuni coefficienti di degrado. Tali coefficienti devono essere adeguatamente stimati per avere una corretta previsione degli

eventi, e per fare ciò verrà proposta una strategia che comporta l'utilizzo sia di metodi sperimentali che computazionali, per la generazione di un algoritmo che avrà lo scopo di fornire come output questi coefficienti.

Contents

List of Figures

List of Tables

Nomenclature

Greek Symbols

β	Pressure ratio
β_{te}	Boat-tail Angle
ϵ	Turbulent Kinetic Energy Dissipation Rate $[m^2/s^3]$
η	Efficiency
Γ	Surface Free Energy [J]
γ_i	Surface Free Energy of Material i [J]
γ_l	Surface Tension of the Liquid Bridge [Pa]
κ	Meniscus Mean Curvature [1/m]
κ_A	Von Karman constant
Λ	Objective Function
Λ_s	Roughness Parameter
μ	Dynamic Viscosity $[Pa\ s]$
μ^*	Isentropic Efficiency
μ_{ν_f}	Mean Experimental Thickness [m]
ν	Generic Poisson Coefficient [Pa]
ν_f	Void Fraction
ν_i	Poisson Coefficient of Material i [Pa]
ν_K	Kinematic Viscosity $[m^2/s]$
ω	Specific Rate of Turbulent Kinetic Energy Dissipation [1/s]
ϕ	Flow Coefficient
Φ_p	Particle Volumetric Fraction $[m_s^3olid/m_a^3ir]$
ψ	Filling Angle [deg]
ψ_0	Clean Static Pressure Rise Coefficiet

ψ_F Fouled Static Pressure Rise Coefficiet

Ψ_j Stochastic Functions

ψ_P Static Pressure Rise Coefficiet

ρ Generic Density $[kg/m^3]$

ρ_f Fluid Density $[kg/m^3]$

ρ_p Particle Density $[kg/m^3]$

σ_i Root Mean Square Turbulence Fluctuations [m/s]

σ_{ν_f} Variance of the Experimental Thickness

τ_e Large Eddy Turnover Time [s]

τ_K Kolmogorov Time Scale [s]

τ_p Particle Response Time [s]

τ_p^+ Non-dimensional Particle Relaxation Time

τ_w Wall Shear Stress [Pa]

θ Contact Angle [deg]

ξ_j Collocation Point

Letters

Δz_{te} Trailing Edge Thickness

δ_G Compenetration Distance [m]

$\dot{m}$ Mass Flow Rate $[kg/s]$

a_H Radius of Hertz Contact Area [m]

A_{f_cell} Frontal Cell Surface Area

a_{JKR} Radius of Johnson-Kendall-Roberts Contact Area [m]

A_{s_cell} Wetted Cell Surface Area

b_i Weight Factors

c Airfoil Chord [m]

C_c Cunningham Slip Correction Factor

C_D Drag Coefficient

C_e Capture Efficiency

C_f Skin Friction Coefficient

c_p Specific Heat $[J/(kg\ K)]$

d_p Particle Diameter [m]

d_{max} Maximum Particle Shape Dimension [m]

d_{med} Medium Particle Shape Dimension [m]

d_{min} Minimum Particle Shape Dimension [m]

D_{pipe} Diameter [m]

e Coefficient of Restitution

E^* Equivalent Young Modulus [Pa]

E_i Young Modulus of Material i [Pa]

E_{act} Activation Energy [J]

E_{ref} Reference Energy [J]

F Generic Force [N]

F_B Body Force [N]

F_D Drag Force [N]

F_S Saffman Force [N]

F_{AM} Added Mass Force [N]

F_{BA} Basset Force [N]

F_{Br} Brownian Force [N]

F_{cap} Capillarity Force [N]

F_{EL} Elastic Limit Load [N]

F_{Ne} Newton Drag [N]

F_{St} Stokes Drag [N]

F_{VdW} Van der Waals Force [N]

g Gravity Acceleration $[m/s^2]$

G_i Gaussian Random Number

h Specific Hentalpy $[J/kg]$

H_A Hamaker Constant

h_{EL} Relative Approach at the Limiting Elastic Case [m]

H_{ts} Test Section Height [m]

K_i Binomial Function

k_s Equivalent Sand-Grain Roughness Height [m]

k_s^+ Non-dimensional Equivalent Sand-Grain Roughness Height [m]

k_a Average Equivalent Sand-Grain Roughness Height [m]

k_{rms} Root Mean Square Equivalent Sand-Grain Roughness Height [m]

k_t Peak-to-through Equivalent Sand-Grain Roughness Height [m]

l Length Scale of the Energy containing Eddies [m]

l_t Mixing Length [m]

L_{pipe} Length [m]

M Generic Force Torque [$N\ m$]

m Mass [kg]

m^* Effective Mass [kg]

M_D Drag Force Torque [$N\ m$]

M_p Weight Force Torque [$N\ m$]

m_p Particle Mass [kg]

M_{cap} Capillarity Force Torque [$N\ m$]

M_{VdW} Van der Waals Force Torque [$N\ m$]

N_p Number of Particles

n_x Number of Particle in the x direction

n_y Number of Particle in the y direction

n_z Number of Particle in the z direction

Q_k Particle Kinetic Energy [J]

Q_{ad} Adhesion Energy [J]

Q_{el} Elastic Energy [J]

$Q_{p,pla}$ Energy Loss due to the Plastic Behaviour of the Particle [J]

Q_{PE} Energy in the Plastic Deformation Zone [J]

$Q_{s,pla}$ Energy Loss due to the Plastic Behaviour of the Substrate [J]

R^* Effective Radius [kg]

R_c Appropriate Radius [m]

R_g Gas Constant $[J/(kg\,mol)]$

R_i Radius of Particle i [m]

r_p Radius of the Plastic Deformed Area [m]

r_T Radius of the Total Deformed Area [m]

R_a Average Roughness Height [m]

r_{EL} Radius of the Elastic Deformed Area [m]

R_{le} Leading Edge Radius

R_{te} Trailing Edge Radius

R_t Peak-to-through Roughness Height [m]

Re_p Particle Reynolds Number

Re_p^* Modified Particle Reynolds Number

Re_m Mean Reynolds Number

S_f Total Frontal Area

S_p Sticking Probability

S_s Total Wetted Surface Area

S_y Yield Stress [Pa]

S_{ref} Reference Area

Sk Skewness

T^* Melting Temperature [K]

t_e Eddy's Lifetime [s]

t_h Deposit Thickness [m]

t_r Particle Residence Time [s]

u^+ Dimensionless Velocity]

u_τ Friction Velocity [m/s]

V_d^+ Deposition Velocity [m/s]

V_f Fluid Volume $[m^3]$

V_m Molar Volume of the Liquid $[m^3/mol]$

v_m Bulk Mean Velocity [m/s]

V_p Particle Volume $[m^3]$

v_p Particle Velocity $[m/s]$

v_{cl} Center line Velocity [m/s]

$v_{i,n}$ Normal Particle Incident Velocity [m/s]

$v_{p,n}$ Normal Component of the Particle Velocity $[m/s]$

$v_{r,n}$ Normal Particle Rebound Velocity [m/s]

W_{ts} Test Section Width [m]

W_{VdW} Van der Waals Interface Energy of Adhesion [J]

x^* Vector Parameters

x_{opt} Optimal Configuration

y^+ Dimensionless Wall Distance

z_0 Minimum Equilibrium Separation Distance [m]

D Minimum Equilibrium Separation Distance [m]

d Height of the Particle Inside the Liquid Bridge [m]

E Generic Young Modulus [Pa]

ES Effective Slope

Fl Flatness

H Approach Distance During Elastic Phase [m]

h Specific Hentalpy $[kJ/(kg\ K]$

k Turbulent Kinetic Energy [J/kg]

L Target Length [m]

p Pressure [Pa]

R Generic Radius [m]

S Distance between neighbouring particles [m]

T Temperature [K]

t Time [s]

Tu Turbulence Intensity [%]

v Velocity [m/s]

v' Fluctuating Turbulent Velocity [m/s]

Acronyms

ANN Artificial Neural Network

ANOVA ANalysis Of VAriance

ARD Arizona Road Dust

BBO Basset-Boussinesque-Oseen

BC Boundary Condition

CB Carbon Black

CCI Coherence Correlation Interferometry

CFD Computational Fluid Dynamics

COR Coefficient Of Restitution

CRW Continuous Random Walk

CSF Corey Shape Factor

CST Class Shape Transform

DfF Design for Fouling

DM Design Margin

DMT Derjaguin-Muller-Toporov

DNS Direct Numerical Simulations

DOE Design Of Experiment

DP Design Point

DRW Discrete Random Walk

EBFOG Energy Based FOulinG

EGT Exhaust Gas Temperature

Exp Experimental

GHG Greenhouse Gas

GT Gas Turbine

HPT High Pressure Turbine

JKR Johnson-Kendall-Roberts

LDV Laser Doppler Velocimetry

LE Leading Edge

LHS Latin Hypercube Sampling

LR Lifetime Ratio

MLP Multi Layer Perceptron

NGV Nozzle Guide Vane

OF OpenFOAM

OSU Ohio State University

PCM Probabilistic Collocation Method

PM Particulate Matter

PS Pressure Side

RANS Reynolds-Averaged Navier-Stokes

RBF Radial Basis Function

RH Relative Humidity

RMS Root Mean Square

RNG ReNormalization Group

SBO Surrogate-Based Optimization

SLP Single Layer Perceptron

SM Surge Margin

SOM Self-Organizing Map

SS Suction Side

SST Shear Stress Transport

TE Trailing Edge

TET Turbine Entry Temperature

VKI Von Karmann Institute

VTS Vortex Tube Separator

Chapter 1

Problem Statement

In this chapter, a global overview of the performance degradation due to the presence of dispersed particles in the working fluid of gas turbines is reported. After exposing the primary sources of particulate in the atmosphere, their effects on both heavy-duty and aeronautical engines are discussed.

1.1 Particulate sources

1.1.1 Air Contaminant

The atmospheric air is contaminated by particles that could be solid (smoke, fly ash, dust, etc.) or liquid (mist, fog, etc.). This particulate can be of different sizes, depending on the source that generates it. In particular, finer particles originate from human processes, such as industrial activities, whereas coarser ones result from natural phenomena, i.e. pollen or volcanic eruptions. Even though these two sources are equally important in terms of the amount of particulate produced, the spatial scale related to the dispersion and the re-entry is quite different. Specifically, man-made contaminants are distributed locally than natural-related ones, which tend to have a more global-scale dispersion. In this work, only solid contaminants are considered, since they are the most critical for the operations and the health of the gas turbines.

In this regard, in the work of Wilcox et al. (2010) an exhaustive explanation of the mechanisms of dispersion of these solid particles can be found. Solid contaminants are spread from their source carried by the wind. Heavier and larger particles (in the range between 30 µm and 50 µm) drop out of the air stream quickly, while smaller ones (smaller than 10 µm) remain airborne until they fall out due to air turbulence dropping off. There are three physical processes by which solid contaminants move from their source: creep, saltation, and suspension. These phenomena are represented in Fig. 1.1. Suspension, which is the one that is of main importance for gas turbines, describes the process with which

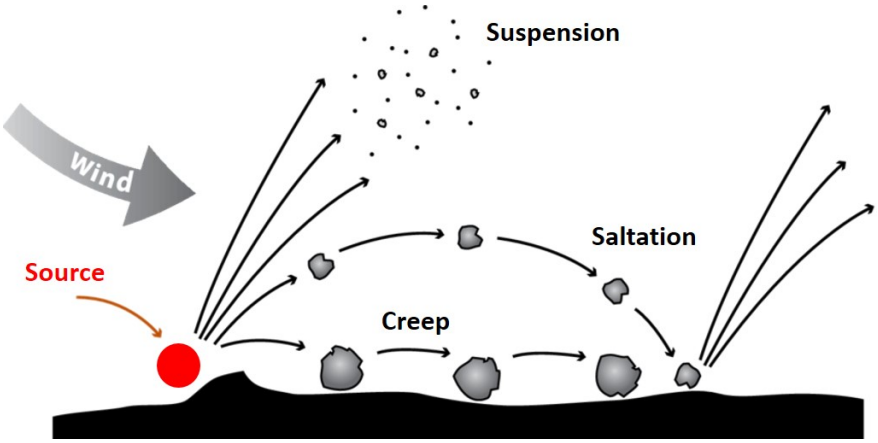

Figure 1.1: Solid Contaminant Transportation Processes. (Tatarko & Presley 2009)

particles are carried by the wind and air currents. This process is favourable for smaller contaminants and strong winds. Smaller particles can be carried for thousands of miles and reach heights of thousands of feet. The suspension process is also strongly dependent on the settling rate of the contaminants. The settling rate is the rate at which the particles fall to the earth. Larger and heavier particles have a faster settling rate, whereas smaller ones have a lower settling rate and can remain suspended in the air for days at a time.

Given the information related to particle transport, is easy to understand that the solid particles influence not only the geographic area close to their source but also areas far away from it. This concept is of main importance for both natural and man-made contaminants. For what concern the first of them, as reported in the work of Zender et al. (2003), the natural particles are carried by the intercontinental winds that spread them as a function of the wind intensity and direction. In their study, they simulated the natural mobilization and deposition tendencies for ten year period from 1990 to 1999. Their results, reported in Fig. 1.2, highlight the global impact of naturally sourced contaminants, showing the effectiveness of the transport from the sources (Fig. 1.2(a)) to the downwind areas (Fig. 1.2(b)). It is also interesting to note the differences between dry deposition (Fig. 1.2(c)) and wet deposition (Fig. 1.2(d)). The latter shows a wide spreading of particles all around the globe, whereas the first, which is very inefficient for particles smaller than 2 µm, exhibits a more localized effect.

Dust deposition reported in Fig. 1.2 is useful for gathering information on the particulate at the ground level, hence the one that land-based gas turbines will be exposed to. When it comes to evaluating the effects of contaminant ingestion in aeronautical engines, different sources have to be considered. Among the others, particular attention is devoted here to sand storms and volcanic eruptions. The former were studied in detail in UNEP et al. (2016) where the global pattern of sand storm frequency estimated in the period from 1974 to 2012 is reported (Fig. 1.3). In terms of frequency, the Sahara and Asian deserts are clearly dominant,

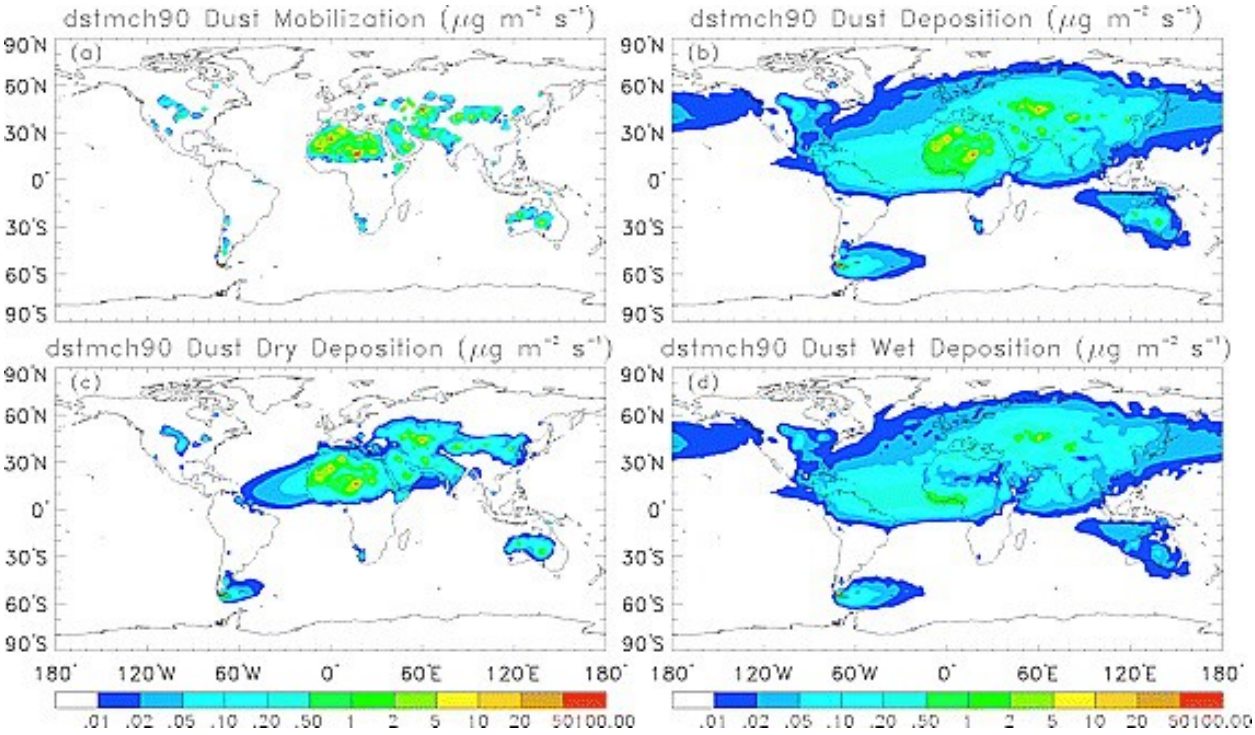

Figure 1.2: Predicted annual mean dust source and sink fluxes in $\mu g/m^2\ s^{-1}$ for (a) mobilization, (b) total deposition, (c) dry deposition, (d) wet deposition. Scale is logarithmic. From (Zender et al. 2003).

whereas values are low in the Southern Hemisphere and the Americas. It is important to note that dust mass concentration during sand storms can reach peaks of 2000 µg/m^3, at altitudes up to 3 km (Wang et al. 2018). For what concerns volcanic eruptions, the resulting volcanic ash can spread over large distances away from the source, disrupting air traffic, hazarding airports (as in Guffanti et al. (2008)), and even altering atmospheric composition

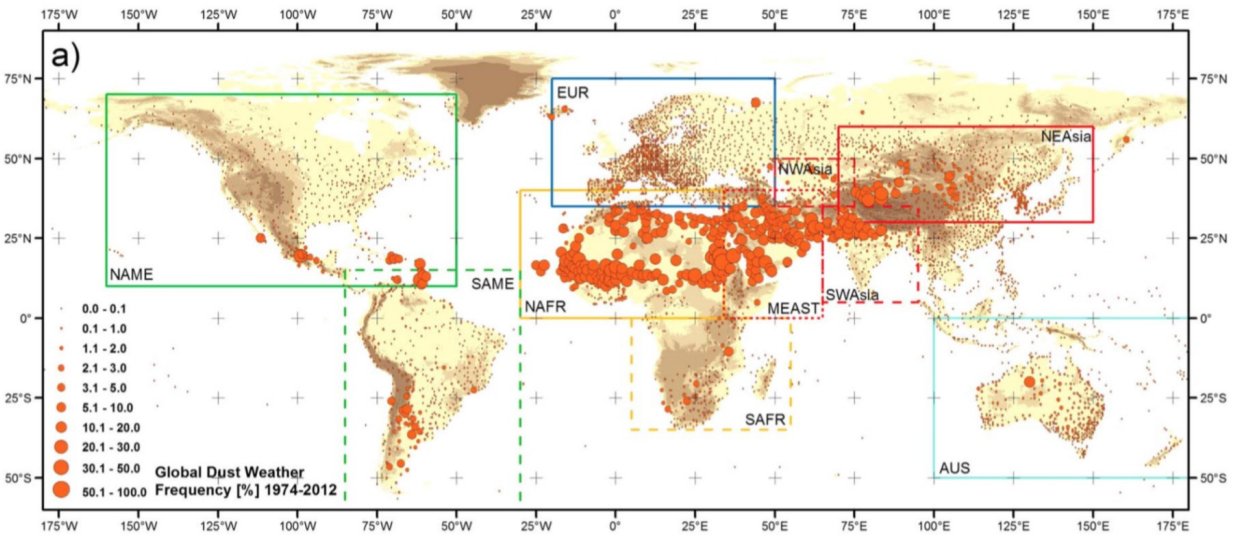

Figure 1.3: Global pattern of sand storms frequency estimated for the period of January 1974 to December 2012. From (UNEP et al. 2016).

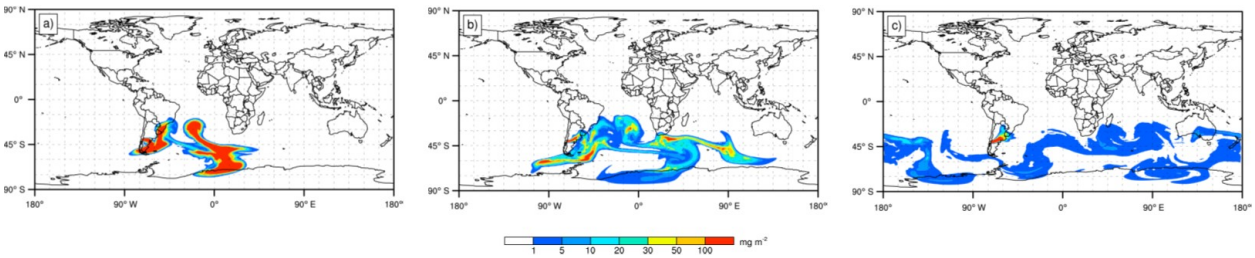

Figure 1.4: Total column concentration (mass loading; $mg\ m^{-2}$) from the global simulation for the 2011 Caulle eruption. Results for (a) 8 June at 09:00 UTC, (b) 10 June at 04:00 UTC, and (c) 14 June at 06:00 UTC. From (Marti et al. 2017).

according to Myhre et al. (2013). For these catastrophic events, different modelisations have to be used to forecast the volcanic cloud evolution and dispersion. For example, the work of Marti et al. (2017) proposes a model in which each volcanic eruption can be considered as a source in a precise location on the earth. Therefore, the time evolution of the originated cloud can be predicted by considering the weather conditions. An example of the application of this model is shown in Fig. 1.4, where the mass loading distribution evolution obtained for the 2011 Cauelle eruption is reported. With techniques such as the one suggested by Marti et al. (2017), it is possible to foresee the volcanic cloud spreading on a global scale, and then find the flight route that could be affected by a volcanic eruption.

As said before, natural air contaminants represent only one side of the coin. The other one is represented by human activities, which strongly influence particle concentration. This aspect was deeply analyzed in the study of Préndez et al. (2019) where the impact of human activities was evaluated by decomposing them into their different types. They found that the principal source of PM_{10} is transport (44 %), the second largest source being the consumption of firewood in homes (33 %). Much less significant are the industrial contributions

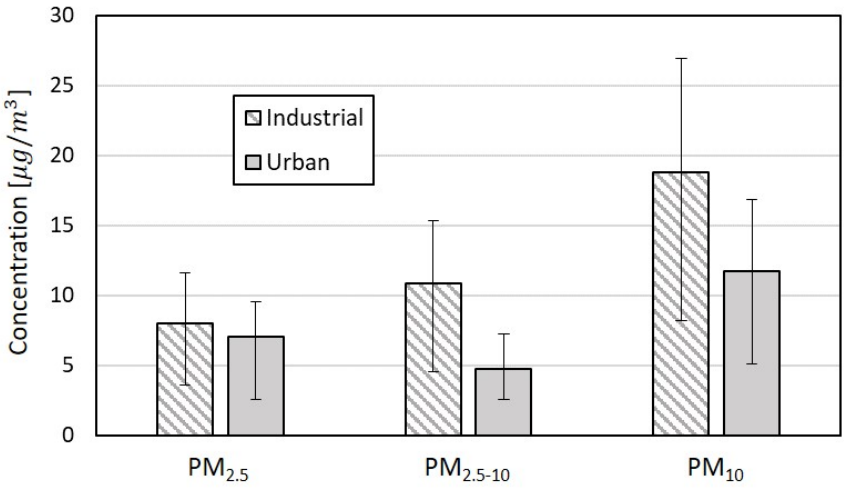

Figure 1.5: Average mass concentration in $\mu g\ m^{-3}$ in two sites to show the effect of the industrial activity. The error bars represent the standard deviation. From (Taiwo et al. 2014).

(11 %). However, considering only the source of $PM_{2.5}$, the most significant sources are domestic emissions (95 %), followed by building, agriculture, industries, and transport. $PM_{2.5}$ always forms more than 80 % of the total PM_{10}. From these results, it can be concluded that human activities, in general, can perturb the background concentration of particulate. In this respect, Taiwo et al. (2014) have highlighted how the presence of industrial processes influences the particle mass average concentration. The study takes into account two neighbouring areas including the effect of the wind to consider the downwind dispersion of the particulate. Their outcomes, reported in Fig. 1.5, show an increase in the concentration due to the presence of the power plants, for all the investigated particle sizes.

1.1.2 Fuel Contaminant

The European Green Deal and the 2030 Climate Target Plan aim to reduce Greenhouse gas (GHG) emissions by at least 55 % in 2030, relative to 1990, and achieve climate neutrality in 2050. Human activities are responsible for almost all of the increase in GHG in the atmosphere over the last 150 years. The largest source of greenhouse gas emissions from human activities is burning fossil fuels for electricity, heat, and transportation. In this respect, the most promising strategy to reach the European target in 2030 is the substitution of fossil fuels with more climate-friendly alternative fuels. A large number of studies in the literature are focused on the assessment of fuels different from fossil ones. Most of them have found biofuels the most valid alternative, also thanks to their low costs, and high availability. Biofuel is produced with the anaerobic digestion of plant and animal wastes and then burnt in a gas turbine combustor. Although synfuels are cleaned and filtered before entering the turbine combustor, impurities are not completely removed. Therefore, the high temperature reached in the turbine nozzle can lead to the deposition of contaminants

Table 1.1: Typical Characteristics of Different Biomass Fuel Types (Bukar et al. 2019)

Biomass Type	**Lower Heating Value [kJ/kg]**	**Moisture Content [%]**	**Ash Content (dry) [%]**
Basasse	7,700 - 8,000	40 - 60	1.7 - 3.8
Rice husk	14,000	9	19
Wood	8,400 - 17,000	10 - 60	0.25 - 1.7
Gin trash	14,000	9	12
Stalks	16,000	10 - 20	0.1
Coffee husck	16,400	5.9	11.4
Bamboo	15,000 - 18,000	Not measured	3.41
Prosopies	18,000 - 23,000	5.7	1.4
Eucaliptus	16,000 - 18,000	3.9	2.2

onto internal surfaces. Table 1.1 lists the heating value of some biomass sources and their corresponding moisture and ash contents. Further details regarding the concentration of particles actually injected are reported in the next sections.

1.2 Degradation in Gas Turbines

"Why does performance degradation of gas turbine engines occur with operating time?"

The question above has tormented and is still to torment the whole gas turbine scientific and industrial community. This fact can be inferred also by analyzing the trend of the studies focused on this specific issue (see Fig. 1.6). As will become clear in the next sections, the problem of degradation can be traced back to the fact that the installation of filtering systems does not prevent a large number of particles carried by air to enter the gas turbine. As reported by Diakunchak (1992), even under normal engine operating conditions, with a good inlet filtration design, and using a clean fuel the engine flow path components will become fouled, eroded and/or corroded. In the literature, the deterioration types that can affect an engine have been identified in the following headings:

- Performance deterioration recoverable with cleaning/washing;
- Performance deterioration non-recoverable with cleaning/washing;
- Permanent performance deterioration, which is not recoverable after an overhaul and the refurbishment of all clearances, replacement of damaged parts, etc.

Despite all these types of degradation highly impact the gas turbine operation, in this thesis, only the recoverable issues have been taken into consideration. They affect the gas

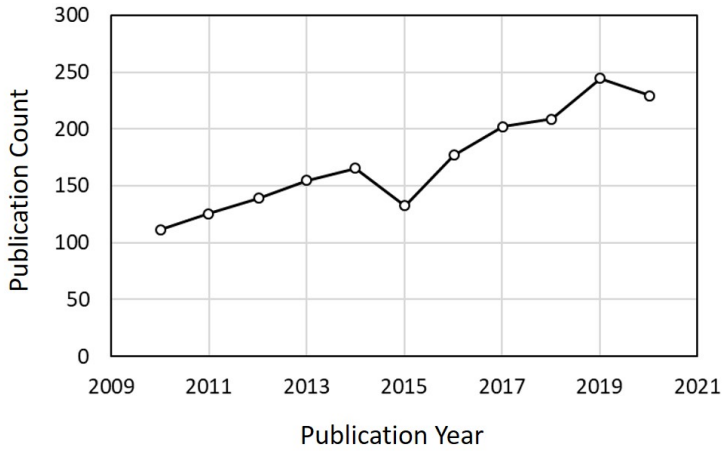

Figure 1.6: Publication trend in the field of gas turbine degradation. From (Sun et al. 2021)

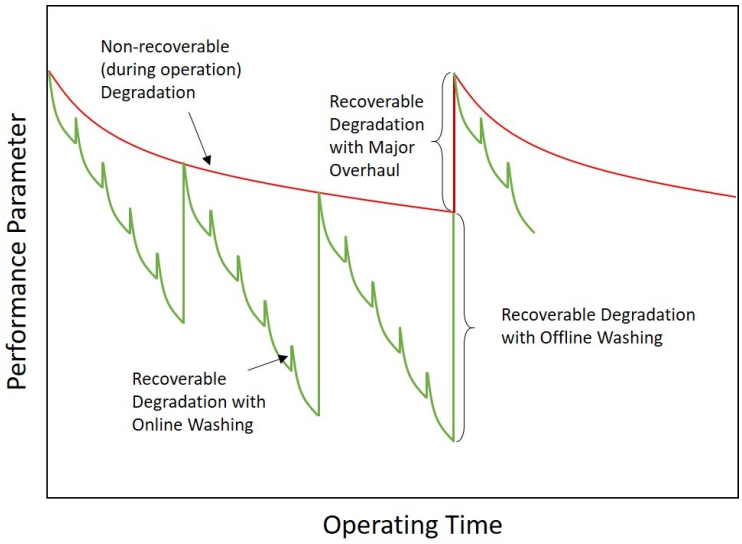

Figure 1.7: Recoverable and non-recoverable degradation. From (Hepperle et al. 2011)

turbine in terms of both performance losses and lifetime reduction. An example of the performance trend affected by these deterioration types has been reported in Fig. 1.7, by adapting the data found in the study of Hepperle et al. (2011). It can be noted, as also reported by Schurovsky & Levikin (1986), that the degradation increases during the first operation period. During this time, the gas turbine unit output and efficiency losses decrease exponentially and they will tend to stabilize.

In order to better understand why the whole engine behaves in this manner when subjected to contaminant ingestion, the effect of degradation in each component of the gas turbine has to be analyzed. In this regard, different works were conducted in the literature focused on the study of the impact of particle ingestion in compressors and turbines singularly. All of them come to the same conclusion: degraded compressors and turbines have deteriorated aerodynamic qualities, which causes a decrease in both the air mass flow rate and efficiency. Simultaneously there is a decrease in the compressor pressure ratio due to

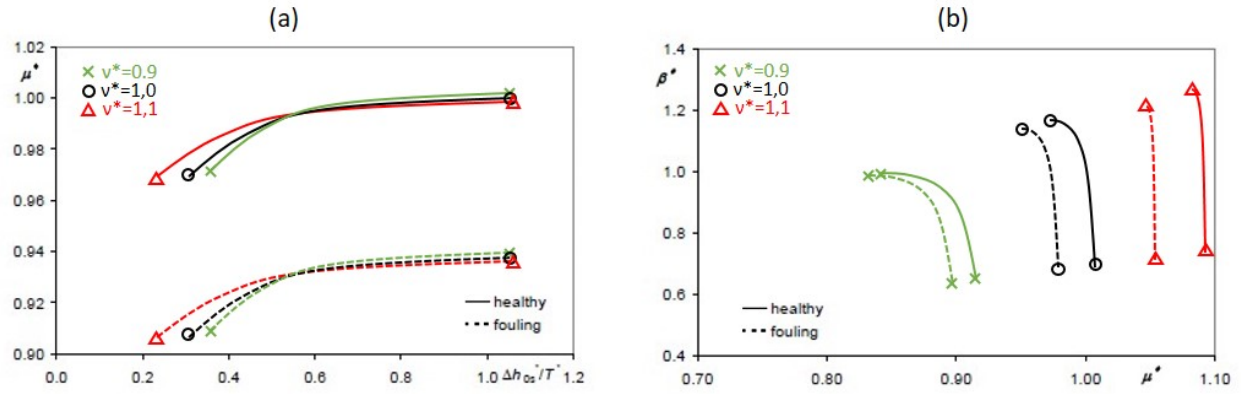

Figure 1.8: Effect of degradation on both axial flow compressors (a) and turbines (b) maps. From (Morini et al. 2009)

reduced gas mass flow through the turbine. This, altogether, leads to a decrease in the gas turbine unit output and to an increase in the specific fuel consumption.

Recently, Morini et al. (2009) reported the actual modification of both compressor and turbine performance maps due to blade deterioration by using a stage-by-stage model. The results are reported in Fig. 1.8 in terms of non-dimensional pressure ratio (β^* and $\Delta h^*_{0S}/T^*$ for the compressor and turbine respectively) against non-dimensional corrected mass flow rate (μ^*) for the turbine (Fig. 1.8(a)) and for the compressor (Fig. 1.8(b)). As can be noticed, degradation causes a shift of the curves toward lower corrected mass flow rate values for both the components.

1.2.1 Degradation Mechanisms

To better understand why particle ingestion leads to performance deterioration and lifetime reduction in gas turbines, all the degradation mechanisms arising from the interaction between these particles and the engine's internal surfaces have to be clear. Among the others, in this thesis, only recoverable issues will be treated, specifically, the ones due to the fouling phenomenon. Nonetheless, in order to report a wide overview of the gas turbine operation problems, also the non-recoverable issues (corrosion and erosion) will be explained in detail in this section.

Corrosion

Corrosion is the loss of material from flow path components caused by chemical reactions between the component itself and certain deposits, such as salts, mineral acids or reactive gases. Generally, is caused both by inlet air contaminants and by fuel and combustion-derived contaminants. Corrosion that occurs in the compressor section is referred to as "cold corrosion" and is due to wet deposits of salts, acid and aggressive gases such as chlorine and sulfides. Corrosion in the combustor and turbine sections is called "hot corrosion". Cold corrosion could be reduced by coating the compressor airfoil. This will protect the compressor sections against the wet corrosion. Hot corrosion, on the other hand, is generally caused by contaminants such as salts (for example sodium and potassium), mineral acids or reactive gases (such as hydrogen sulfide or sulfur oxides). This requires the interaction of the metal surface with another chemical substance at elevated temperatures. It can be considered as a form of accelerated oxidation that is produced by the chemical reaction between a component and molten salts deposited on its surface. A sample of the effects due to the hot corrosion is reported in Fig. 1.9.

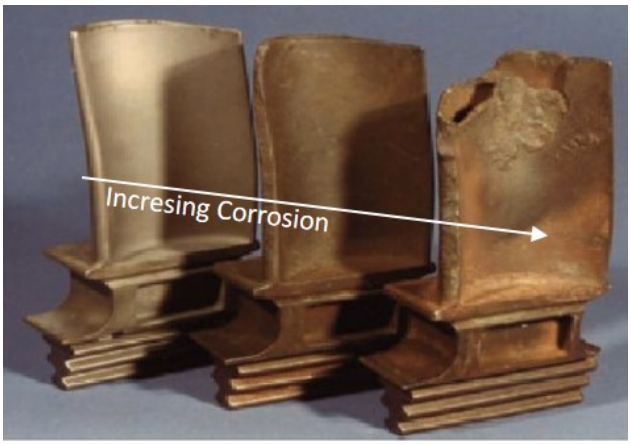

Figure 1.9: Hot corrosion on turbine blades after about 1000 h of operation on distillate fuel containing 2 ppm sodium from sea water contamination. From (Kurz et al. 2012)

Erosion

As suggested by Grant & Tabakoff (1975) and Hamed et al. (2006), erosion, defined as the abrasive removal of blade material by hard particles, is believed to be caused by particles greater than 10 µm in diameter. These particles will rebound on the surface, removing a part of the substrate. Even if the amount of material removed per impact is very small, high particle loads and long operating hours, as turbomachinery usually present, eventually lead to changes in the geometry of the blade. This change in geometry causes deviations in the airflow path (changes in the inlet metal angle) and roughening of smooth surfaces. The latter problem was deeply analyzed in the work of Bons (2010). He found interesting correlations between the roughness levels and the losses at different Reynolds numbers: at low Re, roughness can eliminate laminar separation bubbles (thus reducing loss) while at high Re (when the boundary layer is already turbulent), roughness can thicken the boundary layer to the point of separation (thus increasing loss). In the turbine, roughness has the added effect of augmenting convective heat transfer. While this is desirable in an internal turbine

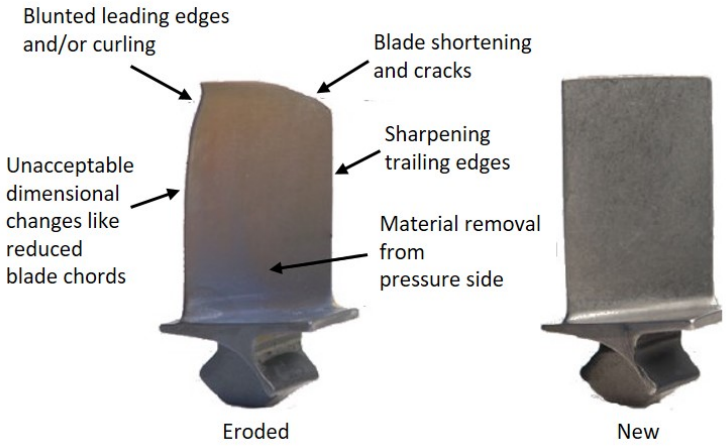

Figure 1.10: Comparison of eroded and new compressor blade. From (Henning et al. 2021)

coolant channel, it is clearly undesirable on the external turbine surface. Erosion problem usually manifests as pitting and cutting back of the leading edges and thinning of the trailing edges, see Fig. 1.10. This last aspect is particularly detrimental since it may result in blade failure even if this damage may be beneficial to performance (Diakunchak 1992). Besides, erosion has different effects on blades and vanes. Typically, eroded rotor blades have reduced solidity at the tip and vanes are affected the most near the root. Particularly in the rotor case, the erosive particles are centrifuged to the outer diameter of the compressor, increasing radial tip clearances or sealing gaps and resulting in higher leakage flows.

Fouling

Particles and drops smaller than 10 µm do not determine erosion phenomena but, in determinate circumstances, cause fouling issues. Fouling consists of the deposit and buildup of material on the flow path surface, as reported in Fig. 1.11. Such deposits are likely to change the shape of the airfoil, the airfoil inlet angle, increase surface roughness, and reduce the airfoil throat opening. The end result is a reduction in the component performance. In particular, fouling restricts flow and causes increased boundary layer thickness both on the blades and along the end walls of the annulus and hub. Blockage of the air path and increased frictional losses reduce the components head and flow, causing an overall reduction in the power capacity and an increase in the specific fuel consumption.

An interesting study of these phenomena was conducted by Suder et al. (1995). In their work, they assessed the effects of an increase in both roughness and thickness on a blade on its performance map. The results obtained are reported in Fig. 1.12 and Fig. 1.13 for the

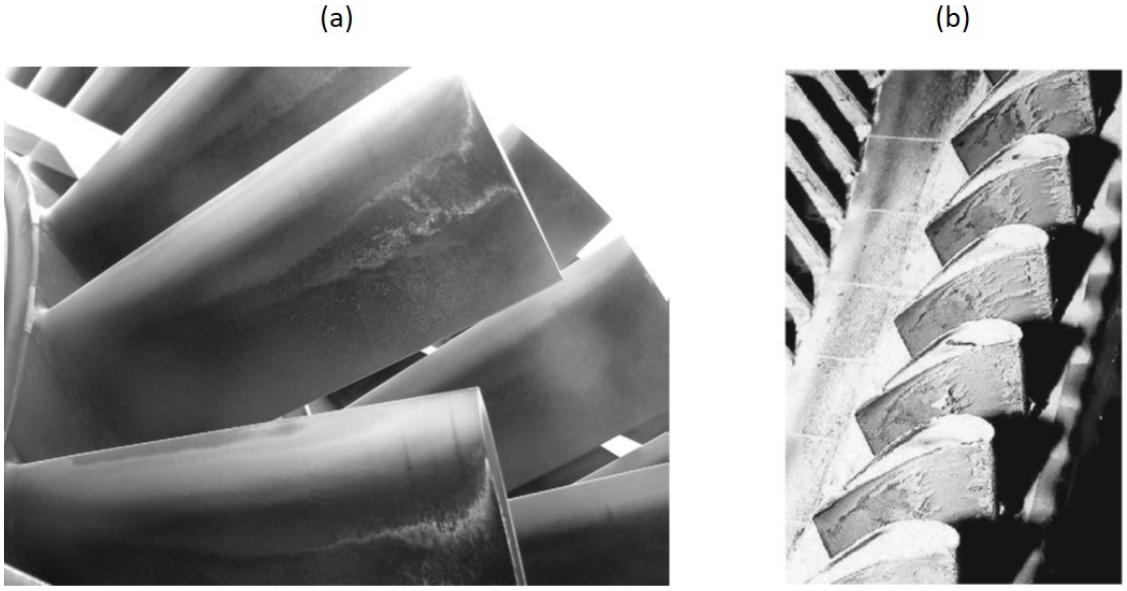

Figure 1.11: Deposits on a compressor rotor (a) and turbine blades (b). From (Kurz et al. 2012) and (Meher-Homji & Bromley 2004).

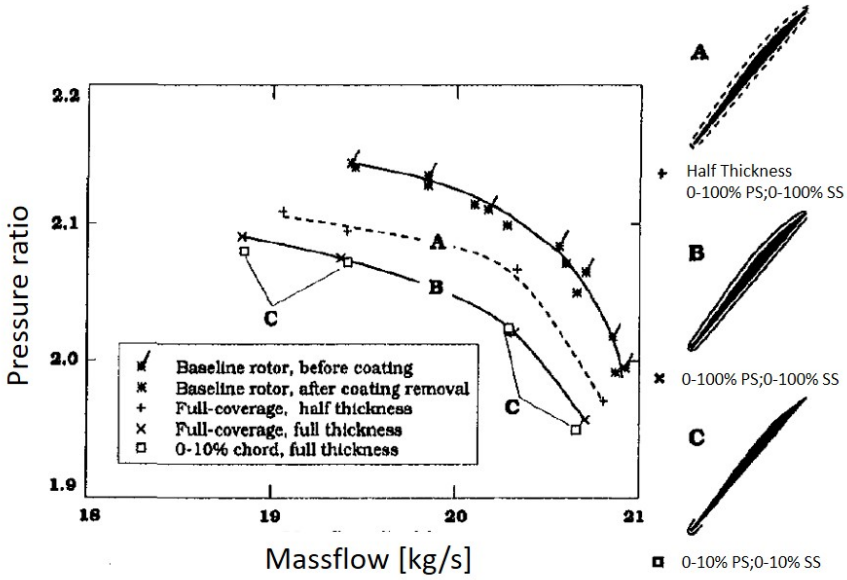

Figure 1.12: Pressure rise characteristics for the smooth coatings at design speed. From (Suder et al. 1995).

thickness and roughness effects respectively. A smooth and rough coating has been applied in precise locations on the blade to understand the areas that are more sensitive to such issues. For what concern the smooth coatings, coatings A and B are full-coverage coatings with coating A being only half as thick as all other coatings.

Coating C covers only the first 10 percent of the blade chord. It can be seen that performance for the half-thickness coating falls approximately halfway between that of the

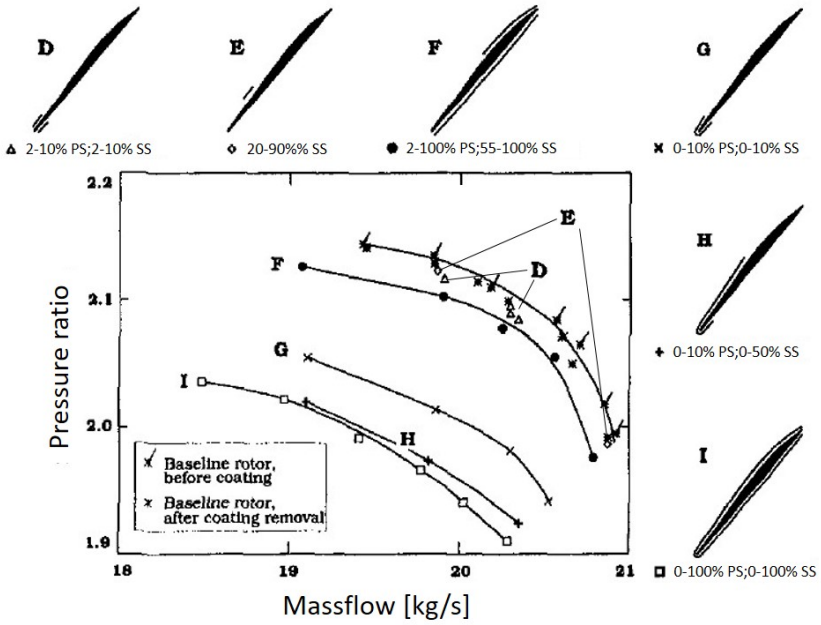

Figure 1.13: Pressure rise characteristics for the rough coatings at design speed. From (Suder et al. 1995).

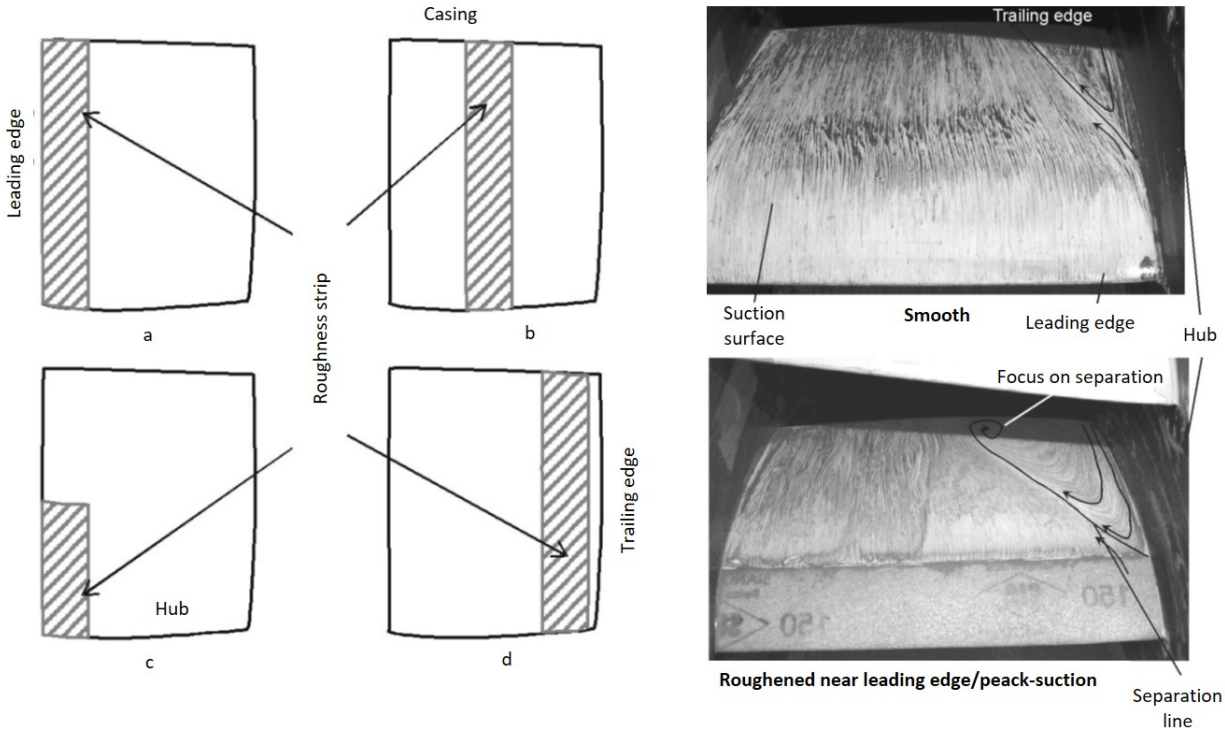

Figure 1.14: Schematic diagram of stator blade with roughness a) full strip (leading edge to peak-suction); b) full strip (midchord); c) 50 % span from hub (leading edge to peaksuction); d) full strip (near trailing edge) and Suction surface flow visualization on smooth and roughened stator around leading edge/peak-suction at design point, ϕ=0.51. From (Gbadebo et al. 2004).

baseline and full-thickness coating. However, the most dramatic result in Fig. 1.12 is that the performance deterioration for case C, in which only the leading edge region is coated, is virtually identical to that of case B, where the entire blade is coated. This result indicates that the added blade profile thickness from 10-90 percent chord does not contribute to the performance deterioration observed for Case B. On the other hand, for the rough coatings, it can be seen that the roughness increase on the suction side and on the trailing edge is more detrimental with respect to the increased roughness on the pressure side. The entire coverage with the rough coating is the worst in terms of performance degradation.
Similar results have been obtained by Gbadebo et al. (2004), by placing emery paper in precise locations on the blade as reported in Fig. 1.14. The roughness results in loss of total pressure, especially in the hub-corner region with a marked increase in the size of the separated region. Surface and flow visualization shows separation on the suction surface/hub corner for the baseline blade and for the roughened blade. With roughness over the leading edge to the peak-suction region, a larger 3D separation on the suction surface and hub wall arise. The separated region is likely to be the cause of the extra loss and deviation when compared with smooth blades.

1.2.2 Heavy-duty Gas Turbines

In their standard operating conditions, gas turbines are designed to process a large amount of air. For example, a 30 000 hp Solar Turbine Titan 250 gas turbine normally ingests roughly 241 000 kg/h of air, and even in a relatively clean environment, for example with a concentration of 1 ppm of contaminants, the amount of particulate that enters the engine without inlet filtration is equalled to 5.78 kg each day (Wilcox et al. 2010). This load of particulate justifies the employment of filtering systems that are placed with the aim of cleaning the air processed by the machine. Properly selecting and maintaining the filtration system can increase the performance and life of the gas turbine and minimize the required and unexpected maintenance. The correct selection of the filtration system is a complicated process that involves the knowledge of the environment in which the engine works (contaminants that the filter needs to remove), and the increased pressure drop compared to the increase in filter efficiency (Wilcox et al. 2010).

Filtration System

Without inlet filtration, particles of every size, depending on the site of installation, could easily enter the gas turbine and then collide with its internal surfaces, leading to issues such as erosion, fouling and corrosion. Although the evident positive side, that is the cleaning of the entering air, inlet filtration has also negative effects. The negative side of filtration is that whatever is placed in the path of air coming into the gas turbine causes a pressure loss, resulting in reduced performance or efficiency of the machine. However, inlet filtration will help to sustain the gas turbine performance above an acceptable level and minimize the occurrence of the degradation effects discussed above. Inlet filtration is hence a trade-off. It is clear that filtration is needed, the challenge is to keep pressure loss to a minimum while removing a satisfactory amount of particles and moisture. To achieve efficacious filtration, the intake of the engine is typically provided with several filter stages, two or three are generally sufficient, in order to remove different types of material from the air. Fig. 1.15 shows an exemplified view of these multistage filtration systems arrangement. In these designs, a prefilter or weather louvre can be used first to remove erosive particles, rain, and snow. The second may be a low to medium-performance filter selected for the type of finer-sized particles present or a coalescer to remove liquids. The third filter is usually a high-performance filter to remove smaller particles less than 2 µm in size from the air.

The filtration efficiency is calculated as the ratio between the weight, volume, area, or the number of particles entering the filter to the weight, volume, area, or the number and the particles captured in the filter and ratings, respectively. The mechanisms employed by the filters to capture these particles are different, and include:

- **inertial impaction:** this type of filtration is applicable to particles larger than 1 µm

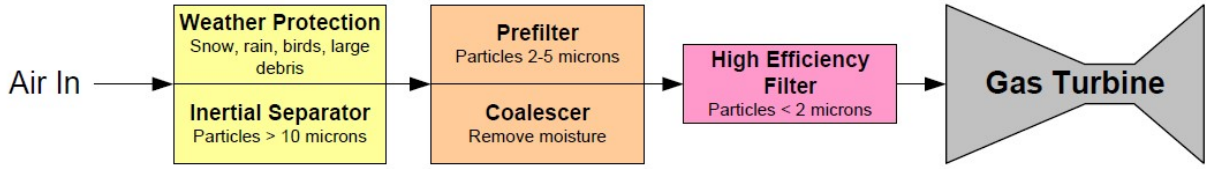

Figure 1.15: Multistage filtration system. From (Wilcox et al. 2010).

in diameter. The inertia of the large heavy particles in the flow stream causes the particles to continue on a straight path as the flow stream moves to go around a filter fibre. The particulate then impacts and is attached to the filter media and held in place. This type of filtration mechanism is effective in high-velocity filtration systems.

- **diffusion:** this type of filtration is effective for very small particles typically less than 0.5 µm in size with low flow rates. These particles are not held by the viscous forces in the fluid and will diffuse within the flow stream along a random path. The path the particle takes depends on its interaction with nearby particles and gas molecules. As these particles diffuse in the flow stream, they collide with the fibre and are captured. The smaller the particle and the lower the flow rate through the filter media, the higher probability that the particle will be captured.

- **interception:** this type of filtration occurs with medium-sized particles that are not large enough to leave the flow path due to inertia or not small enough to diffuse. The particles will follow the flow stream where they will touch a fibre in the filter media and be trapped and held.

- **sieving:** this type of filtration occurs when the space between the filter fibres is smaller than the particle itself, which causes the particle to be captured and contained.

- **electrostatic charge:** This type of filtration is effective for particles in the 0.01 to 10 µm size range. The filter works through the attraction of particles to a charged filter. In gas turbine applications, this charge is applied to the filter before installation during the manufacturing process. Filters always lose their electrostatic charge over time because the particles captured on their surface occupy charged sites, therefore neutralizing their electrostatic charge. As the charge is lost, the filter efficiency for small particles will decrease.

All these mechanisms with their respective efficiency are sketched in Fig. 1.16. The figure report also the total efficiency of the filtration system at the beginning of its life (solid black line), and its alteration consequent to the loss of the electrostatic charge (dashed black line). It can be noticed that the total efficiency of the stages is high above 1 µm and below 0.1 µm. In between, there is a range of diameter in which a considerable amount of particulate can

easily make its way through the filters and reach the inlet of the machine. Unfortunately, as already explained in the previous sections, such a range of particles is the one that is most likely to cause fouling.

Degradation in Land-based gas turbines

Land-based gas turbines are affected the most by compressor fouling, as reported in Fig. 1.17. Zaba (1980) analyzed the performance variation over time, showing the decrease in output power and efficiency. From Fig. 1.17 it can be distinguished recoverable fouling from not recoverable deterioration. It can be seen that even after the washing events (for example points 3 to 4), the initial values of efficiency and power output are not achieved. The missing part is the non-recoverable erosion/corrosion that keeps increasing over time. Nonetheless, it can be seen that the most significant share of the performance losses is due to fouling, which works up to ten times faster than the non-recoverable damage.

Nowadays, compressor fouling is gaining attention since maintenance costs are increasingly important. This is also confirmed by the increase in the publications focused on this particular issue, as can be seen in Fig. 1.18. The first study conducted on deposits on blade surfaces is the one of Aguet & Von Salis (1960). They reported that the only occasion when deposits build up in air compressors is during heavy rain conditions, since water can enter the subterranean air passage between the air intake and the inlet flange of the low-pressure compressor. This water is then carried away as droplets in the airstream and evaporates in

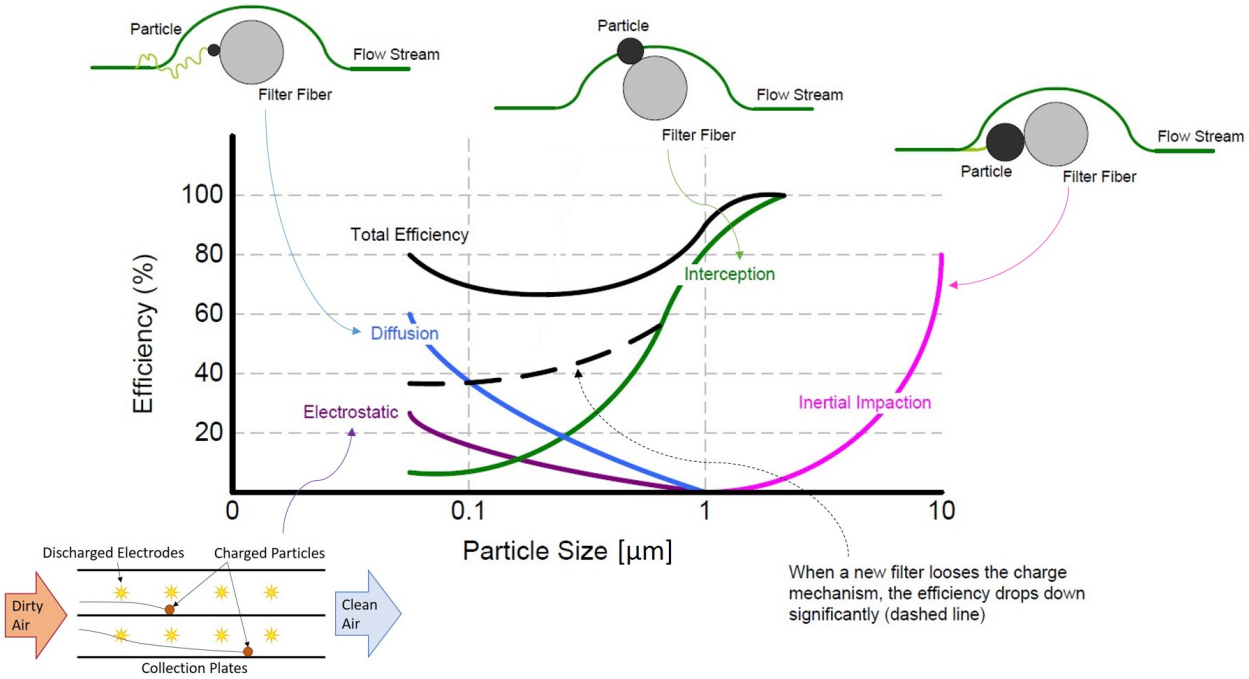

Figure 1.16: Combination of Filtration Mechanisms to Obtain Filter Efficiency at Various Particles Sizes. From (Wilcox et al. 2010)

the compressors, so that the solid particles contained therein remain on the blades. Another heavy-duty application is reported in the study of Hill et al. (1960). During the overhaul, some fouling issues were found in the compressor sections. A particular compressor blade deposit was found by Bultzo (1980). He reported that the fourth to the eighth stages were fouled with the pigmentation material used in paint (titanium dioxide, verified by X-ray diffraction). The use of a scanning electron microscope showed the layering of the primer and finished coats. The author concluded that since the painting was in progress within 30 m of the turbine inlet, airborne aerosol-like droplets were being ingested by the gas turbine. After sufficient work had been done on the air by the axial compressor, the solvent was still contained in the droplets of aerosol, resulting in localized fouling. The heaviest fouling was in the sixth-stage position.

This localized presence of fouled areas along the compressor axis was also found by Tarabrin et al. (1998*b*). In their work, they investigated the contamination of compressor blades for a Nuovo Pignone MS5322 R(B) gas turbine engine. This power unit operated for

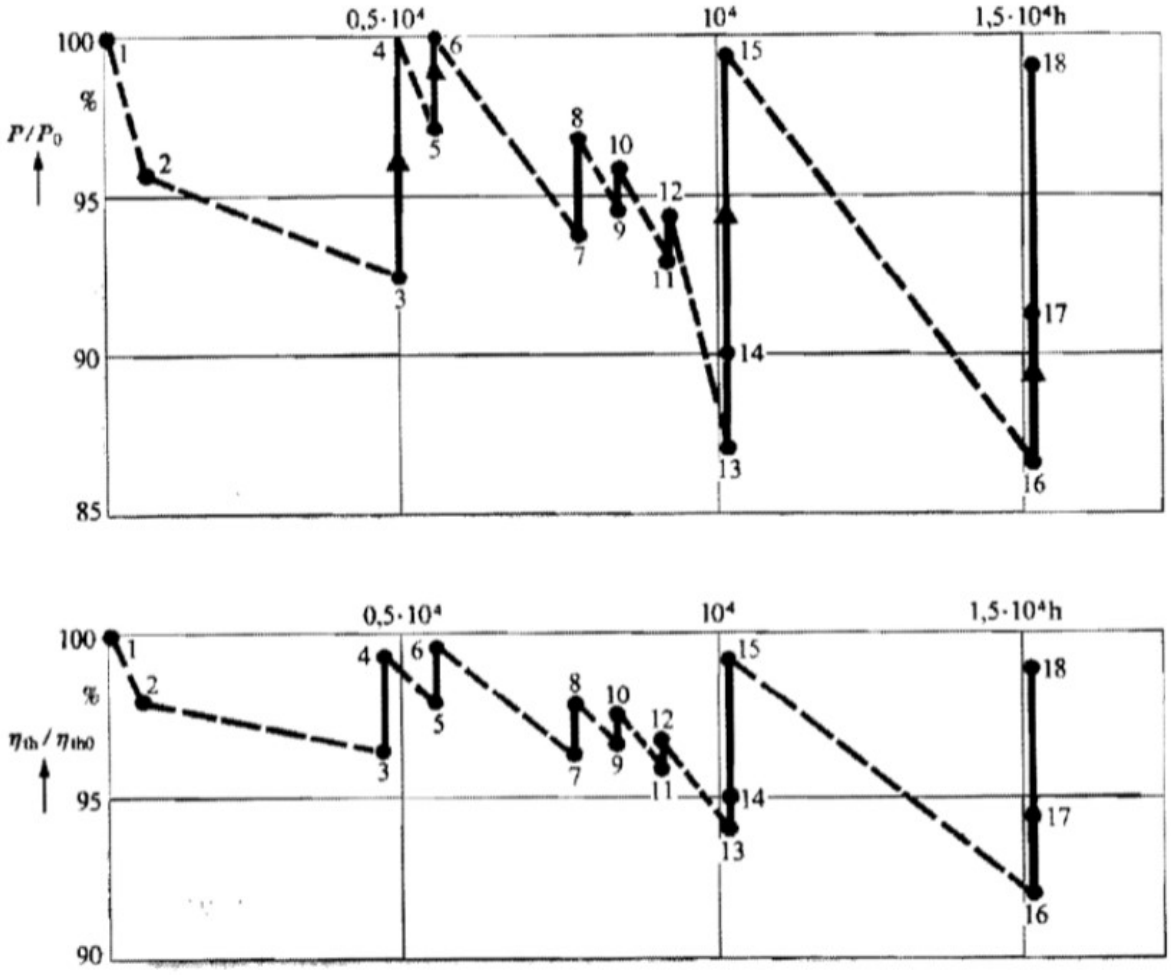

Figure 1.17: Variations in output and thermal efficiency as functions of time (in hours) when compressor is fouled, and recovery obtained by cleaning. From (Zaba 1980)

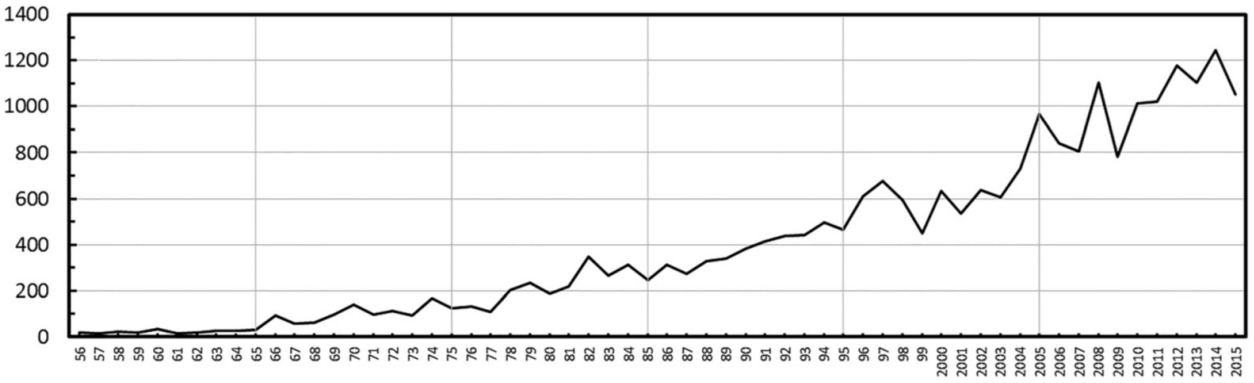

Figure 1.18: Overall ASME Turbo Expo contributions focused on the study of fouling. From (Suman et al. 2017)

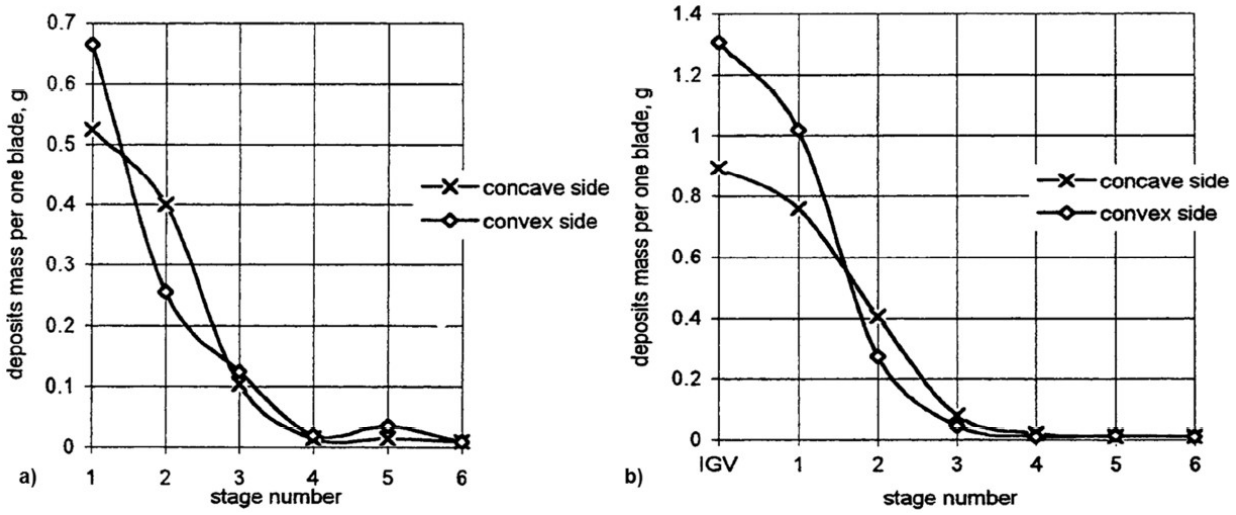

Figure 1.19: Weight distribution of deposits on the convex and concave sides of the axial compressor blades: a) rotor, b) stator. From (Tarabrin et al. 1998*b*)

a long time without blade washing but only the first 5 to 6 stages over 16 are subjected to fouling. Fig. 1.19 depicted the weight distribution of deposits for rotor blades (Fig. 1.19a) and stator vanes (Fig. 1.19b). The inlet guide vane, as well as the rotor and stator blades of the first stage, present more deposits on the convex side. The deposited mass on the other stages is approximately equal for the convex and concave sides. This mass decrease from the first to the sixth stage. Beyond the seventh stage, the amount of deposit is negligible. The authors pointed out that the deposit amount is greater on the stator vanes than on the rotor blades due to the cleaning effects provided by the centrifugal forces on particles.

Another similar study, but more focused on off-shore heavy-duty gas turbines, has been conducted by Syverud & Bakken (2007), where the location of salt deposits in General Electric J85-13 axial compressor was reported. The experimental tests have shown that the salt deposits were mainly located along the leading edge of the first four stages and on the pressure side of the stator vanes along the hub. The contaminants were generated by using salt carried by water droplets. For this reason, significantly fewer deposits were observed

on the rotor blades compared to the stator vanes due to the centrifugal force. The results found by Syverud & Bakken (2007), compared with the ones obtained by Tarabrin et al. (1998*b*), are reported in Fig. 1.20. A good agreement can be observed between the two. More recently, a deeper analysis of the deposition pattern on a multistage axial compressor has been performed by Suman et al. (2021). They conducted an experimental campaign on the Allison C18 compressor unit at two different regimes, varying the contaminant type (Arizona Road Dust, ARD and Carbon Black, CB), its diameter, and the inlet humidity. The common patterns which characterize the particle adhesion over the stages found by the authors are reported in Fig. 1.21. The solid black colour identifies the most affected regions while the honeycomb pattern represents lighter surface contamination. From the analysis, it can be concluded that smaller particles appear more suitable to generate deposits over the compressor stage. Coarser particles seem to be able to generate few deposits, located at the LE and at the separation regions. Regarding the effects of air humidity, it works as a promoter of particle deposition: the presence of a higher value of relative humidity determines a greater particle deposition over all stages, especially in correspondence with the pressure side of the stator vane.

Hot section fouling effects in land-based gas turbines are similar to the aero-engine applications. The reader is therefore referred to section 1.2.3 for further details on this issue.

1.2.3 Aeronautical Gas Turbines

The current in-service aero engines have been designed and developed assuming clean air, free from airborne contaminants. In reality, the environment in which these engines operate

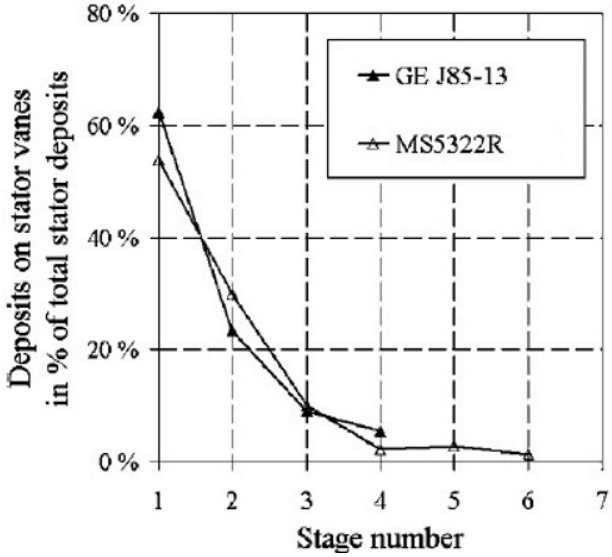

Figure 1.20: Salt deposits found after experimental tests with salt ingestion: percentage distribution of deposits with respect to the total stator deposits on stator vanes. From (Syverud & Bakken 2007)

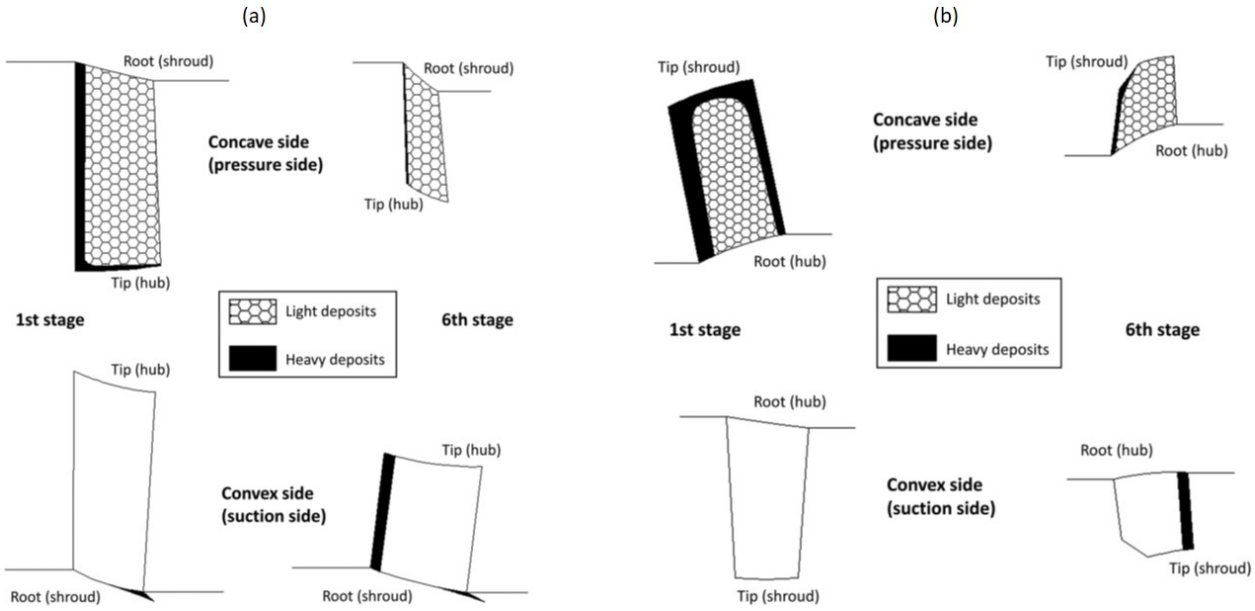

Figure 1.21: Deposit patterns on stator vanes (a) and rotor blades (b). From (Suman et al. 2021)

is often defiled with particulate as already explained in the previous sections. These aero gas turbines can fly through dust clouds for time intervals ranging from a few seconds to several minutes, as reported by Clarkson et al. (2016). As an example, in catastrophic events such as volcanic eruptions, the generated ash clouds can carry particulate with concentrations as high as $250\,\mathrm{mg_{ash}/m^3}$ of air. For a high thrust turbofan engine processing a mass flow rate of approximately $500\,\mathrm{kg/s}$, the resulting rate of ingestion of solid contaminant can reach the order of $1\,\mathrm{kg_{ash}/s}$. The presence of particles at cruising altitude or during take-off, therefore, poses a serious threat to the operation of aircraft engines. The seriousness of this threat is highlighted by the disruption brought to air travel by volcanic events in recent years, in which large civil turbofan engines failed after only a few minutes of ash ingestion (Dunn 2012*a*). Ultimately, for aircraft to fly again operational guidance was updated, allowing safe operations in ash concentrations up to $2\,\mathrm{mg_{ash}/m^3}$. This enabled most of Europe's airspace to re-open but only after over 100000 flight cancellations and an estimated cost to the commercial aviation industry of £1.5 billion.

Filtering actions

In aero gas turbines, both cold and hot sections are affected by deposition. In these applications, no filtering system is placed in front of the intake, since the pressure drop that it generates can dramatically influence the engine thrust, and therefore the rate-of-ingestion of particles is higher than the land-based gas turbines. Nonetheless, there are mechanisms different from the filtration systems already exposed that act in this type of engine. To better understand what they are, it is necessary to distinguish fixed-wing aircraft engines from rotorcraft engines. Specifically, the former ones are generally turbofan, whilst the second

ones are turboshaft.

For what concern the turbofan engines, part of the air does not actually enter the core engine, but it contributes to the thrust (actually, the fan contributes to more than the 85 % of the thrust) since it is processed by the fan. Hence, the fan acts like a particle separator for the entire engine depending on the ingested particle size and flight conditions (i.e., true airspeed and rotating speed of the fan), where smaller particles move along the main airflow and pass through the fan. Therefore, this particle fraction does not have any interaction with fan surfaces and is directly ingested into the core stream flow. In contrast, larger particles have large inertia and detach from the mean flow trajectories. Once detached, these particles can collide with fan surfaces and, depending on the impact forces and impact angle, be centrifuged out of the core stream flow into the bypass stream flow (see Fig. 1.22). Thus, the particle–fan interactions have a direct impact on the particle size distribution and consequently on the resulting particle mass concentration entering the engine core section, which is the most critical part of the engine for air safety (Vogel et al. 2018). Interesting results in the filtration capacity of the fan were found by Vogel et al. (2018). They investigated volcanic ash particle ingestion into a representative engine, powering current wide-body aircraft, for three different fan power conditions and two different flight altitudes, and used a numerical CFD (Computational Fluid Dynamics) particle-tracking model to calculate particle–fan interactions as a function of various volcanic ash particle sizes. The results, reported in Fig. 1.23, illustrate that particles smaller than 2 µm do not often interact with the fan surfaces (probability <5 %), but more interactions occur for larger particles. The interaction probability is also strongly dependent on the rotation speed of the fan. The highest

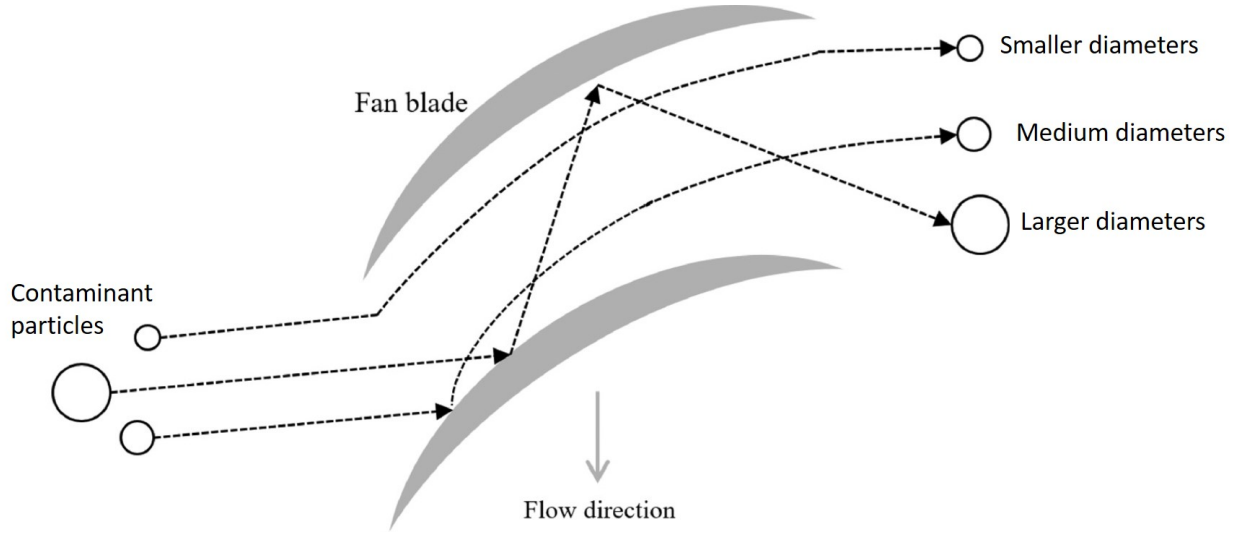

Figure 1.22: Particle trajectories through the fan: (a) smaller particles follow closely streamlines of the gas-phase flow and have no or limited contact with the fan surface and (b) larger particles are dominated by their inertia and detach from the gas-phase flow streamlines, leading to partial or full surface contact. From (Vogel et al. 2018)

investigated fan power, 90 % of full power, resulted in a 100 % interaction probability for volcanic ash particles larger than 63 µm, which represents the upper size of the fine fraction of volcanic ash. The largest volcanic ash particle diameter (1100 µm) and the highest fan power condition (high power) in this study resulted in a maximum concentration reduction factor of 2.53 at 10 700 m.

The other type of engine considered are turboshaft engines, that are mostly used in helicopters. Helicopter employment in civil and military operations is widespread and often essential for critical tasks such as search and rescue missions, firefighting, or medical evacuations. Landing and take-off operations from rugged and harsh sites make these kinds of manoeuvres extremely complex and affected by low margins of error. Lands characterized by dusty floor conditions or poorly aggregated soil (such as arid locations and deserts) are considered the worst scenarios for helicopter operations to be successfully carried out. In such locations, dust cloud-raising events (named brownouts) are extremely likely and potentially harmful to the helicopter's operability (Vulpio et al. 2021). For this reason, helicopter engines are equipped with advanced separator systems to protect their rotating components from erosion and damage. One of the most used separators is called Vortex Tube Separator (VTS), which relies on centrifugal forces created by cyclonelike systems. The diagram shown in Fig. 1.24 is an example of such a vortex particle separator. The outer tube, labelled 12 in Fig. 1.24, has an inner diameter of 18 mm, a total length of 60 mm, and a vortex generating region of length 20 mm; however, these dimensions vary between applications. The area labelled 20 in Fig. 1.24 is known as the separation region, in which the vortex forms a clean air core. Adjacent to this and common to all VTS is the second tube of smaller diameter but

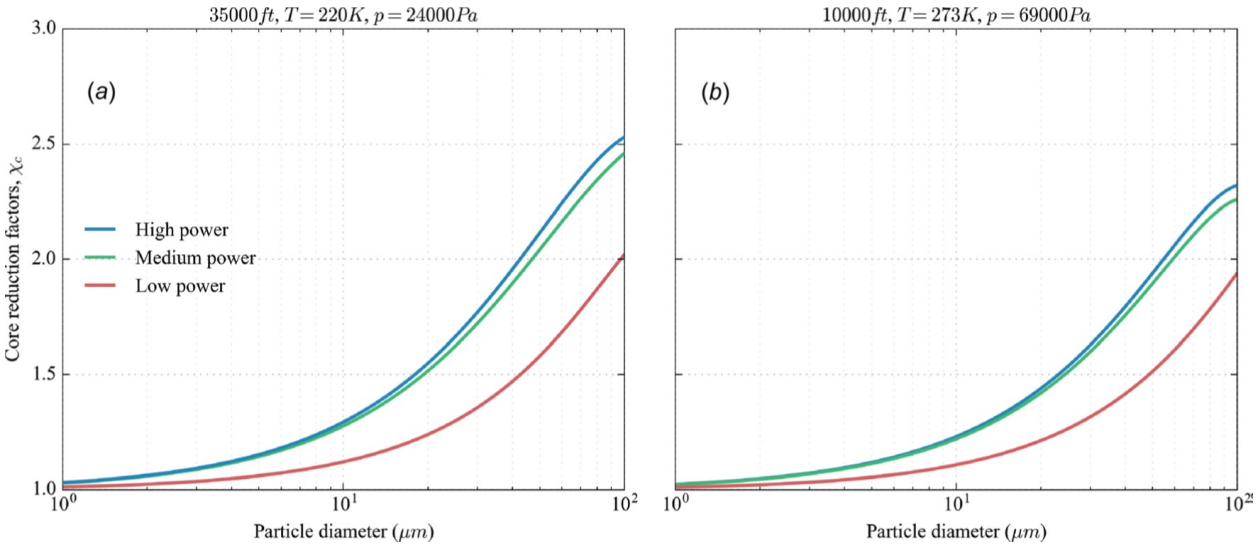

Figure 1.23: Simulated core stream reduction factors for (a) 10 700 m and (b) 3000 m altitudes as a function of fan rotation rates and volcanic ash particle diameter. The coloured lines represent the low power (red), medium power (green) and high power (blue) condition of the fan. From (Vogel et al. 2018)

co-axial with the main tube, through which the clean core air (26) flows. In this example it is tapered, increasing in diameter downstream, but in other inventions, the diameter may remain constant. The design often depends on the means of removing the dirty air. The centrifuged particulate matter (22) proceeds through the annular orifice between the inner and outer tube and arrives at a scavenge passage, such as that labelled 46. The dirty air is then often scavenged away through holes either in the base of the passage, or the tube walls (48) and proceeds into a chamber common to all scavenge tube outlets and discharged to the environment (Bojdo 2012). As for the intake protection for land-based gas turbines, also for the particle separators, there is a constant battle between achieving good separation efficiency for a minimum pressure loss.

Degradation in Aeronautical gas turbines

Although the presence of the fan or the VTS manages to remove the larger particles from the core stream flow, a huge amount of medium and smaller particles is able to bypass these systems and enter the core engine. These particles can cause both erosions and fouling in the compressor section, and mostly deposition in the turbine section. In this thesis, only the deposition issue is treated. For what concern the compressor fouling, the mechanisms and the effects are similar to what was already reported in section 1.2.2 for land-based machines. Since the hot components deposition is the main performance degradation driver when the TET (Turbine Entry Temperature) is above 1283 K (that basically includes all the current operating engines, Kyprianidis (2011)), only this part of the engine is treated in this section.

Hot deposition happens since the particles following the core flow are heated through the combustor. If the Turbine Entry Temperature (TET) is sufficiently high, particles soften (or even become molten) and can adhere to the surrounding solid surfaces. This commonly occurs on the first component encountered, the high-pressure turbine nozzle guide vanes (see Fig. 1.25(a)). The extent, location and distribution of this deposition depend on multiple factors including the chemical composition of the particles, operating conditions in the NGV

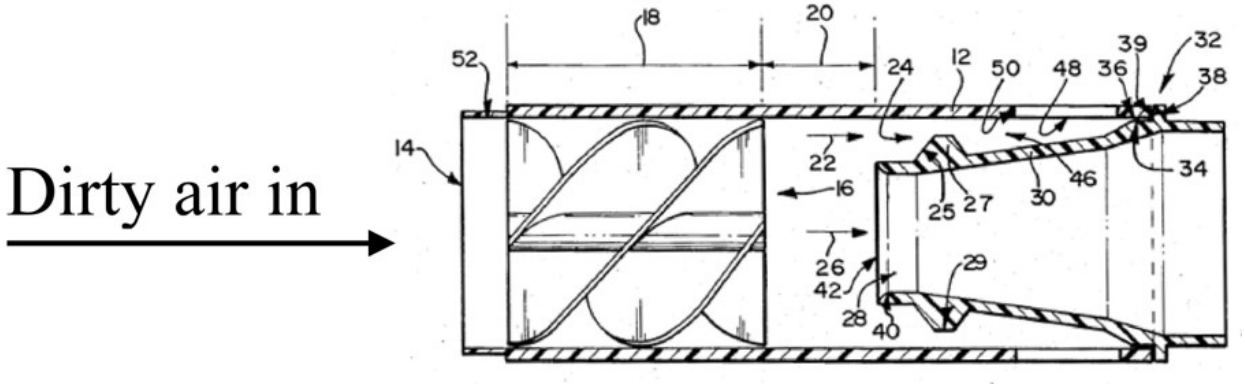

Figure 1.24: Vortex tube separator according to US Patent 4,985,058. From (Bojdo 2012)

(Nozzle Guide Vane) stage, NGV geometry and the architecture of the engine (Adams et al. 1987, Kim et al. 1993). In general, the deposition of particles can change the shape of the vane in an uncontrolled way. Particles sticking on the first stage nozzle of the high-pressure turbine result in performance reduction by means of two mechanisms. Firstly, localized changes in the surface roughness determine premature boundary layer separation, hence an increase in the overall stage pressure drop (Kellersmann et al. 2018). Fig. 1.25(b) reports an example of the effect of this phenomenon in terms of the downstream total pressure coefficient for a fouled HPT NGV. Secondly, the thickening of the airfoils caused by the deposit build-up results in a constriction of the nozzle throat between adjacent vanes, reducing the flow area and capacity. This not only affects the local performance of the high-pressure turbine but has implications throughout the engine. This is observed most significantly in the compressor, which is required to operate with a reduced flow rate whilst maintaining the required pressure ratio. As a result, the operating point of the compressor moves towards the stability line as depicted in Fig. 1.26(a), reducing the available surge margin and therefore operating safety margins. It follows that with the increase in the deposit thickness the combination of restricted mass flow and deteriorated compressor efficiency results in an unstable condition operating point at which the engine will surge.

An additional implication of deposition damage on nozzle guide vanes is seen in the reduced performance of the high-pressure turbine, where, as a result of reduced stage efficiencies due to increased surface roughness and premature boundary layer separation, the enthalpy drop across each stage reduces, leading to increased temperatures in the following turbine stages. This can be monitored on-wing through the exhaust gas temperature (EGT) and corresponding EGT margin, defined as the difference between the maximum allowable EGT or redline limit and that measured in the exhaust gases, as shown in Fig. 1.26(b). Ultimately, with the combined effects of flow rate restriction and efficiency reduction due to

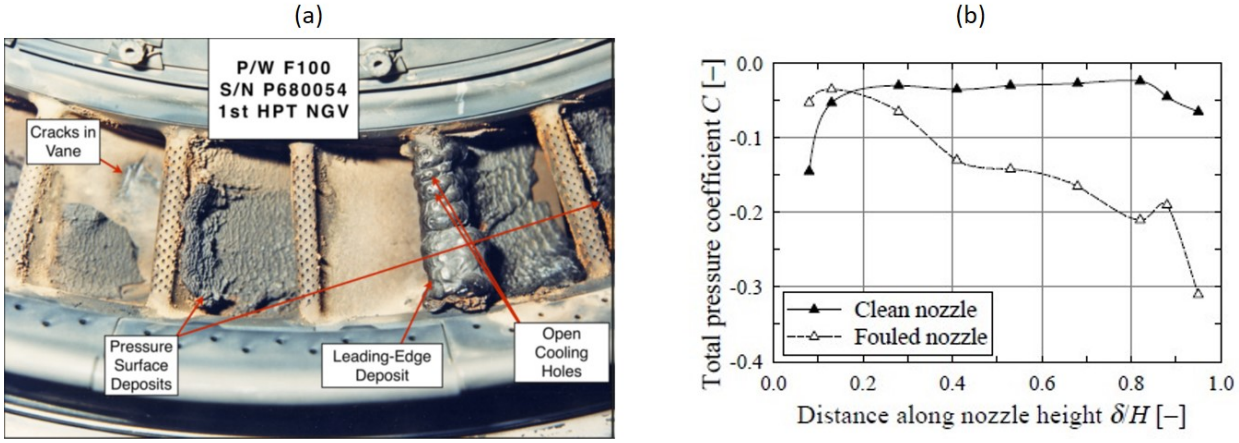

Figure 1.25: Examples of: (a) Deposits on high-pressure turbine vane leading edge for P/W F100 S/N P680054 (from Dunn (2012*a*)), and (b) Distributions of the downstream total pressure coefficent for a fouled HPT NGV (from El-Batsh (2001)).

deposition, the exhaust gas temperature can increase to a point where the available EGT margin is expended. This results in compromised fatigue life of individual components due to increased thermal stresses, leading to reduced component lives, more frequent maintenance intervals and elevated costs for the operator. Another damage mechanism, the deposition of particles in cooling channels, also occurs in the high-pressure turbine. This results in reduced cooling air flow rates, a reduction in the heat transfer rate between the vane surface and core flow and therefore elevated metal temperatures on the vanes. This in turn increases the thermal stresses endured by these components and reduces their usable life. In severe cases, elevated metal temperatures have been observed to cause burn-through of the vane surfaces and structural failure of components (Dunn 2012*a*).

As already exposed, one of the most hazardous consequences of hot section deposition is the shut-down risk of the whole engine. This is unacceptable for allowing scheduled commercial flights to take place in case of excessive ash or dust concentration in the air. This remark is the basis of the safe-to-fly chart proposed by Rolls-Royce and reported in Fig. 1.27. The two lines represent the mass flow of ash through an engine core for each ash concentration in the atmosphere for two different flows (45 kg/s and 22.5 kg/s, representative of large to medium civil turbofans at cruise). The mass flow of ash (y-axis) is the concentration of ash in the environment (the x-axis) times the ratio of the mass flow of air through the engine's core to the density of air. Therefore, given the power and altitude, all the ash concentrations of interest are on a diagonal line (as the blue and green lines). The events in the top-right region of the chart are representative of failures reported in the past, either in test conditions

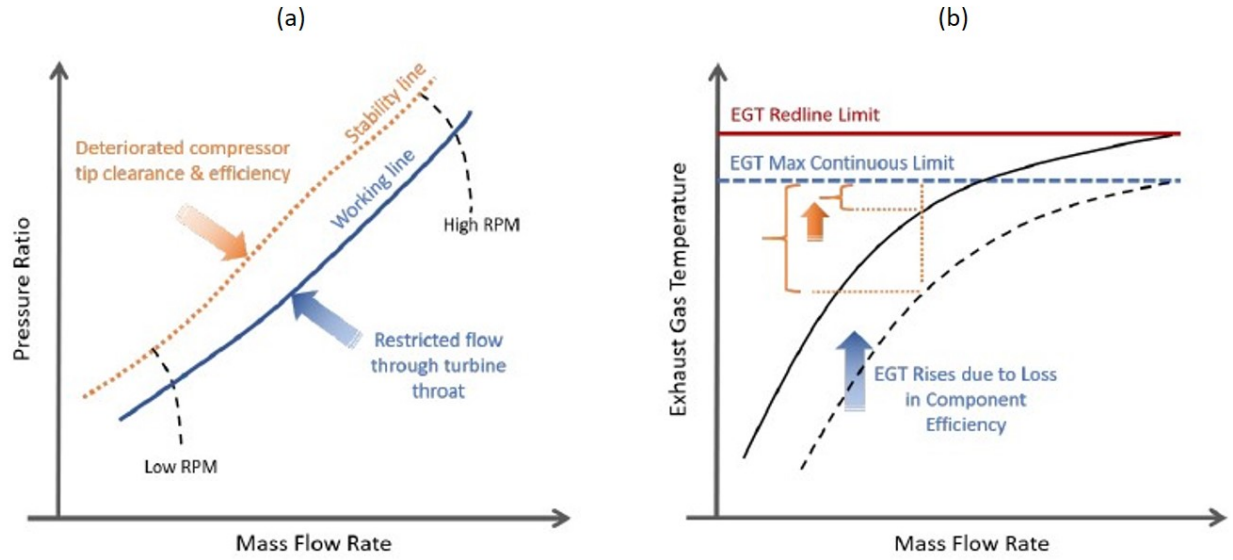

Figure 1.26: An example compressor map showing (a) how the combined effects of turbine flow restriction and degraded compressor efficiency result in reduced surge margin and (b) an example of how rising exhaust gas temperature due to reduced turbine component efficiency can cause the exhaust gas temperature red-line limit to be exceeded. (from Ellis (2021)).

(Calspan tests, Dunn (2012*a*)) or actual encounters. What is important to notice here is the different time scales of hot-section-deposition-related failure events, with respect to the loss of efficiency of the land-based units due to compressor fouling. The BA-009 event, for example, reports a flight of about 7 minutes into the cloud, before losing the 4 engines in rapid succession. This remark should be considered when planning and designing numerical investigations of hot section deposition. The time scale of the performance variation is not completely "uncoupled" from the time scale of the particle deposition phenomenon.

1.2.4 Washing operations

The degradation caused by the adherence of particles on the compressor airfoil and annulus surface can be partially recovered by compressor washing. In this regard, the state-of-the-art method consists of the injection at the front end of the gas turbine of a specific liquid (it could be simple water or a detergent), that penetrates the gas path, and dissolves and removes the deposits. There are currently two washing methods in use for liquid washing: offline wash and online wash. Offline cleaning can restore almost entirely the performance but requires the stop and the disassembly of the engine. This operation is extremely costly and time-consuming (Casari et al. 2021). Online washing can relieve the effect of fouling

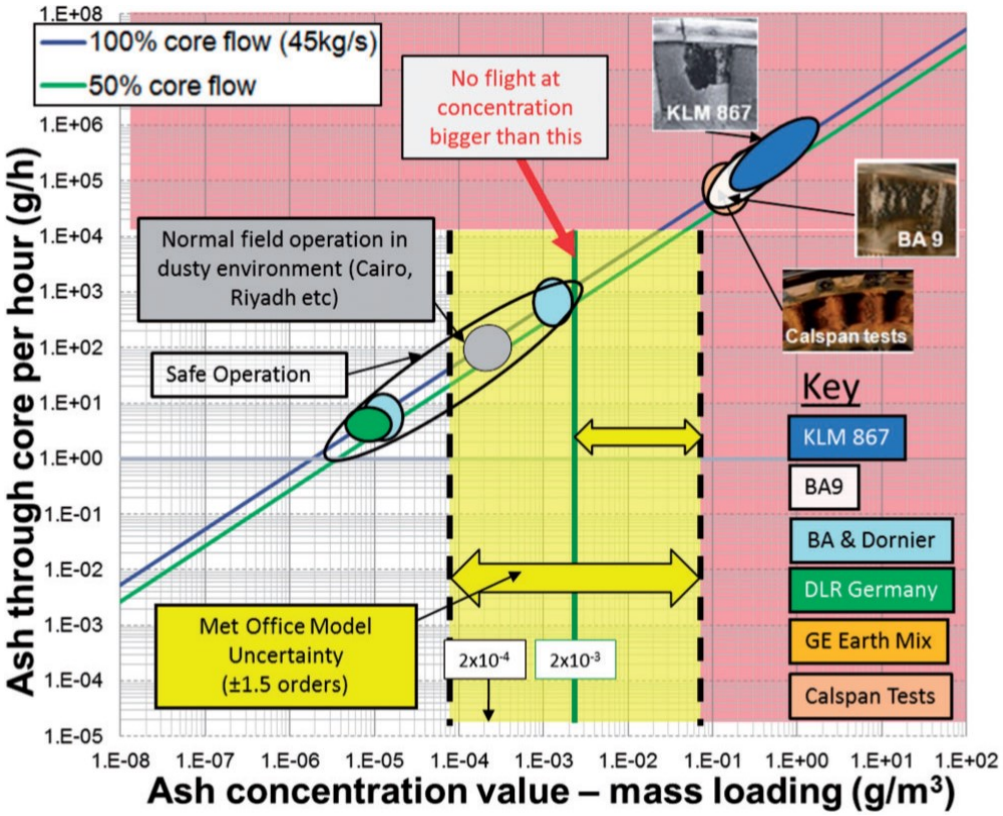

Figure 1.27: Safe-To-Fly Chart, Rolls-Royce. No flight should take place at the right of the green line ($2\,\mathrm{mg/m^3}$). The yellow-shaded area is the uncertainty level that affects current prediction models from MET Office. (from Clarkson et al. (2016)).

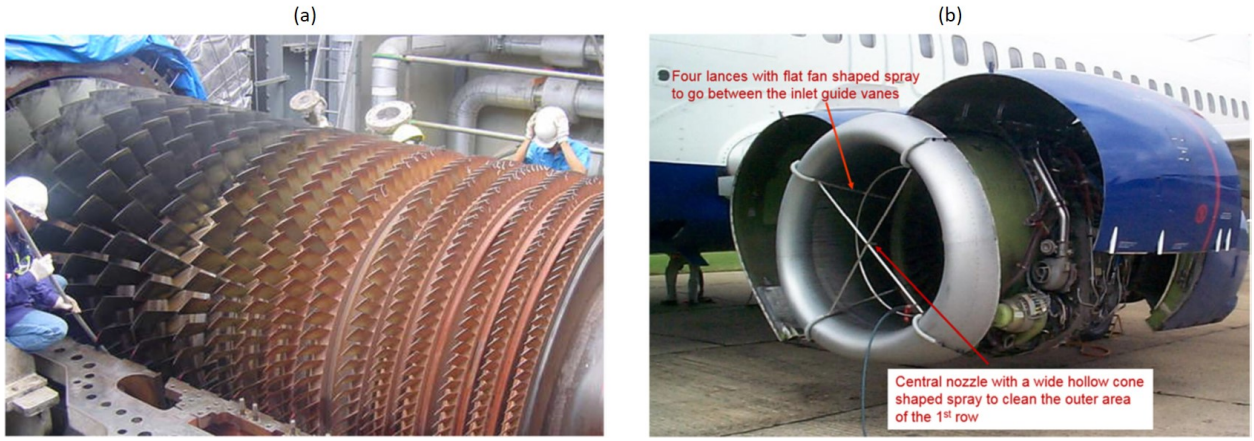

Figure 1.28: Examples of offline (a) and online (b) washing. from Igie (2017).

if provided with a certain frequency (Mund & Pilidis 2005, Stalder 2000). This technique does not require the engine to be stopped or dismounted and can be carried out on site. Examples of offline and online washing are reported in Fig. 1.28. Many attempts have been done by maintenance operators to improve the effectiveness of online washing by developing new techniques and cleaner products. Online washing is done during gas turbine operation by injecting the cleaning solution into the compressor section while the engine is running in normal operation, hence avoiding the associated downtime cost. Therefore, fouling mechanisms and the related performance losses as well as the washing operation act together during the normal operation of each gas turbine. The systematic detection of these occurrences is difficult to be assessed and, usually, only on-field detection is reported in the literature (Tarabrin et al. 1998*a*, Perullo et al. 2015).

A deep investigation of the performance recovery thanks to washing after particle ingestion in an axial flow multistage compressor has been conducted by Casari et al. (2021).

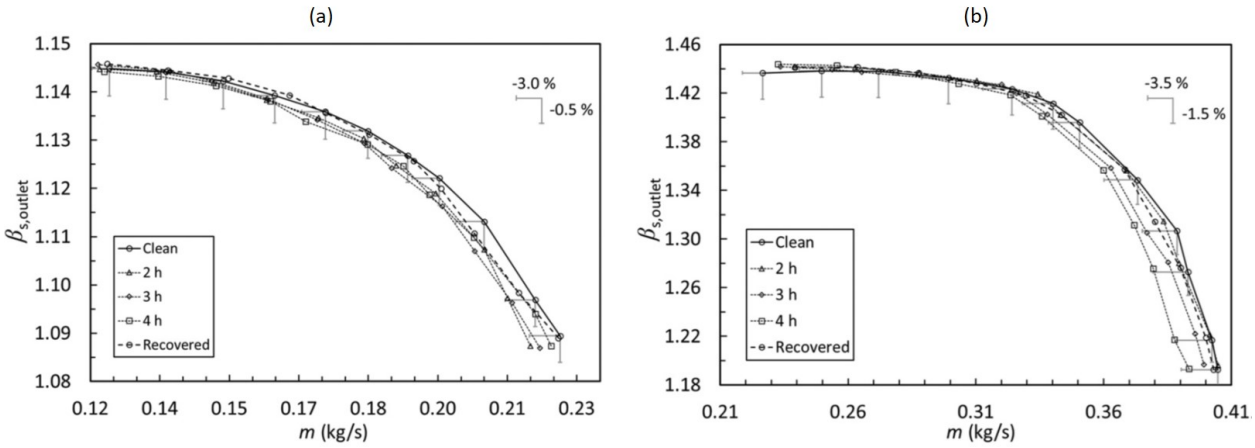

Figure 1.29: Performance loss and online washing recovery of the compressor at (a) 12 000 rpm and (b) 20 000 rpm. The fixed bars allow an easier quantification of the performance loss. from Casari et al. (2021).

In their work, the compressor has been fouled at two operating points corresponding to two rotational regimes, which corresponds to 'sub-idle' and 'quasi-idle' states. This is of main importance because these speeds are significantly off the design point, hence the flow patterns in the compressor will be sub-optimal, which may promote deposition through eg. the separation. The relative humidity at the inlet of the compressor has been increased to promote particle adhesion. For the two analyzed operating points, the tests have been realized in three runs and the performance curves have been recorded at the end of each run. The compressor has been online washed, and the performance curve has been recorded again. The results, reported in Fig. 1.29 in terms of characteristic curves, show the loss of performance after the ingestion of a dosed amount of contaminant during the operations. They found that the performance losses change according to the operating point of the machine at which particle ingestion occurs. The operating point at 12 000 rpm seems to be less sensitive to particle ingestion in terms of performance losses. The modification of the curve at this regime appears less influenced by particle ingestion than the 20 000 rpm operating point. The online washing procedure at 12 000 rpm and 20 000 rpm showed an incomplete recovery of the performance, especially in the zone of the curve characterized by a higher mass flow rate. This statement is confirmed by the pictures taken after the online washing (see Fig. 1.30). Fig. 1.30(a) shows the suction side of the rotor blades from the second to the sixth stage. All the blades are characterized by a streamwise pattern of residual dust. The pattern on the blades is characterized by a succession of dust tracks and a clean surface. In Fig. 1.30(b), a representative sketch is reported: the water droplets seem to reach the suction side surface close to the blade root, and then it seems to push toward the shroud forming spanwise rivulets. These rivulets do not cover the entire blade surface compromising the effectiveness of the cleaning process.

It can be concluded that operating the gas turbine under fouling is associated with significant costs, while the compressor wash service also adds costs. The question to answer is, therefore, how to schedule the wash services so that the total revenue loss of the operation is minimized? Some works in the literature have tried to address this question based on the cost factors and the information on the compressor fouling rate (Boyce & Gonzalez 2005, Sánchez et al. 2009, Rao & Naikan 2008, Basendwah et al. 2006, Hanachi et al. 2018). All of them use data-driven techniques to assess the fouling coefficients, which are very powerful tools but lack physical meaning.

1.3 Aims of the Work

The aim of this work is to propose different methodologies capable to mitigate the effects of fouling or predicting the performance degradation that it generates. For this purpose, both

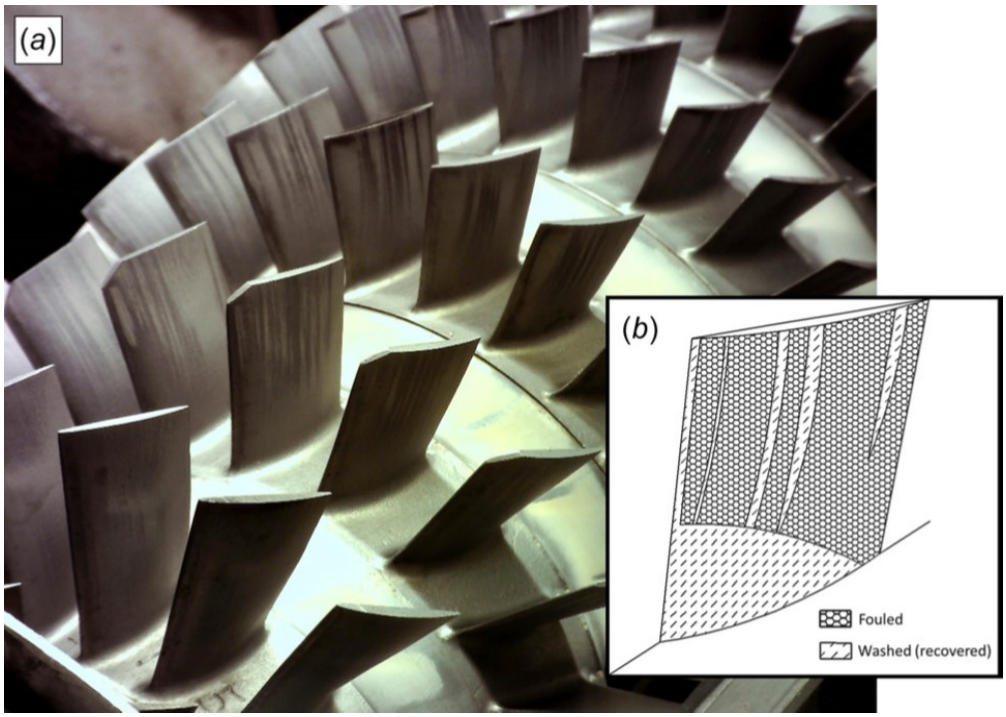

Figure 1.30: Blade surface detection: (a) rotor blades from second to the sixth stage and (b) sketch of a deposit pattern after the online washing at 20 000 rpm (fourth rotor stage). from Casari et al. (2021).

hot and cold engine sections are considered.

In particular, concerning the turbine section, new design guidelines are presented. This is because, for this specific component, the time scales of failure events due to hot deposition can be of the order of minutes, which makes difficult the application of predictive models, since they must be really precise in the forecasting of the effects in time. In this respect, design optimization techniques were applied to find the best HPT vane geometry that is less sensitive to the fouling phenomena. After that, machine learning methods were adopted to obtain a design map that can be useful in the first steps of the design phase. Moreover, after a numerical uncertainty quantification analysis, it was demonstrated that a deterministic optimization is not sufficient to face highly aleatory phenomena such as fouling. This suggests the use of robust or aggressive design techniques to front this issue. The research branch that tries to face this problem has been called Design for Fouling (DfF) by the author since represents the first attempt to optimize a gas turbine geometry against deposition in the literature.

On the other hand, with respect to the compressor section, the research was mainly focused on the building of a predictive maintenance tool. This is because the time scales of failure events due to cold deposition are longer than the ones for the hot section, hence the main challenge for this component is the optimization of the washing schedule. As reported in the previous sections, there are several studies in the literature focused on this issue, but almost all of them are data-based instead of physics-based. The innovative strategy proposed

here is a mixture between physics-based and data-based methodologies. In particular, a reduced-order model has been developed to predict the behaviour of the whole engine as the degradation proceeds. For this purpose, a gas path code that uses the components' characteristic maps has been created to simulate the gas turbine. A map variation technique has been used to take into account the fouling effects on each engine component. Particularly, fouling coefficients as a function of the engine architecture, its operating conditions, and the contaminant characteristics have been created. For this purpose, both experimental and computational results have been used. Specifically for the latter, efforts have been done to develop a new numerical deposition/detachment model.

1.4 Publications

Some of the contents presented in this thesis have leaded to the publication of scientific papers in international journals and conferences. Sections or extracts of these articles are included in the chapters of the current work. A list of these publications is provided below.

Peer-Reviewed Journal Papers:

- Oliani, S.; Friso, R.; Casari, N.; Pinelli, M.; Suman, A.; Carnevale, M. **Progresses in Particle-Laden Flows Simulations in Multistage Turbomachinery With OpenFOAM.** Journal of Turbomachinery, Volume 144(10), 2022, 101007.
- Friso, R.; Suman, A.; Vulpio, A.; Zanini, N.; Casari, N.; Pinelli, M. **Towards an innovative mechanistic model to predict the detachment process of a deposited layer.** International Journal of Heat and Mass Transfer, Volume 200(10), 2023, 123525.

Peer-Reviewed Conference Papers:

- Friso, R.; Casari, N.; Suman, A.; Pinelli, M.; Montomoli, F. **A design for fouling oriented optimization of an HPT nozzle.** Proceedings of the TurboExpo 2019 - Paper no. GT2020-91627, 2019.
- Friso, R.; Casari, N.; Suman, A.; Pinelli, M.; Montomoli, F. **Uncertainty Analysis of Inflow Conditions on an HPT Gas Turbine Nozzle: Effect on Particle Deposition.** Proceedings of the TurboExpo 2020 - Paper no. GT2019-15370, 2020.
- Friso, R.; Casari, N.; Suman, A.; Pinelli, M.; Montomoli, F. **Towards a Machine Learning Based Design for Fouling of an Axial Turbine Vane.** Proceedings of the TurboExpo 2021 - Paper no. GT2019-59520, 2021.

- Oliani, S.; Friso, R.; Casari, N.; Pinelli, M.; Suman, A.; Carnevale, M. **Progresses in Particle-Laden Flows Simulations in Multistage Turbomachinery With OpenFOAM.** Proceedings of the TurboExpo 2021 - Paper no. GT2019-59474, 2021.

- Oliani, S.; Friso, R.; Casari, N.; Pinelli, M.; Suman, A.; Carnevale, M. **A comparative analysis of particle-mixing plane interaction in multistage turbomachinery simulations.** ETC14 - Proceedings of 14th European Conference on Turbomachinery Fluid dynamics & Thermodynamics, 2021.

- Aldi, N.; Casari, N.; Fadiga, E.; Friso, R.; Oliani, S.; Pinelli, M.; Spina, P. R.; Suman, A.; Vulpio, A. **A strategy for the robust forecasting of gas turbine health subjected to fouling.** E3S Web of Conferences, 2021.

- Aldi, N.; Casari, N.; Fadiga, E.; Friso, R.; Oliani, S.; Pinelli, M.; Spina, P. R.; Suman, A.; Vulpio, A. **Off-line washing effectiveness on a multistage axial compressor.** E3S Web of Conferences, 2021.

- Friso, R.; Zanini, N.; Suman, A.; Pinelli, M. **A Microscale-based Methodology to Predict the Performance Degradation in Turbomachinery due to Particle Deposition.** Proceedings of the TurboExpo 2022 - Paper no. GT2020-82425, 2022.

- Friso, R.; Zanini, N.; Suman, A.; Pinelli, M. **An innovative prediction strategy for the compressor fouling effects during an airline mission.** Proceedings of the GPPS 2022 - Paper no. GPPS-TC-2022-0085, 2022.

- Zanini, N.; Suman, A.; Friso, R.; Pinelli, M. **Analysis of satellite-derived data for the study of fouling in aircraft engines.** E3S Web of Conferences, 2022.

- Colantuono, R.; Friso, R. **Aviation and the EU ETS: an overview and a data-driven approach for carbon price.** Conference "Transport, Tourism and Sustainable Development" XXIV Scientific Meeting Società Italiana degli Economisti dei Trasporti e della Logistica (SIET), University of Insubria, Varese (Italy) September 8th-9th, 2022.

Chapter 2

Particles Transport and Impact Behavior

This chapter will describe the computational approaches for particle transport used in all the models. Besides, after a review of the existent sticking and detachment modelization techniques, a new physics-based approach will be introduced to model particle deposition and removal for the cold section.

2.1 Particle Motion in Fluids

The modelization of multiphase flows can be mainly performed with two different strategies: the Eulerian or the Lagrangian approach. In both cases, the carrier flow is solved by using an Eulerian approach, hence it is treated as a continuous medium, and the difference regards the way the particulate is managed. The latter can be treated from both an Eulerian or a Lagrangian standpoint.

In the Eulerian approach, both phases are considered to exist at the same time and are treated as continuum media. Particle transport is caused by the concentration gradient. Particle velocity is represented as the average over the computational cell. The consideration of a particle size distribution requires the solution of a set of basic equations for each size class to be considered. Hence the computational effort increases with the number of size classes. The method is however preferable for dense two-phase flows with uniform particle size.

In the Lagrangian approach, particle transport is modelled by tracking a large number of particles through the flow field by solving the equations of motion taking into account the relevant forces acting on the particle. Generally, the particles are considered as points, i.e. the finite dimension of the particles is not considered and the flow around the individual particles is not solved. Since the number of real particles in a flow system is usually too large for tracking all the particles, the trajectories of computational particles which represent a number of real particles with the same properties (i.e. size, velocity and temperature) are

calculated.

In this work, the Lagrangian approach was used to model the deposition and detachment process since it provides a detailed and realistic model for particle transport. In addition, it gives complete information on particle impact at the surface required for sticking studies. Furthermore, particle size distribution could be considered easily to represent reality.

2.1.1 Lagrangian Approach

In the Lagrangian approach, the motion of a solid particle in a fluid is described by an ordinary differential equation which allows the computation of its position and velocity at each time step. This equation, which is called the Basset-Boussinesque-Oseen (BBO) equation, is the translation of Newton's second law. The general form of the BBO equation can be written as follows:

$$m_p \frac{d\boldsymbol{v}}{dt} = \boldsymbol{F_D} + \boldsymbol{F_{AM}} + \boldsymbol{F_B} + \boldsymbol{F_{BA}} + \boldsymbol{F_{Br}} + \boldsymbol{F_S} \tag{2.1}$$

where m_p is the particle mass, $\boldsymbol{v}$ is the particle velocity, and t is the time. The right-hand side of the equation 2.1 is the sum of all the forces acting on the particle, which are respectively the drag force ($\boldsymbol{F_D}$), the added mass force ($\boldsymbol{F_{AM}}$), the body (gravity and buoyancy) forces ($\boldsymbol{F_B}$), the Basset force ($\boldsymbol{F_{BA}}$), the Brownian force ($\boldsymbol{F_{Br}}$), and the Saffman force ($\boldsymbol{F_S}$). The contribution to particle motion of the different forces is studied by several authors (i.e. Brooke et al. (1992)) and depends on the particular application. For high values of density ratio (the ratio between the particle density and the fluid density) forces other than the drag do not give relevant contributions to the particle motion, thus they can be neglected (Crowe et al. 1996, Armenio & Fiorotto 2001, Rispoli et al. 2015). Given these considerations, the most important among the actions involved in equation 2.1 is the Drag force. Therefore, the choice of the proper formulation of the drag terms represents the most important step. Since different particle types were considered throughout this work, the actual formulation implemented will be reported for the specific case.

2.1.2 Turbulent Dispersion of Particles

The dispersion of particles in the fluid phase can be predicted using a stochastic tracking model. The instantaneous turbulent fluid velocity may be computed directly by a DNS approach. Often, a Monte Carlo simulation (also known as discrete random walk modelling in this context) is performed instead. In this approach, a particle's stochastic trajectory is modelled as a succession of interactions with turbulent eddies. The time-mean fluid velocity $\overline{\boldsymbol{v}}$ is calculated by a suitable turbulent computational method (e.g., the k-ϵ model). A simulated fluctuating velocity field is then superposed to calculate the instantaneous fluid

velocity ($\boldsymbol{v} = \overline{\boldsymbol{v}} + \boldsymbol{v'}$). A fluid eddy is assigned a fluctuating velocity $\boldsymbol{v'}$, which is assumed to stay constant during the lifetime of the eddy t_e. As a particle encounters an eddy on its pathline, equation 2.1 is integrated to calculate the particle velocity and position at the end of the particle residence time t_r. Small particles usually stay within the same eddy during the eddy's lifetime (then $t_r{=}t_e$); particles with large inertia may leave the eddy before the eddy decays (in this case, $t_r{<}t_e$). Once the particle has left the eddy or the eddy lifetime is over, the particle encounters a new eddy at its current location, and the integration of equation 2.1 is repeated in the same manner. The calculation for a particle is continued until the particle is captured by a wall (deposition has then taken place) or goes out of the computational space. The calculation procedure is repeated for many particles (Guha 2008).

In this work, for generating the instantaneous turbulence fluctuations, the DRW stochastic model of Gosman & loannides (1983) and implemented in OpenFOAM-v1912 is used. In this approach, the turbulence fluctuation is estimated as a discrete random walk model given as (indicating with the subscript i the i^{th} velocity component)

$$v_i' = \sigma_i \, G_i \tag{2.2}$$

where σ_i is the RMS turbulence fluctuations as obtained from the RANS simulations of the flow, and G_is are the selected from a population of independent Gaussian random numbers with zero mean and unit variance.

To test the reliability of the DRW already implemented in OF-v1912, the test case reported in the work of Liu & Agarwal (1974*a*) was numerically replicated. In their tests, they figured out the number of deposited particles in the test rig reported in Fig. 2.1(a). The test section reproduced is highlighted in red in the figure. It consists of a circular straight pipe with an internal diameter (D_{pipe}) of 1.27 cm, 102 cm length (L) and smooth walls (glass). This simple domain was discretized with a structured hexahedral mesh composed of 3 380 000 cells as reported in Fig. 2.1(b). The mesh was generated using Salome-v9.3 with a first cell thickness of 35 µm, which guarantees a maximum value of y^+ of 1.1 in the whole domain, and a growth ratio of 1.1. In the length, the domain was decomposed in 400 parts, obtaining a cell stream-wise length of 0.255 cm. The flow field simulation was conducted with the steady

Table 2.1: Boundary conditions for the replication of the test case reported in Liu & Agarwal (1974*a*).

Patch	**p [Pa]**	**v [m/s]**
Inlet	zeroGradient	11.84
Walls	zeroGradient	noSlip
Outlet	100 000	zeroGradient

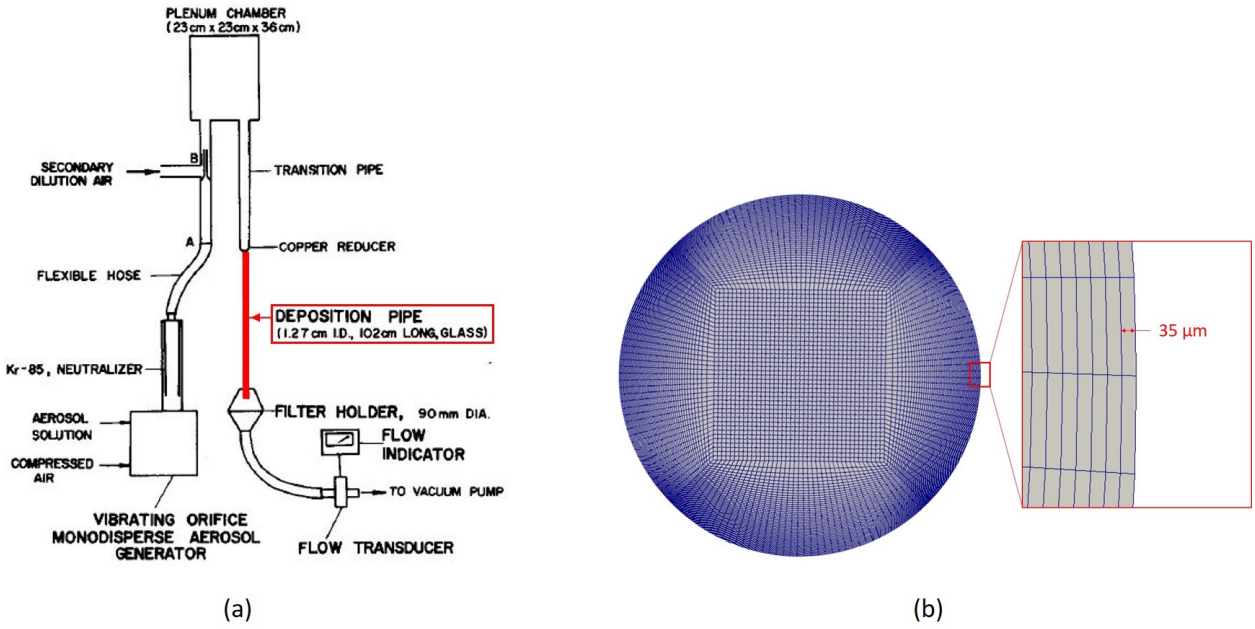

Figure 2.1: (a) Test case reported in the work of Liu & Agarwal (1974*a*), and (b) discretization of the reproduced test section.

state incompressible solver *simpleFoam* and the SSTk-ω turbulence model. The boundary conditions used are reported in Tab.2.1. The continuous phase considered is air with unitary density (ρ_f=1 kg/m^3) and kinematic viscosity μ equals to 10×10^{-5} Pas. A turbulent intensity (Tu) of 10% and a mixing length (l_t) of 0.003 m were assumed at the inlet of the domain. A uniform inlet velocity distribution and outlet environmental conditions were also imposed as described by the experiments. The dispersed phase injected by Liu & Agarwal (1974*a*) was olive oil with a density (ρ_p=0.92 kg/m^3). The experiments were conducted in the fully developed flow regime, hence the measurements were performed in the central section of the pipe, between 0.255 m and 0.763 m (0.508 m). The latter consideration was reproduced also in the computational domain as reported in the figure below. The particle-wall interaction was imposed as a pure sticking behaviour (a particle that hit a wall will deposit on it), but the deposition statistics were computed only in the active section.

In order to validate the DRW against the experimental deposition, the flow field into the pipe has to be validated first. Since flow field data is not reported in the work of Liu & Agarwal (1974*a*), the flow validation has been conducted using the experiments made by Durst et al. (1995) and the CFD simulations performed by Parker et al. (2008) and Tang et al. (2015). The results are reported in Fig. 2.2. In the first instance, the velocity evolution in the boundary layer has been compared with the experiments of Durst et al. (1995).

As can be seen in Fig. 2.2(a), the dimensionless velocity (u^+) against dimensionless distance from the wall (y^+) follows almost perfectly both the experimental results and the theoretical values. Besides the velocity evolution, the turbulent quantities have to be also

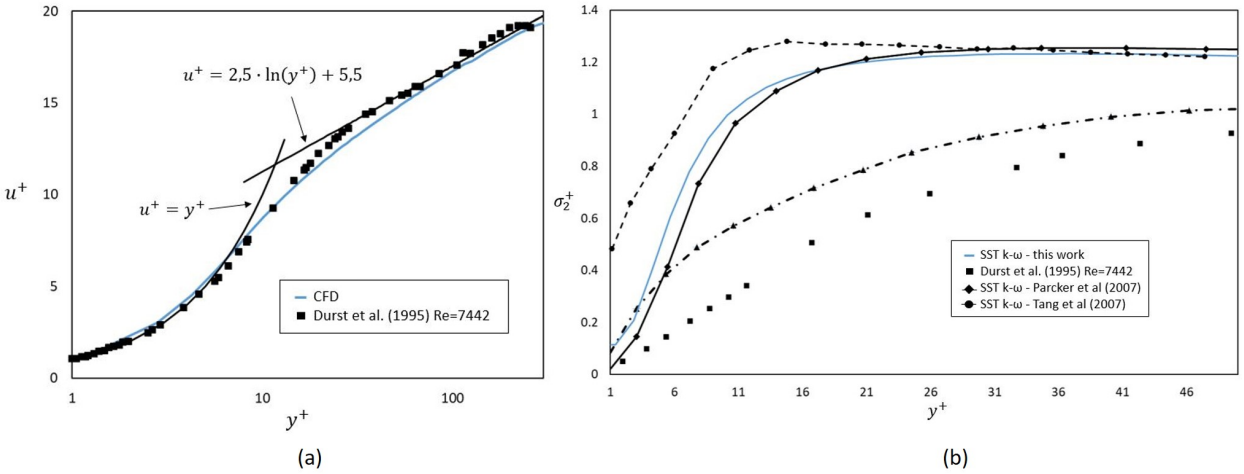

Figure 2.2: (a) Velocity evolution in the boundary layer, and (b) RMS velocity values in the bulk region.

validated, since they are the main contributors to the dispersion. To perform this validation, the RMS velocity values in the bulk region have been analysed. Since the SSTk-ω turbulence model is used to model the turbulence effects, the isotropic hypothesis of the turbulence has to be made. With this regard, the RMS velocity values are the same for all the three dimensions and are equal to:

$$\sigma = \sigma_1 = \sigma_2 = \sigma_3 = \sqrt{2/3\, k} \tag{2.3}$$

The comparison of this quantity with the experimental results of Durst et al. (1995) and the CFD simulations performed by Parker et al. (2008) and Tang et al. (2015) is reported in Fig. 2.2(b) only for the wall normal component. In the figure, a good agreement of this work's results with both experiments and CFD simulations can be recognized. The wall normal component is the only one considered for the validation because it is the main cause of nonphysical concentration of particles in the proximity of the wall.

Once validated the flow field, particle deposition has to be analyzed. In this context, the numerical results found by Forsyth et al. (2016) have been considered as the reference together with the experimental results of Liu & Agarwal (1974a) and Papavergos & Hedley (1984). The simulations reported in the work of Forsyth et al. (2016) were carried out with ANSYS-FLUENT. The results are reported in Fig. 2.3 in terms of the non-dimensional deposition velocity (V_d^+) and the non-dimensional relaxation time (τ_p^+) formulated as follows

$$V_d^+ = \frac{D_{pipe}\, v}{4\, L_{pipe}\, u_\tau} \left(\frac{C_{in}}{C_{out}} \right) \tag{2.4}$$

$$\tau_p^+ = \frac{C_c\, \rho_p\, \rho_f\, d_p^2\, (u_\tau)^2}{18\, \mu^2} \tag{2.5}$$

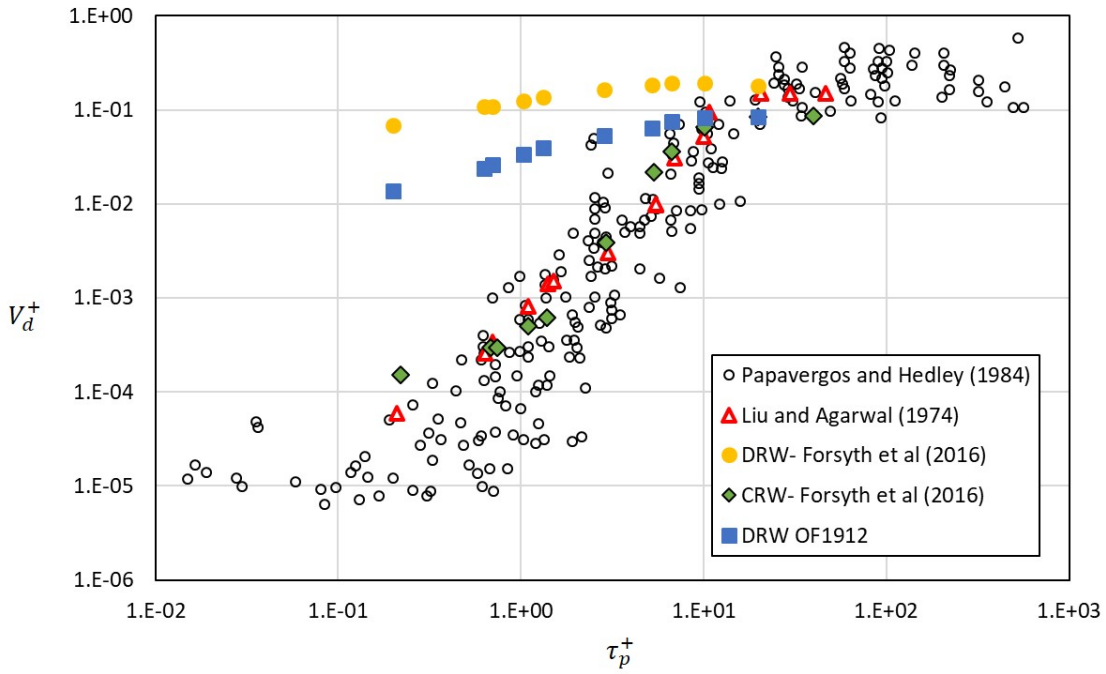

Figure 2.3: (a) Velocity evolution in the boundary layer, and (b) RMS velocity values in the bulk region.

where u_τ is the friction velocity, C_{in} and C_{out} are the incoming and outgoing concentration respectively, C_c is the Cunningham slip correction factor, and d_p the particle diameter. As can be seen, in the figure a model called CRW (Continuous Random Walk) is present. In this model, the flow is split into isotropic and anisotropic at y^+=100. In the bulk region, fluctuating velocities are calculated from turbulent kinetic energy, while at the boundary layer the anisotropic turbulence is accounted for by extracting statistics from DNS simulations. From Fig. 2.3, it can be clearly seen that a higher deposition velocity is predicted as the DRW is used. The authors suggest the passage to CRW for diffusion-dominated flows (lower non-dimensional relaxation time). The difference tends to be smaller as the inertial regime is approached (for τ_p^+=101). In this work, the vast majority of the particles injected belong to the τ_p^+>100 regime, thus slightly affected by the such difference. No modification has been introduced to the DRW since the error due to its application in the inertial regime is very small. However, this represents a limitation of the current analysis and efforts should be put into improving the modelling here presented. Interestingly, it can be noted that the modelization implemented in OF-v1912 can better replicate the experimental outcomes than the one implemented in ANSYS-FLUENT.

2.1.3 Coupling between the Dispersed and the Continuous Phases

In two-phase flow systems, it is important to determine if the dispersed phase influences the continuous phase. In this context, the terms one-way coupling, two-way coupling and

four-way coupling are often used. In the one-way coupling, the particle phase has no effect on the fluid flow. In the two-way coupling, fluid dynamic interactions between the particles and the fluid are considered. In the four-way coupling, fluid dynamic interactions between the particles and the fluid in addition to the collisions between particles are included. To discriminate with which interaction type a particle-laden flow can be approximated, the quantities of interest are the volumetric fraction of particles Φ_p (Eq. 2.6), the particle aspect ratio (S/d_p), the particle response time τ_p (Eq. 2.5), the Kolmogorov time scale τ_K (Eq. 2.8)), and the large eddy turnover time τ_e (Eq. 2.9).

$$\Phi_p = \frac{N_p\, V_p}{V_f} \tag{2.6}$$

$$\tau_p = \frac{\rho_p\, d_p^2}{18\, \mu^2} \tag{2.7}$$

$$\tau_K = \frac{\mu\, \epsilon}{\rho_f} \tag{2.8}$$

$$\tau_e = \frac{l}{v} \tag{2.9}$$

where N_p is the number of particles, V_p is the particle volume, V_f is the fluid volume, S is the distance between neighbouring particles, ϵ is the dissipation rate of turbulence kinetic energy, and l is the length scale of the energy containing eddies. The time scale dependency upon the volumetric fraction of particles is reported in Fig. 2.4.

Very low volumetric fractions ($\Phi_p<10^{-6}$) identify the regime in which particles have a negligible effect on the turbulence, meaning the particle dispersion depends on the turbulent structures, but vice versa does not hold. This regime is termed "one-way" coupling, meaning no effects of particles on turbulence are considered. By increasing the volumetric loading ($10^{-6}<\Phi_p<10^{-3}$), the turbulence is somehow affected by the presence of the particle and it is therefore called "two-way" coupling. An extra remark should be highlighted here: lowering τ_p (e.g. smaller diameter for the same particle material, particles number and fluid viscosity) increases the surface area of the particulate phase, and thus increases the dissipation rate of turbulence energy. By increasing particle size, and therefore increasing particle Reynolds number $Re_p = (v - v_p)\, d_p/\nu_K$ to a value greater than 400, vortex shedding behind particles takes place enhancing turbulence. The suspensions in these two regimes are usually referred to as dilute. The third regime, with higher particle loading, is referred to as dense suspension, and the "four-way" coupling should be introduced: the particle-particle interaction should be considered as well (in addition to the former mechanisms).

Particulate flow in either the compressor or the turbine when low-grade fuels are used is classified as dilute flow and the influence of the particle phase on the fluid flow can be neglected. Consequently, all the calculations performed in this study considered only the

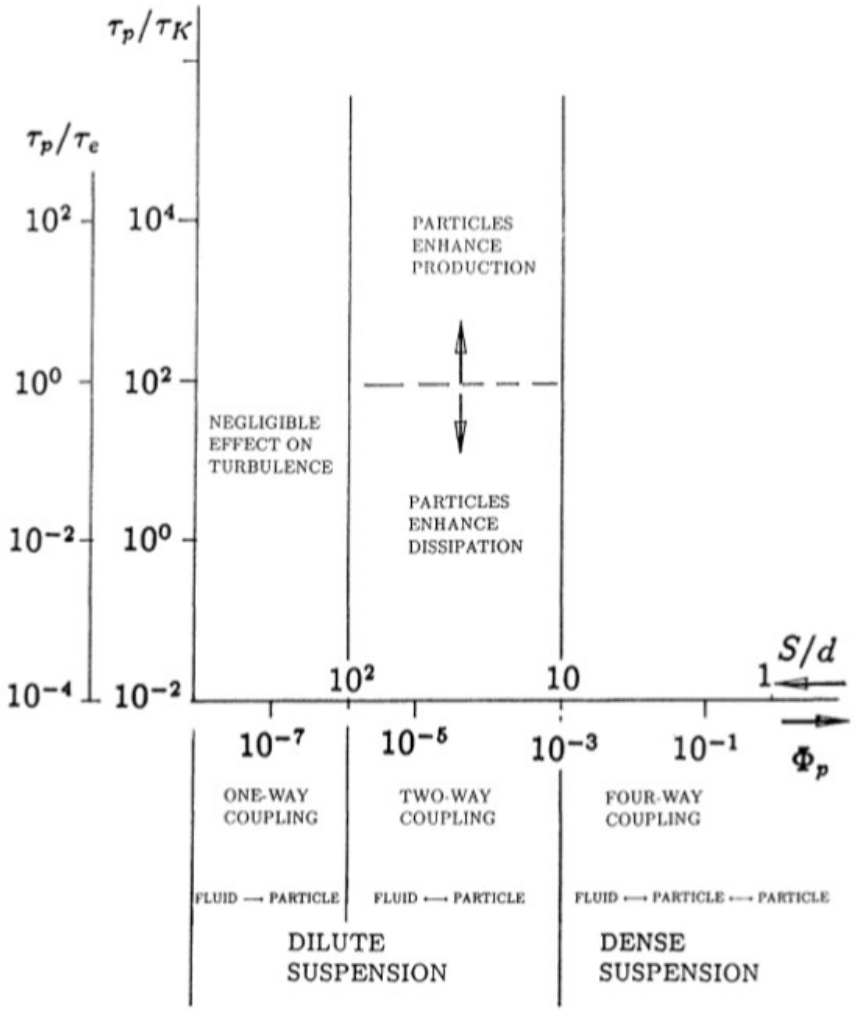

Figure 2.4: Map of flow regimes in particle-laden flows. From Elghobashi (1994)

one-way coupling (El-Batsh 2001).

2.2 Particle-Wall Interaction

The particle-wall interaction is the part of the deposition process which determines the fraction of incident particles that remain on the surface. In this study, both hot and cold deposition were considered, in order to face the fouling problem in the turbine and the compressor sections. For what concerns the hot deposition, the EBFOG model developed by Casari, Pinelli, Suman, di Mare & Montomoli (2018) was used. On the other hand, for cold deposition, a new mechanistic model was conceived. In this model, the particle-wall interaction considered falls into two categories. First, pure mechanical interaction in the absence of the fluid force. It aims to determine the condition at which no rebound occurs and is called in this study the sticking process. Second, fluid dynamic interaction between the fluid and the stuck particles. It studies the stability of the particles at the surface and

is called the detachment process. Different sticking forces and mechanisms are explained. The detachment mechanisms are also discussed and the dominant mechanism of particle detachment is obtained.

2.2.1 Hot Deposition

Sticking Model

As already mentioned, the particle adhesion model applied in this work is the Energy Based Fouling of Gas Turbines (EBFOG) model proposed by Casari, Pinelli, Suman, di Mare & Montomoli (2018). The model assumes that the probability of a particle sticking (S_p), can be described using an Arrhenius-type equation. This type of equation is used to describe the temperature dependence of a wide range of processes in which an energy threshold must be overcome to initiate the process. Casari, Pinelli, Suman, di Mare & Montomoli (2018) applied it to the particle deposition process under the assumption that only particles with an energy greater than some threshold value will stick on impact. In this specific application, the probability of sticking (S_p), depends on a rate constant (A), and the ratio between an activation energy (E_{act}), and a reference energy (E_{ref}), of the particle. The activation energy defines the energy threshold of the particle-wall adhesion process based upon the physical state of the particle and the reference energy is specified as the kinetic energy of the particle normal to the vane. The sticking probability can therefore be expressed mathematically in the form of Eq. 2.10.

$$S_p = A\, e^{-\frac{E_{act}}{E_{ref}}} \tag{2.10}$$

In the formula, the energy is comprehensive of both the kinetic and thermal terms. In particular, the temperature influences the activation energy of the process: the higher the temperature the lower the activation energy. This remark can be formalised by expressing the exponential ratio in the following way:

$$\frac{E_{act}}{E_{ref}} = \frac{C_1}{\frac{1}{2}\, m_p\, v_{p,n}^2\, \left(1 + C_2\, \frac{T}{T^*}\right)} \tag{2.11}$$

where T^* is a certain temperature which causes the physical properties of the material to change, and T is the fluid temperature. Casari, Pinelli, Suman, di Mare & Montomoli (2018) showed that C_2 is a universal non-dimensional constant equal to 3027 that applies to all particle types. The constants A and C_1 both depend upon the composition of the dust and can only be determined by curve fitting experimental results for different particle types. Whether these constants also depend on the particle size is currently unknown. This fitting process was carried out by Casari, Pinelli, Suman, di Mare & Montomoli (2018) for the volcanic ash particles, giving C_1=2.51×10^{-5} J and A=0.897. The outcome of the model

is a number belonging to the range [0–1]. The decision of whether a particle sticks or not is taken by a Metropolis-Hasting algorithm. This method uses an auxiliary random number in the range [0–1] that is compared with (S_p). If the randomly generated number is greater than the coefficient provided by Eq. 2.10, the algorithm rejects the sticking of the particle and vice-versa. In this way, the overall probability is respected and the results should reflect the actual statistics for every time step of the computation.

Deposit-Flow Field Interaction Model

Every time an impact takes place, the sticking model decides if the particle sticks or rebounds. If the particle sticks, the geometry is modified according to the characteristics of the impinging parcel, by applying a displacement in the direction normal to the surface. The normal-to-the-surface vector is assumed to be the vector normal to the boundary face where the impact takes place. Since the faces of the cells are flat, this assumption does not imply any interpolation error. In order to preserve the mesh quality, the displacement of the boundary is spread onto the domain in such a way that the cells that belong to a deforming patch retain an acceptable quality. The movement of the boundaries is followed by a smoothing of the displacement across the internal points. The displacement of internal nodes is determined by solving a Laplace smoothing equation with constant diffusivity. It should be pointed out that the order of magnitude of the displacement due to the boundary motion for each time step is very small (i.e. 10^{-7}), and thus the numerical grid can bear such deformation with the aid of smoothing without problems.

2.2.2 Cold Deposition

Unlike hot deposition, cold deposition experimental and numerical studies are not widespread in the literature, the first ones mainly due to the complexity in the quantification of the deposits that stick to the blade and vane surfaces, whereas the second ones principally for the complexities due to the particle motion and the lack of an adequate impact modelization. In this context, the deposition models commonly used in the turbomachinery fouling simulations are the one proposed by Poppe et al. (2000) successfully employed by Aldi et al. (2017), and the one developed by Bons et al. (2017), even though the latter was originally conceived for hot deposition. A comparison among these two modelizations was conducted by Casari et al. (2020). In their work, the two techniques were analyzed in the context of axial compressor fouling. Specifically, they numerically reproduced the experimental tests conducted by Döring et al. (2017*a*), finding the deposition patterns reported in Fig. 2.5. As it can be noted, the Bons model well approximates the deposition pattern in regions (B), (C), (D), and (G) while slightly over-predicting (E). Regarding regions (A), (F) and (H), the model approach by Poppe promises more precise predictions. Considering the pressure side

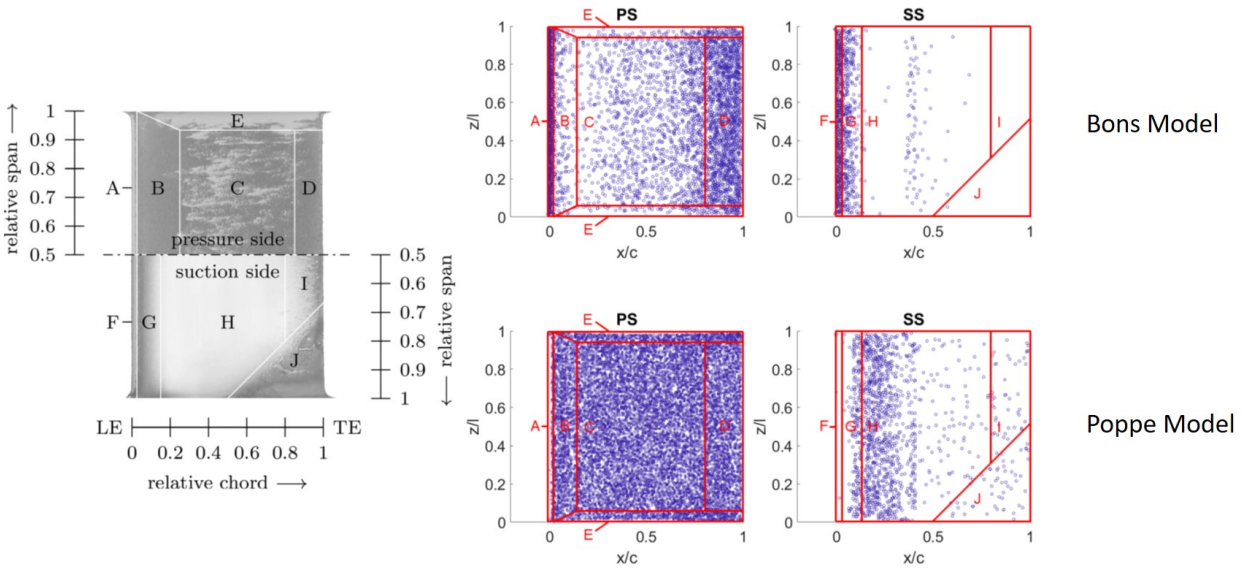

Figure 2.5: Simulated deposition pattern by using the model proposed by Bons et al. (2017) (top right) and the one proposed by Poppe et al. (2000) (bottom right). From Casari et al. (2020).

pattern, the numerical investigation under steady-state conditions catches the phenomenon in the region (A) of a leading edge with less deposit than the rest of the surface accurately. The same applies to the uniform pattern just downstream in the region (B). The non-uniform pattern further downstream (C), on the other hand, as well as the rare deposition in the region (E), are not so well predicted. Also, region (D) is not well replicated. On the other hand, the deposition is well predicted for regions (F) and (G) on the suction side. Region (H) is also reasonably approximated as its concentration is considered to be low compared to the upstream region (G). Similar to the pressure side, an increasing deposition pattern in the TE region (I) can not be detected to the same extent as observed in the experiment. Also, region (J) is not clearly more soiled compared to the nearby areas. A reason for this mismatch in the region (I) might be related to the same causes highlighted for the PS. Regarding the (J) zone, a lower amount of deposit with respect to experiments has been found. Overall, the authors concluded that neither the Poppe model nor the Bons model completely fulfils the engineering and the scientific community. In this respect, efforts have been done to find an innovative particle deposition/detachment model that better predicts the cold fouling issue.

2.2.3 New Cold Deposition/Detachment Model

Sticking Model

Once a particle hits a surface, to predict deposition rate the impact/adhesion phenomenon has to be modelled determining whether the particle sticks or rebounds. Thus it is crucial to analyse the mechanics of impact. At the end of the 19^{th} century, Hertz was one of the

first scientists who introduced elasticity in impact problems. Consider two spheres of mass $1\,m$ and $1\,m$, and radii R_1 and R_2 respectively, in contact with a contact load F. Define the effective mass m^* and radius R^* as

$$\begin{cases} \frac{1}{m^*} = \frac{1}{m_1} + \frac{1}{m_2} \\ \frac{1}{R^*} = \frac{1}{R_1} + \frac{1}{R_2} \end{cases} \tag{2.12}$$

Hertz demonstrated that the shape and size of the zone of contact are directly connected to the elastic deformations of the bodies. The shape is a circle and its radius is computed by

$$a_H^3 = \frac{3}{4}\,\frac{F\,R^*}{E^*} \tag{2.13}$$

where F is the contact load, and E^* is the equivalent Young modulus calculated as

$$\frac{1}{E^*} = \frac{1-\nu_1^2}{E_1} + \frac{1-\nu_2^2}{E_2} \tag{2.14}$$

with E_1, ν_1 and E_2, ν_2 the Young modulus and the Poisson coefficient respectively of the two bodies in contact.

Hertz's theory is correct only for high values of contact load since it does not take into account the adhesion forces which develop at contact. As also reported in Johnson et al. (1971), some experimental works by Roberts (1968) and Kendall (1969) demonstrate that at low loads contact areas between two smooth rubber spheres were considerably larger than those predicted by Hertz (see the sketch in Figure 2.6). On the other hand, they closely fitted the Hertz theory at high loads. These experiments suggested that during the contact, attractive surface forces act. Moreover, although these forces are negligible at high loads, they become relevant as the load reduces to zero.

Johnson et al. (1971) modified the Hertz theory by considering the surface force and obtained

$$a_{JKR}^3 = \frac{R^*}{(4/3\,E^*)}\left(F + \frac{3}{4}\,\Gamma\,\pi\,R^* + \sqrt{3\,\Gamma\,\pi\,R^*\,F + \left(\frac{3}{2}\,\Gamma\,\pi\,R^*\right)^2}\right) \tag{2.15}$$

where Γ is the surface energy (also called work of adhesion).

The Johnson-Kendall-Roberts (JKR) theory became a milestone in the contact/impact of elastic bodies. Several authors started from Hertz and JKR theories in order to study the impact or extend it to the elastic-plastic case. Among the others, the work of Rogers & Reed (1984) is one of the most cited and clear. They extended the energy analysis of JKR to the elastic-plastic impact of a particle with a (stationary) surface, but their analysis can be readily extended to the case of impact between two spherical bodies. When two bodies

collide first they undergo elastic deformations. A contact surface develops and part of the kinetic energy of the two bodies is stored as elastic energy. An elastic repulsive force rises and the particle gradually decelerates. Simultaneously, some irreversible effects take place (i.e. acoustic and elastic waves, internal friction) thus a part of the energy is dissipated. In the case that the stress within the particle exceeds the elastic limit plastic deformations occur, and an additional part of the energy is lost. Deformations increase until the particle velocity becomes zero. Now elastic energy stored starts to be returned and the impacting particle moves away from that impacted one. Accordingly, elastic deformations start to be released. If the initial energy content of the particle is high enough to overcome the adhesion energy, the particle bounces otherwise it sticks.

But now a problem arises. In the theory proposed by Rogers & Reed (1984), the substrate is considered to be rigid and non-deformable. This could be a reasonable assumption for particle impact in high-temperature environments, but it is nonphysical when particle impact at low temperatures is considered. In these conditions, also erosive effects could arise, hence both particle and substrate elastic-plastic behaviour have to be taken into account. In this context, the work of Bitter (1963) helps us to face this problem. In his work, he developed a model similar to the one proposed by Johnson to describe the erosion behaviour of particle impact on a substrate. By integrating this latter theory with the one presented by Rogers & Reed (1984), a more comprehensive adhesion model can be obtained. An overview of all the possible cases that could happen during the impact is shown in Figure 2.7. As it can be noted, both particle (in red in the figure) and substrate (in black in the figure) can behave either elastically or plastically. To decide if the impact leads to plastic or elastic behaviour, the critical velocity approach has been used. This is based on the assumption of

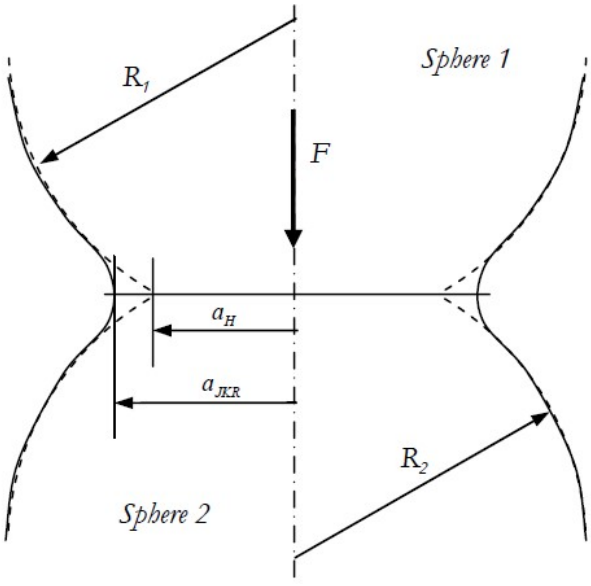

Figure 2.6: Difference between Hertz and JKR theories. From Venturini (2009).

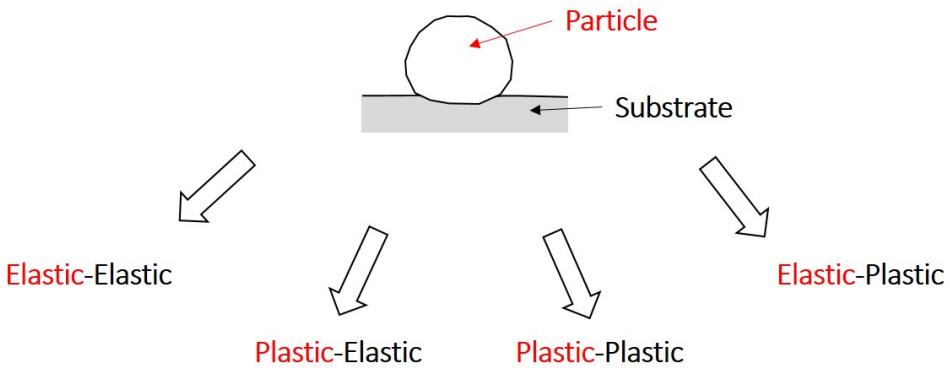

Figure 2.7: Sketch of all the possible behaviour that particle and substrate can have during the impact.

parabolic pressure distribution at the contact area. The critical velocity is then determined by equalizing the kinetic energy of the impinging particle and the pressure energy derived by imposing a load equal to the yield stress of the materials. The resulting critical velocity assumes the following formulation for both the theory of Rogers & Reed (1984) and Bitter (1963)

$$v_{lim} = \frac{\pi^2 \sqrt{S_y^5}}{2\, E^{*2} \sqrt{10\, \rho}} \tag{2.16}$$

where S_y and ρ are the yield stress and the density of the material respectively. If the normal component of the particle velocity overcomes the critical velocity of the material, hence the latter will behave plastically.

Generally speaking, the sphere has kinetic energy $Q_{k,1}$ and as it approaches the surface it gains additional energy due to the attractive force, which develops at the contact surface and depends on the surface itself. While the impact process continues gradually the kinetic energy

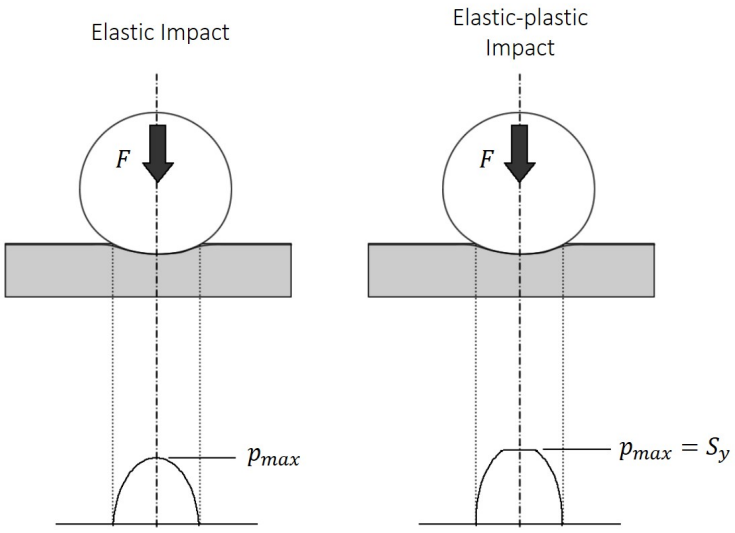

Figure 2.8: Contact between a sphere and a flat surface. Elastic (left) and elastic-plastic (right) deformations and pressure distribution. From Venturini (2009).

transforms into elastic energy (Q_{el}) and the particle decelerates until its velocity becomes zero. Since the contact surface increases as the approach proceeds, the adhesion energy (Q_{ad}) increases too. This produces a pressure distribution on the contact zone which, according to Hertz's theory, shows a peak at the centre of the contact zone (see Fig. 2.8 left). As said before, dissipative effects, i.e., acoustic and elastic waves, internal friction, etc., are always present even in an elastic impact. However, their contributions are very small thus they can be neglected considering a pure elastic impact. During the approach phase pressure acting on the contact surface may exceed the elastic limit thus also plastic deformations occur. It is commonly assumed the approximation which considers that pressure distribution in the zone of plastic deformations stays constant (see Fig. 2.8 right). With this assumption, plastic deformation starts around the centre of the contact surface and is surrounded by an annulus of only elastic deformation. Due to the irreversible nature of this deformation, a part Q_{pla} of the particle energy is lost. The energy balance that has to be performed to decide if the particle stick or rebounds assumes the following form

$$\begin{cases} Q_{k,1} > Q_{ad} - Q_{p,pla} - Q_{s,pla} \Rightarrow Rebound \\ Q_{k,1} < Q_{ad} - Q_{p,pla} - Q_{s,pla} \Rightarrow Stick \end{cases} \tag{2.17}$$

where Q_{ad} is the adhesion energy, $Q_{p,pla}$ is the energy loss due to the plastic behaviour of the particle, and $Q_{s,pla}$ is the energy loss due to the plastic behaviour of the substrate.

For what concerns the first term on the right-hand side of Eq. 2.17 (Q_{ad}), represents the energy that has to be overcome to allow the particle to rebound in a perfectly elastic impact. To better understand the meaning of the net adhesion energy, consider a sphere impacting a stationary flat surface. This situation is represented in Fig. 2.9 in terms of contact load (F) against the relative approach during the contact (δ). In view of the short range of adhesion forces, they will have no appreciable effect until the surfaces are on the point of contact (O in Fig. 2.9). This is an unstable point. As soon as the surfaces touch, they will snap into contact at point A on the equilibrium curve. Since this action takes place at elastic wave speed, the change in δ from zero at this time is negligible. We assume that the energy is entirely dissipated in wave motion so that the sphere gains no significant additional kinetic energy through being accelerated by surface forces. Subsequent compression, until the sphere comes to rest at some point of maximum compression B, is reversible, as is the following expansion back along the same curve BCAE. Clearly, the criterion for separation of the bodies after impact is whether or not the internal energy, on recoil, reaches point D on the curve. As reported in Van Beek (2001) the net adhesion energy is computed by integrating the force-displacement relation as given in Johnson et al. (1971) between zero

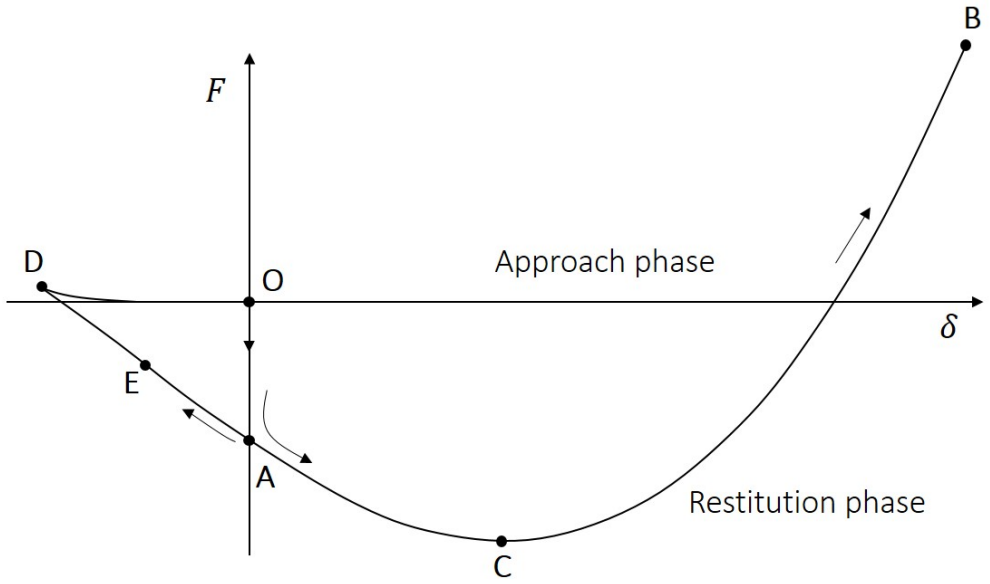

Figure 2.9: Contact between two bodies: relative approach as a function of contact force. From Johnson et al. (1971).

and -δ_D

$$Q_{ad} = \int_0^{-\delta_D} F \, d\delta = 7.09 \left(\frac{R_c^4 \, \Gamma^5}{E^{*2}} \right)^{\frac{1}{3}} \tag{2.18}$$

where $\Gamma = 2\sqrt{\gamma_1 \, \gamma_2}$, and R_c is the appropriate radius that is equal to R^* in elastic impact, while in elastic-plastic one it depends on the deformation of the sphere. Specifically, by applying the Hertz theory for the conditions at the end of the approach phase, in the elastic-plastic case it results

$$R_c = \frac{\frac{4}{3} \, E^{*2} \, r_T^3}{F} \tag{2.19}$$

with r_T the radius of total deformed area equals to

$$r_T^2 = r_{EL}^2 + r_P^2 \tag{2.20}$$

where

$$r_{EL} = \frac{\pi \, R^*}{2 \, E^*} \, S_y \tag{2.21}$$

$$r_P = \frac{F - F_{EL}}{\pi \, S_y} \tag{2.22}$$

with F_{EL} is the elastic limit of the load.

Let's now consider the second and the third terms on the right-hand side of Eq. 2.17, which describe the plastic behaviour of both substrate and particle. Among the two, the simplest one is the term regarding the substrate, which can be approximated as proposed

by Bitter (1963)

$$Q_{s,pla} = \frac{1}{2}\, m_p\, \left(v_{p,n} - v_{s,lim}\right)^2 \tag{2.23}$$

where m_p is the particle mass, $v_{p,n}$ is the normal component of the particle velocity, and $v_{s,lim}$ is the critical velocity for the substrate. The model gets more complex when the plastic behaviour of the particle occurs. In this case, the procedure reported by Rogers & Reed (1984) is employed. In particular $Q_{p,pla}$ is computed by integrating the contact load F between 0 and H (the approach distance during plastic phase), and can be approximated by:

$$Q_{p,pla} = \int_0^H F\, dH \approx \frac{\left(F - F_{EL}\right)^2}{4\,\pi\, R^*\, S_y} \tag{2.24}$$

In the deposition model proposed in this work, the striking decision is made not by directly solving the force balance, but by using the coefficient of restitution (COR), e, defined as the ratio between the rebound and the incident (normal) velocities.

$$e = \frac{v_{r,n}}{v_{i,n}} \tag{2.25}$$

COR takes into account the dissipation of energy during the impact, thus its expression derives from energy analyses of the impact phase. In the case of elastic impact, there is no energy dissipation ($e = 1$) and the particle bounces with a velocity equal to that of impact but in the opposite direction. However in real impacts energy dissipations always take place (i.e. wave propagation, plastic deformations, friction, adhesion, etc.) hence usually COR is lower than unity. COR can also be used to predict whether an impacting body sticks or bounces. Consider the normal impact of a particle, having velocity $v_{i,n}$, with a stationary flat surface (or sphere), and rebounding with a velocity $v_{r,n}$. During the impact, the particle undergoes a variation of kinetic energy ΔQ, given by

$$\Delta Q = \frac{1}{2}\, m_p\, v_{r,n}^2 - \frac{1}{2}\, m_p\, v_{i,n}^2 \tag{2.26}$$

which equals the energy loss due to adhesion, plastic deformations, and other irreversible effects. Then it writes

$$\Delta Q = \frac{1}{2}\, m_p\, \left(1 - e\right)\, v_{i,n}^2 \tag{2.27}$$

and COR becomes

$$e^2 = 1 - \frac{\Delta Q}{\frac{1}{2}\, m_p\, v_{i,n}^2} \tag{2.28}$$

Finally, in the model of Rogers & Reed (1984) is equal to

$$\Delta Q = Q_{ad} - Q_{p,pla} - Q_{s,pla} \tag{2.29}$$

Now, in order to solve equation 2.29 and compute the COR by equation 2.28, as well as to compute R_c in equation 2.19, the contact load F has to be evaluated. To this aim, the energy balance at the end of the approach phase can be used. At the end of the approach phase, particle velocity is zero then its kinetic energy, added with the adhesion energy developed during the approach phase $Q_{ad}(F)$, is split into a stored elastic energy in the only elastic deformations zone Q_{el}, a stored elastic energy in the plastic deformations zone $Q_{PE}(F)$, and an energy loss for plastic deformation $Q_{pla}(F)$:

$$Q_K + Q_{ad}(F) = Q_{el} + Q_{PE}(F) + Q_{pla}(F) \tag{2.30}$$

Once the expression of each term is known, equation 2.29 can be solved to find the contact load, thus equations 2.28 and 2.19 can be computed.

In elastic-plastic impact elastic energy is stored in the annulus Q_{el} of only in elastic deformation, but also in the zone of plastic deformation Q_{PE}. These elastic energies are computed following Bitter (1963) again. Besides the aforementioned assumptions, the author assumes also that the pressure distribution remains the same; this assumption results in the elastic energy stored in the annulus being constant. Therefore Q_{el} can be evaluated by integrating the contact load $F = F_{EL}$ between 0 and δ_{EL} (Venturini (2009)):

$$Q_{el} = \int_0^{\delta_{EL}} F_{EL}\, d\delta = \frac{2}{5}\, \frac{F_{EL}^{5/3}}{(4/3\, E^*)^{2/3}\; R^{1/3}} \tag{2.31}$$

then assuming from the Hertz theory

$$F_{EL} = \left(\frac{2}{3}\,\pi\right)^3\; \frac{R^{*2}}{(4/3\, E^*)^2}\, S_y^3 \tag{2.32}$$

2.31 reads

$$Q_{EL} = \frac{2}{5}\, \left(\frac{2}{3}\right)^5\; \frac{\pi\, R^{*2}}{(4/3\, E^*)^2}\, S_y^5 \tag{2.33}$$

which results independent from the contact load.

The elastic energy stored in the plastically deformed area is expressed by

$$Q_{PE} = \frac{1}{2}\, h_{EL}\, (F - F_{EL}) \tag{2.34}$$

where h_{EL} is the relative approach at the limiting elastic case, that is when the contact load equals the elastic limit F_{EL}.

On the left side of equation 2.30 the only energy unknown is now Q_{ad}. Its expression for

elastic-plastic impact is a function of the contact load:

$$Q_{ad} = \Gamma \, \pi \, \left(r_{EL}^2 + \frac{F - F_{EL}}{\pi \, S_y} \right) \tag{2.35}$$

Now that all the terms of 2.29 are known, it can be solved to find the load F.

Validation of the Deposition Model To test the reliability of the deposition model, two test cases were considered. The first is the experimental campaign performed by Bons et al. (2015), which uses 100–400 µm quartz particle impacting a 2024 aluminium plate at 30–80 m/s. The properties used in the model are for quartz (E =72 GPa, ν = 0.17, ρ =2200 kg/m^3), and aluminium (E =69 GPa, ν = 0.32) yielding an E^* =38 GPa. The model results are for a particle size (150 µm) and velocity (50 m/s) centered on the experimental distribution. The results are reported in Fig. 2.10. The agreement between the proposed model and the experimental data is truly remarkable. Moreover, it can be observed that the model under investigation performs better than the OSU model proposed by Bons et al. (2017), who honestly admits to having modified the yield stress of aluminium to reach the shown results.

The second case considered to evaluate the reliability of the model is the test bench described by Suman et al. (2021-22). The basic idea is to evaluate the weight change on a reference surface, weighing it before and after each deposition test and outlining the deposit growth trend. In this track, a small-scale wind tunnel was designed, and the deposit was evaluated on a flat target. The latter, a 20 mm x 20 mm x 3 mm square plate of AISI 316 set on adjustable support, is placed along a section of straight pipe, as reported in Fig.

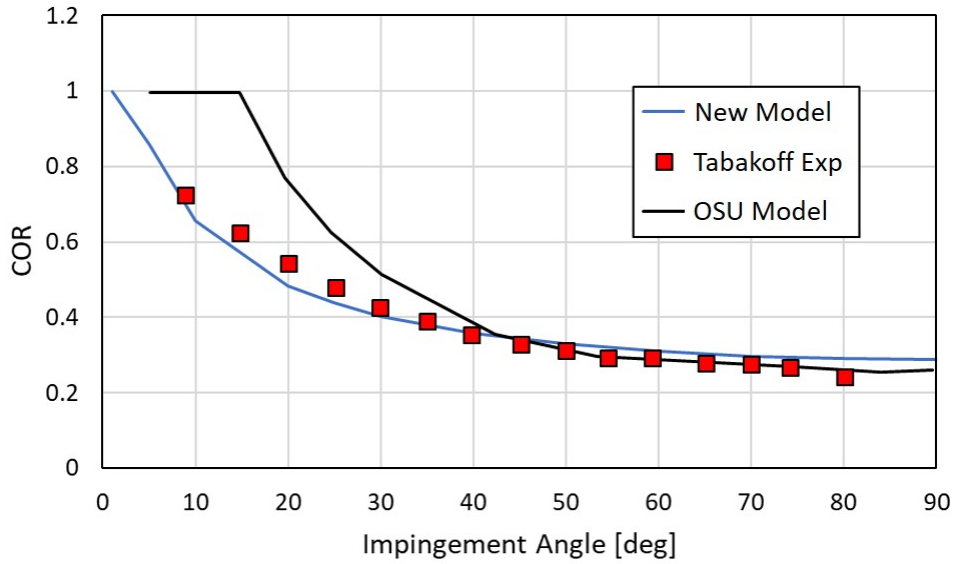

Figure 2.10: COR versus the impingement angle for quartz particle impact on aluminium. Model for 150 µm particles compared to data from Bons et al. (2015) and Grant & Tabakoff (1975).

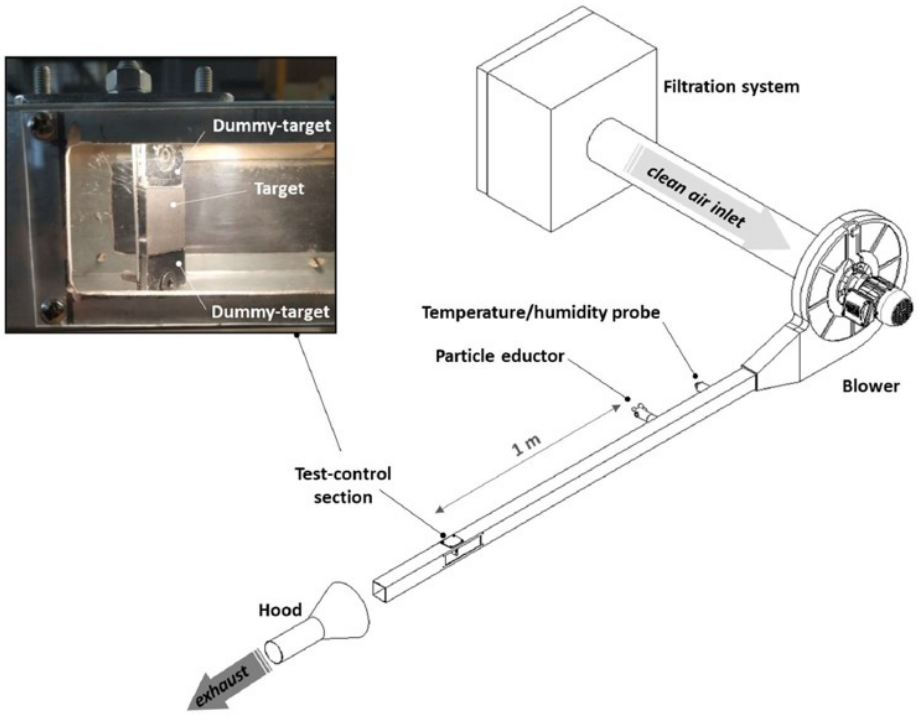

Figure 2.11: Experimental test bench arrangement Suman et al. (2021-22).

2.11, and it is invested by an airflow contaminated with ARD (Arizona Road Dust) nano-sized particles. For the contaminant characterization, refer to Suman et al. (2021-23). The air-sand mixture is obtained through the solid aerosol generator TOPAS SAG 410, which allows the injection of a constant sand mass flow rate in the test duct. An inverter-controlled centrifugal blower ensures constant airflow, whereas a filtration system at the suction of the blower avoids ingestion of contaminants from the external. Temperature and relative humidity (RH) are monitored through a barometric station. Each deposition test was recorded with a 1080p full HD camera; this allowed the identification of the detachment processes that occurred after a certain amount of deposit had been reached on the target. Tests for normal and tangential impact and two different kinetic energy values of particles were carried out. For a more detailed description of the apparatus, the reader is referred to the work of Suman et al. (2021-22). The experimental section of the cited study was reproduced numerically. Specifically, the computational grid was generated with ANSYS Meshing, whereas the numerical calculations were carried out with the open-source software OpenFOAM-v2021. The solid domain under study is reported in Fig. 2.12(a). The computational grid, shown in Fig. 2.12(b), comprises 932,483 tetrahedral elements, with a structured 5-layer prism mesh to resolve the near-wall region. After a sensitivity analysis with three meshes, grid independence was achieved with the mesh described above. The duct internal flow field was modeled by the traditional Reynolds-Averaged Navier-Stokes equations (RANS). The resolution was carried out using the rhoSimpleFoam solver of OpenFOAM-v2021. The operating conditions considered for the study reproduces the settings used for the experimental campaign. At

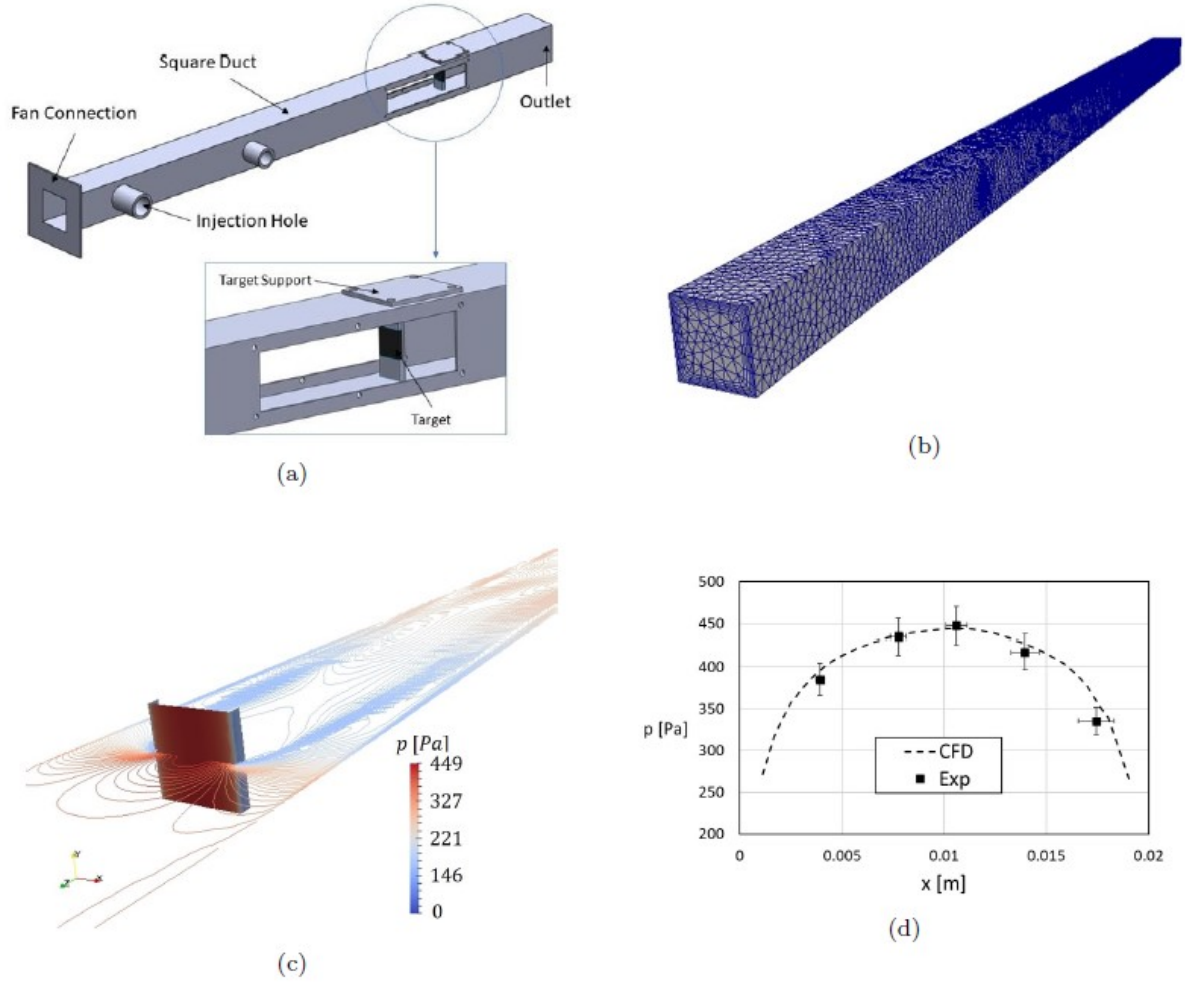

Figure 2.12: a) Geometry of the test section, b) computational grid of the studied section, c) static pressure distribution on the target surface and at the mid duct height, and d) validation of the mid-height pressure distribution numerically computed against experimental measurements.

the inlet of the domain, a mass flow rate equal to 0.055 kg/s, and a uniform temperature equal to 293.15 K were imposed, whereas a static pressure of 101 325 Pa was set at the outlet section. What concerns the turbulence is accounted for by using the $k-\omega$ SST model. The version available in OpenFOAM is based on Menter et al. (2003), which needs the use of wall functions to model the behavior at the wall since it is implemented as a High-Re model. Therefore, standard wall functions are used for this scope. The CFD results obtained are reported in Fig. 2.12(c) in terms of pressure distribution. Their reliability was tested by comparing the pressure distribution at the mid-height of the target obtained with numerical computations and experimental measurements (Fig. 2.12(d)). The latter was obtained by measuring the total pressure distribution in front of the eductor. A set of five pressure taps was realized in the front of the target with a hole diameter equal to 1 mm. An array of five holes was designed to span the entire frontal surface. As can be seen, good agreement was achieved from the comparison.

Once the flow field was solved and validated, particles were seeded from the inlet of the domain with a uniform distribution between 0.8 µm and 1.2 µm. The injection location is randomly chosen across the patch. Since in Suman et al. (2021-23) the tests was conducted with the Arizona Road Dust as the reference contaminant, particles density is set to $\rho_p = 2700\,\mathrm{kg/m^3}$. For the particle tracking, the estimation of the drag action is typically simplified by assuming spherical particles. This assumption could lead to a considerable underestimation of the force, especially when particles with highly irregular shapes are treated, i.e. Arizona Road Dust Connolly et al. (2020). For this reason, the non-spherical drag coefficient ($C_{D,shape}$) has been used to predict the drag force on the deposit:

$$F_D = \frac{1}{2}\,\pi\,R^2\,C_{D,shape}\,\rho_f\,u_\tau^2 \tag{2.36}$$

where R is the particle radius, ρ_f is the fluid density, and u_τ is the friction velocity. Specifically, the formulation proposed by Connolly et al. (2020) was employed for $C_{D,shape}$:

$$C_{D,shape} = \frac{24\,F_{Ne}}{Re_p}[1 + 0.1\,(Re_p^*)^{0.6}] + 0.3 \tag{2.37}$$

where Re_p is the paticle Reynolds number, and F_{Ne} and Re_p^* are the Newton drag and the modified particle Reynolds number respectively, calculated as follows:

$$F_{Ne} = \frac{\sqrt{6}}{CSF} - 1 \tag{2.38}$$

$$Re_p^* = \frac{F_{Ne}\,Re_p}{F_{St}} \tag{2.39}$$

where F_{St} is the Stokes drag:

$$F_{St} = CSF^{-0.18}. \tag{2.40}$$

As can be seen, both the Stokes and the Newton drag equations involve the Corey Shape Factor (CSF), which is a parameter that describes the irregular particle shape. This factor was firstly introduced by Corey Corey (1949), and defined as follows:

$$CSF = \frac{d_{min}}{\sqrt{d_{max}\,d_{med}}} \tag{2.41}$$

where d_{min}, d_{max}, and d_{med} are the minimum, the maximum, and the intermediate/medium dimension of the shape respectively. For more details about this parameter and its determination, the reader is referred to Connolly et al. (2020).

In his work, Connolly deeply analyzed also the normal variation of the CSF value for the ARD. He found that this parameter follows a normal distribution with a mean of 0.55 and

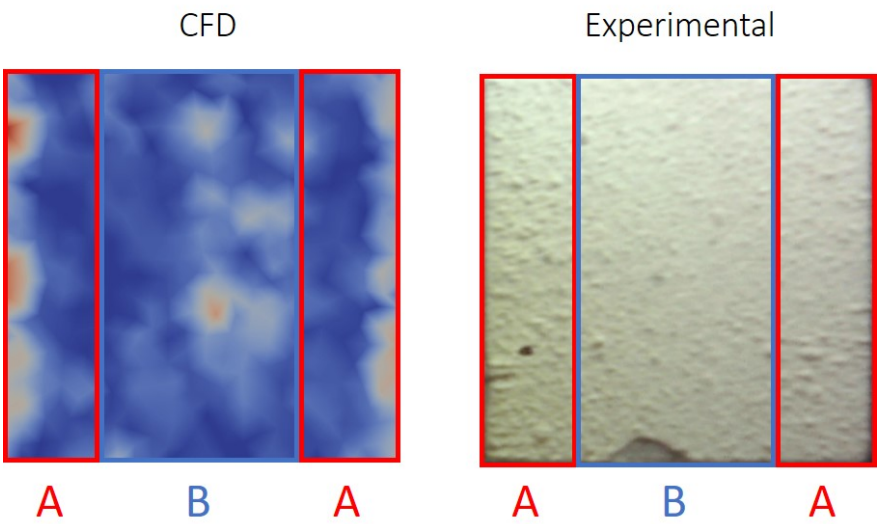

Figure 2.13: (left) CFD results by applying the deposition model to the simulation of the test section, (right) experimental results of the tests reported in Suman et al. (2021-23).

a standard deviation of ±0.2. To take this effect into account, in this study, the CSF was defined as a normally distributed random variable, with mean and standard deviation equal to the ones reported above. This, in turn, involves an aleatory drag force.

The results obtained by applying the proposed deposition model in the CFD simulation of the test section are reported in Fig. 2.13. Even if the comparison is qualitative, a good agreement between the pattern obtained by the experimental tests and those resulting from the CFD simulations can be recognized. Specifically, the sticking model proposed in the present work is capable to capture the globular deposit distribution in areas A (sides of the target), and the more uniform distribution in area B (center of the target).

Detachment Model

The evolution of the deposit corresponds to a change in the fluid flow, then to a variation in the forces that act on the adhered mass. In particular, when the build-up reaches a critical thickness value, the deposit can detach from the surface and resuspend (Casari, Pinelli, Suman, di Mare & Montomoli 2018). This phenomenon is called deposit detachment. Different models are present in the literature to approximate the removal of the adhered mass. Some of them are mainly based on the imposition of a threshold value to a flow property close to the adhered particle considered to establish if it detaches or not from the surface (El-Batsh 2001). Among the others, one of the most used strategies in this group is the one proposed by Konstandopoulos (2006). The author found a critical impact angle beyond which the particle cannot adhere to the surface in his work. Other studies, on the other hand, try to approximate the physics of the phenomenon in terms of forces and moments balance (Nasr et al. 2019). These models are widely applicable but more complex, and due

to their high complexity, they are often simplified in terms of the actions considered. In this second model type, a deposited layer detaches from the surface when the external excitations overcome the adhesion forces (Nasr et al. 2017). Different techniques are proposed in the literature to approximate the detachment of the deposit with this process (Nasr et al. 2019), but almost all of them focus on the single particle and not the whole deposit layer. This is a crucial aspect because when a solid particle adheres to a build-up deposit, it begins to behave as an aggregate of particles as asserted by Suman et al. (2021-22). Thus when detachment occurs, the deposit resuspends as a particle agglomerate. In addition, these models are helpful only when multiphase CFD simulations are performed, which are known to be computationally expensive, mainly due to the need to track the particles through the domain. For example, Bons et al. (2017) proposed a deposition-detachment model in which the particle removal is governed only by the drag force. A step forward was carried out in the work of Casari, Pinelli & Suman (2018*b*), where all the known physical detachment actions were considered. Nonetheless, they applied the procedure to the single-particle, neglecting the deposit layer growth and weight.

This work proposes a new strategy composed of existing and new physical models to predict deposit detachment in terms of area of interest and critical thickness. The novelty of the present investigation matches the need for a comprehensive model which accounts for the micro-sized particle adhesion and detachment. The model hypotheses are based on experimental evidence, while the basic models used in the present investigation are taken from the literature. The step forward proposed in the current manuscript is related to the fact that the models are tuned and connected to obtain a feasible prediction of the deposit evolution over time. One of the main advantages is the absence of multiphase CFD simulations, with a consequent saving in computational costs. At the same time, the process proposed here is physics-based and can be easily implemented in a CFD code. Furthermore, it does not focus on the single particle but on the whole deposit layer. The results carried out with this strategy are validated against experimental outcomes obtained with an ad-hoc test rig.

Experimental campaign The experimental campaign considered is the one already explained as the second validation case in section 2.2.3. To facilitate the comprehension of the work process, some of the experimental results are recalled in this section. Specifically, the ones gathered with perpendicular particle impact are exposed. The tests were conducted with a fixed air mass flow rate equal to 0.055 kg/s, which corresponds to roughly 17 m/s as a free field velocity. The analysis was carried out for an exposure time of over 60 h during which the nanoparticle layer grows and detaches. An example of the results obtained is depicted in Fig. 2.14, where the deposited mass data over time is shown Suman et al. (2021-22). As can be seen, initially, the deposited layer grows almost uniformly and linearly in time. However,

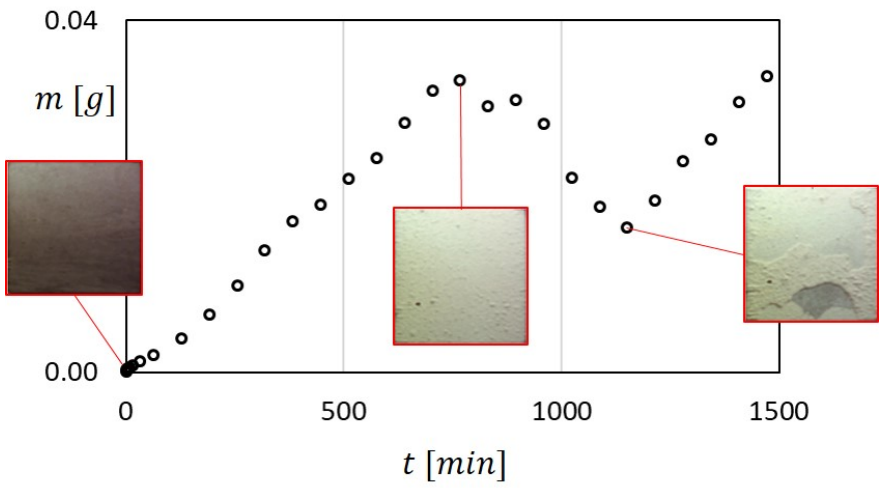

Figure 2.14: Deposited mass over time for normal particles impact.

when the thickness of the deposit reaches a critical value (peak), detachment occurs, and the mass accumulated by the target drops suddenly.

Detachment modeling This section reports a theoretical and experimental analysis of the phenomenon of flow-driven deposit layer detachment. In this study, a deposited layer is defined as a pile of stacked particles as sketched in Fig. 2.15. This hypothesis is supported by the experimental observations reported in Suman et al. (2021-3). The theory presented is mainly based on the following assumption: *the decision of whether the local deposit detaches or not can be made after a force balance is carried out on it.* Specifically, the forces considered in this study were divided into two groups: detaching forces and adhesion forces.

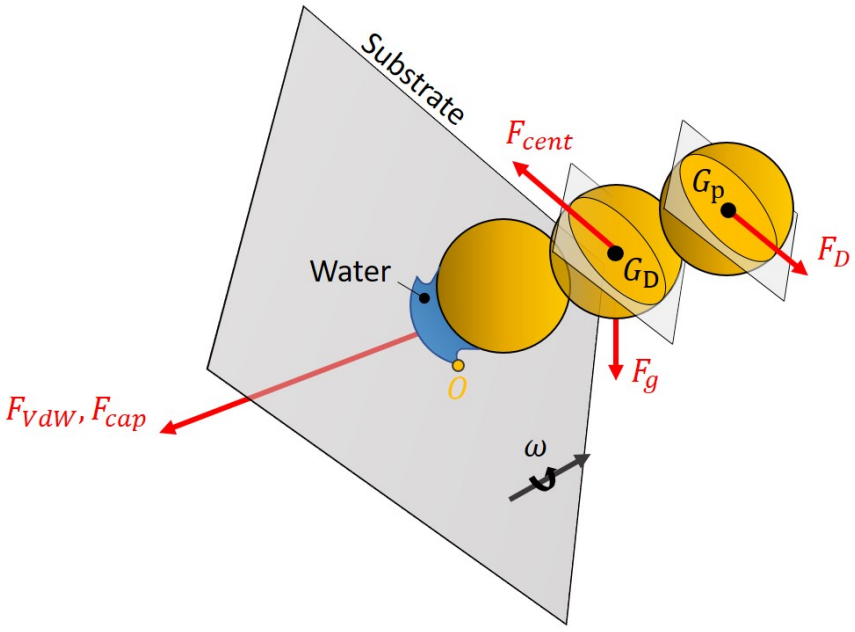

Figure 2.15: Schematic diagram of force balance for a deposit layer on a surface.

Typically, forces belonging to the first group are the centrifugal (F_{cent}) and the drag (F_D) force. Especially for the latter, the knowledge of the near-wall flow in the turbulent regime is required for its accurate determination. The centrifugal force could belong in the detaching or adhesion group depending on the surface orientation. Typically, it acts in the same direction as the weight force (F_g), which is generally considered significantly smaller than the centrifugal one. However, this is not true if non-rotating cases are considered. In this respect, stationary experiments are conducted in this work, then the centrifugal force was ignored and the gravitational one was accounted for. Other effects, such as turbulent bursts, were not considered since they could be considered negligible (see Soltani & Ahmadi (1994) for reference). In particular, this is even more true for the deposited layer instead of the single particle.

The second group contains the forces that tend to keep the deposit attached to the substrate. These are the Van der Waals (F_{VdW}), and the capillarity (F_{cap}) force. In the vast majority of engineering applications (such as turbomachinery and energy systems), the electrostatic force is commonly neglected (Nasr et al. 2019, Kurz et al. 2016), mainly because the size of contaminants is usually larger than 100 nm (Mittal & Jaiswal 2015). Besides, information about the charge state of the particles or the surfaces is often unknown (Nasr et al. 2017). For these reasons, the electrostatic force was neglected in this work, but, if necessary, it can be easily added to the model (Israelachvili 2011). The deposit is removed from the surface when the detachment actions overcome the adhesion forces. The schematic diagram of force balance on a spherical particle deposit layer is shown in Fig. 2.15, where G_D and G_p are the centers of gravity of the deposited layer, the last particle, respectively. As reported by Soltani & Ahmadi (1994), there are three main mechanisms for removing a deposit from the surface: (1) rolling, (2) sliding, and (3) lifting. Soltani & Ahmadi (1994) showed that deposits are more easily removed by the rolling mechanism compared to lifting and sliding (the flow velocity required to roll a particle is much lower than that required to lift/slide the particle from/on the surface (Nasr et al. 2017)). This evidence leads the authors to consider only the rolling mechanism in the detachment analysis. In this track, a torque balance for the onset of rolling has to be performed.

It is known from the literature that when a particle approaches a surface in a humid environment, capillary force dominates until the particle is located at a certain critical distance, beyond which the dominant action becomes the Van der Waals force. Nonetheless, detachment is modeled in this work as an on/off process (steady state detachment), and the distance between the particle and substrate is considered constant. To detach, the particle has to overcome the attractive force which is considered as the sum between capillary and Van der Waals forces making an easier and ready-to-be-done force balance (instead of an iterative calculation that could be used to find out the equilibrium between the forces). Be-

sides that, since the target, hence the deposit, is invested by a constant humid flow field, the liquid bridge is considered stable over time. All the forces acting on the deposit are listed and explained in the next paragraphs.

Adhesion Forces

- *Van der Waals*: The Van der Waals forces are attractive forces that originate between the neutral molecules due to dipolar interactions. After London had published his explanation of the dispersion forces (London 1930) it was recognized that the dispersion interaction could cause these attractive forces between macroscopic objects. This idea prompted Hamaker (Hamaker 1937) to develop a theoretical description of the Van der Waals forces by exploiting the earlier work by Bradley (1932), and de Boer (1936). In its theory, the Van der Waals interface energy of adhesion can be calculated as follows

$$W_{VdW} = \frac{H_A}{12\,\pi\,z_0^2} \tag{2.42}$$

where H_A is the Hamaker constant and z_0 is the minimum equilibrium separation distance between the objects ($z_0 \simeq 4\,\text{Å}$). For micrometer-sized particles, there are mainly two theories in the literature to quantify the Van der Waals force given the adhesion energy: the Johnson-Kendal-Roberts (JKR) (Johnson et al. 1971) and the Derjaguin-Muller-Toporov (DMT) (Derjaguin et al. 1975) theory. According to Muller et al. (1980), the DMT model is appropriate for small-size and hard particles with high Young's modulus. The JKR model, however, is more applicable for larger particles with low Young's modulus (soft material). Since ultrafine particles, that is, the ones that contribute the most to fouling, are generally complex (Bojdo & Filippone 2019), with high Young's modulus (Casari, Pinelli & Suman 2018*b*) the DMT approach was chosen to compute the Van der Waals interaction. In this model, considering d_p as the particle diameter, the Van der Waals force of adhesion has the following form,

$$F_{VdW} = \pi\,W_{VdW}\,d_p \tag{2.43}$$

At this point, only the Hamaker constant has to be figured out to calculate the force. For this purpose, among the others, the relation proposed by Visser (1972) is used (Eq. 2.44), mainly for its simplicity, where the constant representative of the case is obtained by the union of the constants of the elements in contact.

$$H_A = C_t\,(H_{12} + H_{33} - H_{13} - H_{33}) \tag{2.44}$$

In this specific case, 1 refers to the particle (ARD), 2 to the surface (stainless steel), and

3 to the condensed liquid (water). Their values will be defined later in the manuscript. Furthermore, C_t is a constant that depends on the medium material 3 and is equal to 1.6 for condensed water due to humidity. As noted, in the Eq. 2.44 only mixed terms H_{ij} are present. These should be evaluated using the geometric average

$$H_{ij} = \sqrt{H_{ii}\, H_{jj}} \tag{2.45}$$

- *Capillarity*: When two solid surfaces approach, the micro contacts act as active sites for condensation in a humid environment if the relative humidity (RH) is high enough. These sites are known in the literature as nuclei of condensation (Yamamoto et al. 2021). A liquid meniscus originates in the contact region when condensation occurs, bridging the two solid surfaces. This bridge contributes to increasing the adhesion energy by a further force composed of three parts: a surface-tension force that resides in the meniscus, a capillary pressure force that is transmitted by the liquid but originates in the curvature of the meniscus, and a buoyancy force associated with the wetted segments of the sphere. The contributions can be computed by solving the Young-Laplace equation, that in the case of sphere-plate contact (particle-substrate) leads to the following result (Orr et al. 1975)

$$F_{cap} = 2\pi\, R\, \gamma_l\, \frac{cos(\theta_1) + cos(\theta_2)}{1 + D/d} + 2\pi\, R\, \gamma_l\, sin(\psi)\, sin(\psi + \theta_1) \tag{2.46}$$

where γ_l is the surface tension of the liquid bridge, θ_1 and θ_2 are the contact angles, D is the minimum equilibrium separation distance, d is the height of the particle inside the liquid bridge, R is the particle radius, and ψ is the filling angle. All these geometric quantities can be recognized in Fig. 2.16. Among the parameters present in the relation, the filling angle plays a crucial role in the computation since it is directly

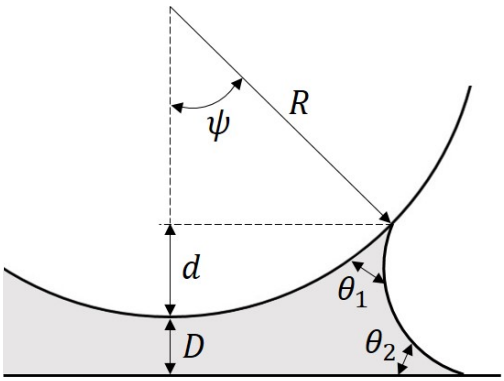

Figure 2.16: Schematic of the particle, meniscus and substrate.

related to the relative humidity according to the Kelvin equation (Eq. 2.47):

$$\kappa(\psi) = \frac{R_g\, T}{V_m\, \gamma_l} \ln(RH) \tag{2.47}$$

where κ is the mean curvature of the meniscus, R_g is the gas constant, T is the temperature expressed in K, and V_m is the molar volume of the liquid. As pointed out, the curvature is a function of the filling angle. The general formula to compute the mean curvature of the meniscus includes the calculation of elliptic integrals (Kim & Bhushan 2007), which is expensive to compute. For this reason, the assumption of a circular meniscus profile was used in this work, leading to the following more straightforward formula for the mean curvature Orr et al. (1975):

$$\kappa(\psi) = \frac{1}{2R}\left[\frac{sin(\theta_1 + \psi)}{sin(\psi)} - \frac{cos(\theta_1 + \psi) + cos(\theta_2)}{1 - cos(\psi)}\right] \tag{2.48}$$

Now, the filling angle can be computed by an iterative procedure using the Eqs.2.47 and 2.48. After that, the calculation of the capillary force is straightforward.

As reported above, the extent of the condensation depends on the relative humidity. Furthermore, its distribution could not be uniform on the surface. A local RH value was calculated on the target to account for this phenomenon. A sensitive heating process for the air from the inlet to the target was assumed. In other words, the process is considered at constant absolute humidity (x). Therefore, in this track, the first step consists of the calculation of x:

$$x = 0.622\, \frac{RH_{inlet}\, p_s(T_{inlet})}{p_{inlet} - RH_{inlet}\, p_s(T_{inlet})} \tag{2.49}$$

where p_s is the saturation pressure of water at the temperature T. The second step involves the computation of the local relative humidity:

$$RH_i = \frac{x\, p_i}{0.622\, p_s(T_i) + x\, p_s(T_i)} \tag{2.50}$$

where the subscript i stand for the i^{th} point on the surface where pressure and temperature are known.

Removal Forces

- *Weight*: Generally, the weight of the deposit is considered negligible in detachment problems. This hypothesis is acceptable when small deposit thickness occurs but becomes unrealistic when they outweigh several orders of magnitude the particle size. In the specific case, to take into consideration the gravitational effects of the deposit, the

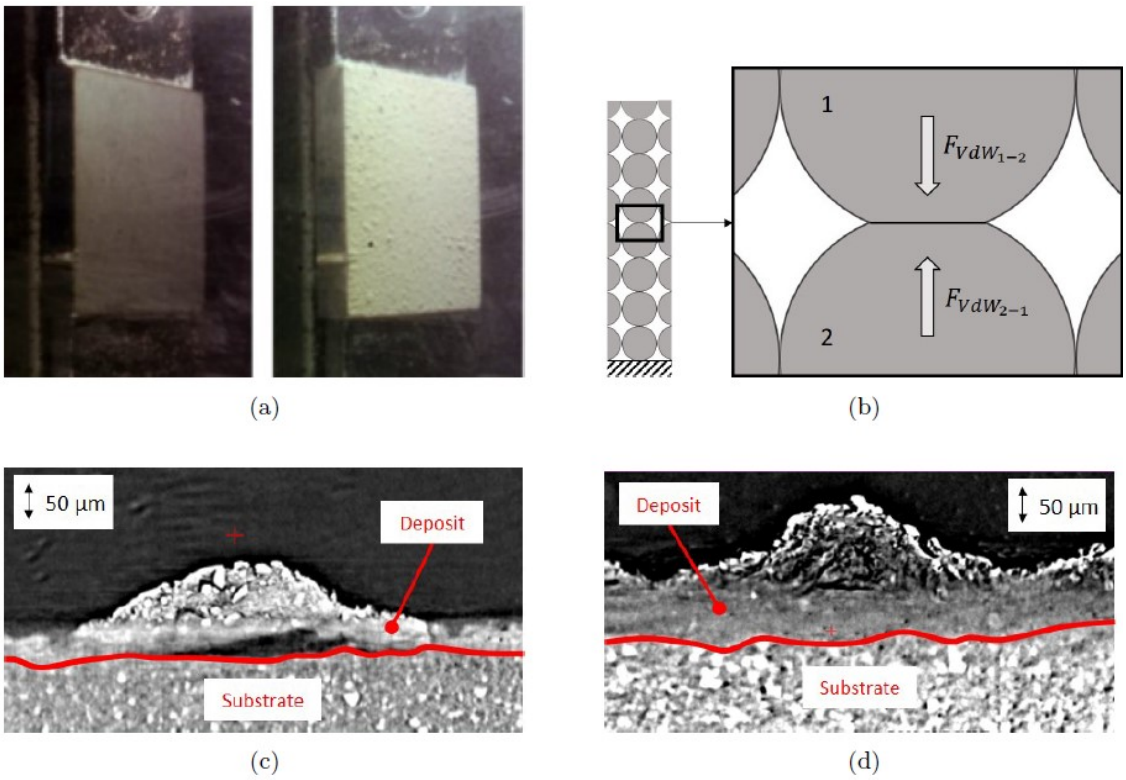

Figure 2.17: a) Target before and after exposure to ARD contaminant, b) schematic of the cohesion between particles of the same pile, c) photo of ARD deposit on stainless-steel substrate (Suman et al. 2021-3), and d) photo of Soot deposit on a stainless-steel substrate (Suman et al. 2021-3).

following assumptions were made:

1. Uniform deposit distribution on the surface;
2. When the detachment takes place, the whole deposit pile corresponding to the detachment position detaches.

The first assumption can be justified by considering the picture of the target before and after the exposure (Fig. 2.17(a)). As can be noted, the deposit distribution onto the surface appears uniform. This hypothesis is no longer valid in two cases:

- in the first few moments in which the deposition process begins, which correspond to a non-uniform deposit accretion.
- when detachment occurs. In this case, localized steps produced by deposit detachment originate.

The second assumption, on the other hand, depends on the contaminant considered. Presuming perfect particle stacking, the deposit structure can be schematized as in Figure 2.17(b). Let's consider two particles belonging to the same pile. Their adhesion strength is mainly guided by the Van der Waals force, which is proportional to the

Hamaker constants of the materials in contact (Eq. 2.45). Now, it is obvious that the deposit detachment is likely to take place where the Van der Waals adhesion is weaker, that is where the Hamaker constant is smaller. If we consider the contact ARD-ARD, we obtain a Hamaker constant equals to 5×10^{-19} J (Israelachvili 2011). On the other hand, the contact of ARD with stainless steel (SS) involves a value of 3.3×10^{-19} J for the constant (Israelachvili 2011). This led to the conclusion that the adhesion strength of ARD deposit on the SS surface is weaker compared to the ARD-ARD contact. Thus, these contaminants are more prone to detach from the substrate interface, leaving a clean surface. In the same manner, as reported earlier, the same situation with Soot instead of the ARD led to different Hamaker constants (2×10^{-19} J (Liu et al. 2018) for Soot-Soot, and 2.1×10^{-19} J for Soot-SS (Israelachvili 2011, Liu et al. 2018)), involving a detachment at a position within the deposit. The theoretical reasoning just exposed found its ground when the experimental results obtained by Suman et al. (2021-3), reported in Figure 2.17(c) ad 2.17(d), were analyzed. The former reports the ARD deposit on the SS surface, whereas the latter reports the Soot deposit on SS. The pictures show how the ARD detaches from the substrate interface, whereas several cracks within the deposit thickness originate in the Soot. These results support the above conclusions and justify the present study's second assumption. At this point, the explained assumptions allow the schematization of the single deposit pile as a uniformly loaded cantilever beam, where the load is the deposit overlying the pile in the direction of the gravitational force. A sketch of the concept is reported in Fig. 2.18. As it can be seen, a specific pile (in red in the figure) is uniquely defined by

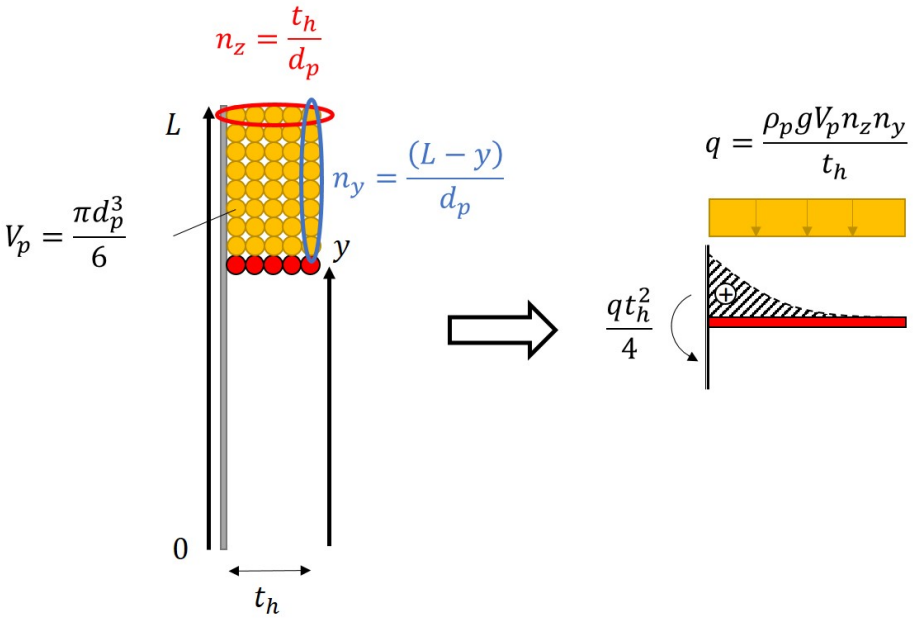

Figure 2.18: Analogy between a deposit pile and a uniformly loaded cantilever beam.

its distance from the bottom of the target (y). To compute the load (q) that weighs on the pile considered, the number of particles in the y (n_y) and z (n_z) directions has to be computed. This was done by knowing the target height (L), the deposit thickness (t_h), the particle density (ρ_p), and the diameter of the particles (d_p), with which the particle volume (V_p) can be estimated. The results depend on the packing law chosen for the layers. In this specific case, simple packing was enforced.

- *Drag*: the drag fomulation is the same described in the second case of section 2.2.3.

Moment balance All the torques of the forces described have to be computed with the same rotation center, indicated as O in Fig. 2.15. Furthermore, the deposit thickness has to be considered for those forces that act parallel to the surface (drag and weight). With this in mind, in this work, the torque arms are computed in the following fashion:

- **drag**: The drag force is thought to be applied in the center of gravity of the last particle in each pile. This is because according to the uniform and packed deposit distribution hypothesis Suman et al. (2021-3), the only particle that contributes to the drag is assumed to be the one directly exposed to the flow, so the last of the whole pile, since it is the only one wetted by the flow. Thus, the drag torque arm is approximately equal to the deposit thickness reduced by the particle radius.

$$M_D = F_D \left(t_h - \frac{d_p}{2} \right) \tag{2.51}$$

- **weight**: the weight torque is the one computed with the assumption of a uniformly loaded cantilever beam, so

$$M_p = \pi \rho_p g \frac{d_p t_h^2}{24} (L - y) \tag{2.52}$$

- **capillary and Van de Waals**: these forces are considered perpendicular to the surface and applied to the center of the meniscus bridge. The arm should therefore be equal to the radius of the ring, but, to avoid further uncertainties, the particle radius was used:

$$M_{VdW} = F_{VdW} \frac{d_p}{2} \tag{2.53}$$

$$M_{cap} = F_{cap} \frac{d_p}{2} \tag{2.54}$$

Deposit characteristics Besides those already exposed, two additional points should be considered to increase the reliability of the results: the deposit thickness and the deposit roughness. The former is related to the torques since it represents the arm of the forces, whereas the latter only influences the drag force. In particular, it is well recognized that a

rough surface involves high shear stresses, then high shear velocity gradients (Moody 1944). This, in turn, affects the drag force and then the drag torque. Since the latter effect is hard to estimate with a simple model, specific computational fluid dynamics (CFD) results have been exploited in this respect.

Deposit thickness As just explained, to compute the torques, the calculation of the deposit thickness is needed. Specifically, a critical thickness value defined as the thickness to which the detachment occurs was determined. To assess the reliability of the theoretical critical thickness, it was compared with an approximation of this quantity estimated by the results obtained by Suman et al. (2021-22). In their work, the accumulated ARD mass on the target was measured over time. From this information, the calculation of the thickness in time using the uniform deposit assumption is straightforward. Let us consider the mass evolution for the test with the normal impact of particles. Here, the target was oriented to guarantee a mean orthogonal impact of the particles. The measurements show that the peak value of the mass at which the detachment occurs is $3.9 \times 10^{-5}\,\mathrm{kg}$, and it takes place after eleven hours of exposure. With the assumption of uniform deposit, the mass at a specific time can be defined as

$$m_p = \rho_p \, V_p \, n_x \, n_y \, n_z \, \nu_f \tag{2.55}$$

where n_x, n_y, n_z, and ν_f are the number of particles in the x, y, and z directions and the void fraction, respectively. These quantities are defined as

$$n_x = n_y = \frac{L}{d_p} \tag{2.56}$$

$$n_z = \frac{t_h}{d_p} \tag{2.57}$$

$$\nu_f = \frac{real\ deposit\ volume}{deposit\ volume\ without\ void\ parts}. \tag{2.58}$$

The thickness height value can be then expressed as

$$t_h = \frac{6\, m_p}{\pi\, \nu_f\, \rho_p\, L^2}. \tag{2.59}$$

Deposit induced roughness The common way to model roughness in CFD simulations is by using the well-known equivalent sand-grain roughness height (k_s), which is the size of uniformly packed sand-grains tested by Nikuradse (1933) and utilized by Schlichting (1937). The magnitude of k_s represents the size of sand grains which give the same skin friction coefficients of the roughness being evaluated. Considering the characteristic dimensions of the particles responsible for fouling (Suman et al. 2017) and the effects induced by the deposition of particles, it appears necessary to consider the effect of the local variation

of roughness in the estimation of losses. In the literature, several correlations are proposed (Bons 2010) to compute the k_s value given a set of statistics. Most of them are suitable for machined surfaces but not for fouled ones, mainly because the latter are difficult to be described by the standard statistics (Bons 2010). For this reason, a study was conducted in order to find the existing correlation that best defines the surface of interest of this work. To do so, the reference relation considered is the following one:

$$Statistics \rightarrow k_s \rightarrow \Delta p \tag{2.60}$$

where Δp is the losses induced by the rough wall. The first step of the study was to verify that the roughness model implemented in the software used is suited to model the phenomenon under investigation ($k_s \rightarrow \Delta p$). This was done by reproducing the experimental test conducted by Schultz & Flack (2013). After that, the experiments of Bons et al. (2008) was numerically reproduced to find the best correlation that describes fouled surfaces ($Statistics \rightarrow k_s$). In their work, they reported the surface statistics of fouled surfaces and the corresponding skin friction coefficient. These two steps are explained below:

- *Validation of the k_s law*: Referring to Eq. 2.60, in this section the relationship between the k_s and the Δp induced by skin friction is analyzed in order to test the reliability of the modelization employed in the open-source software used. Schultz & Flack (2013) and Flack et al. (2020) conducted experimental tests with water on smooth and rough surfaces respectively in the high Reynolds number turbulent channel flow facility at the United States Naval Academy. The facility has a rectangular test section of 25 mm in height (H_{ts}) and 200 mm in width (W_{ts}), equipped with nine pressure taps that allow measuring the streamwise pressure gradient. The achievable bulk mean velocity in the test section ranges from 0.4-11.0 m/s with a corresponding Reynolds number based on the channel height and the bulk mean velocity (Eq. 2.61) between 10 000-30 000.

$$Re_m = \frac{v_m H_{ts}}{\nu_K} \tag{2.61}$$

Table 2.2: Experimental test conditions from LDV measurements

Re_m	v_m $[ms^{-1}]$	v_{cl} $[ms^{-1}]$	u_τ $[ms^{-1}]$	$Viscous\ length$ (ν_K/u_τ) $[\mu m]$
39 800	1.48	1.69	0.075	12.50
84 300	3.13	3.48	0.145	6.47
188 900	6.99	7.73	0.300	3.13

Through the experimental test, they derived k_s from the pressure drop measured along the test section as described next. For each test, velocity measurements were carried out using a two-component laser Doppler velocimetry (LDV) whose use and description is reported in Schultz & Flack (2007). The speed components measured with LDV are indicated in the Tab. 2.2. Roughness-covered plates form the top and the bottom walls of the test channel starting from $60H$ (where H here represents the channel height) from the inlet section. The wall shear stress is calculated as reported in Eq. 2.62 with the pressure drop measured between $90H$ and $110H$ downstream from the inlet.

$$\tau_w = -\frac{H}{2}\frac{dp}{dx} \tag{2.62}$$

Typically, τ_w is found in the definition of the skin-friction coefficient C_f:

$$C_f = \frac{\tau_w}{\frac{1}{2}\rho v_m^2} = 2\Big(\frac{u_\tau}{v_m}\Big)^2 \tag{2.63}$$

The rough surfaces tested by Flack *et al.* Flack et al. (2020) were generated mathematically in MATLAB using a circular Fast Fourier Transform and so, they had known surface statistics from which to derive roughness parameters. Then, these surfaces were reproduced using a high-resolution 3D printer. For other details, the reader is referred to the aforementioned paper. Seven different rough surfaces were tested for the entire allowable range of Re_m then, the roughness function is computed following Granville's method (Granville 1987):

$$\Delta u^+ = \sqrt{\frac{2}{C_{fS}}} - \sqrt{\frac{2}{C_{fR}}} \tag{2.64}$$

where C_{fS} and C_{fR} are the skin-friction coefficients in the *smooth* and *rough* case respectively, at the same $Re_m(C_f)^{1/2}$ or Re_τ. From the roughness function, k_s can be determined from the following equation:

$$\Delta u^+ = \frac{1}{\kappa_A}\ln k_s^+ + A - B \tag{2.65}$$

where $\kappa_A = 0.40$ is the von Kármán constant, B = 5.0 is the log-law intercept for a smooth wall, and A = 8.5 is the intercept for a uniform sand-grain surface. In the end, the authors concluded that the root mean square of the roughness height ($k_{rms} = \sqrt{(1/N)\sum_{i=1}^{N} z_i^2}$) and the skewness ($Sk = (1/N)\sum_{i=1}^{N} z_i^3/[(1/N)\sum_{i=1}^{N} z_i^2]^{3/2}$) are the roughness parameters that best predict the value of k_s, then proposing the following correlation:

$$k_s = 4.43 k_{rms}(1 + Sk)^{1.37}. \tag{2.66}$$

It is interest of this work to predict reliably the pressure losses induced by skin friction

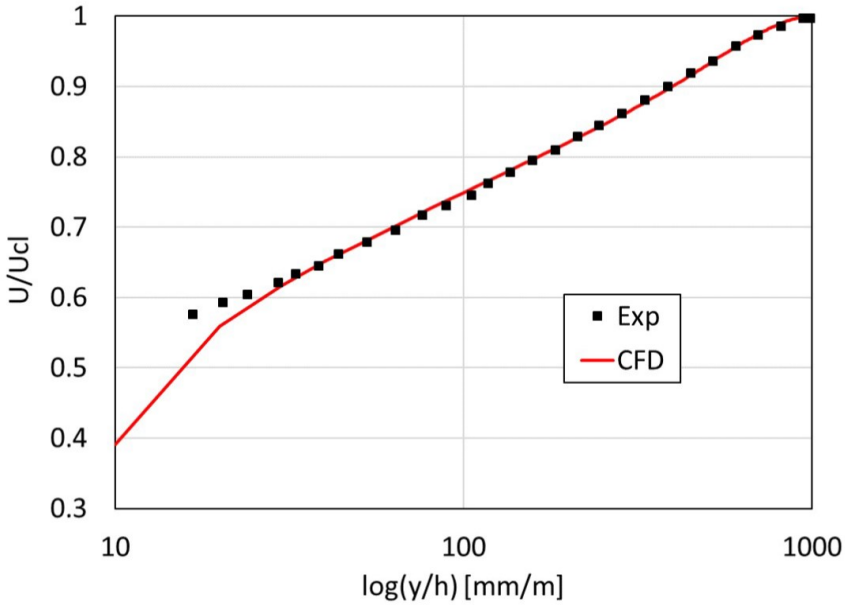

Figure 2.19: Flow validation of Schultz & Flack (2013) at $90H$ downstream from the inlet of the test section for $Re_m = 84300$.

imposing the k_s value on rough walls. For this purpose, CFD simulations of the experimental test described above are carried out with the OpenFOAM-v2006 software. The flow validation of the Schultz and Flack's test section with smooth walls Schultz & Flack (2013) is reported in Fig. 2.19. This chart shows the experimental velocity profile along with the height of the test section at 90 H_{ts} downstream from the inlet compared with the results of the simulations for the smooth case with a $Re_m = 84300$.

Two of the seven surfaces tested experimentally by Flack et al. (2020) were numerically reproduced and simulated, with respectively low and high k_s value, in addition to the smooth one for three different Re_m. The statistics of each rough surface tested ($R.S.$) are reported in Tab.2.3. Among the available experimental data, skin-friction coefficients are known, and, reworking the equations 2.62 and 2.63, it is possible to relate the pressure gradients with the friction velocity obtaining the Eq. 2.67:

$$\frac{d\left(\frac{p}{\rho}\right)}{dx} = 2\frac{{u_\tau}^2}{H_{ts}} \tag{2.67}$$

The results obtained in terms of pressure gradient from the simulations between 90 H_{ts}

Table 2.3: Statistics of the simulated rough surfaces tested by Flack et al. (2020)

$R.S.$	k_s $[\mu m]$	k_{rms} $[\mu m]$	k_a $[\mu m]$	k_t $[\mu m]$	Sk	Fl	ES
1	65	44.9	36.0	397	-0.07	2.95	0.19
5	245	87.7	71.5	681	0.35	3.05	0.37

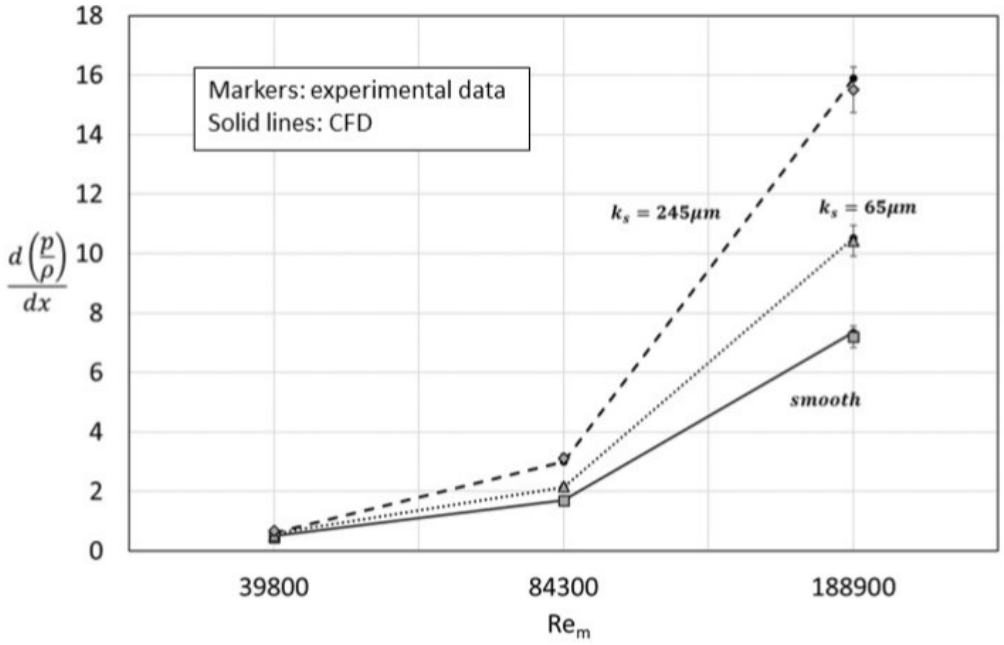

Figure 2.20: Pressure gradient between $90H$ and $110H$ downstream from the inlet for surfaces with different roughness: experimental data compared with simulation results

and $110H_{ts}$ down from the inlet for three different Reynolds numbers are summarized in Fig. 2.20. Pressure gradient predictions are in good agreement with the corresponding experimental data. The relative errors for both *smooth* and *rough* cases do not exceed 12% and the greater values are found for the lowest Reynolds number simulated. Overall, the higher the velocity, the smaller the error.

- *Derivation of k_s from roughness*: As discussed in the previous section, the equivalent sand-grain roughness height is widely used to model the viscosity effect near walls. To estimate the appropriate value of this height, several approaches can be found in the literature. The first method consists of deriving the value of k_s from the statistics of surface roughness applied to empirical correlations: parameters like the centerline average roughness height (R_a) or the peak-to-trough roughness height (R_t) are the most frequently used. Bons (2010), for example, reported the most widespread empirical roughness correlations to derive k_s from roughness statistics for gas turbines. However, the value attributed to k_s when it is derived from surface roughness statistics is not often representative of the updated skin-friction that arises from a modification of the roughness due to particles deposition, especially for irregular, three-dimensional distributed surface roughness. A second method to estimate the k_s, introduced by Sigal & Danberg (1990), foresees to take into consideration the topology of the analyzed surface through a roughness parameter Λ_s. Their approach consists of considering uniformly-sized and uniformly-shaped "two-dimensional" roughness elements spread in a uniform pattern over a test surface. Afterward, Van Rij et al. (2002), extended the

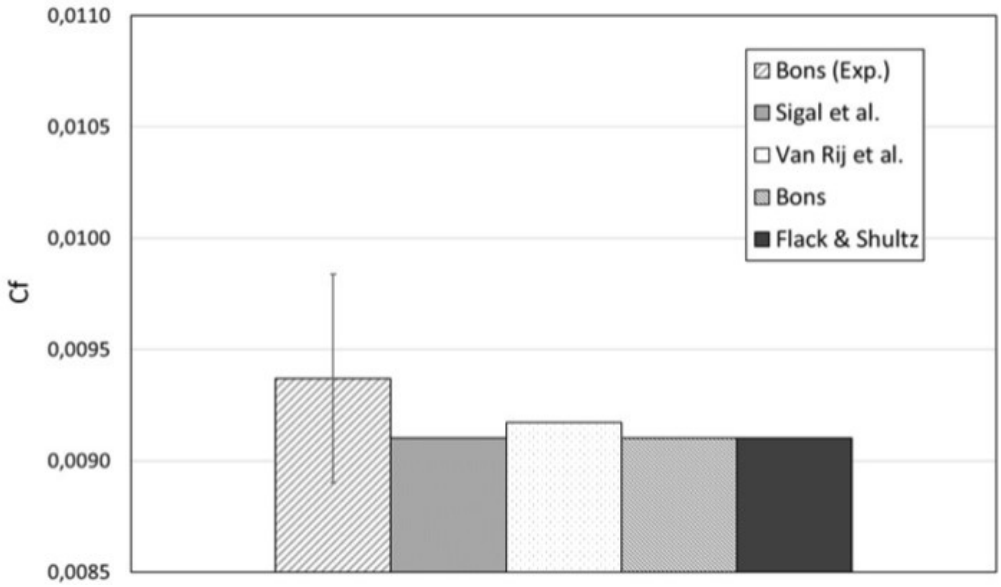

Figure 2.21: Comparison between experimental data and predictions of C_f with literature models: Sigal & Danberg (1990), Van Rij et al. (2002), Bons (2002), Flack & Schultz (2010).

validity of this approach for three-dimensional, non-uniform, randomly placed roughness reworking the formulation of Λ_s. The resulting formulation assumes the following form:

$$\Lambda_s = \left(\frac{S_{ref}}{S_f}\right)\left(\frac{S_f}{S_s}\right)^{-1.6} \tag{2.68}$$

where S_{ref} is the reference area, S_f is the total frontal area and S_s is the total wetted surface area. To reasonably predict k_s, experimental data of pressure drop related to surface roughness are needed. Bons et al. (2008) obtained the skin friction coefficients by performing tests at the open-loop wind tunnel located at Wright-Patterson AFB with smooth and rough surfaces. The wind tunnel and the test procedure are well described by the authors in Bons (2002), Bons et al. (2008). The test case was numerically reproduced and simulations for the rough case were carried out using dif-

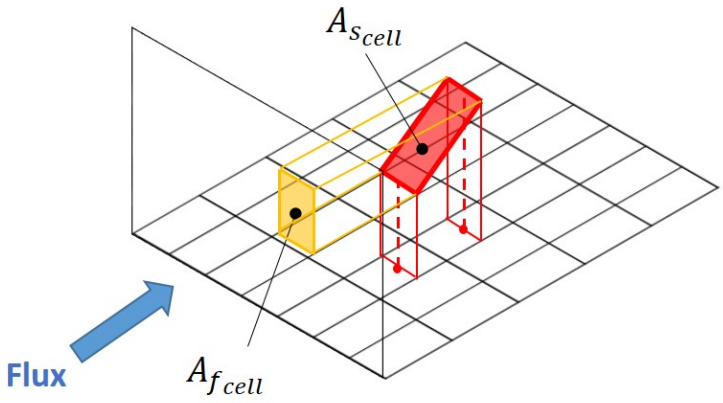

Figure 2.22: Roughness parameters calculation strategy.

ferent k_s values derived from some of the most widespread models in the literature. In particular, the considered models are the ones provided by the following authors: (i) Sigal & Danberg (1990) derived k_s from roughness parameter Λ_s, (ii) Van Rij et al. (2002) proposed a modified formulation for Λ_s, (iii) Bons (2002) predicted k_s through the root-mean-square deviation of surface slope angles and (iv) Flack & Schultz (2010) used roughness statistics (k_{rms}, Sk). Subsequently, in order to understand which of them preaches k_s value closest to the experimental conditions, skin-friction coefficients obtained from the simulations are compared with the experimental one. The results are summarized in Fig. 2.21. As can be seen, all the considered models give comparable results with the experimental ones, however the authors opted for the closest prediction of C_f which is obtained using the approach proposed by Van Rij et al. (2002). The relative error is about 2.1%. Referring to Fig. 2.22, S_s is calculated as the sum of each quadrilateral surface facing the flow direction ($\sum_{k=1}^{N} A_{s_{cell\_k}}$), and S_f is calculated as the sum of each surface square projected onto a plane perpendicular to the flow direction ($\sum_{k=1}^{N} A_{f_{cell\_k}}$).

Comparison Between the Detachment Model and the Experimental Results In this paragraph, the main results obtained in this study are reported. Firstly, an analysis of the time-varying roughness of the fouled surface is exposed. Then, the outcomes obtained were used as boundary conditions for the CFD analysis to get the drag effects on the rough wall.

As stated before, a correct value of k_s is paramount to quantify the real drag effects on the deposit. The Van Rij correlation was chosen in this track to find the k_s from the roughness statistics. The latter were obtained by analyzing the surface topological feature of the target after deposition by using a Talysurf CCI-Lite non-contact 3D profilometer (Taylor-Hobson, Leicester, UK). Such an instrument, which is a Coherence Correlation Interferometry (CCI), measures the surface features thanks to interference. The vertical resolution (i.e., the ability of the instrument to resolve a surface profile along the z-axis) of the Talysurf CCI-Lite non-contact 3D profilometer is 0.01 nm, while the lateral resolution (i.e., one-half the spatial period for which the instrument response falls to 50 %) is dependent on the objective Casari et al. (2022). Since the instrument's resolution is considerably smaller than the diameters of the particles considered in the present work, it does not influence the roughness measurement or the reported results. More details about these measurement techniques are reported in Casari et al. (2022).

Not all the target area was scanned, but only its central part of dimension 1 mm x 1 mm. In particular, this area is representative of the entire surface for both the clean and the heavy fouled conditions Suman et al. (2021-3, 2022), but not for the mild fouled ones. The latter presents a highly non-uniform roughness distribution, and to overcome this problem,

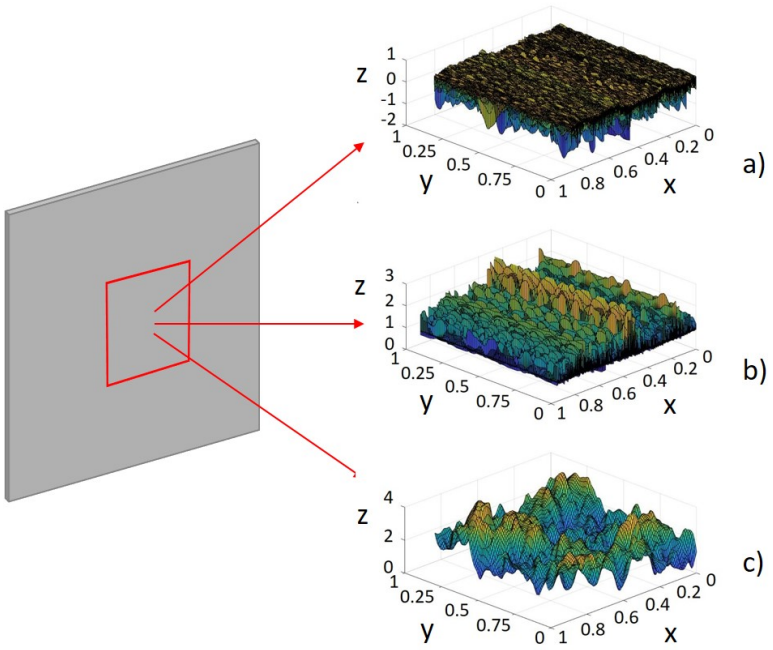

Figure 2.23: Roughness acquisition in mm for a) initial deposition, b) mid deposition, and c) high deposition

a set of 10 areas (each 1 mm x 1 mm) was randomly chosen and scanned to ensure statistical reliability. The acquisitions, reported in Fig. 2.23 were carried out for three specific instants:

- first deposition: the first few particles start to adhere to the surface (Fig. 2.23a));
- mid deposition: the target surface is completely covered by the deposit (Fig. 2.23b)) but the layers formed are not yet compact;

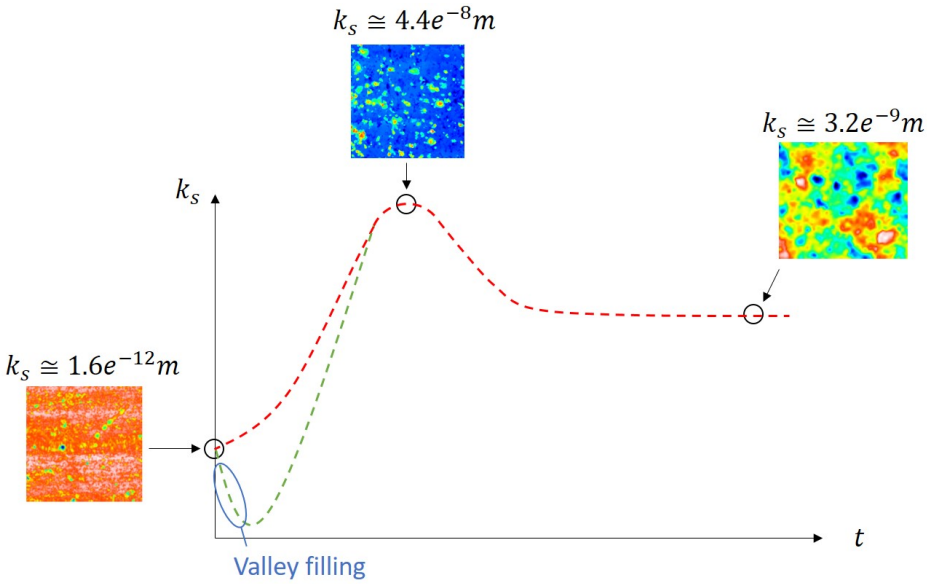

Figure 2.24: k_s evolution over time for the fouled target surface.

- high deposition: just a few moments before the detachment take place (Fig. 2.23c)). Uniform and compact layers are formed. Further particles deposition starts to generate surface irregularities.

The Van Rij correlation was directly applied to the acquired data, leading to the roughness history depicted in Fig. 2.24. As can be seen, the trend of the k_s overtime starts with a low value, correspondent to a clean, valley-dominated surface typical of the machine-tool operation or millwork, and reaches its maximum when deposition starts, as shown by the detections reported in Suman et al. (2021-23) and then drop to an intermediate value. The latter is most likely guided by a valley-filling process that tends to level out and smooth the surface. In this case, the size and the morphology of the particles dominate the surface roughness.

Clearly, the trend reported in Fig. 2.24 is only one of the possible ways in which the k_s results can be connected. The red line that connects the first and the mid deposition k_s values could be enormously different from the one sketched. For example, all the valleys composing the clean surface may be subjected to the valley-filling phenomenon when deposition starts. This, in turn, would lead to a k_s smaller than the one for the initial surface, then to a different trend (see the green line in Fig. 2.24). Nevertheless, since the detachment analysis was based on the three calculated k_s, a different trend does not affect the results and the conclusions of the present study.

The reported roughness history was used as boundary conditions for the CFD simulations. In particular, the three values of k_s were imposed at the target wall. This directly affects the boundary layer of the fluid flow and impacts the drag friction of the surface. Once the simulations reached convergence, the target's local values were stored and used offline to analyze the detachment. Specifically, the local values of τ_{wall} (for the u_τ calculation), p and T (for the local RH calculation), were gathered. These were entered in the formulas exposed earlier to compute the torques acting on the target wall.

To robustly test the model exposed, two different particle impact directions were studied: normal and tangential, which correspond to a target wall exposed at 90° and 40° with respect to the duct axis, respectively. For what concerns the normal impact, the results of this analysis are reported in Fig. 2.25, where the total adhesive (grey plane) and detachment (red circles) torques are depicted. The results are obtained using the three deposit thicknesses corresponding to the three k_s values computed. At this point, two primary considerations can be made:

- since uniform deposit distribution was assumed, shear stresses (τ_{wall}) higher than the real ones were found at the target left and right extremities. The real shape of the deposit in these areas would be smoother and rounded, leading to smaller torques arms, then lower torques magnitude. This is due to the boundary effects that are difficult to

be reproduced (e.g., the fillet of the target edges due to the manufacturing process).

- as the thickness increases, the detachment torques increase more at the lower part of the target due to the deposit weight. This is because the particles piles at the lower extremity have to sustain the whole deposit.

As discussed in Sec.2.2.3, in the experimental tests, a deposited mass equal to 3.9×10^{-5} kg was found as the peak value just before the detachment. Entering this value in Eq. 2.55, considering a unitary void fraction coefficient, a critical thickness of 6.89×10^{-5} m was obtained, which is close to that estimated by using the model proposed in the present study, which is 6.95×10^{-5} m. This means that, with the strategy here exposed, the thickness at which the detachment occurs can be accurately predicted, considering the approximation of the void fraction of the deposited layer.

In addition to that, the detachment area was studied. The results are depicted in Fig. 2.26. As can be seen, the lower target edge is the zone where the detachment torques overcome the adhesion ones. This means that the removal is likely to take place in this region. The outcome was compared to the experimental observations (reported in Fig. 2.26), and a good agreement was observed on what concerns the area where detachment occurs. As noted, the first detachment was detected in the same area predicted by the model. This means that in addition to the critical thickness, the region where the detachment occurs can also be adequately expected by the current approach.

To test the limits of the process proposed here, the tangential particle impact was also tested. In this track, the target was rotated to set an angle of 40° with respect to the duct axis. Now, the hypothesis of the uniform deposit distribution becomes inappropriate. This has led the authors to the assumption of a triangular deposit distribution as sketched in Fig. 2.27. This assumption was done in accordance with the experimental results, in which rather than a uniform distribution a sort of triangular one takes place. In the figure are reported the two quantities that the algorithm needs to be executed, the maximum (th_{max}) and the minimum (th_{min}) thickness.

As was done for the normal impact, CFD simulations were carried out for this configuration to get the local values of the thermo-fluid-dynamics quantities. The same algorithm reported earlier was then used, which led to the results reported in Fig. 2.28 with a th_{max} equals 1.5×10^{-4} m and a th_{min} equals 0 m.

As can be seen, the detachment zone experimentally observed is different when the impact angle becomes tangential. Nonetheless, a good agreement can be recognized between the model and the experimental results. In particular, the wall part most likely subjected to the deposit detachment is the one most exposed to the air flux, thus the one closer to the inlet section. The shear stresses here are higher than in the rest of the target, which is the main reason for the rise of the detachment torques. Furthermore, it can be noted that also the

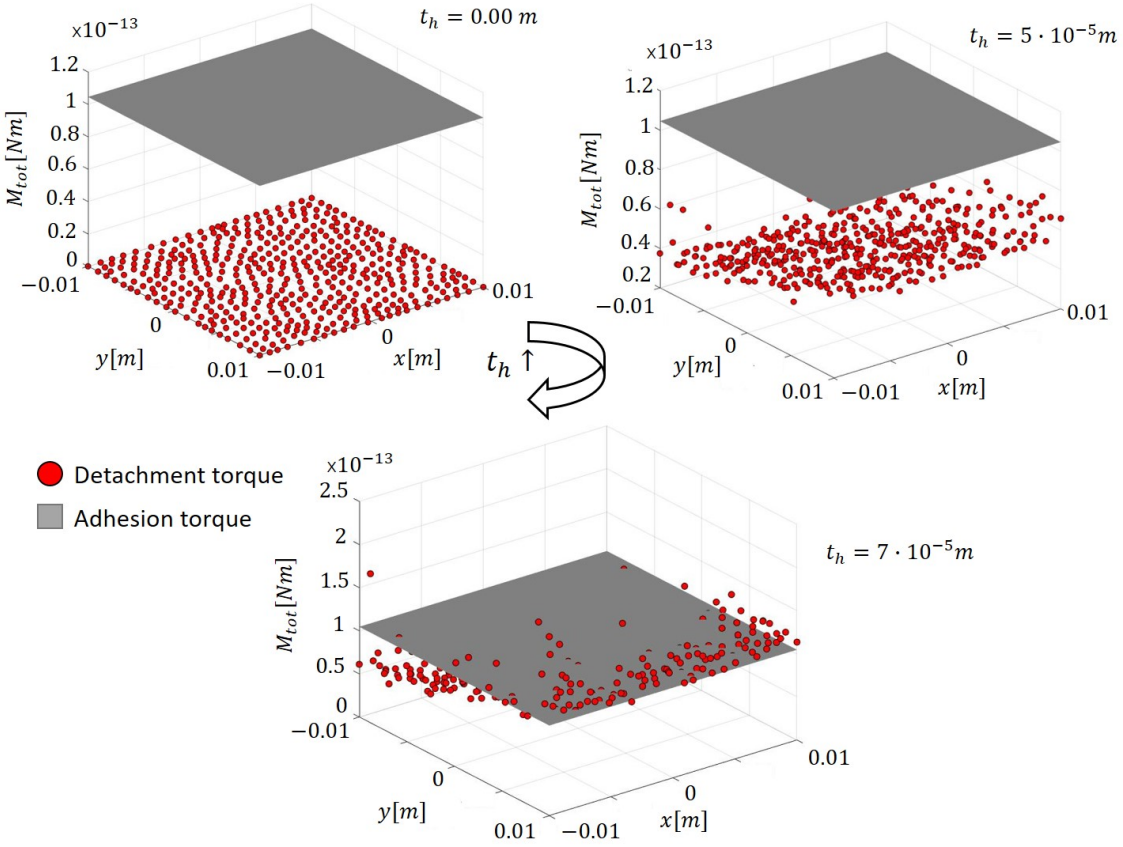

Figure 2.25: Adhesion (grey) and detachment (red circles) torques at the target surface, at different values of deposit thickness and roughness.

deposit weight contributes to the detachment (as the y coordinate drops, the detachment moment rises), but in a less pronounced way.

Despite the promising results regarding predicting the detachment area, the model does not perform well in estimating the critical thickness. This was approximated in the same manner as for the uniform deposit distribution but considering the new triangular shape. In this track, a critical thickness equal to 5.5×10^{-5} m was found experimentally, whereas a value of 1.5×10^{-4} m results from the model. These outcomes conclude that the reported model performs well when normal particle impact occurs and performs less well when tangential impacts occur.

To increase the usefulness, a summary of the critical thickness prediction against the experimentally estimated one is reported in Fig. 2.29. Here, an experimental error was added in terms of deposit void fraction. Specifically, the void fraction, which for spherical particles is approximately equaled to $\pi/6$ (μ_{ν_f}), was varied with a standard deviation (σ_{ν_f}) of ± 0.1, to account for the non-sphericity of the particulate.

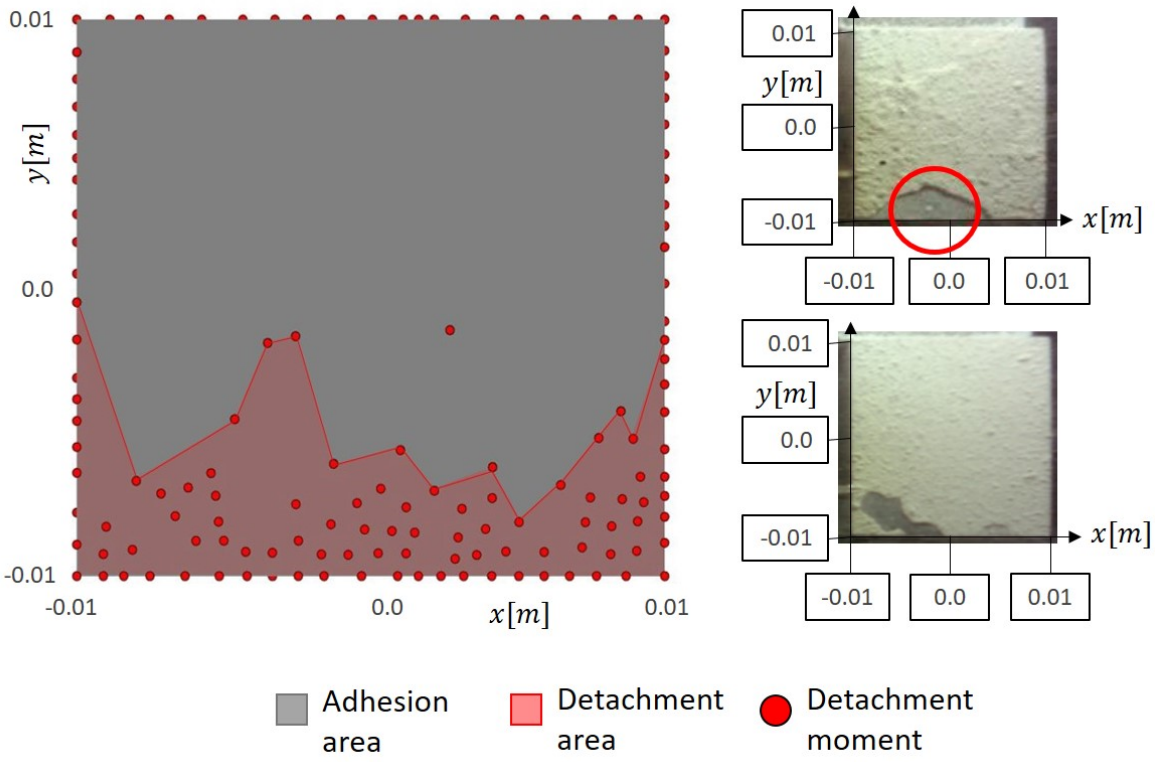

Figure 2.26: Comparison between the predicted and the experimentally observed detachment area for the normal particles impact.

Deposit-Flow Field Interaction Model

The effects of the deposit on the flow field were accounted for by means of roughness variation. For this purpose, the microscale strategy proposed by Casari, Pinelli & Suman (2018*a*) was used. If the incoming particle sticks, as decided by the deposition model described in the previous section, then it contributes to the local roughness variation. First of all, a collection of the deposit on the boundary face is done by creating a 2D subgrid on the impact surface.

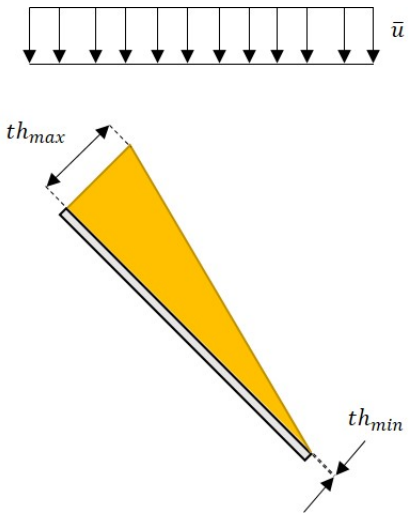

Figure 2.27: Sketch of the triangular deposit imposed at the target.

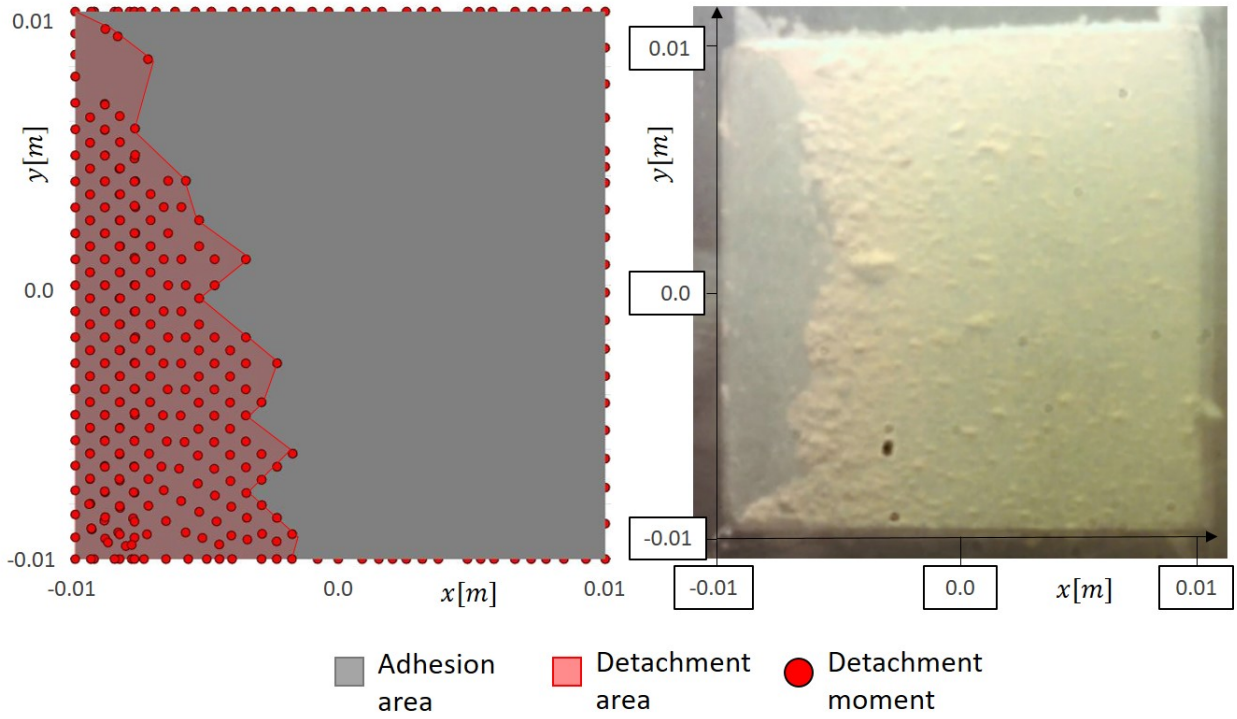

Figure 2.28: Comparison between the predicted and the experimentally observed detachment area for the tangential particles impact

This subgrid is generated by using the transfinite interpolation algorithm (Casari, Pinelli & Suman 2018*a*). After that, the tracking algorithm locates the particle impact point inside one facet of the so-generated subgrid. The deposit is hence accumulated in every impact boundary face in the form of a histogram distribution as sketched in Fig. 2.30. The height of each column of the histogram is computed by summing up the diameters of all the particles that are stuck in the corresponding facet of the subgrid.

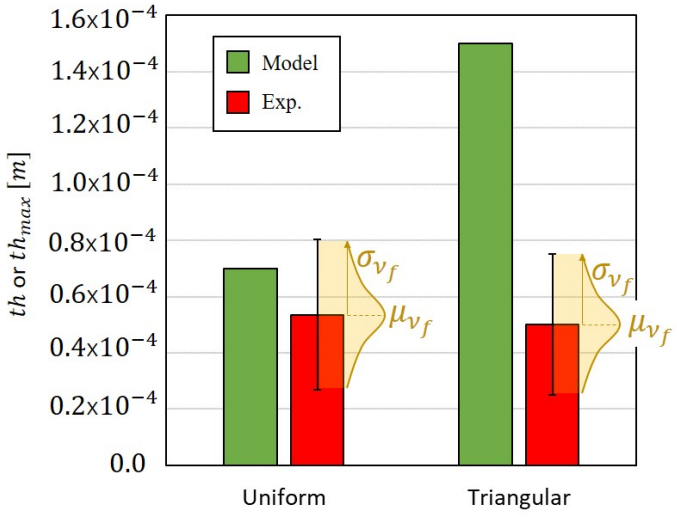

Figure 2.29: Comparison between the predicted critical thickness and the experimentally estimated one for uniform and triangular deposit distribution.

When the last particle is tracked through the domain, a pattern similar to the one reported in Fig. 2.30 will be present in every boundary face in which deposition occurred. For each pattern, a specific set of statistics is calculated in order to compute the local k_s value. In order to test the reliability of the method, the experimental tests conducted by Döring et al. (2017*b*) was numerically reproduced. The proposed strategy follows the process reported in Fig. 2.31. Starting from a smooth wall (k_s=0), a steady-state CFD simulation with no particle injection is performed. Once the flow field is solved, particles are seeded into the domain and tracked through it. Every time a particle impacts a surface, a deposition model decides if it sticks or rebounds. Once the last particle has been computed, the microscale model proposed by Casari, Pinelli & Suman (2018*a*) is used to calculate the k_s value for each mesh face in which deposition occurred, in order to obtain a non-uniform roughness distribution along the wall surface. After that, the k_s distribution is updated, and the steady-state CFD runs again with the modified roughness as a new boundary condition. This implies a stepwise variation of the flow field consequent to a nonuniform deposit-induced roughness distribution.

The performance deterioration of the cascade due to contaminant adhesion was assessed by using the static pressure rise coefficient

$$\psi_P = \frac{|\Delta p_{1\to 2}|}{q_1} \tag{2.69}$$

where $\Delta p_{1\to 2}$ is the static pressure rise, and q_1 is the inflow dynamic head. Specifically, its

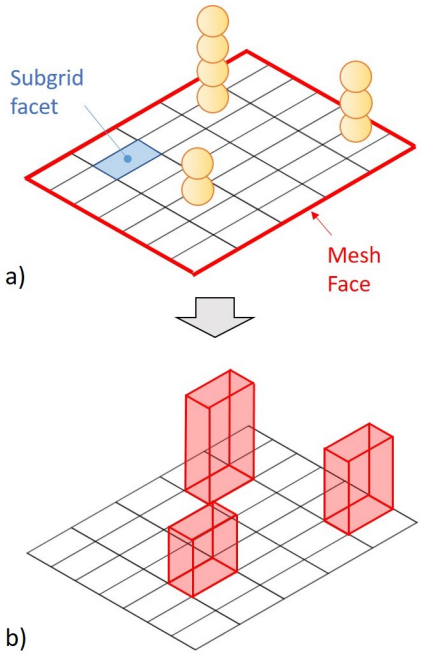

Figure 2.30: Schematic of the histogram created on the fouled mesh face (b) starting from the deposit distribution on the subgrid (a).

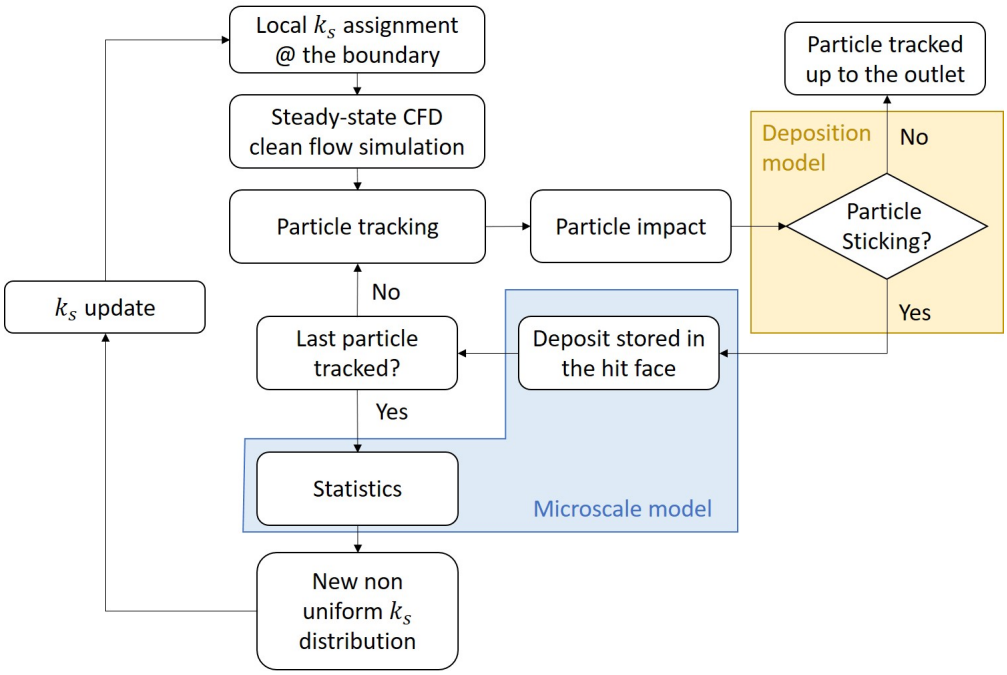

Figure 2.31: Outline of the procedure for the proposed strategy

relative variation from the clean (ψ_0) to the fouled (ψ_F) condition was used

$$\frac{\Delta\psi_P}{\psi_0} = \frac{\psi_F - \psi_0}{\psi_0}. \tag{2.70}$$

The simulations were carried out by injecting subsequent batches of $m_{p,i}$=2 g of contaminants. Every injection involves a loop of the procedure reported in Fig. 2.31. The resulting static pressure rise coefficient with increasing injected contaminant is reported in Fig. 2.32. Also, the experimental values with the respective uncertainties are depicted.

In both numerical and experimental results, the deterioration curve tends to approach an asymptotic value with the increase in the mass injected. This represents the typical behavior of the performance degradation in real engines (Vulpio et al. 2021-22). Starting from the clean conditions, a drastic reduction of performance is experienced at the beginning of the deposition process. As the deposition proceeds, the magnitude of the reduction in performance tends to diminish, leading to a sort of asymptotic behavior. This result was also encountered in the work of Melino et al. (2010), where a study of engine degradation by means of a lumped-parameter approach has been conducted. This phenomenon may depend on the distribution of the deposited mass. Specifically, when the contaminants start to adhere, a sparse deposit distribution occurs. This, as concluded in the comparison between the deposit areas and the k_s distribution, lead to a highly rough surface. On the other hand, as the deposition grows, the phenomenon of valley filling takes place. In other words, more uniform and compact deposit layers are formed, leading to a less rough surface.

For what concerns the magnitude of the effects, it can be observed that the prediction

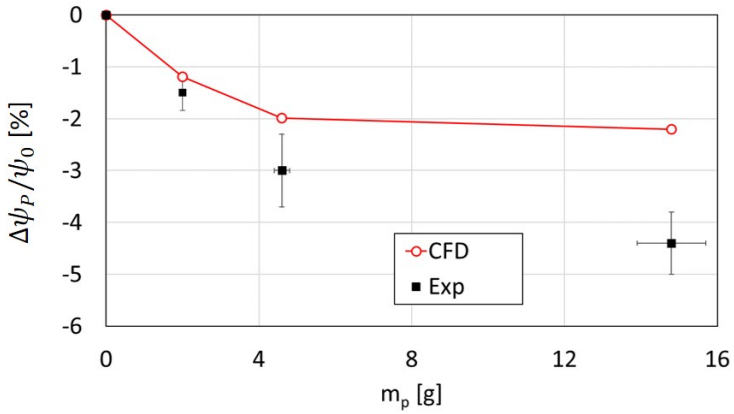

Figure 2.32: Performance deterioration results.

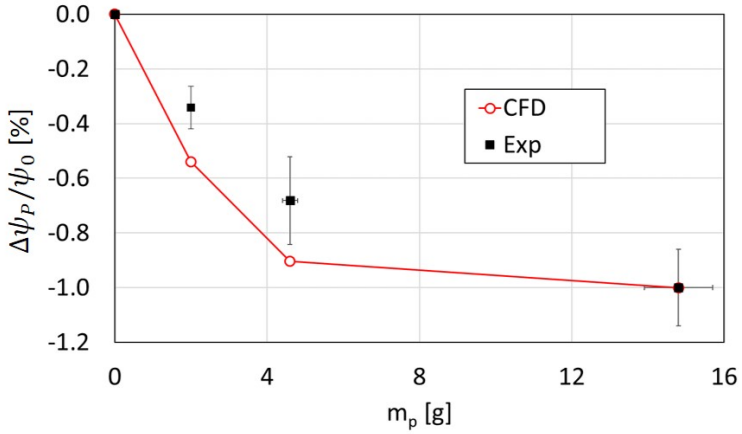

Figure 2.33: Normalized performance deterioration results.

error between numerical and experimental results increases with the increase in the injected mass of contaminant. There are many causes that could be the source of this mismatching. An example is the occurrence of micro-detachments during the deposit accretion as reported by Suman et al. (2021-22). This phenomenon is difficult to be predicted, and no specific modeling techniques are present in the literature. This source of error can be amplified if the different sensitivity to fouling of the pressure side and the suction side is considered. It is well-known that for axial flow compressors, the suction side of the vane is more sensitive to particle deposition Morini et al. (2011), Aldi et al. (2013). In this track, if a micro-detachment occurs in this area, the effects can be significant in real operations, but not detected by the deposition/detachment model. Besides the micro-detachment, it is of main importance that with the increase of the deposited layer, the effects of the thickness variations become relevant. Since only deposit-induced roughness is modeled here, these effects are not taken into account.

From the exposed results, it can be concluded that the strategy proposed is able to catch the physics underlying the phenomenon of deposition-induced deterioration, since the overall trend is quite well predicted. This can be appreciated in Fig. 2.33, where the quantities

are normalized with their maximum values. Concerning the magnitude of the effects, the approach proposed in this work is more suitable to predict the deterioration in its initial phases. This is mainly because the effects of the thickness variation become important with the increase in the size of the deposited layers.

It is worth highlighting that with the methodology reported in the present work, the effects of the deposit on the fluid flow can be predicted without a moving grid technique. Furthermore, every time the flow is updated because of the modified roughness (k_s), the deposition pattern varies as a consequence, leading to more realistic results.

2.3 Conclusions and Remarks

In this chapter, an innovative procedure for explaining particle deposit and detachment has been introduced. Firstly, the phenomenon was observed by using an ad-hoc test rig. Then, all the forces that hypothetically act on the deposit were defined and modeled. After that, the theoretical results were tested against the experimental ones. Good agreement was found between theoretical and empirical events. This prompted the Authors to convert the analysis into an innovative theoretical procedure having the main purpose of predicting particle deposit detachment area and its critical thickness. The proposed strategy has to be intended as the first step towards a tool for predicting the deposit detachment both in terms of area interested and critical thickness.

In the second part of the chapter, the deposition/detachment model proposed has been used to predict the effects of particle deposition on turbomachinery. In particular, deposit-induced roughness was considered the main cause of performance degradation. A preliminary study of the existing k_s correlations was conducted in order to find the one that best describes fouled surfaces. Here, the relation proposed by van Rij results in the best among the ones analyzed. The whole strategy was then used to replicate an experimental compressor fouling test, in order to assess the reliability of the approach. In the first instance, the deposit areas predicted by the model were compared with the experimental ones. A good agreement was found for what concerns the pressure side of the vane. On the other hand, the suction side deposition was found to be not optimally predicated. Finally, the performance reduction in terms of the static pressure rise coefficient was evaluated. The results obtained lead to the following observations:

- the overall trend of the degradation is well caught by the modelization. Both experimental and numerical deterioration curve tends to approach an asymptotic value with the increase in the mass injected;
- the prediction discrepancy between experimental and numerical results tends to increase with the increase of the injected mass of contaminants.

The strategy here proposed can be considered as the first step towards a general methodology to quantify the effects of particle deposition in turbomachinery.

Chapter 3

Turbine Section: Design for Fouling

In this chapter, the first step toward a design of an HPT section in order to make it less sensitive to the fouling problem is presented. This branch of research has been called Design for Fouling (DfF). For this purpose, several machine learning techniques were used to obtain new design guidelines. The main outcome of the whole study is a map, that outlines the best design parameters combination to generate a geometry less sensitive to degradation. Moreover, the impact of the inflow uncertainty conditions on deposition in an HPT vane was analyzed to be certain that a deterministic design optimization is sufficient to face the DfF.

3.1 Towards a Machine Learning Based DfF of an Axial Turbine Vane

In today's competitive environment, the turbomachinery design phase needs to be not only efficient but also fast and with low costs. This concept is especially valid in the aeronautical industry, where the complexity of the shapes and the need for computational fluid dynamics (CFD) simulations lead the design process to a difficult level to be undertaken with classic methods (Li & Zheng 2017). For this purpose, nowadays the design process often includes an optimization procedure. Specifically, the shape optimization of aeronautical gas turbine (GT) blades plays a critical role, due to the complex multi-physics phenomena which occur in this component and its crucial importance in the machine operation. Despite the huge amount of work that has been undertaken on the aerodynamic shape optimization problem during the last three decades, no specific algorithm has appeared to be really adequate for all problems related to GT operating conditions, or at least for a very wide range of them (Peter & Marcelet 2008).

One of the first works that tried to solve this issue was conducted in 1974 by Hicks et al. (1974). They proposed a procedure for the optimum design of aerodynamic shape using the

method of feasible directions, using the finite difference method for computing the gradient. The study was extended in 1978 to a three-dimensional problem, coupling a numerical optimization program with an aerodynamic solver (Hicks & Henne 1978). As pointed out by these studies, aerodynamic shape optimization is often performed with a large number of geometric variables. This renders the computation of the gradient using a finite difference method prohibitive. This issue was partially solved in the late 80s by the development of the so-called adjoint method (Martins & Hwang 2013), which is less expensive than the finite difference one. Nowadays this technique is still studied, with the purpose of combining it with other approaches and finding the best platform with the lowest computational cost. The main efforts related to the above-mentioned optimization methods are directly linked to gradient computation. To overcome this issue, so-called heuristic optimization methods were developed in the late 80s and the beginning of the 90s. These avoid the calculation of the gradient conducting the optimization with a form of stochastic search. The most famous and used heuristic approach is the genetic algorithm (Goldberg 1989). All the attempts to find the best technique for the aerodynamic design had to face the bottleneck of the huge computational cost of the numerous design evaluations (i.e. CFD simulations) requested by the algorithm used. Nowadays, this problem remains a research topic. To find a solution, starting from the early 90s, many authors substituted some of the exact evaluations (deriving from CFD simulations) with approximated ones, derived by a procedure of response approximation called metamodel or surrogate model. One of the first attempts to implement these approximation methods was explained in the work of (Booker et al. 1998), which reported a simplified but rigorous optimization framework for a helicopter rotor blade, considering only geometric constraints. Aerodynamic applications of this method were studied in the mid-90s (Sun 2011, Giunta et al. 1994), generating the response surfaces with second-order polynomials. Specifically, Giunta & Watson (1998) applied the technique to an optimization process of High-Speed Civil Transport aircraft. In their work, they encountered convergence difficulties due to the numerical noise in the aerodynamic computational calculations. Since the 2000s, the response surface methodology has become the main tool for aerodynamic optimization procedures, due to the increasing number of design variables considered in the design phase to describe increasingly complex shapes. This has led the CFD simulation cost to a critical level. The complexity of the phenomena that take place in an aircraft engine, forced the designers to focus their efforts to find new surrogate techniques able to capture the complex physics with lower computational costs. For example, Rai & Madavan (2000) incorporates traditional polynomial-based response surfaces and neural networks for the optimization of a gas turbine airfoil. They developed a strategy that has the capability of neural networks to maintain the economy of low-order polynomials. Representative and exhaustive comparisons among all of them were reported in the studies of Giunta et al. (1994) and Jin et al. (2001).

Despite the vast number of papers that have addressed approximation methods, there is no univocal approach for aerodynamic design in the aircraft industry (Yondo et al. 2018). The latter consideration forced the authors to focus on the study of optimization procedures that are of general application purpose. Nevertheless, optimization processes still strongly relate to the specific problem.

In this work, an innovative open-source automatic tool-chain for a 2D surrogate-based optimization applied to an aircraft engine was studied. The open-source software constituting the tool-chain are OpenFOAM for the CFD analysis, Dakota for the surrogate model, and Salome for the geometry update and mesh generation (`https://github.com/rFriso/Geometry_and_mesh.git`). The specific problem considered by the authors is the critical effects the particulate ingestion of volcanic ash have on the high-pressure turbine (HPT) vane of the GT, namely turbine degradation. Turbine degradation can be traced back to two main causes: the erosion of the blade/vane surface and deposition of contaminants (Igie et al. 2014, Granovskiy et al. 2013). The main consequences of these detrimental conditions are the reduction in engine lifetime and machine performance. There are several works focused on capturing the particles' behavior in GTs. Among them, Suman et al. (2017) assessed and compared over seventy experimental tests, identifying qualitative thresholds for further development of sticking models. Concerning the effects of deposition and erosion in gas turbines, the works of Kurz & Brun (2000) and Hamed et al. (2006) reported all the major problems related to these detrimental issues. Please refer to these works for further insights. In the present study, the EBFOG in-house model and the Tabakoff model (both implemented in OpenFOAM) (Casari, Pinelli, Suman, di Mare & Montomoli 2018, Tabakoff & Malak 1987) were used to replicate the particle deposit and erosion respectively on the HPT vane (`https://github.com/rFriso/EBFOG.git`).

In this scenario, the need for adequate guidelines about design against deterioration conditions is getting stronger. The detrimental effects of degradation on the aeronautical engines, forced Rolls Royce to undertake the study of conditions considered safe-to-fly (Clarkson et al. 2016), developing a safety map currently used in the aeronautical sector. The preliminary optimization results of the problem mentioned above were reported in Friso et al. (2019), where a neural network surrogate model was used. This paper aims to take a step forward. Firstly, a sensitivity analysis on that surrogate for a reduction of the problem dimensions has been performed. For this purpose, statistical instruments such as analysis of variance (ANOVA) and self-organizing map (SOM) were used. This analysis is fundamental since each objective function evaluation is computationally expensive, due to the complexity of the modelled phenomenon, and a reduction of design parameters leads to a significant drop in computational time. The sensitivity analysis results are then used for a critical investigation of the response surface. This includes the study of the metamodel, pointing

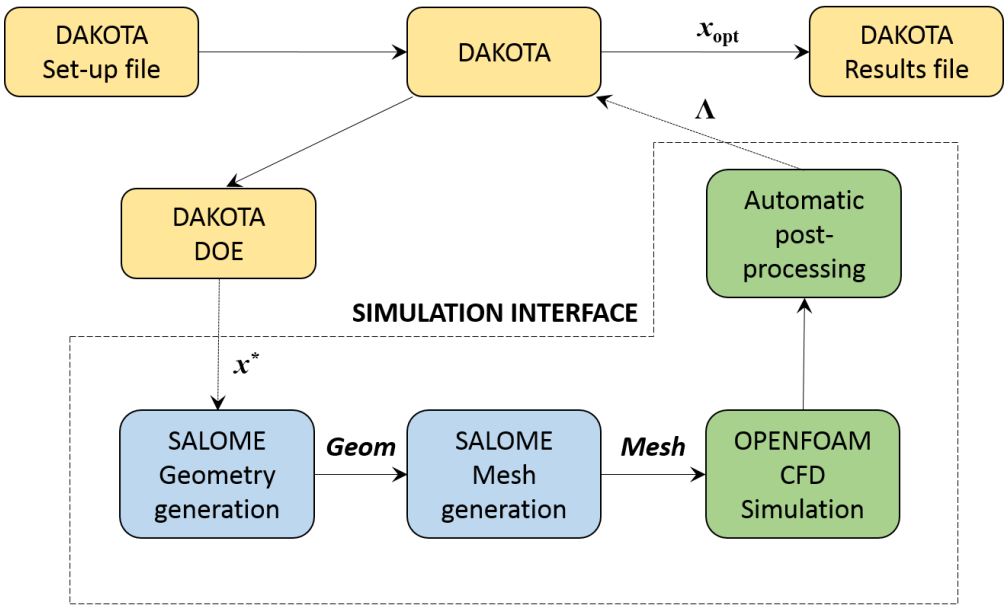

Figure 3.1: Open-source software toolchain and direct design optimization process employed in this work

out parameter combinations that lead to the best nozzle performance. The sensitivity and stability of the surrogate will be then evaluated, highlighting the most critical and influential factors. The main outcome of the whole study is a map, that outlines the best design parameters combination to generate a geometry less sensitive to degradation.

3.1.1 Design optimization platform

Aerodynamic design optimization methods can be split into inverse and direct methods. Different authors use different definitions for these terms (Wilson & Korakianitis 2014). For the scope of this paper, the inverse design is characterized by specifying a pressure distribution to develop a profile shape by iterative modifications of the vane shape, whereas direct design is the method where the shape is optimized based on secondary aerodynamic properties like aerodynamic losses (Li & Zheng 2017). In the optimization platform developed by Friso et al. (2019) the direct approach was used, thanks to its lower computational cost involving a lower number of flow calculations. The open-source software tool-chain and the direct design optimization process considered in Friso et al. (2019) and analyzed in this work are shown in Fig. 3.1. The figure reports the entire optimization platform with the three open-source software used: Dakota-v6.4.0 for the design of experiment (DOE) and surrogate-based optimization (SBO), Salome-v8.4.0 for the generation of vane geometry and computational grid, and OpenFOAM-v3.0.1 for the flow field calculations (CFD simulations). The steps that compose the algorithm platform is reported and explained below:

1. DOE: In this step, all the input vectors x* (composed by the shape parameters which will be used for the simulations) are chosen. This is a crucial step since a large sample

size involves a large number of simulations and so large computation time. On the other hand, a small sample size reflects in an underrating of the whole space of geometric configurations, and so poor accuracy. In order to reduce the sample size maintaining a reasonable accuracy, the Latin hypercube sampling (LHS) method as proposed by Helton et al. (2006) was used.

2. Geometry generation: Each point sampled in the previous step represents a geometry, and therefore for each point, a 2D parameterized vane shape is generated. For this purpose, the class shape function transform (CST) method in the version proposed by Cicic et al. (2002) was used.

3. Mesh generation: Once the 2D fluid domain was generated, the discretization process takes place. In order to guarantee the best results as possible, an automatic mesh generation algorithm is developed using the Salome library. This grid generator allows for geometric variations of the vane shape maintaining good mesh quality metrics. This feature is of primary importance since the vane shape is subjected to geometric variations due either to the optimization process and the deposition/erosion due to the particles.

4. CFD simulation: In this step, the flow field and particle injection effects are analyzed. This is the actual bottleneck of the entire process. When the convergence of the numerical simulation is reached, an automatic post-process is conducted in order to extract the objective function value (Λ).

5. After the calculation of the objective function, Dakota processes the data, identifying what the optimal point may be. Such point may or may not correspond to one of the given set of parameters. When the optimal combination is found, this step gives the best geometry for the given problem (x_{opt}).

Test case description

Overview of the problem The test case considered as a specific problem for the optimization purpose is the effects of particulate ingestion of contaminants by an aircraft engine. Aeronautical GTs are often forced to operate in harsh operating conditions due to the contaminants present in the working fluid (atmospheric air) and in the fuel, (Suman et al. 2017, Ogiriki et al. 2015). In these critical circumstances, the gas turbine components experience different forms of degradation, that often lead to off-design behaviours (Casari, Pinelli, Suman, di Mare & Montomoli 2018) or their premature failure (Ogiriki et al. 2015). Some of the principal causes of degradation include fouling, erosion, damage, and abrasion (Ogiriki et al. 2015, Lanzillotta et al. 2017), due to the ingestion of contaminants. The removal of all

kinds of impurities without affecting the performance of the turbomachinery (pressure drop, an overall increase in engine weight) is difficult, mainly since even very small particles can cause serious damage (Hamed & Kuhn 1995). These harmful degradation conditions can manifest either in the compressor or turbine components. However, the main issues occur in the hot section part, specifically in the high-pressure turbine (HPT) (Dunn 2012*b*). The particle behaviour considered in this paper is only deposition.

Geometry The geometry definition and parameterization are the first steps of every shape optimization problem. It consists of a description of the entire geometry by a finite number of parameters. By modifying these parameters different geometries can be obtained. Many parameterization methods are available in the literature for airfoils, like Ferguson Curves, Hicks-Henne bump functions, B-Splines, PARSEC, and CST (Ceze et al. 2009). Several attempts aimed to compare these methods have been done, each with different comparison criteria (Sripawadkul et al. 2010). One of the most recent ones is the work done by Sripawadkul et al. (2010), where the most used parameterization methods are compared using five parameters: parsimony, orthogonality, completeness, flawlessness, and intuitiveness. The comparison shows that the most suitable approaches are the PARSEC and CST methods for their completeness, which allows the parameterization to describe any airfoil, and orthogonality, which guarantees that each airfoil shape corresponds to a unique set of input parameters. In this work, the CST method in the version proposed by Kulfan & Bussoletti (2006) was chosen. This geometric representation has the advantage of directly controlling

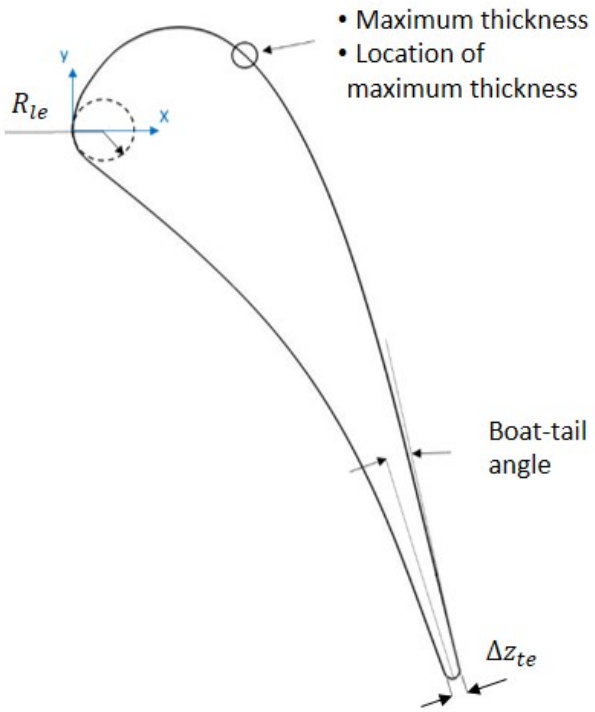

Figure 3.2: The 5 CST parameters for the description of airfoil shape

key engineering parameters, namely the leading edge radius (R_{le}), the boat-tail angle (β_{te}), maximum thickness and its location and trailing edge thickness (Δz_{te}). Figure 3.2 shows these five variables/parameters definition for a symmetric airfoil. Such method represents a two-dimensional geometry by the product of a class function, $C\left(\frac{x}{c}\right)$, where c is the airfoil chord, and a shape function, $S(x)$ plus a term that characterizes the trailing edge thickness (Δz_{te}) and the TE position in the y-axis (y_{te}):

$$\frac{y}{c} = C\left(\frac{x}{c}\right) S\left(\frac{x}{c}\right) + \frac{x}{c}\left(\frac{\Delta z_{te}}{c} + y_{te}\right) \tag{3.1}$$

where the latter term (y_{te}) is a modification to the version of Cicic et al. (2002) introduced by the authors, and so not comprised in the original form. The class function is given in a generic form by:

$$C\left(\frac{x}{c}\right) = \left(\frac{x}{c}\right)^{N_1}\left[1 - \frac{x}{c}\right]^{N_2}, 0 \leq \frac{x}{c} \leq 1 \tag{3.2}$$

where The exponents N_1 and N_2 define the type of geometry to be represented. An airfoil is represented by N_1=1/2 and N_2=1. The shape function, that acts as a scale function for $C\left(\frac{x}{c}\right)$, is built with the following constraints:

$$S\left(0\right) = \sqrt{\frac{2R_{te}}{c}} \tag{3.3}$$

$$S\left(1\right) = \tan\left(\beta_{te}\right) + \frac{\Delta z_{te}}{c} \tag{3.4}$$

and defined on the basis of the Bernstein binomials, by the introduction of weight factors b_i as follows:

$$S\left(\frac{x}{c}\right) = \sum_{i=0}^{n}\left[b_i K_{i,n}\left(\frac{x}{c}\right)^i\left(1 - \frac{x}{c}\right)^{n-i}\right] \tag{3.5}$$

where $K_{i,n}$ is the binomial function:

$$K_{i,n} = \frac{n!}{i!\left(n-i\right)!} \tag{3.6}$$

For a 4^{th} order binomial series as $S(x)$, the influence factors for each binomial at each control point were studied by Ceze et al. (2009). They found how much each weight influences the overall geometry variations, concluding that only the first and the last ones have the 100% of control respectively to the LE and the TE. All the other influence factors have definitely lower impact than the two above mentioned. In this work, a 4^{th} order polynomial was chosen as the airfoil CST representation function. The LS89 vane nozzle of the VKI test case (Arts & Lambert de Rouvroit 1992) was used as base geometry. Figure 3.3 depicts the weighted Bernstein functions derived by the parameterization procedure in order to fit the baseline of

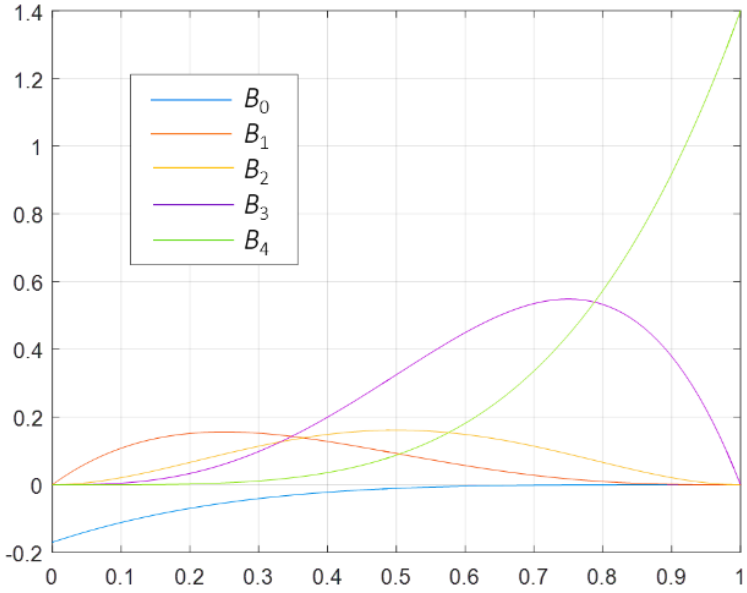

Figure 3.3: 4^{th} order shape functions for the LS89 fitting with CST parameterization method

the LS89. The name associated with each binomial is B_i, where the subscript indicates the binomial order. The weights directly associated with each binomial for the baseline fitting are:

$$\mathbf{b} = \begin{cases} b_{SS} = [0.8, 1.8, 2, 3.3, 2.9] \\ b_{PS} = [-0.17, 0.37, 0.5, 1.3, 1.4] \end{cases} \tag{3.7}$$

where the subscript 'PS' stands for the pressure side and the subscript 'SS' is for the suction side. Another important characteristic of this parameterization method is related to the ability to generate a 2D geometry with constant local curvature and slope-of-curvature (Ceze et al. 2009), which is the fundamental conditions to avoid surface Mach number spikes (Wilson & Korakianitis 2014). Since the principal vane zone affected by deterioration is the pressure side (PS) Casari, Pinelli, Suman, di Mare & Montomoli (2018), this is the only area of the geometry that will be changed for optimization. The bounds chosen for this purpose correspond to a variation of $\pm 20\%$ for each parameter.

Mesh After the geometry generation, the computational mesh of the entire fluid domain has to be created. For this purpose, Salome-v8.0.4 was used. Specifically, a python code using the Salome library was developed for the creation of an automatic grid generator. The purpose of this generator is the construction of a semi-structured mesh, which is completely structured near the airfoil (with a user-specified thickness) and non-structured in the remaining fluid domain. The structured part of the mesh is of fundamental importance since the EBFOG algorithm utilizes a mesh-morphing technique for taking into account the geometric variations due to the particle impacts. These variations are considered moving the grid cells near the impact point outward (deposition) of the geometry. Another important

Table 3.1: Boundary conditions for the flow field calculation

	Quantity	**Value**
Inlet	Total pressure	15.23 bar
	Total temperature	1708 K
	Turbulence intensity	5%
	Turbulent mixing length	0.004 m
Walls	Temperature	1100 K
Outlet	Isentropic Mach number	1.02
	Pressure	7.766 bar

characteristic the mesh must have is related to particle tracking. The tracking algorithm used by OpenFOAM consists of a tetrahedral decomposition of each cell, which in turn must have the adequate topological shape that allows this decomposition. The coupling model is an Eulerian-Lagrangian type, which computes each particle trajectory (Lagrangian) into the fluid flow field (Eulerian).

Flow computation The numerical flow field analysis was conducted using the sonicFoam solver from OpenFOAM-v3.0.1 set for compressible flow. For the turbulence modeling the two-equations SST k-ω turbulence model was used, thanks to its robustness in the resolution of the near-wall region. The boundary conditions (BCs) considered for each simulation is reported in Table 3.1.

In the surrogate generation process, each CFD simulation starts with the initialization of the flow field, in which no particles were seeded until the converged solution was reached. When the latter condition was satisfied the particulate was injected from the inlet patch of the domain. A total mass of 9x10^{-7} kg of ash particle has been injected, considering a concentration of contaminant equals 250 $\mathrm{mg}_{ash}/\mathrm{m}^3_{ash}$, that is well above the Safe-to-fly limit(Clarkson et al. 2016). The amount of particulate injected is derived considering also the One-way Lagrangian flow conditions coupling (Elghobashi 1994) in which the volumetric fraction of contaminant at the inlet must be less than 1 ppm (part per million). The main physical properties of the particles are the density (ρ_p = 3000 kg m^{-3}) and the specific heat capacity (c$_p$ = 800 J kg^{-1} K^{-1}) which are used in Ghosal & Self (1995*b*) for ash particles. As reported above, the analysis of the behaviour of the particles was carried out using a Lagrangian tracking model with the integration of numerical modelling for the deposit and erosion implemented in the CFD software by Casari, Pinelli, Suman, di Mare & Montomoli (2018). They also take into account the heat transfer between the gas and the particles using the Ranz-Marshall equation for the Nusselt number. The impact modelling between the particles and the blade was built considering that a particle that does not stick to the surface erodes it. The erosion of the deposit is not considered in the model used for

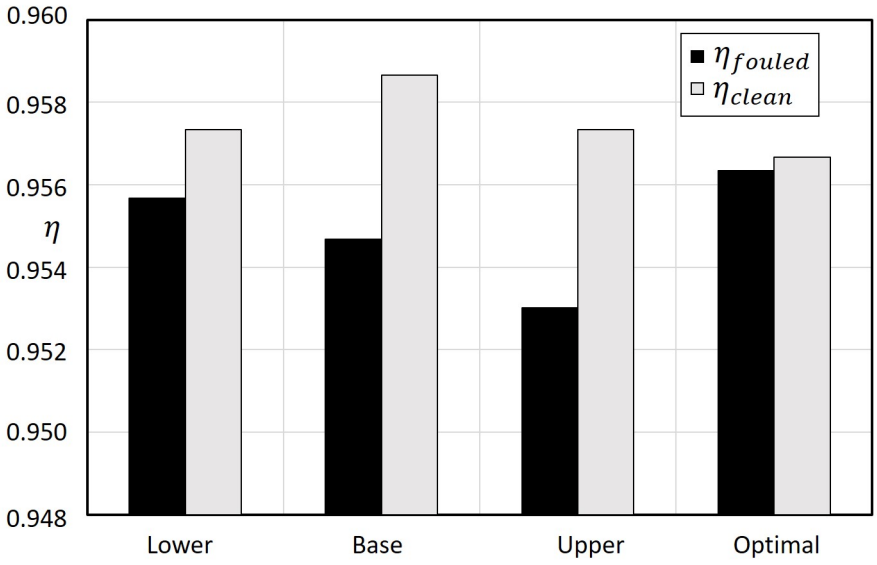

Figure 3.4: Objective function for all the fouled and clean cases

this work. The objective function chosen for the surrogate optimization purpose was the isentropic efficiency calculated as follows:

$$\eta = \frac{h_{inlet} - h_{outlet}}{h_{inlet} - h_{outlet,is}} \tag{3.8}$$

where, since this study is focused on the HPT vane, h is the static enthalpy. The purpose of the optimization is the maximization of this quantity. The isentropic efficiency is of paramount importance since a reduction of the performance of the nozzle reflects immediately on its value.

Optimisation results

The results of the preliminary optimization above described are reported in details in Friso et al. (2019). Here we recall the main outcomes of the cited study to ease the reader. As the optimization process is guided by the objective function (Eq. 3.8), this is the first parameter analyzed. In Fig. 3.4 is reported the isentropic efficiency for all the four cases considered in the study, either clean and fouled (lower and upper are the bounds of parameters variation). In the clean ones, the best performance is related to the base case, whereas the optimal one shows the lower value of the objective function. In the fouled case instead, the higher isentropic efficiency has been found for the Optimal configuration. The main considerations have to be done not for the absolute values of the objective function but for its relative ones. As a matter of fact, Fig. 3.4 shows a bigger performance loss for the base configuration compared with the optimal one, going from the clean to the fouled case. This means that the Optimal geometry found by the optimization process is less sensitive to the degradation

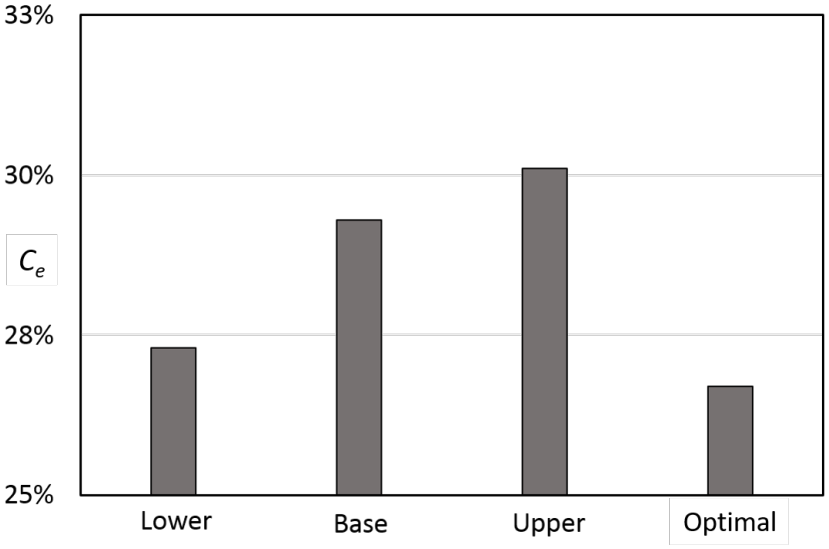

Figure 3.5: Capture efficiency for the four cases considered

problem. Another important parameter considered in the analysis is the capture efficiency (C_e) calculated as follows:

$$C_e = \frac{particulate\ stick\ on\ vane\ surface}{particulate\ seeded} \tag{3.9}$$

The values of this parameter for all the cases considered are shown in Fig. 3.5. As can be seen, the capture efficiency of the Optimal configuration is lower than the one of the Base geometry. Moreover, the isentropic efficiency trend (Fig. 3.4) seems to be closely related to the capture efficiency variation: decreasing when the latter increases.

Sensitivity analysis

Since the computational cost related to each CFD simulation is remarkably high, a reduction of the number of total objective function observations is desirable. This can be obtained, for example, by reducing the number of parameters to be considered. There are several statistical instruments that can be exploited for this purpose, such as ANOVA (Jeong et al. 2005), scatter plot matrix (Tatsukawa et al. 2008) and Self-Organizing Map (SOM) (Asan & Ercan 2012). In this work, the ANOVA test and SOM were used. The first was used for evaluating not only the quantitative effect of the single design variables but also the effect of the interactions between each of them on the objective function (Li & Zheng 2017). The SOM is employed because it offers a qualitative but useful overview of the influence of each parameter. The statistical ANOVA test, as well as the SOM, was conducted using the Matlab Machine learning toolbox.

ANOVA ANOVA (ANalysis Of VAriance) describes the observations of the objective function with the so called "effects model", which for a two factors problem has the following formulation:

$$y_{ijk} = \mu + \tau_i + \beta_j + (\tau\beta)_{ij} + \epsilon_{ijk} \tag{3.10}$$

where i is the treatment level, j is the observation, k is the replication and:

$$\mu = \int ... \int y\left(x_1, ..., x_n\right) dx_1 ... dx_n$$

$$\tau_i = \int ... \int y\left(x_1, ..., x_n\right) dx_1 ... dx_{i-1} dx_{i+1} ... dx_n - \mu$$

$$(\tau\beta)_{ij} = \int ... \int y\left(x_1, ..., x_n\right) dx_1 ... dx_{i-1} dx_{i+1} ... dx_{j-1}$$

$$dx_{j+1} ... dx_n - \tau_i - \beta_i \mu$$

In the formulas above μ is the overall mean effect, τ_i is the effect of the i^{th} level of the first factor, β_j is the effect of the j_{th} level of the second factor, $(\tau\beta)_{ij}$ is the effect of the interaction between τ_i and β_i, and ϵ_{ijk} is a random error component. For hypothesis testing, the model errors are assumed to be normally and independently distributed random variables with mean zero and variance σ^2. The variance σ^2 is assumed to be constant for all the levels of the factors. The test hypothesis can be performed as follows:

$$hypothesis = \begin{cases} H_0 : \tau_1 = ... = \tau_a = 0 \quad \text{for all levels} \\ H_1 : \tau_i \neq 0 \quad \text{for at least one } i \end{cases} \tag{3.11}$$

Thus, in this phase the equality of treatment means is under test or, in other words, the test is devoted to proving that the treatment effects (the τ_i) are zero.

SOM SOM (Self-Organizing Map) is a qualitative comparison tool based on an unsupervised learning algorithm. The special principle that SOM aims to imitate is the mapping of high-dimensional input data to a low-dimensional output network in a topology-preserving way (Fig. 3.6). The learning algorithm behind the method is based on an organization process of the single neuron, which in turn possesses two attributes: a fixed position and a mutable weight. The positions of the nodes are initially set up once and not altered by the map organization process. The attribute that will be altered is the nodes' weights, which is the key to topological preservation.

After the generation of the topology of the neural networks with random initialization of neurons' weight, for each learning cycle and for each input vector the algorithm acts as follows (Asan & Ercan 2012):

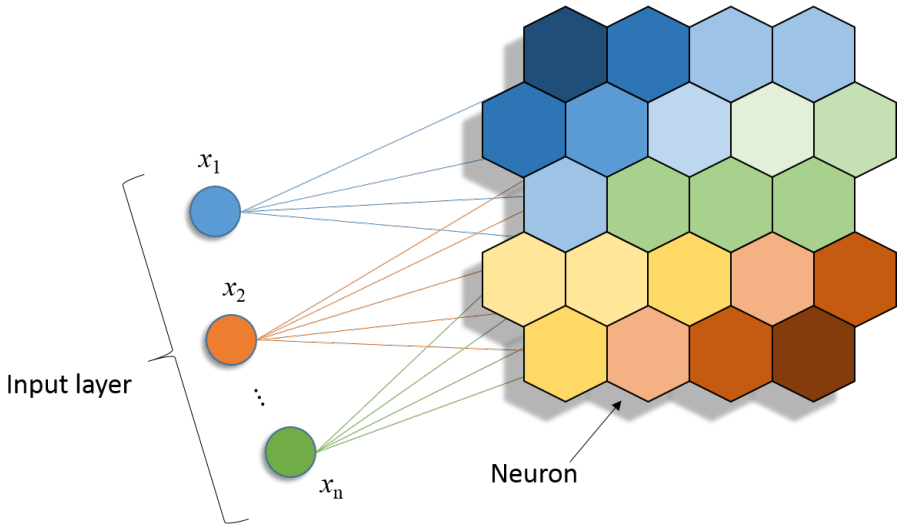

Figure 3.6: SOM map architecture

1. Find the single node (neuron) whose weight matches the input vector most closely. If there are multiple output nodes that equally match the input vector, chose a random one of those;

2. Adjust the weight of the winning output node just found to closely match the input vector and adjust the weights of this node's topological neighborhood as well.

The neural networks' topology for this work is a 20x20 square map, training with 200 epochs. The winning node (n_{winner}) is identified based on the input vector (v) with a function *bmu(v)* defined as:

$$bmu(v) = arg\ min\ diff(v, n_{i_{weight}}) \quad i = 0, ..., card(S) - 1 \tag{3.12}$$

where S is the output node set space and *diff( )* is a function denoting the difference between the input vector and the node's weight. In this work, the input vector space is the R^n space, so the Euclidean distance is used as a difference function. The determination of the winning node is followed by the adaptation of all output nodes' weight according to the given formula:

$$n^{k+1}_{i_{weight}} := n^k_{i_{weight}} + \alpha^k h(||n_{winner} - n_i||, k) diff(v_i, n^k_{i_{weight}}) \tag{3.13}$$

where the apex indicates the k^{th} learning cycle, and α and $h(||n_{winner} - n_i||, k)$ are the learning rate function and neighbourhood function respectively. The two latter functions are implemented in the SMO toolbox as follows:

$$\alpha^k = \frac{0.05}{1 + 100\frac{k}{T}} \tag{3.14}$$

$$h(d, k) = e^{\frac{-d^2}{2r_n^2}} \tag{3.15}$$

where T is the training length and r_n is the neighborhood radius at learning cycle k, which

determines to what degree neighborhood nodes adapt depending on their distance to the winning node, calculated as:

$$r_n = ||n_{winner} - n_i|| \tag{3.16}$$

Surrogate model

Suppose the simulation results can be written as a function:

$$f(x), \quad f : R^n \rightarrow R^m \tag{3.17}$$

A metamodel (or surrogate model) is a function:

$$\tilde{f}(x), \quad \tilde{f} : R^n \rightarrow R^m \tag{3.18}$$

with much lower computational cost than f (x) and such that:

$$||f(x) - \tilde{f}(x)|| < \epsilon \tag{3.19}$$

where || || is an appropriate L_p norm and ϵ is sufficiently small. This type of model provides us with a novel optimization framework in which the conventional optimization algorithms, e.g. gradient based are used for sub-optimization. In the following section the ANN surrogate model, which is the metamodel used in this work, will be explained.

ANN Artificial neural networks (ANNs) implement an algorithm that attempts to achieve a neurological-related performance, such as learning from experience, making a generalization from similar situations, and judging states where poor results were achieved in the past (Meireles et al. 2003). Nowadays there are several ANN types. Some of the more popular methods include multilayer perceptron (MLP), learning vector quantization, and radial basis function (RBF), to name a few. A comprehensive review of many of these techniques for industrial applications was given by Meireles et al. (2003). The metamodel used in the present work is the Artificial Neural Networks (ANNs) fitting model with stochastic layered perceptron (SLP), designed to have a lower training cost than traditional ANNs (Eldred 1998), based on the direct training approach of Zimmermann (1996). The main difference between SLP ANNs and traditional ANNs is that, in addition to having a transfer function for each perceptron, it also contains an activation function with a stochastic discriminant. The software used for this purpose is Dakota, which implements the SLP ANN model in the form:

$$\tilde{f}(x) = tanh(tanh((aA_0 + \theta_0)A_1 + \theta_1)) \tag{3.20}$$

where x is the current point in n-dimensional parameter space and terms $A_0, \theta_0, A_1, \theta_1$ are

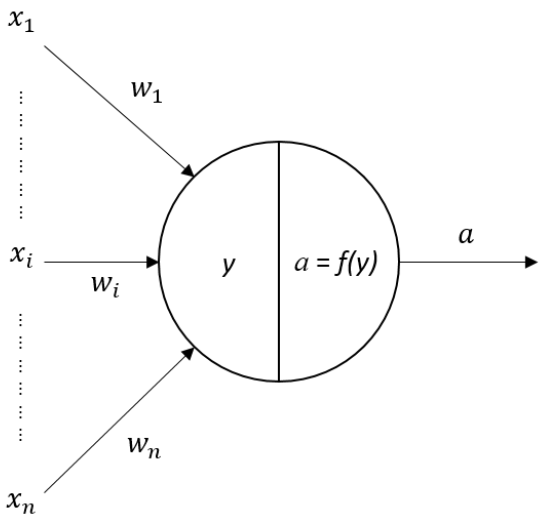

Figure 3.7: Perceptron architecture used for ANN MLP

the matrices and vectors that correspond to the neuron weights and offset values in the ANN model. The general structure of perceptron is shown in Fig. 3.7.

The principal components of neural networks are the input layer which receives the shape parameters as input, one or more hidden layers, and an output layer. The latter carried out the results of the training (i.e. the isentropic efficiency), which must be as near as possible to the training points. The training is done using 10 training data points, which is the minimum number for the model chosen (Eldred 1998). The learning algorithm used for the training is the backpropagation. In this algorithm the least-mean-square error E of the output is used to evaluate the convergence:

$$E = \sum_{i=1}^{N_s} \sum_{k=1}^{N_0} (d_k^i - y_k^i)^2 \tag{3.21}$$

where N_s is the number of samples, N_o is the number of outputs, d_k^i is the value of the k_{th} output of the i_{th} sample and d_k^i is the corresponding approximated output value. To prevent the over-fitting problem, the leave-one-out cross-validation technique has been performed.

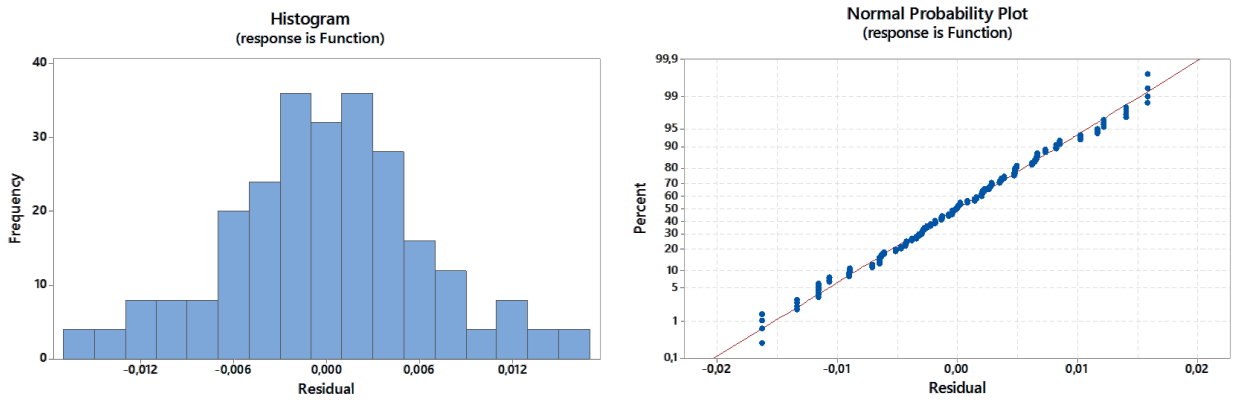

Figure 3.8: Residuals: histogram frequency representation (left) and normal plot analysis (right)

The ANN structure used in this work is composed of 2 hidden layers, guided from the comparison results reported by Li & Zheng (2017), which assert that a network with 2 hidden layers gives better results for the non-linear function than a network with 1 hidden layer.

3.1.2 Results

Sensitivity analysis

ANOVA results The ANOVA test consists of the decomposition of the variability in the observations. However, the use of partitioning to test formally for no differences in treatments means requires that certain assumptions be satisfied. Specifically, these assumptions are that the observations are adequately described by the effects model and the errors are normally independently distributed with zero mean and constant but unknown variance σ^2. Violations of the basic assumptions and model adequacy can be easily investigated by the examination of residuals. In the ANOVA test, the residuals are defined as the difference between the observed values and the predicted values. If the normal distribution of the errors is satisfied, the residuals have to be normally distributed. The analysis of the residuals is reported in Fig. 3.8. The normal probability distribution of the residuals could be checked qualitatively from Fig. 3.8. For a quantitative result, a χ^2 test was conducted with the following hypothesis:

$$H_0 : \text{The data comes from a normal distribution with zero mean}$$
$$H_1 : \text{The data does not come from a normal distribution}$$

The test was performed with Matlab, and led to the acceptance of the null hypothesis at the 5% significance level, confirming the normal distribution of the residuals with a p-value = 0.093. Since residuals are normally distributed, the normal probability distribution of the errors can be considered satisfied Montgomery (2017). With this validation, the ANOVA test can be considered an exact test for the problem under investigation. ANOVA was conducted limiting the analysis to second-order interactions between the factors. The results are shown in Fig. 3.9.

In Figure 3.9a) is reported the importance of the single factor on the objective function. Two main considerations could be done:

1. The 4^{th} parameter (b_4) is not depicted in Fig. 3.9a), because it is considered almost not significant by test (<1%);

2. The two parameters that significantly influences the objective function are b_1 and b_2, with a significance of 72% and 19% respectively. Furthermore, neglecting the b_3 parameter results in an 8% error.

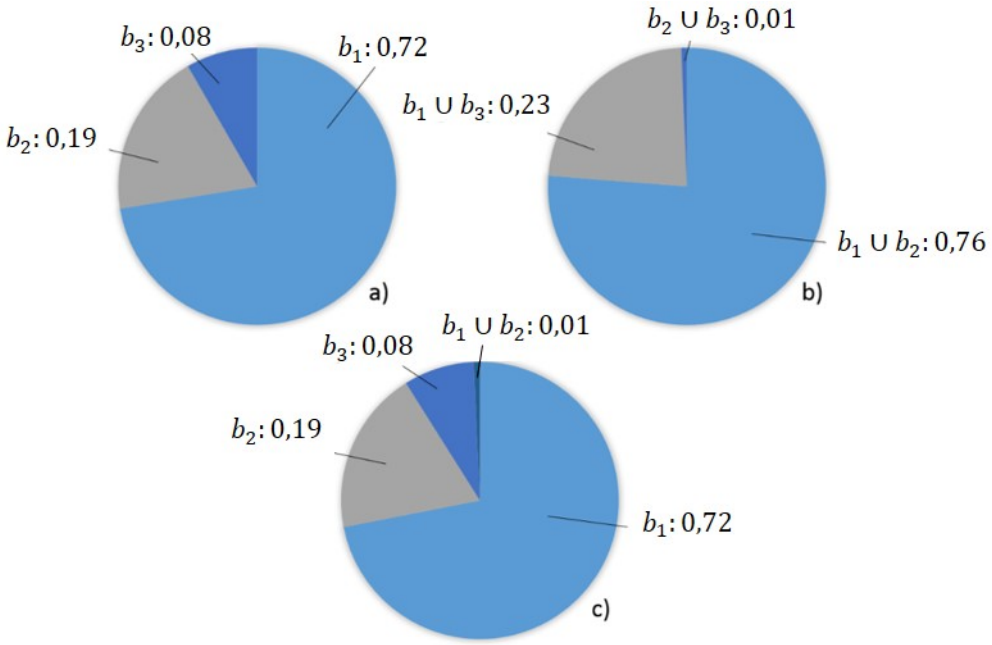

Figure 3.9: ANOVA results for a) single factor, b) second-order interaction and c) comparative results

In Figure 3.9b) is reported the importance of the factors for the second-order interactions between the parameters. Even in this Figure, two main observations can be drawn:

1. All the interactions comprising the 4th factor are considered not important by the test;
2. The most important interactions are the ones which include the 1st factor (b_1), with an importance rate of 23% when b_1 and b_2 interacts, and importance of 76% when b_1 and b_3 interacts.
3. The interaction between b_2 and b_3 can be considered negligible with an error of less than 1%.

Finally, the comparison between first and second-order interactions influence are conducted and reported in Fig. 3.9c). The Figure shows that they almost do not affect the objective function. Their negligibility involves an error of less than 1% . The major impacts are due to the single factor variations. The analysis exposed above points out that the main parameters that most influence the objective function are b_1 and b_2, which are the parameters most related to the LE of the airfoil. This means that the most important geometric parameter that governs the objective function behavior is the LE. The analysis showed also that the influence of the factors' interactions is negligible.

SOM results The results carried out by the SOM analysis are reported in Fig. 3.10. In the Figure, the colours represent the neuron weights values (darker colours represent higher weights). The fundamental principle on which the SOM has based consists of the qualitative

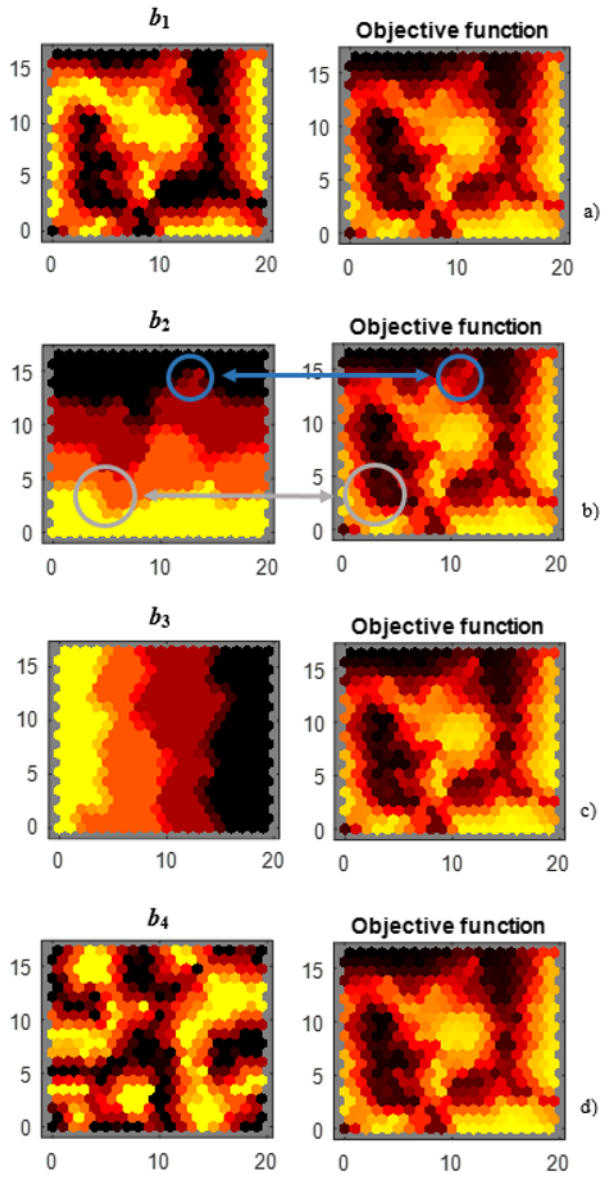

Figure 3.10: SOM resulting maps for a) b_1 b) b_2 c) b_3 d) b_4 and the objective function

comparison between the coloured maps. Similar maps mean influence among the parameters that generate those maps. In this track, a comparison between the objective function and the parameters maps was performed. As can be seen in Fig. 3.10, the parameter map more similar to the objective function map is the one generated by the first parameter (b_1) (Fig. 3.10a)). The two maps seem almost identical, which means a strong influence between this parameter and the isentropic efficiency. Also, the second parameter (b_2) map presents local similarities to the objective function map.

Some of these local zones are highlighted in Fig. 3.10b) with circles of different colours. Concerning the other two parameters (b_3 in Fig. 3.10c) and b_4 in Fig. 3.10d)), no similarities were found. The b_4 parameter presents a map completely different from the isentropic efficiency map, thus meaning they have no influence on each other. Besides, there are no

similar maps among each parameter, which means no joint influence of parameters on the cost function is present. The results of the SOM analysis pointed out that only b_1 and b_2 influence significantly the isentropic efficiency. The first has a higher influence than the second. This conclusion reinforces the ANOVA test results using a qualitative analysis of the entire objective function space.

Surrogate model assessment

In the wake of the previous results, an analysis of the response surface was conducted. Since the most influential parameters are b_1 and b_2, a graphical representation of the surrogate is possible. The response surface as a function of these two parameters is reported in Fig. 3.11. The first observation that can be done regards the presence of an optimal configuration (green point). This means that the optimization problem explained above can be undertaken as possible design optimization. In the mathematical formalization of the optimization problem, a range of possible geometric configurations was imposed as a feasible solution. As it can be seen, surrogate surface topology allows asserting that near the optimal configuration a variation of the two parameters has a low influence on the isentropic efficiency. This can be pointed out by the examination of the flat portion of the surface in the zone close to the optimum. To test the effective flatter shape of the surface on the mentioned zone, a further configuration (blue point in Fig. 3.11) was simulated. The objective function calculated from this simulation results near the value of isentropic efficiency of the optimal case. This piece of information can be exploited by generating a line dividing the optimal zone (yellow, with higher isentropic efficiency) from the bad zone (blue, with lower isentropic efficiency). Such schematic is reported in Fig. 3.12 to ease the reader. This line, called Design margin (DM), has the following form:

$$DM = -\frac{17}{26}b_2 + \frac{561}{6500} - b_1 = 0 \tag{3.22}$$

This means that when a geometric configuration (a couple of parameters b_1 and b_2) lies in a region at the right-hand side of the DM, a higher isentropic efficiency under deterioration conditions is ensured.

If the designers want to take into consideration the deterioration effects due to particle ingestion, this map can be a useful indicative helping tool in the design phase of the HPT vane. An illustrative and critical analysis of the extreme configurations allowed by the map (points P_1, P_2 and P_3 in Fig. 3.12) was performed. An overview of these three geometric layouts is depicted in Fig. 3.13. In the figure is reported the comparison between the baseline (red) and the extreme configurations (black) for the entire geometry and the LE area zoomed. The main difference between these configurations regards the LE radius,

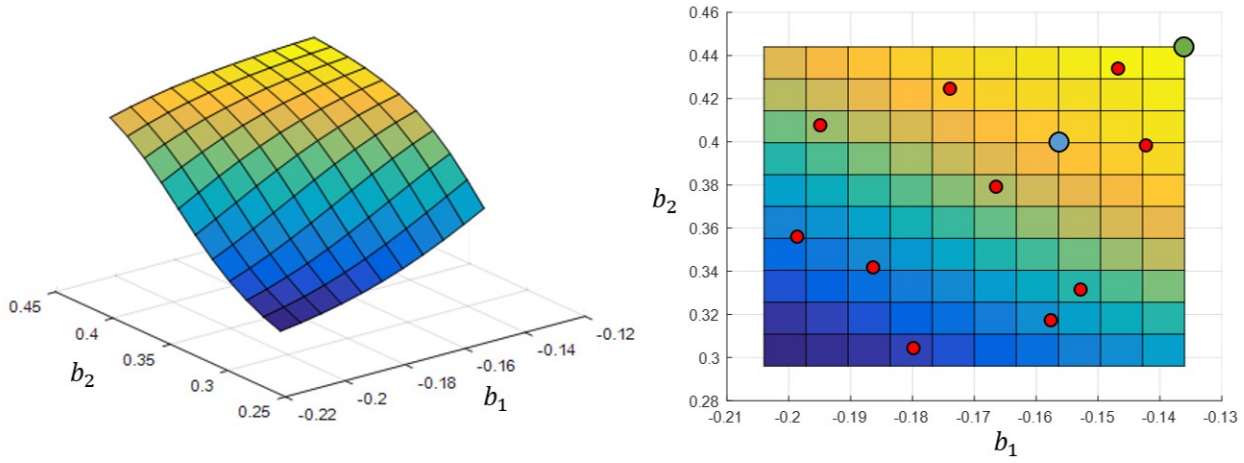

Figure 3.11: Response surface as a function of b_1 and b_2 3D (left) and 2D with samples (right)

which is larger than the baseline one in the P_1 geometry, and smaller in the other P_2 and P_3 geometries. Nonetheless, all the configurations have in common the tendency to create a flatter pressure surface. This means a larger stagnation area in front of the vane, then greater losses in terms of isentropic efficiency. The main reason the optimization seems to lead to this type of SS surface can be explained with the help of the sketch in figure 3.14. In this figure, three situations are reported: baseline geometry (top), geometry with flatter SS (mid), and a flux-orthogonal flat surface (bottom). For each configuration, the streamlines are reported in red.

As can be noted, flatter suction surfaces (mid) lead to a greater stagnation zone, which in turn conducts to larger deviations of the streamlines. Since only small particles are

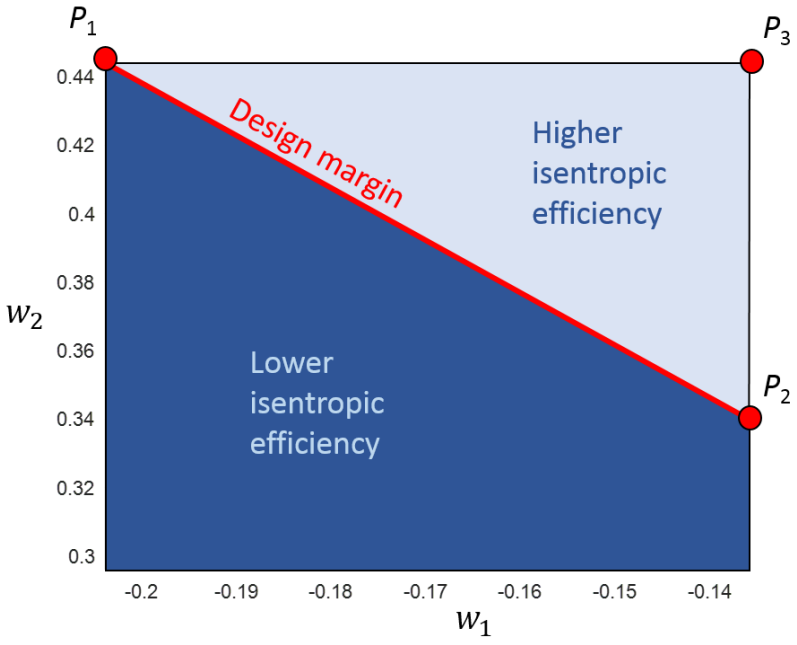

Figure 3.12: Isentropic efficiency map under deterioration conditions

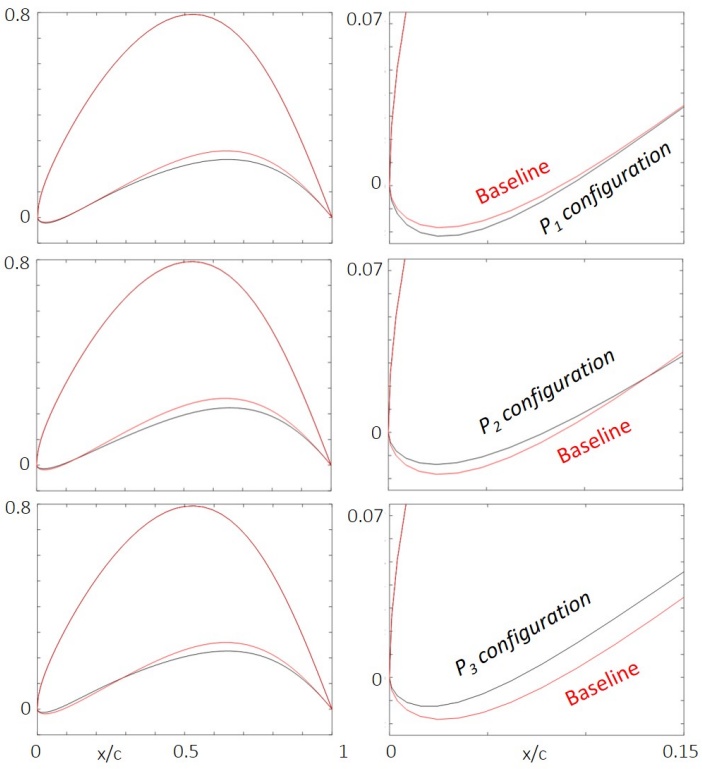

Figure 3.13: Comparison between extreme configurations of Design map in point P_1 (top) P_2 (mid) and P_3 (bottom)

considered, their tendency to follow the flow causes fewer impacts with the vane surface, than a smaller deposit. The extreme case of a flat surface is reported at the bottom of the

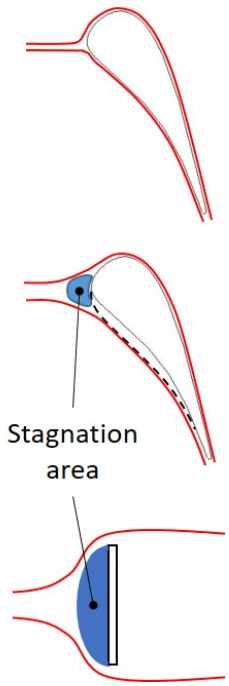

Figure 3.14: Sketch of streamlines behaviour in case of baseline geometry (top), flatter surface baseline geometry (mid), and flat-surface (bottom)

figure. These considerations are in agreement with the capture efficiency trend (3.9). On the other hand, larger stagnation areas lead to greater losses. This is in accordance with the trend of the isentropic efficiency reported in figure 3.4. In other words, the optimized geometry conducts greater losses when clean but smaller ones when fouled since the larger stagnation area allows lower deposits.

3.2 Uncertainty Analysis on a HPT Vane: Effect on Particle Deposition

In the literature, several studies focused on the analysis of the principal effects of deposition and erosion in the HPT has been conducted. These works are mainly centered on the influence on film cooling and vane geometry variations. The first theme is deeply analyzed in the study of Borello et al. (2014), where numerical simulations on 2D and 3D E^3 HPT vane with cooling system has been performed. The main outcome of the study is the strong influence of the film cooling on the deposit along the nozzle, due to the effect of the jet on the particle trajectories and the wall temperature. They stated that film cooling allows to reduce the total amount of deposit. The second theme was tackled by Casari, Pinelli, Suman, di Mare & Montomoli (2018), who analyzed the VKI LS89 HPT vane. In this work, it has been found that geometrical variations due to deposition and the flow field are strictly coupled. In particular, displacement of the shock structures and a variation in the coefficient of pressure are the main consequences.

In all the works centered on deposition and erosion in gas turbines, specific steady operating conditions were considered for the analysis. Unfortunately, these conditions can vary drastically in real life applications, and they cannot be treated as deterministic. Their stochastic variations greatly affect the forecasting of life and performance of the components. An example can be found in the study of Salvadori et al. (2011), where different combustion chamber exit temperature distributions were examined. They highlighted that two temperature distributions with same mean values but different radial configurations can greatly influence the rotor life. Sadly, in most of the cases, probabilistic distribution of temperature profile is unknown. Another source of uncertainty that can alter the HPT lifetime is the turbulence level, as stated by Ames & Moffat (1990). In their study, a turbulence level of 19% was proved to affect significantly the nozzle life.

To the authors' knowledge, in the literature there are no studies coupling uncertainty quantification and deposition problem in gas turbines. In this work, the impact of the inflow uncertainty conditions on deposition in an HPT vane was analyzed. Specifically, hot core location and turbulence intensity were considered as statistical inputs. Erosion action was not considered here, since its impact is still of secondary importance in HPT

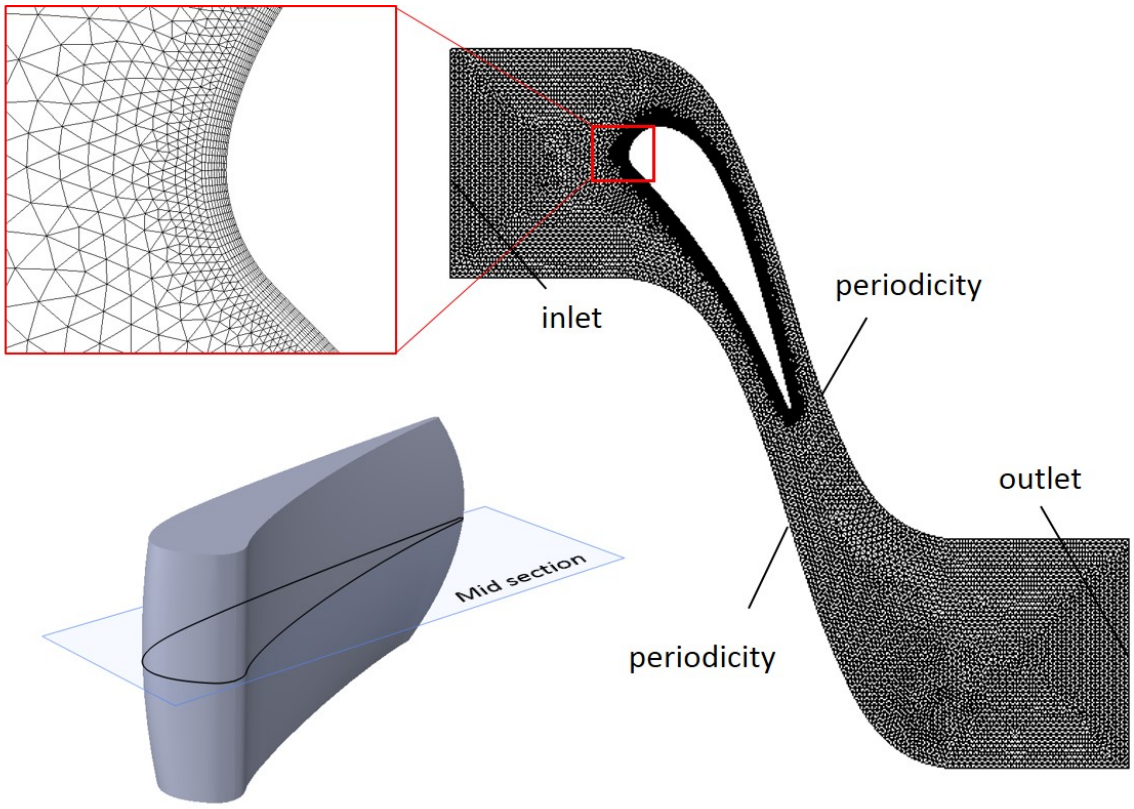

Figure 3.15: Section plane location on the 3D vane geometry and computational domain.

vane (Friso et al. 2019, Casari, Pinelli, Suman, di Mare & Montomoli 2018). The GT's component treated as a reference is the HPT nozzle of the Energy-Efficient Engine (E^3) tested by L.P.Timko (1990). Since the computational efforts for conducting particle-laden flow simulations are significantly high, the probabilistic collocation method (PCM) is used as uncertainty quantification technique. Furthermore, considering that several types of particles can enter the engine, the specific event regarding volcanic ash ingestion was treated here. Flight through volcanic cloud is one of the most dangerous events. Studies of Clarkson et al. (2016) and Clarkson & Simpson (2017), tried to investigate the effects of this occurrence on aircraft engine and suggest safe-to-fly conditions. In the present work, residual creep-lifetime and engine stability by means of mass flow rate are the quantities considered representative of the reliability of the gas turbine.

Table 3.2: Design characteristics of the E^3 1^{st} stage HPT vane.

Description	**Unit**	**Value**
Radial position	mm	345.76
Pitch	mm	47.23
Chord length	mm	62.01

3.2.1 Geometry and Computational Domain

In this study, the high-pressure turbine of the General Electric Energy Efficient Engine (EEE) is considered as industrial application (L.P.Timko 1990). Specifically, the first stage vane is used. Since the analysis of the midsection still the first step in design problems, the 2D cross-section at the midspan depicted in Fig. 3.15 has been considered for the analysis. Thus, the three-dimensional effects of the flow field were not modeled here. Furthermore, the cooling system was not taken into consideration in this study. Vane design properties are reported in Tab. 3.2. The absence of cooling system represents a limitation of the current work. On the other hand, the present analysis is devoted to the understanding of the extent to which a variation in the hot core location or the turbulence intensity affects the deposition pattern. These parameters are of crucial importance as these are the boundary conditions that are requested to carry out numerical simulations on cooled or uncooled blades. The computational domain was generated around the 2D geometry using Salome-v9.3 (see Fig. 3.15). It extends 1/2 chord upstream of the inlet section and 2 chords downstream from the exit section of the vane. A 2D unstructured grid was used for discretizing the domain, whereas a structured 10-layers prism mesh was introduced to resolve the near-wall region. The growth rate of the prism layers was set to provide a wall y^+ grater than 11. Grid sensitivity analysis was conducted with meshes of roughly 32,000, 56,000 and 80,000 cells. Grid independence was achieved with the finer one, which is the computational grid used in this study and shown in Fig. 3.15.

CFD Flow Field Resolution

The numerical flow field resolution was carried out using the *sonicFoam* solver of the open-source software OpenFoam-v1706. The solver has added the support for particle tracking, allowing the exchange of momentum and heat with the carrier flow. Particle tracking is carried out in a Lagrangian framework, choosing a Eulerian-Lagrangian coupling method.

Continuous phase

The continuous phase was modeled by the conventional Reynolds-averaged Navier-Stokes equations. The operating conditions considered for the study reproduces the design point described by the technical report written by L.P.Timko (1990). At the inlet of the domain, the hot core has been specified by means of temperature distribution. The profile of the normalized temperature is reported in Fig. 3.16, where T_{0max} is set to 1650 K. A uniform total pressure of $p_0 = 13.25$ bar has been assumed at the inlet. The inlet velocity profile has been changed according to the position of the hot core, and results similar to the temperature profile. Besides, the turbulence intensity at the outlet of the combustion chamber is

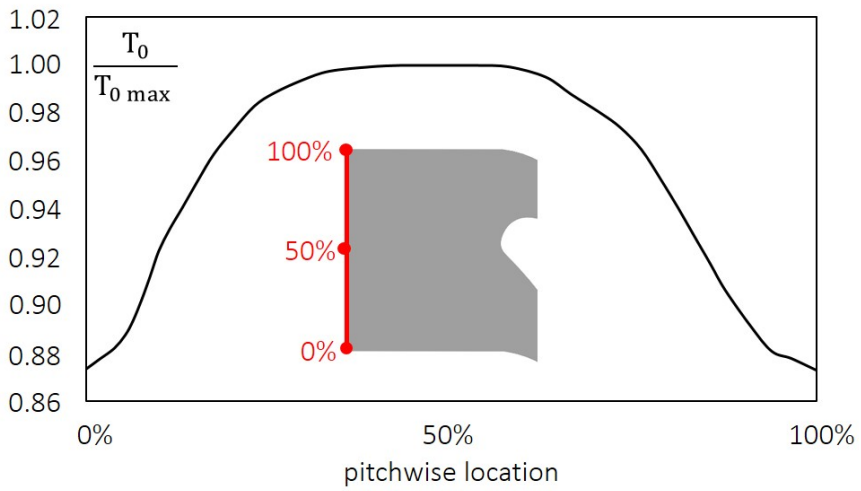

Figure 3.16: Pitchwise normalized inlet temperature distribution.

significantly high, making two-equations turbulence model of questionable accuracy (I.Lee et al. 2002). For this purpose, the Reynolds stress model proposed by Speziale et al. (1990) is used. Every CFD simulation was firstly initialized with the two-equations renormalization group (RNG) k-ε turbulence model. When the converged solution was achieved, the switch to the SSG Reynolds stress model was performed. The vane surface temperature is of main importance for particle adhesion mechanisms and an adiabatic condition has been imposed at the nozzle wall. This consideration allows to capture the temperature variation along the vane due to particle deposition. A static pressure of p = 8.02 bar has been set at the outlet of the domain, in order to guarantee an isentropic exit Mach number of 0.878 as reported in the technical report.

Dispersed phase

Once the flow field was solved, particles were seeded from the inlet of the domain with a uniform distribution between 1μm and 30μm as can be gathered by Taltavull et al. (2015). Since volcanic ash is considered, particles density (ρ_p = 3000 kg/m^3) and specific heat capacity ((c_p = 800 J/(kg K)) can be found in the study of Ghosal & Self (1995*a*). The amount of particles injected is derived considering a concentration of contaminant equal to 250mg$_{ash}$/m$^3_{air}$, which is well above the safe-to-fly limit reported in the work of Clarkson et al. (2016). A total mass of ash equals to 1.44x10^{-8}kg has been seeded, which correspond to an exposure time of 0.1s.

Particle trajectories were computed by integrating the force balance acting on each of them. The maximum particle volume fraction of roughly 10^{-7} is small enough to consider negligible the effect of particles on turbulence. This statement allows to model the interaction between particles and fluid flow with the one-way coupling Elghobashi (1994). Particles are tracked through the domain until they either stick to the vane or escape from the do-

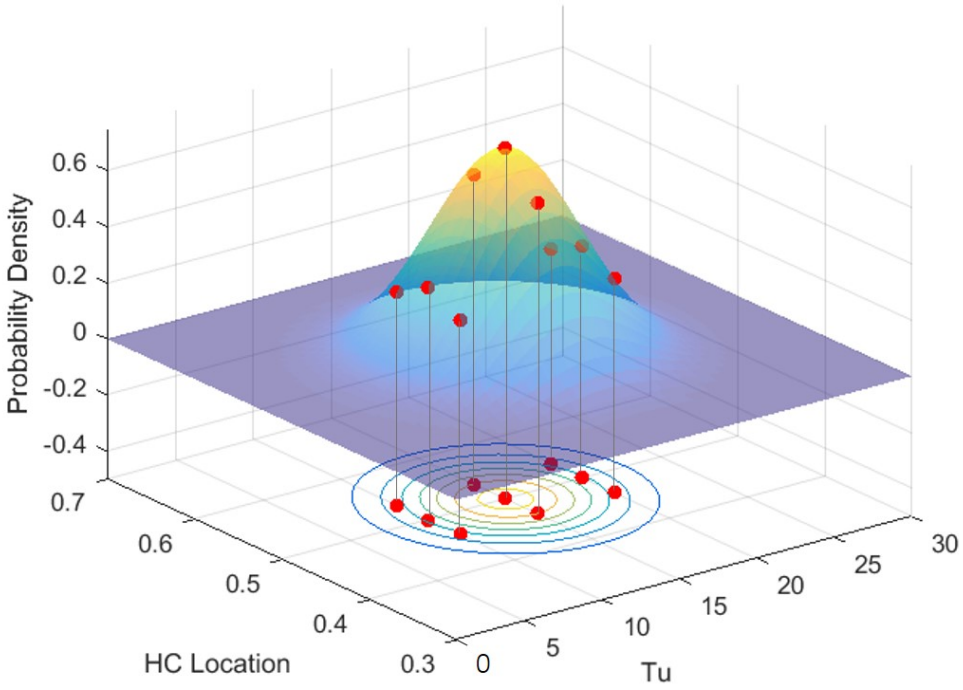

Figure 3.17: Collocation points location and projection on the inputs PDF function.

main. The impact behavior was modeled using EBFOG (Casari, Pinelli, Suman, di Mare & Montomoli 2018).

3.2.2 Uncertainty Analysis

Stochastic analysis has been carried out considering two uncertain variables: the hot core position and the level of turbulence intensity at the inlet. In the literature, one of the most simple and robust approaches to perform the uncertainty analysis is the Monte Carlo method (Montomoli 2019). It consists of a set of randomly distributed samples generated according to a probabilistic distribution. This method requires thousands of deterministic simulations to obtain accurate statistics of the outputs (Montomoli et al. 2013). This necessity makes the method prohibitive for the application considered in this study. For this reason, the more computationally cheap probabilistic collocation method (PCM) is used.

Since the reliability is the main characteristic that the HPT must have, the impact of the uncertainties on deposition profile, residual creep-lifetime, and mass flow rate has been evaluated.

Input uncertainties

One of the most critical operations of uncertainty quantification studies is to provide the correct probabilistic distribution of the uncertain parameters (Montomoli et al. 2014). For

Table 3.3: Input statistics.

Parameter	Mean value	Standard deviation
Hot core location	0.5	0.14 (1.14 deg)
Turbulence level	15%	5%

the E^3 HPT, no data are available in the literature to generate a statistical distribution of the input conditions. Therefore, statistics of the hot core location and turbulence level measured by Montomoli et al. (2013) has been used. They conducted experimental tests on the HP nozzle of an F-type MHI gas turbine, obtaining the statistical properties for both the hot core location and inlet turbulence level. In this study, Gaussian distribution was assumed for both the parameters as suggested by Montomoli et al. (2013). The statistics used for the analysis are resumed in Tab. 3.3.

Probabilistic Collocation Method

The PCM belongs to the family of methods that use the polynomial chaos expansion (PCE) proposed for the first time by Wiener (1938). It consists of describing the stochastic output $\boldsymbol{y}(\mathbf{x},\xi)$ by orthogonal polynomials based on the probability distribution of the random inputs in the form:

$$\boldsymbol{y}(\mathbf{x},\xi) = \sum_{j=0}^{N_p} a_j(\mathbf{x})\Psi_j(\xi) \tag{3.23}$$

In this study, an order $d = 2$ is set as suggested by Montomoli et al. (2013), which leads to a minimum number of CFD simulations equals to $N_p = 6$. However, the total number of evaluations that have to be performed for covering the space completely is $N_{av} = (d+1)^{nv} = 9$. As stated by Eldered & Burkardt (2009), an oversampling of 2 makes the algorithm more robust, hence a number of $N_s = 9$ CFD simulations has been conducted.

Since Gaussian distribution has been assumed for both the uncertain parameters, Hermite polynomials as orthogonal basis are the best choice for modelling the uncertainty propagation as stated by Ghanem & Spanos (2003). In this track, the choice of the sample points is done using the zeros of the orthogonal polynomial of order $(d+1)^{th}$. These points are called collocation points and are shown in Fig. 3.17 with their location on the input joint PDF.

Once all the deterministic computations have been completed, the evaluation of the PC coefficients has to be carried out. It consists of a resolution of the following over-determined

system:

$$\begin{bmatrix} \Psi_0(\xi_{\mathbf{1}}) & \Psi_1(\xi_{\mathbf{1}}) & \dots & \Psi_{N_p}(\xi_{\mathbf{1}}) \\ \Psi_0(\xi_{\mathbf{2}}) & \Psi_1(\xi_{\mathbf{2}}) & \dots & \Psi_{N_p}(\xi_{\mathbf{2}}) \\ \vdots & \vdots & \ddots & \vdots \\ \Psi_0(\xi_{\mathbf{N_s}}) & \Psi_1(\xi_{\mathbf{N_s}}) & \dots & \Psi_{N_p}(\xi_{\mathbf{N_s}}) \end{bmatrix} \begin{pmatrix} a_0 \\ a_1 \\ \vdots \\ a_{N_p} \end{pmatrix} = \begin{pmatrix} y(\xi_{\mathbf{1}}) \\ y(\xi_{\mathbf{2}}) \\ \vdots \\ y(\xi_{\mathbf{N_s}}) \end{pmatrix} \tag{3.24}$$

where ξ_j are the couples of collocation points coordinates (inputs of CFD simulations) and y(ξ_j) the correspondent output evaluation (outputs of the CFD simulations).

For the system resolution, the least-squares method is used. The final step of the analysis consists of the estimation of the statistics of the output. In this work, the computation is conducted using the method proposed by Hosder *et al* Hosder et al. (2006) and shown below:

$$\mu = a_0(\mathbf{x}) \tag{3.25}$$

$$\sigma = \sum_{j=1}^{N_p-1} a_j^2(\mathbf{x})\Psi_j^2(\xi) \tag{3.26}$$

Where μ and σ are respectively the mean value and the standard deviation with respect to the stochastic output.

3.2.3 Results

The typical quantities that are of interest for particle deposition analyses are: deposition profile along the vane, impact on the engine stability by means of the mass flow rate and residual creep-lifetime. For each output of interest, a convergence analysis against the number of collocation points has been performed. The analysis shows that after the 7^{th} sample both mean and variance do not vary appreciably with the number of collocation points.

Overall effects and sensitivity analysis

As a global overview, a sensitivity study was performed in order to identify the relative importance of the two uncertain parameters on the quantities of interest. Since global sensitivities of outputs are considered here, Sobol sensitivity analysis was carried out (Tang et al. 2010). Sobol's method is based on the decomposition of the model output variance into a sum of inputs variances (Montomoli 2019). Considering $I = [I_1,\ I_2]$ the uncertain input parameters, the decomposition takes the following form:

$$\mathbf{y}(\mathbf{I}) = y_0 + \sum_{j=1}^{2} y_j(I_j) + \sum_{j=1}^{2}\sum_{i=1}^{2} y_{ij}(I_i, I_j) \tag{3.27}$$

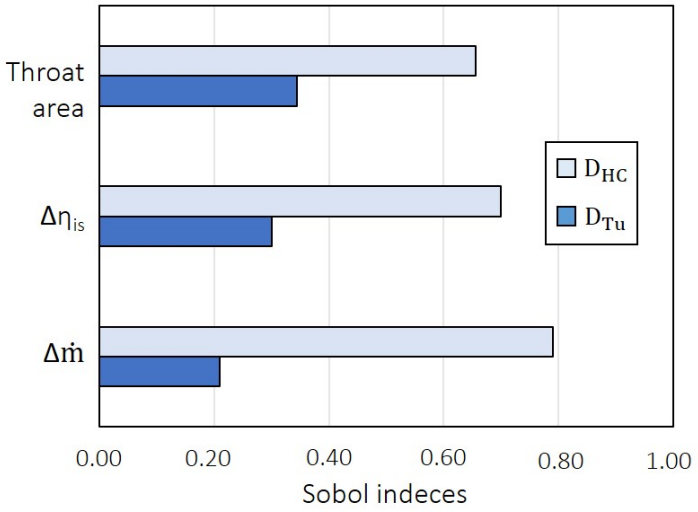

Figure 3.18: Sobol sensitivity results for throat area, isentropic efficiency, and mass flow rate.

where y_0 is the mean value of the output. The Sobol sensitivity indices, which provide the contributions of inputs variability, are computed as the ratio of each term of the sum in Eq. (3.27) (partial variance contribution separated) over the total variance. Therefore, Sobol indices are numbers between 1 and 0. To conduct this study, no additional evaluations beyond those needed to construct the probabilistic expansion were used as suggested by Tang et al. (2010). The results of the sensitivity analysis are reported in Fig. 3.18, where D_{HC} and D_{Tu} are the Sobol indices for hot core location and turbulence intensity respectively.

As can be seen, the contributions of the uncertainties on several quantities are evaluated. Specifically, the impacts on isentropic efficiency, mass flow rate, and throat area reduction due to deposition were analyzed. The indices computations were done using the simulations results of both clean and fouled vane. From the study, it can be inferred that each parameter is mainly governed by the hot core location. Each HC (Hot Core) Sobol index (D_{HC}) exceeds the 50% of the total influence.

These results are in line with what has been found by Montomoli et al. (2013), namely that hot core location is the operating uncertainty that most affects the global HPT vane parameters.

Effect on deposition profile and performance

In the first instance, uncertainties impact on deposit profile is evaluated. Its evolution along the vane is reported in Fig. 3.19. In the figure, the red line represents the mean value calculated by PCM Eq. (3.25) using the 9 simulations. Black lines limit the uncertainty's bandwidth computed by maximum and minimum values. The first observation regards the overall uncertainty of the deposit. The overall maximum value of variance was found in a point in the middle of the pressure side (PS) and equals to 1.14μm. Deeper analysis has

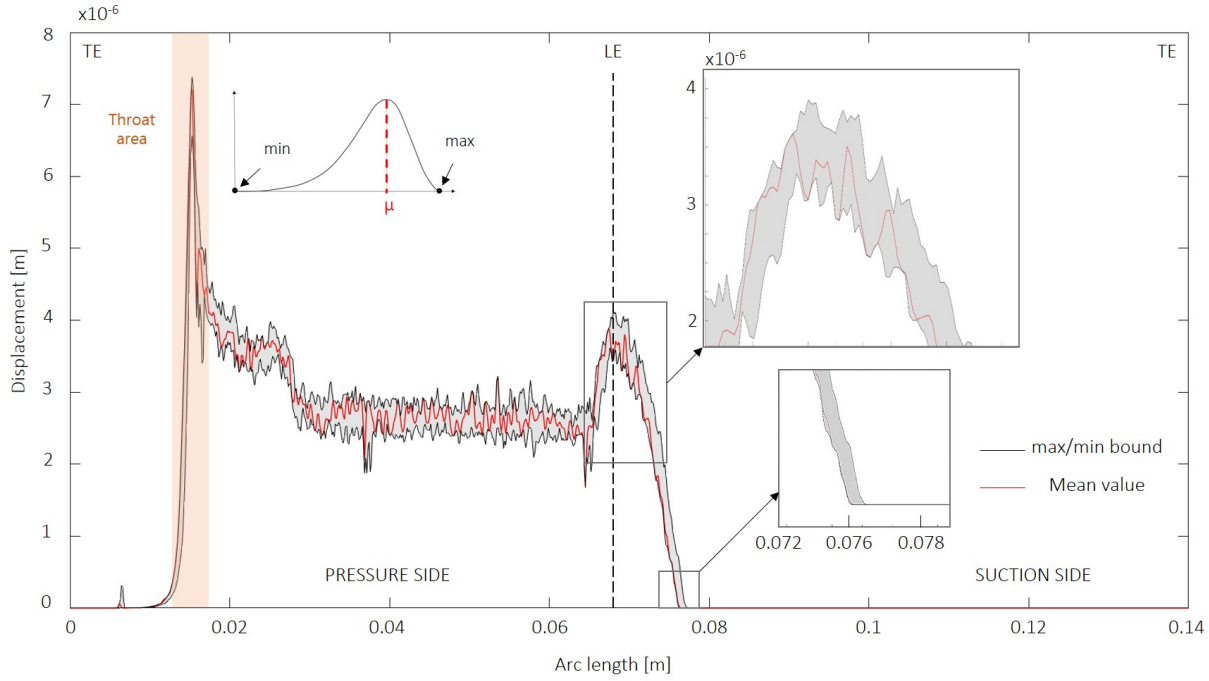

Figure 3.19: Deposit evolution along the vane. Mean value (red), and max/min bound (black).

been conducted in 2 particular areas: Throat area and leading-edge (LE).

Concerning the throat area (shaded in pink in the figure), it is the zone with the major deposition and the most dangerous when degradation occurs, since it governs the flow capacity of the engine (Kurz et al. 2009). Input uncertainties influence the alteration of this part of the vane leading to a probabilistic distribution as the one sketched on the side of the pink shade ($\mu = 7\mu$m, $\sigma = 0.4\mu$m). The distribution reported in Fig. 3.19 shows mean (μ), min and max values. As can be seen, the most likely event tends to be closer to the max value of the deposit. The overall variability between min and max values is equal to 0.82μm, which corresponds to 12% of the mean value. Two main observations can be pointed out at this stage:

1. The overall variation of the vane throat area and leading-edge area (the latter in the close-up at the top-right of the figure) due to deposition is significantly high ($\sim 1\mu$m). This can lead to several problems if a transonic vane is considered since in that case, the entire engine is dramatically sensitive to the throat variations.

2. Since the output variability is high, the use of a deterministic simulation can involve in the risk of underestimating the problem. The implications of this occurrence can be seriously detrimental for the engine.

In order to further investigate the performance alterations due to particle ingestion, a set of response surfaces using the samples in Fig. 3.17 has been generated. The surfaces are reported in Fig. 3.20. Considering the variation rate in the uncertain inputs space, the most

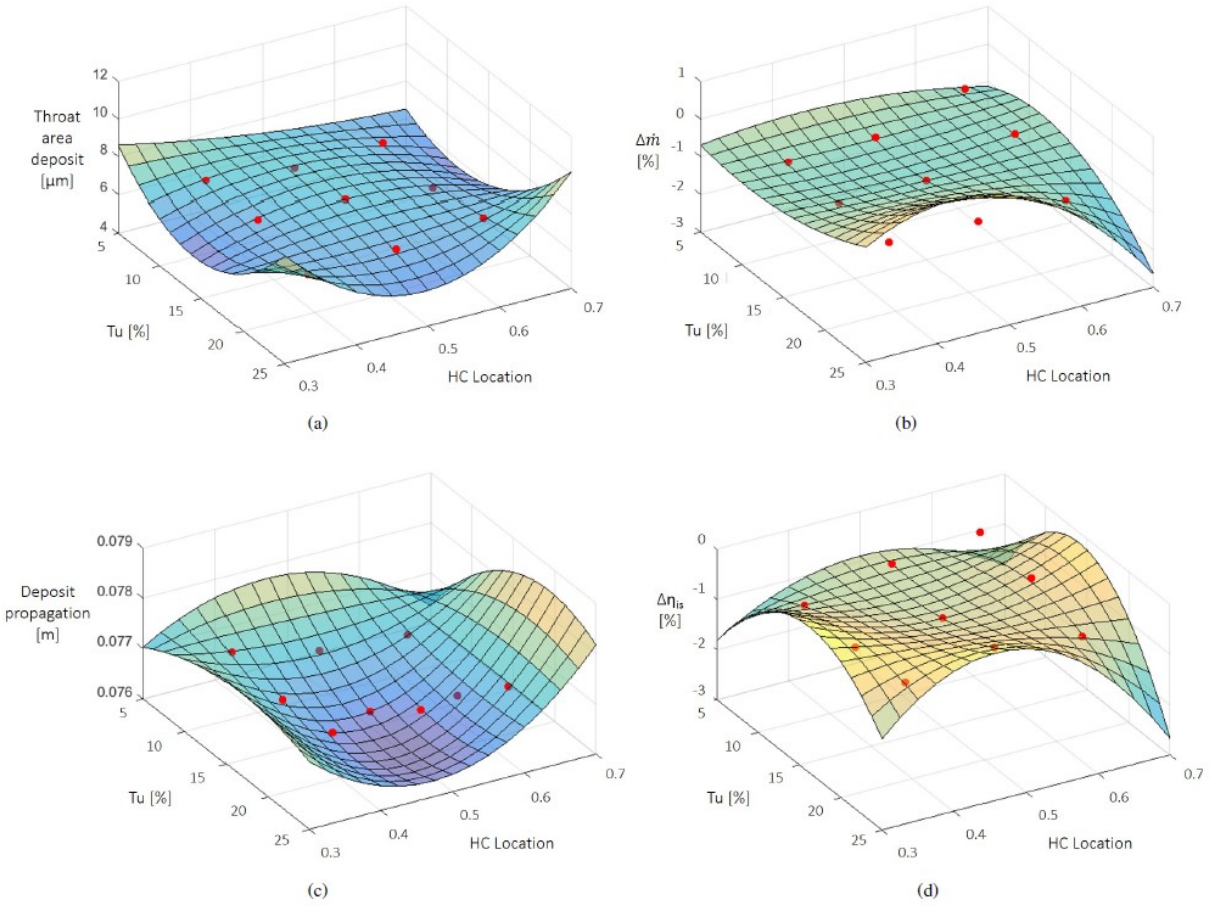

Figure 3.20: Response surface of a) throat area, b) mass flow rate, c) deposition propagation, and d) isentropic efficiency.

marked alterations take place at high turbulence levels.

When low turbulence intensity is considered (less than 15%), no appreciable alterations can be highlighted except for the isentropic efficiency. The latter still remains sensitive to the HC location. Overall variations up to 2% can be experienced. On the other hand, when higher turbulence intensity is considered (greater than 15%), even a small variation on inlet temperature causes high modifications. Particularly, when the HC moves toward the 100% of the pitchwise coordinate, abrupt alterations occur: mass flow rate, throat area and isentropic efficiency drops (up to 3%, 10μm, and 3% respectively) and deposit propagate more toward the SS. Since turbine inlet temperature and turbulence intensity still two of the major uncertainties in GT simulations, either uniform or steady assumed distributions, routinely used in the literature, can alter significantly the results of the study.

For completeness, a study of the evolution of throat area deposits over time was conducted. Furthermore, an artificial neural network (ANN) with the multilayer perceptron (MLP) structure was trained with the time sampled data. The ANN MLP used for the analysis is the one implemented in Matlab-v2019. A total of 2 hidden layers was set, and the Bayesian regularization was imposed as a training algorithm. The latter is considered

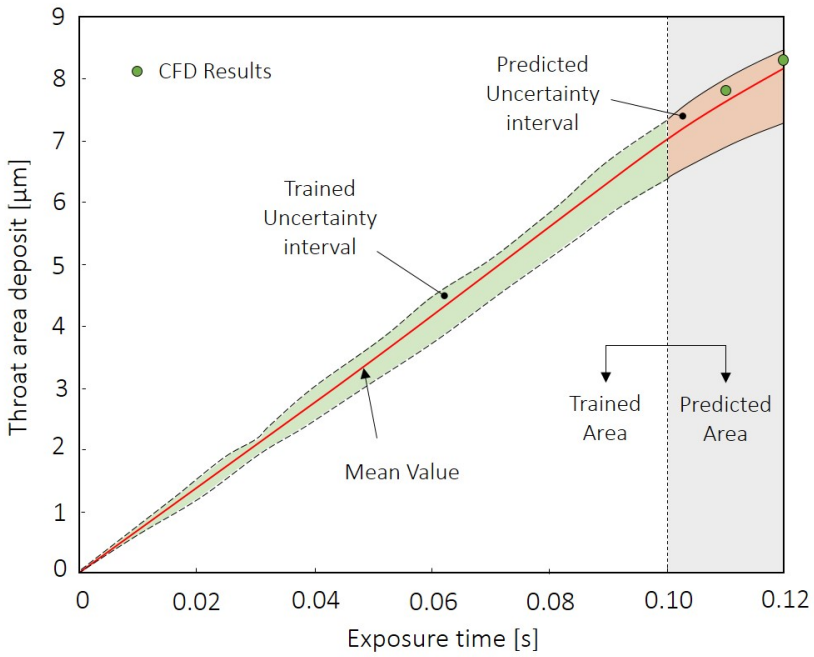

Figure 3.21: Evolution of the throat area deposit over the time and ANN prediction capability.

more robust than the standard back-propagation nets and can reduce or eliminate the need for lengthy cross-validation (Livingstone 2009). A convergence analysis has been conducted in order to verify the reliability of the ANN. The results are reported in Fig. 3.21, where "trained" and "predicted" areas are differentiated. To forecast the throat area deposit over time, the ANN MLP was trained against mean, maximum and minimum values. These trends are represented in the "trained" area, where the trained uncertainty range is depicted. The solid red line represents the mean value of the throat area deposit, whereas black dashed lines represent the uncertain limits. The latter delimit the range of uncertainty calculated with the PCM (green area).

Once the training ends, a prediction of the deposit after 0.02s was performed. The predicted mean, maximum and minimum values are depicted in the "predicted" area of Fig. 3.21. The prediction capability was proved to solve the CFD problem of one of the samples used for the analysis for 0.02s after the simulation end. The sample used is the one representative of the mean value of either HC location and turbulence intensity (HC located at the pitch's mean and Tu of 15%). The results of the simulation after 0.01s and 0.02s are reported in the figure as green dots. As a major result, the trained ANN seems to have a good predictive capability. Even if the CFD simulation has been conducted for a random chosen sample, the CFD results lay close to the predicted mean and still in the uncertainty limits predicted by the ANN. Furthermore, the predictions are aligned with the results carried out by Casari et al. (2017), where a quasi-linear trend of the deposit over time was found. This linearity allows to extrapolate the throat area deposit even after an exposure time longer than the simulated one.

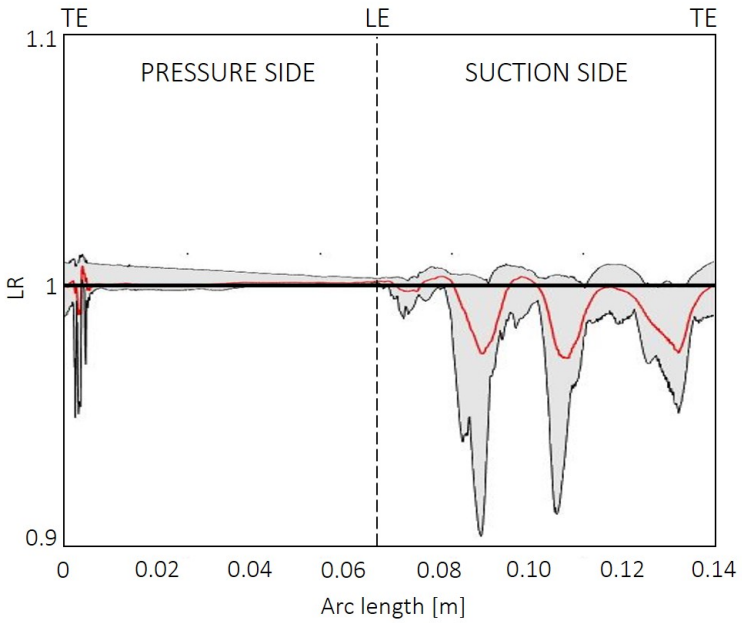

Figure 3.22: Evolution of mean residual creep-lifetime (red line) with uncertainty bounds.

Effect on residual creep-lifetime

The residual creep-lifetime will be estimated using the well known Larson-Miller relation (Larson & Miller 1952). It estimates the residual lifetime considering only the rupture limit due to the creep effect, which means the lifetime variation will be quantified in terms of change in vane metal temperature. Particularly, the formulation used in this work is the one

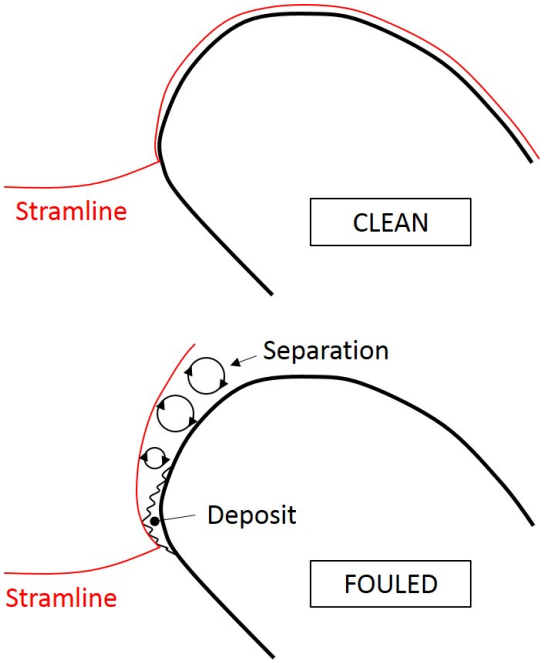

Figure 3.23: Sketch of streamline behaviour with and without leading edge deposit.

suggested by Larson & Miller (1952) and rearranged as follows:

$$t_{r2} = e^{\frac{\log(t_{r1}) - \frac{\Delta T}{T_1} C}{1 + \frac{\Delta T}{T_1}}} \tag{3.28}$$

where t_{r2} is the residual creep-lifetime after exposure, t_{r1} is the design lifetime set to 10,000h (L.P.Timko 1990), T_1 is the vane temperature before exposition, C is a material constant set to 20 as suggested by Montomoli (2019) and ΔT is the temperature variation after the exposure to contaminated air. Even though the cooling system is not considered in this study, qualitative considerations regarding the residual lifetime of the HPT can be carried out. Specifically, the residual creep-lifetime is analyzed by means of wall temperature variations due to deposition. These variations are mainly due to the boundary layer alterations due to the spiked deposit profile along the vane. The parameter used for the analysis is the residual lifetime ratio (LR) calculated as follows:

$$LR = \frac{t_{r2}}{t_{r1}} \tag{3.29}$$

where t_{r2} is calculated as in Eq. (3.28) using the vane temperature, that coincides with the temperature of the deposit for the study's assumptions. Clearly, when LR is greater then one, an increase of residual creep-lifetime is experienced by the HPT nozzle and *vice versa*. The evolution of this parameter along the vane is reported in Fig. 3.22.

The major variability of the residual lifetime, without considering the TE, occurs in the SS with peaks up to 12%. This means that a significantly high uncertainty affects the reliability of the vane even after a small exposure time. Furthermore, in the SS a reduction of the lifetime is the more likely circumstance. In order to asses the causes of the wider variability of the SS residual lifetime, a deeper analysis has been conducted. The results carried out can be explained with Fig. 3.23. The figure depicts a sketch of the behavior of a streamline approaching the LE. when the clean case (top) is considered,, the streamline that leaves the LE remains close to the suction side. On the other hand, in the fouled case (bottom), unsteady effects are triggered by the LE deposit. This unsteadiness propagates along the SS of the vane causing higher fluctuations of flow field parameters. From the analysis of all the samples, it can be concluded that higher inlet turbulence intensity intensifies the amplitude of these fluctuations. Among others, the fluctuations in the velocity field reflect directly on the heat transfer between vane and fluid, then on the temperature distribution. In the SS zone where the velocity field reach maximum values, higher surface temperature occur.

Effect on compressor stability

One of either rarest and dangerous outcomes related to deposition is its impact on compressor stability. Since the HPT nozzle governs the mass flow rate of the engine, its deterioration reflects directly on the operating point. In the present work, mass flow rate variations were computed by 2D vane geometry simulations. Therefore, a uniform distribution of deposit in the spanwise coordinate was assumed. This assumption is not entirely true, as deposit distribution varies approaching the endwalls. Nonetheless, order of magnitude considerations can be easily explained by considering uniform distribution. Estimation of mass flow variation impact can be carried out considering Fig. 3.24. It reports the E^3 high-pressure compressor (HPC) characteristic at a corrected speed of 87% L.P.Timko (1990). The design point (DP) represents the operating conditions considered in the simulations carried out in this work.

If the uncertainty distribution of the mass flow rate variation due to deposition is considered (green distribution in the abscissa), three operating points can be highlighted: P_1, P_2, P_3. Each point is represented by a specific probability by means of the standard deviation (σ, 2σ and 3σ respectively).

The main results that can be pointed out from Fig. 3.24 are:

1. the design point tends to approach the surge margin (SM) even after 0.1s of exposure. A 3σ (P_3) event can cause a reduction of 0.82% in flow capacity, and a consequent

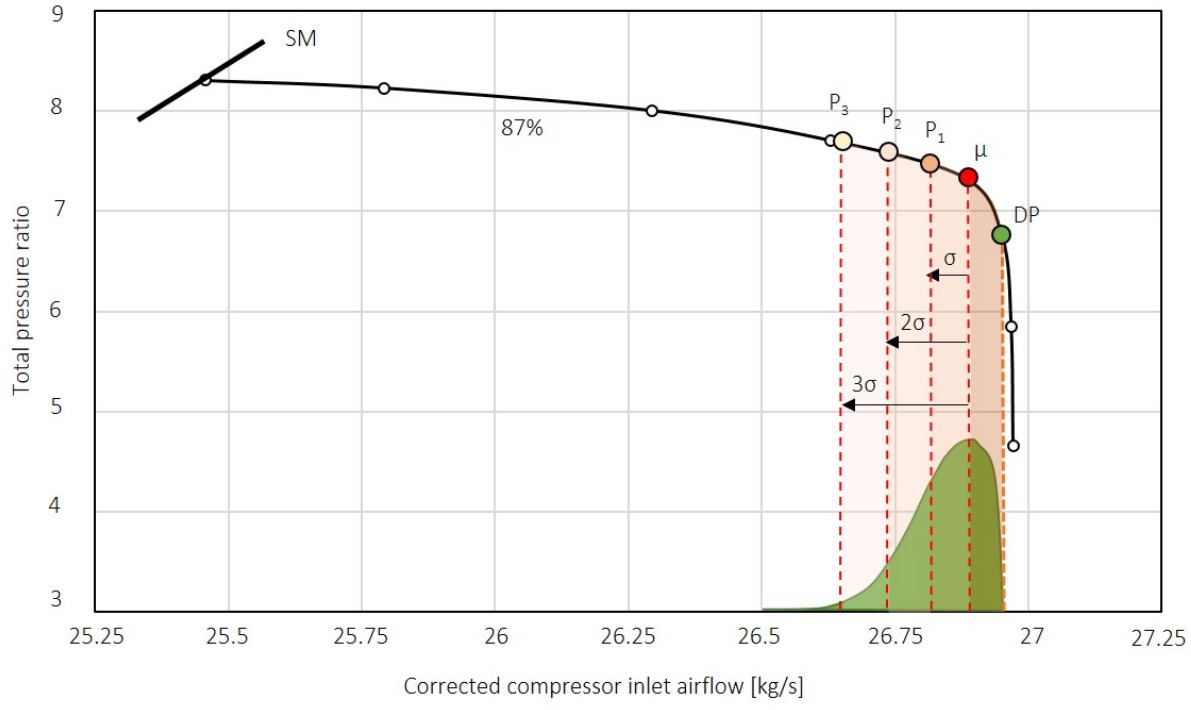

Figure 3.24: Uncertainty on the operating point due to the mass flow rate statistic distribution.

approaching to the surge margin of roughly 5%;

2. even though only the higher probability event is considered (μ), an abrupt modification of the total pressure rate will be experienced by the HPC compared with the design condition (DP). The direct consequence involves a change in HPT inlet pressure, which can lead to off-design behavior of succeeding stages and engine premature failure.

Despite the low injection time, inflow uncertainties considering deposition can affect seriously the HPC stability. All the effects exposed have a higher impact on two-shaft engines Kurz et al. (2009). Engine shut down, its premature failure or off-design behavior are the major consequences.

3.3 Conclusions and Remarks

This chapter presents the first attempt to tackle the problem of fouling with an ad hoc design procedure. In particular, a deterministic design optimization has been performed on a well-known test case from the VKI, the LS89 HPT vane. With the method shown, a geometry less sensitive to volcanic ash fouling can be obtained. A sensitivity analysis of the problem was conducted in order to reduce the problem dimensions, and the results lead to the conclusion that only the parameters related to the LE radius are significant for the accounting of isentropic efficiency variations due to degradation. The main outcome of the first part of the chapter is the generation of a map, which can be useful in the design phase. One of the principal advantages of this map is the prompt availability in this phase, supporting the design decision process often obtained by designer experience or experimental tests. In this map, a higher isentropic efficiency zone is outlined, offering a large manoeuvre space in terms of viable vane shapes.

In the second part of the chapter, the impact of the most important inflow uncertainties on deposition in the GT HPT nozzle has been analyzed, in order to determine if a deterministic design optimization is sufficient to face the DfF. In particular, hot core location and turbulence intensity at the inlet of the domain have been set as stochastic conditions. From the analysis, it can be inferred that deterministic assumptions on the operating conditions of the engine can alter significantly the results of the study. In particular, the evolution of the deposit along the vane can be subject to a variation of the order of 15%. The throat area, which in certain circumstances governs the mass flow rate of the engine, shows an uncertainty equal to 12% (0.82μm over a mean value of 7μm). In this track, the subsequent impacts on performance, residual lifetime and stability have been studied. Concerning the performance, the major alterations have been found at the highest turbulence intensity (greater than 15%), where even a small temperature variation causes abrupt modifications of throat area (up to 42%), flow capacity and isentropic efficiency (up to 3%). Moreover, a high impact of

NGV variation on compressor stability has been also found. Considering the mass flow rate stochastic distribution, the design point after the exposure tends to approach the surge line at decreasing probability. A 3σ event can cause a reduction of 0.82% in flow capacity and a consequent approaching the surge margin of roughly 5%. With this regard, and assuming a linear trend of the deposit over time, a 2s exposure to volcanic ash can lead to the surge of the HPC.

To summarize, the author suggests the use of robust or aggressive design techniques to face the DfF, since the uncertainty analysis shows that deterministic assumptions on the operating conditions of the engine can alter significantly the deposit distribution and their effects on the whole gas turbine.

Chapter 4

Compressor Section: Digital Twin for Fouling Prediction

In this chapter, a digital-twin strategy for the prediction of compressor fouling effects on the whole aircraft mission is proposed. In particular, both the aircraft and the engines are physics-based modeled. It will be shown in the following sections that the main problems that have to be faced to reach this goal are related to the finding of the correct contaminant concentration the aircraft encounters during the mission, and to the modeling of the components' degradation in the entire engine operative range. Two different strategies will be proposed to tackle these problems, and hence get one step closer to a general digital twin strategy for the maintenance prediction in gas turbines.

4.1 Overview

The digital twin model proposed in this chapter is basically a multiscale model that, starting from the microscale deposition pattern occurring into the engine's internal surfaces, provides the GTs fuel consumption during an airline mission. The conceptual map of the model is depicted in Fig. 4.1.

The starting point is the link between fouling and engine performance. As can be seen, this can be evaluated experimentally (Vulpio et al. 2021) or numerically. In particular, Suman et al. (2017) concluded that deposition can be numerically modelled by imposing an added thickness (Δt_h) and/or an added roughness (Δk_s) to the fouled surface. Among the two, the one that mainly affects the aerodynamic performance of a turbomachinery's internal surface is the roughness variation (Suder et al. 1995). This surface modification can be imposed in a CFD simulation as a uniform or non-uniform distribution. Since the deposition process is inherently aleatoric, the uniform distribution would be definitely unphysical, hence only non-uniform distribution should be considered. There are mainly two

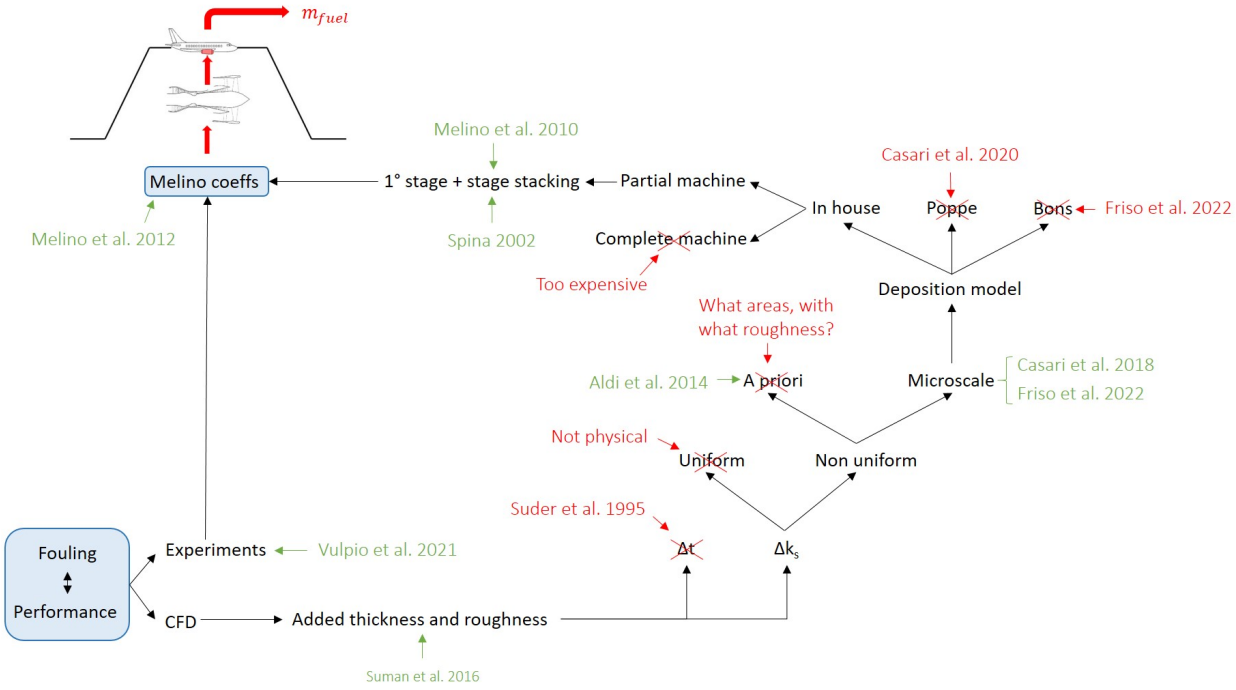

Figure 4.1: Digital Twin conceptual map

modelization techniques in the literature for deposit-induced non-uniform roughness. The first of them is the one proposed by Aldi, Morini, Pinelli, Spina, Suman & Venturini (2014), where *a priori* assigned k_s values in *a priori* chosen areas on the compressor surfaces is imposed. The main drawback of this approach is the fact that the k_s values and the areas have to be known *a priori*, which is absurd in real applications. The second approach is called the microscale model (Casari, Pinelli & Suman 2018*a*). If the incoming particle sticks, as decided by the deposition model, then it contributes to the roughness variation. First of all, a collection of the deposit on the boundary face is done by creating a 2D subgrid on the impact surface by using the transfinite interpolation. After that, the tracking algorithm locates the particle impact point inside one facet of the so-generated subgrid. The deposit is hence accumulated in every impact boundary face in the form of a histogram distribution as reported in Fig. 2.30. The height of each column of the histogram is computed by summing up the diameters of all the particles that are stuck in the corresponding facet of the subgrid. For each face, a specific set of statistics is calculated in order to compute the local k_s value. The problem with using this modelization is that it needs an adhesion model. For this purpose, since in this chapter only the compressor section will be considered, a cold deposition model has to be utilized. As already explained in Sec. 2.2.2, there is a lack of an adequate cold adhesion model in the literature, hence a new one has to be developed. That's why a new deposition model capable to well describe the adhesion in cold conditions has been developed. A detailed description of the model has been already provided in Sec. 2.2.3.

Now that all the elements for the CFD-based performance degradation evaluation have been introduced, another problem arises, which is the computational effort of simulating the entire turbomachinery. To face this issue, the Author decided to use the strategy called "stage stacking", proposed by Spina in 2002 (Spina 2002), and modified by Melino et al. in 2010 (Melino et al. 2010). With this technique, it can be easily derived the performance of the whole machine with the knowledge of the ones of the first stage only. This is done by the use of degradation coefficients, here called Melino coefficients, which modify the component maps in its entire operative range. The maps so modified are used to feed a gas path code developed by the Author, which in turn is used as a part of the digital twin for the aircraft mission modelling. All the concepts reported in this section will be described in detail in the following.

4.2 Gas Path Engine Model

In the literature, several studies have tried to analyze the effects of particle ingestion by using either GPA and CFD. For what concern the GPA, the only way to take into account degradation due to particle deposition and/or erosion is by imposing a degradation rate function (Hanachi et al. 2015). Typically, this function is estimated by using data-driven techniques (Hanachi et al. 2015). The main drawback of this approach is that the data-driven degradation rate lacks physical meaning. This may lead to unrealistic and un-physical results (Allen et al. 2018). An example of this type of analysis is the work of Hanachi et al. (2015). They estimated two correction factors for the compressor corrected mass flow rate and efficiency. These were used to calculate the modified compressor maps when degradation occurs. Another example is the work of Igie (2017), where a reduction of both fan capacity and efficiency was enforced to analyze the engine response during a complete mission. In this section, the GPA code developed by the Author is reported.

4.2.1 Engine Description

The aero-engine architecture chosen for the study is the twin-spool high-bypass unmixed flow turbofan, which is considered the best configuration for high subsonic commercial aircraft (Saravanamuttoo et al. 2009). Its section view is reported in Fig. 4.2. In turbofan engines, a fraction of the total flow bypasses the core components (compressor, combustion chamber and turbine) before being ejected through a separate nozzle. Thus, the total thrust is the sum of two factors: the cold thrust, due to the fan, and the hot thrust, which results from the stream entering the engine core.

Since these engines aim to generate the desired propulsive thrust, the typical performance parameter chosen as representative is the Thrust Specific Fuel Consumption (SFC). It is

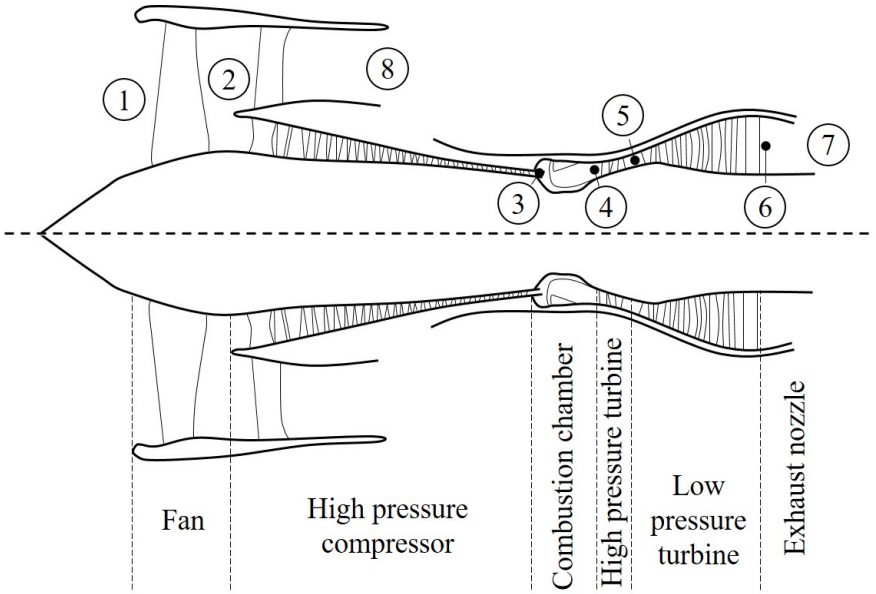

Figure 4.2: Section view of the twin-spool unmixed flow turbofan engine.

mathematically defined as the engine fuel mass flow rate ratio to the amount of thrust developed. Thus, it represents the mass of fuel needed to provide the required thrust. Since the purpose of this study is to propose a general strategy, the reference turbofan engine chosen is the default one present in the commercial software GasTurb9. This choice is mainly guided by the difficulty to find real engine data in the literature.

4.2.2 Components Maps and Algorithms

In their standard format, the fan and the compressor maps cannot be used directly in a performance calculation program. The solution to this problem is to introduce auxiliary coordinates (β-lines) as proposed by Kurzke (1996). These lines are parabolas parameterized by an index β, which can span from 0 (choke line) to 1 (surge line). The parabolas intersect the speed lines and allow to access to the maps quantities. An example of how β-lines look is reported in Fig. 4.3, which shows the corrected mass flow rate (Γ_c) vs the corrected pressure ratio (π_c).

Intake

The intake module receives the altitude and the flight Mach number as inputs. The former is used to calculate the ambient conditions (p_{amb}, T_{amb}) at the inlet using the ISA relations (Fletcher & Walsh 2008), whereas the second is used to compute the flight conditions in terms of total temperature and pressure:

$$\frac{T_1}{T_{amb}} = \left(1 + \frac{k-1}{2} M_a^2\right) \tag{4.1}$$

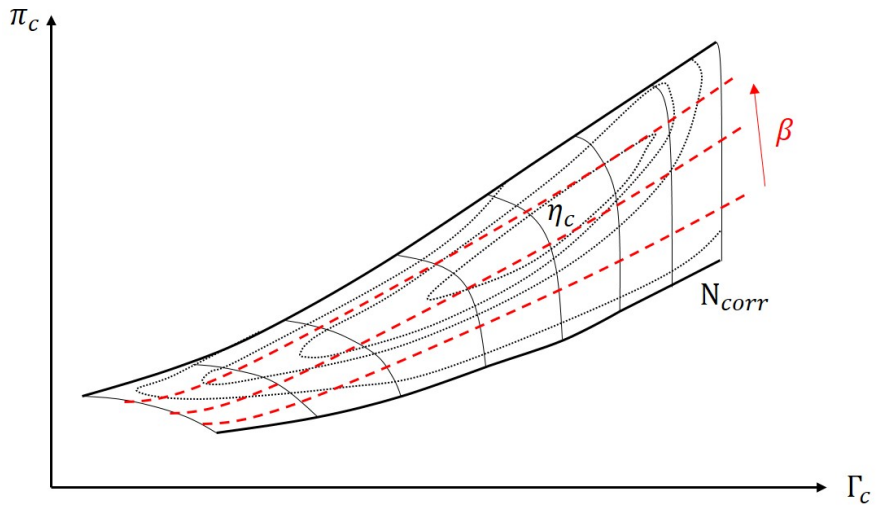

Figure 4.3: Schematic of the β-lines method.

$$\frac{p_1}{p_{amb}} = \left(\frac{T_1}{T_{amb}}\right)^{\frac{k}{k-1}} \tag{4.2}$$

where M_a is the Mach number, and k the specific heat ratio.

Fan

The total quantities computed represent the inlet conditions for the fan. To find the output values of this element, the fan maps have to be used. Furthermore, the design operating conditions (supplied by GasTurb9) were assumed for this component. With the design pressure ratio (π_{Fan}) and the design rotational speed (N_L), the corrected mass flow rate (Γ_{Fan}) and the efficiency (η_{Fan}) can be obtained from the maps:

$$[\Gamma_{Fan},\ \eta_{Fan}] = Maps_{Fan}(N_L,\ \pi_{Fan}) \tag{4.3}$$

After that, the estimation of the output quantities is straightforward:

$$p_2 = \pi_{Fan}\, p_1 \tag{4.4}$$

$$T_2 = T_1 \left(1 + \frac{\pi_{Fan}^{\frac{k-1}{k}} - 1}{\eta_{Fan}}\right) \tag{4.5}$$

$$\dot{m}_{tot} = \Gamma_{Fan}\, \frac{\delta_{Fan}}{\sqrt{\theta_{Fan}}} \tag{4.6}$$

where $\dot{m}_{tot}$ is the mass flow rate entering the engine, δ_{Fan} is the normalized pressure at the inlet, and θ_{Fan} the normalized temperature at the inlet.

In the turbofan, a portion of the total flow bypasses the core unit, forming the cold stream and then the cold thrust. A high-bypass configuration as the one considered, admits

a bypass ratio (B) between 5 and 8. In order to proceed, this quantity has to be also provided by the user. The cold and the hot mass flow rate can be then computed as follows:

$$\dot{m}_C = \frac{\dot{m}_{tot}\, B}{B+1} \tag{4.7}$$

$$\dot{m}_H = \dot{m}_{tot} - \dot{m}_C \tag{4.8}$$

Compressor

The high-pressure compressor (HPC) is the first component of the core engine. Its task consists of raising flow temperature and pressure before it enters the combustion chamber. Inputs of this component are the temperature, the pressure and the mass flow rate exiting from the fan. Here, the first interactive loop begins. The scope is to guess the value of beta (β_H) that meets the continuity constraint using the quantities extracted from the component maps:

$$[\pi_{HPC},\, \eta_{HPC},\, N_H] = Maps_{HPC}(\beta_H,\, \Gamma_{Fan}) \tag{4.9}$$

As can be inferred, knowing the value of β, all the output quantities can be computed. In the GPA constructed, the possibility of bleeding a portion of the HPC flow was also considered.

$$p_3 = \pi_{HPC}\, p_2 \tag{4.10}$$

$$T_3 = T_2 \left(1 + \frac{\pi_{HPC}^{\frac{k-1}{k}} - 1}{\eta_{HPC}}\right) \tag{4.11}$$

$$P_{HPC} = \dot{m}_H\, c_{p\_}(T_3 - T_2) \tag{4.12}$$

where P_{HPC} is the thermodynamic power output of the HPC and c_p the constant pressure specific heat of the air.

Combustion Chamber

The air delivered by the compressor mixes with the fuel in the combustion chamber. Here, the second iterative process takes place. The value of the combustor outlet temperature (T_{4cc}) varies into a specified range in order to meet the continuity constraint at the HPT. Since the possibility of bleeding of the compressor flow, the computation of the temperature at the inlet of the HPT is computed as follows:

$$T_4 = \frac{(\dot{m}_H - \dot{m}_{Bleed}\, T_{4cc} + T_3\, \dot{m}_{Bleed})}{\dot{m}_H} \tag{4.13}$$

Turbine

Given the similarity of the procedure adopted for either the HPT or the LPT, only the former is described. The inputs available for the turbine part are the mass flow rate, the thermodynamic power developed, the rotational shaft speeds, the temperature and the pressure. The first output calculated is the turbine outlet temperature by the use of the power compatibility:

$$T_5 = T_4 - \frac{P_H}{\dot{m}_H \, c_p} \tag{4.14}$$

where P_H is the thermodynamic power generated by the high-pressure components (P_L for the low-pressure ones). The next step involves the use of turbine maps. Specifically, the efficiency of the turbine can be extrapolated.

$$\eta_{HPT} = Maps_{HPT}(N_H, \, \Gamma_{HPT}) \tag{4.15}$$

Finally, the pressure ratio and then the outlet pressure can be obtained:

$$\pi_{HPT} = \left(1 - \frac{T_4 - T_5}{\eta_{HPT} \, T_4}\right)^{\frac{k}{k-1}} \tag{4.16}$$

$$p_5 = \frac{p_4}{\pi_{HPT}} \tag{4.17}$$

Nozzle and Bypass

To calculate the output values for either the nozzle or the bypass, the expansion ratio is firstly compared with the critical one. If choked conditions occur, the thrust is raised by the pressure contribution. Otherwise, only the velocity term contributes.

$$F_H = \dot{m}_H \, (V_7 - V_0) + A_7 \, (p_7 - p_{amb}) \tag{4.18}$$

$$F_C = \dot{m}_C \, (V_8 - V_0) + A_8 \, (p_8 - p_{amb}) \tag{4.19}$$

The whole algorithm implemented is shown in Fig. 4.4.

4.2.3 Validation

Since the commercial code GasTurb9 was used for validating the code developed, the default software inputs reported in Tab. 4.1 were chosen. The comparison was carried out in terms of temperature distribution along with the engine, SFC, and thrust. The Temperature results are reported in Fig. 4.5. As can be seen, a perfect matching occurs for the two codes' results. The same is for the other two quantities. The SFC and the thrust found by GasTurb9 are 19.2 g/(kNs) and 3.3 kN respectively, whereas the values found by the in-house code are

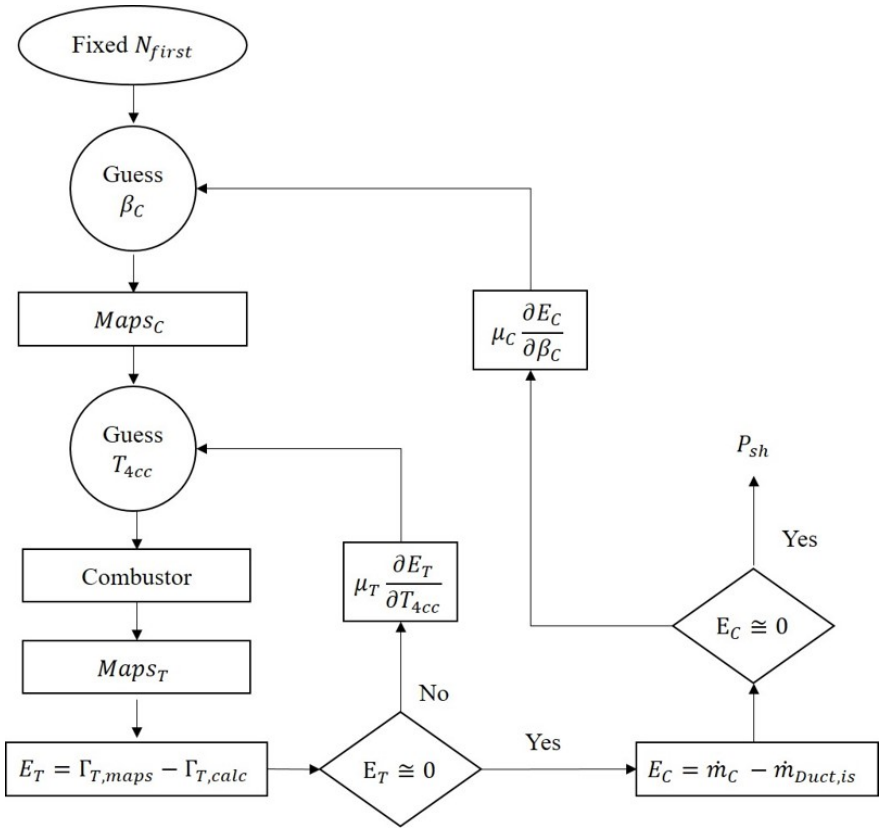

Figure 4.4: GPA algorithm.

20.4 g/(kNs) and 3.7 kN. The authors ascribe the small differences to the hidden parameters in the commercial software, which cannot be integrated into the in-house code.

4.3 Digital Twin for Mission Modelling

The model here proposed aims to replicate the engine behaviour along with a complete airline mission. Since the study is focused on the assessment of the methodology, no specific aircraft and engines were selected. In particular, general geometric parameters found in the literature were considered to describe the airframe (Howe 2000), whereas the performance

Table 4.1: Input for the GPA.

Parameter	**Value**	**Units**
Altitude	11,000	m
Mach number	0.8	-
RAM recovery factor	0.99	-
Bypass ratio	6	-
Low-pressure corrected shaft speed	100	$\%N_{corr,design}$
Bleed flow	0	$\%\dot{m}_H$

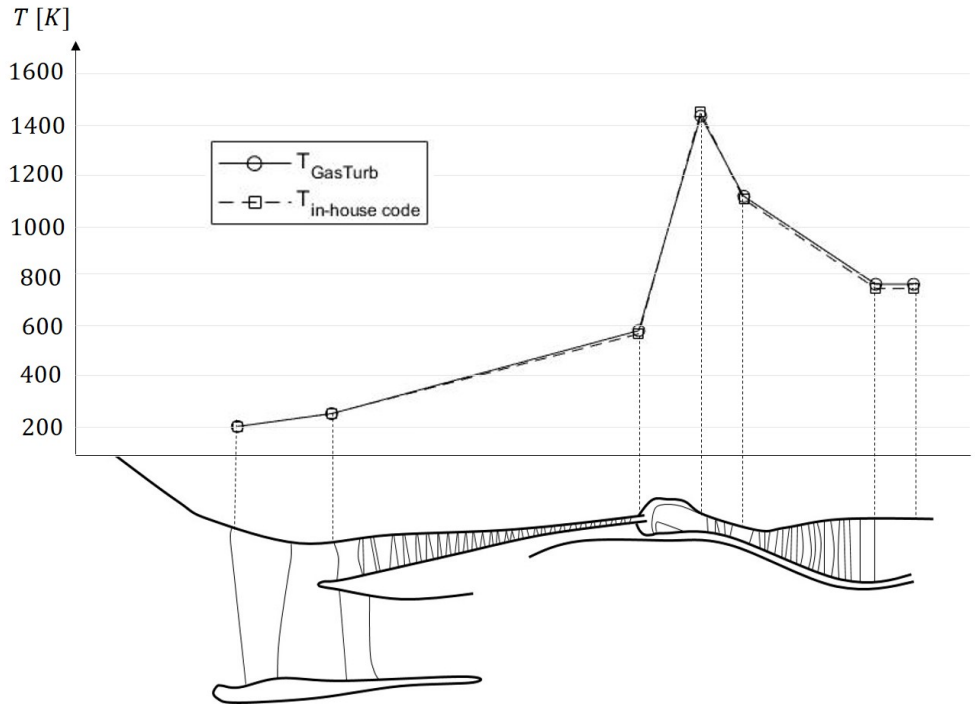

Figure 4.5: Comparison between the temperature distribution along with the engine. Results from GasTurb9 and the in-house code.

maps available in the commercial software GasTurb9 were used to represent the engines. Furthermore, a short-haul mission was considered to evaluate the approach. Among the different outputs that can be extracted from the model, fuel consumption is the one that is of interest in this specific study. The algorithm developed is sketched in Fig. 4.6. The information required as input for running the model are:

- Mission information in terms of altitude profile;
- Aircraft geometry details necessary to estimate the weight and the aerodynamic forces;
- Performance maps of each engine component in order to model their behaviour.

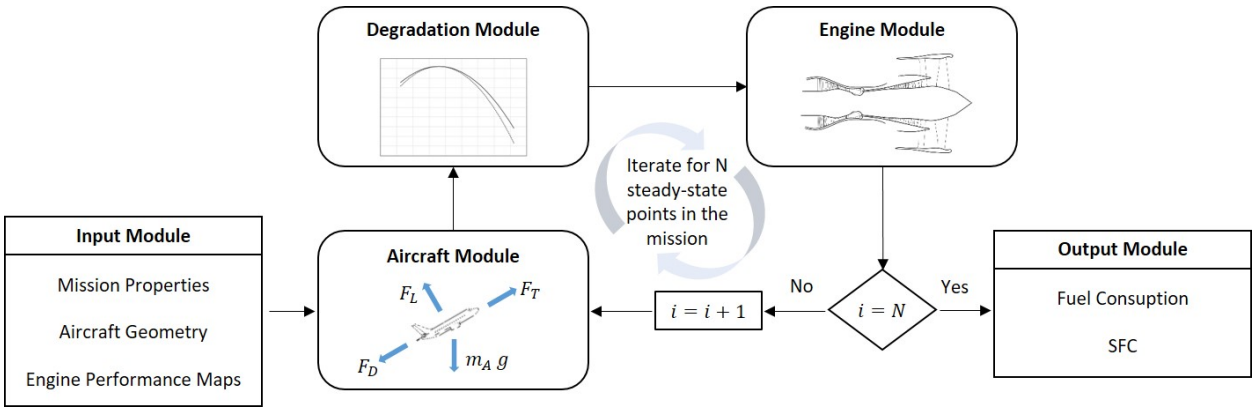

Figure 4.6: Outline of the mode algorithm.

The first step of the method consists of the discretization of the mission profile. Here, the whole mission is discretized into a user-specified number of segments, each delimited by two altitude values. Steady-state conditions were assumed in every segment for both aircraft and engines. After that, an iteration process along with the mission starts. For each segment, a force balance is performed on the aircraft, which is considered frozen in a specific position (Aircraft Module). This allows the estimation of the thrust needed for the aircraft for being at the specified altitude in the predefined position. The value of the thrust thus found is used as a constraint to compute the engine operating point, and then the corresponding fuel mass flow rate (Engine Module). Before engine performance evaluation, the update of the components maps in consideration of the particle ingestion phenomenon is done. In this respect, the maps are modified to take into consideration the effects of fouling. Each module is detailed in the following paragraphs.

4.3.1 Aircraft module

The first module composing the methodology is the aircraft module. Here, the required net thrust F_T is determined for each discrete point, by solving the aircraft equations of motion (Eqs. 4.20 and 4.21) (Brandes et al. 2021). The equations can be easily derived by performing a force balance on the stability axes of the aircraft (see Fig. 4.7 on the left).

$$F_t - F_D - m_A\, g\, sin(\alpha) = m_A\, a \tag{4.20}$$

$$F_n + F_L - m_A\, g\, cos(\alpha) = 0 \tag{4.21}$$

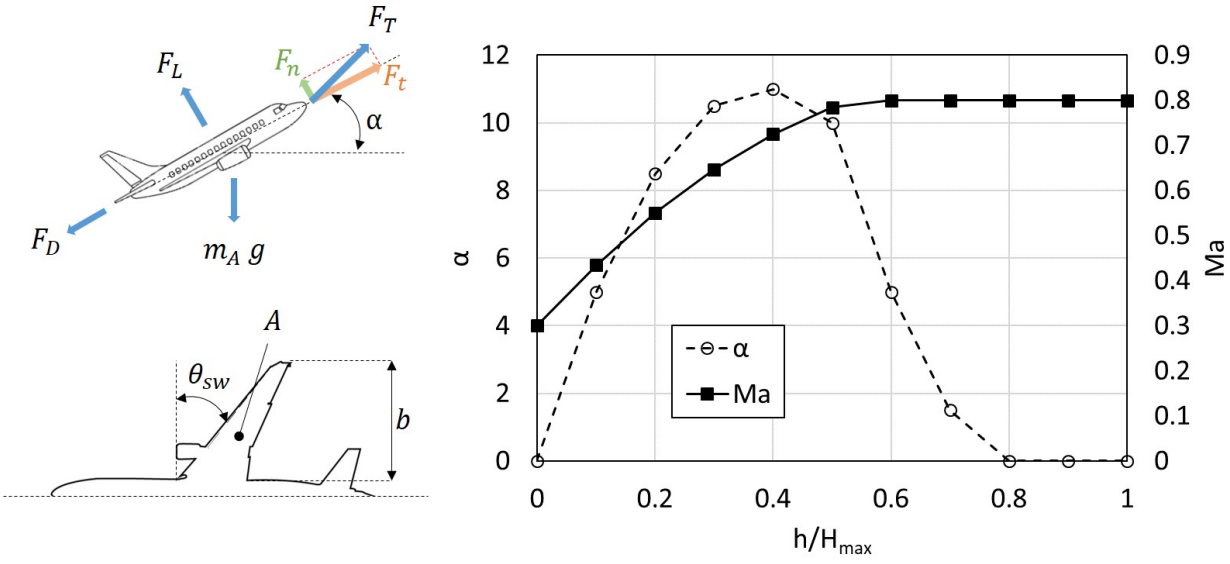

Figure 4.7: Sketch of aircraft force balance (upper-left) and geometric details (bottom-left), and assumed Ma and α along the mission (right).

The quantities that enter the equations are the normal and the tangential components of the thrust (F_n and F_t), the drag and the lift forces (F_D and F_L), the aircraft mass (m_A), and the flow angle of attack (α). Among them, the most important ones are the drag and the lift actions, which require knowledge of the aircraft geometry, its airspeed, and the air angle of attack. For the last two, the trend along the mission reported in Fig. 4.7 on the right is assumed, where h/H_{max} represents the fraction of the altitude at which the aircraft is located. The reported profiles represent only half the mission, that is the ascending period since a mirrored behaviour is assumed for the descending one. As it can be noted, the airspeed is computed by assuming a Mach number (Ma) spanning from 0.3 (at the take-off and landing) to 0.8 (cruise). The angle of attack is calculated by assuming a maximum value of 11° at almost the mid of the ascending/descending period (Filippone 2012).

In order to estimate both the lift and the drag forces, Prandtl's lifting line theory is used. Specifically, to compute the lift coefficient (C_L) the methodology used by Brandes *et al.* (Brandes et al. 2021) is adopted (Filippone 2012). This formulation allows the calculation of C_L as a function of the angle of attack, the zero-lift angle (α_0), the wing aspect ratio ($\Lambda = b^2/A$), the wing sweep angle at the half-chord line (θ_{sw}), and the flight Mach number as shown in Eq. 4.22.

$$C_L = \frac{2\,\pi\,\Lambda(\alpha - \alpha_0))}{2 + \sqrt{(\Lambda/cos(\theta_{sw}))^2 + 4 - (\Lambda\,Ma)^2}} \tag{4.22}$$

The wing aspect ratio is in turn computed as a function of the wingspan (b) and the wing area (A). All these parameters are indicated in Fig. 4.7 bottom-left side. The drag coefficient is determined by the summation of three components (Eq.4.23), which expressed in coefficient form are: Zero lift drag coefficient (C_{D_0}), Vortex drag or lift induced drag (C_{D_L}), Wave drag (C_{D_W}).

$$C_D = C_{D_0} + C_{D_L} + C_{D_W} \tag{4.23}$$

The first and the second drag coefficients are calculated according to Howe (Howe 2000) (Eq.4.24 and 4.26), while the third is calculated according to Torenbeek (Torenbeek 1982) (Eq.4.25). Other drag contributions, such as the spillage drag, were not considered here, but they can be taken into account by adding drag terms to Eq.4.23 (Coats 1986).

$$C_{D_0} = 0.005\,\left(1 - \frac{2\,C_L}{R_W}\right)\,\overline{\tau}\,\left[1 - 0.2\,Ma + 0.12\,\left(\frac{Ma\,\sqrt{cos(\theta_{sw})}}{0.8 - t/c}\right)^{20}\right]\,0.84\,R_W \tag{4.24}$$

$$C_{D_L} = \frac{C_L^2}{\pi\,\Lambda\,e} \tag{4.25}$$

$$C_{D_W} = \frac{0.026}{\Lambda^{0.33}} \tag{4.26}$$

In the equations above, the following parameters are introduced: the Oswald factor (e), the ratio of overall wetted area to the reference (R_W), the pitch to chord ratio (t/c), and the correction factor for wing thickness ($\overline{\tau}$). All these quantities are determined according to Howe (Howe 2000). Particularly, for the last one, Eq.4.27 is used.

$$\overline{\tau} = \left[\frac{R_W - 2}{RW} + \frac{1.9}{R_W} \left(1 + 0.526 \left(\frac{t/c}{0.25} \right)^3 \right) \right] \tag{4.27}$$

To ease the reader, since no specific aircraft type was chosen, the summary of the aircraft geometric parameters needed for the model is reported in Tab. 4.2 with the respective references. With the configuration chosen, the thrust needed for the take-off is roughly 200 kN.

Degradation Module

The output of the Aircraft module is the net Thrust that the engine has to develop to contrast the aerodynamic actions and the weight. Before entering the Engine module, the preparation of the components maps is required, that is what the Deterioration module does. In this specific case, the performance maps available in the commercial software GasTurb9 are used. In particular, these were adapted in order to achieve a net thrust of approximately 177 kN. This is because, since two engines were considered, the total net thrust of 200 kN meets the need of the aircraft configuration chosen.

The main purpose of the Degradation module is to parameterize the maps in order to allow their modification subsequently to compressor fouling. This is done by scaling them to obtain the generalized maps in terms of ψ and ϕ, defined as follows

$$\psi = \frac{\Delta h_T}{U^2} \tag{4.28}$$

$$\phi = \frac{v_a}{U} \tag{4.29}$$

Table 4.2: Airframe parameters needed as inputs for the model

Parameter	**Value**	**Unit**	**Reference**
R_W	5	-	(Howe 2000)
t/c	0.1	-	(Howe 2000)
θ_{sw}	32	°	(Howe 2000)
Λ	10	-	(Igie et al. 2016)
e	0.95	-	(Howe 2000)
m_A	220000	kg	-

where h_T is the total enthalpy, U is the blade velocity at the mean radius, and v_a the mean axial flow velocity. The curve thus obtained is then interpolated by using the formulation proposed by Spina (Spina 2002) and modified by Melino *et al.* (Melino et al. 2010) and expressed in Eq.4.30.

$$\psi = \psi_{max} - \frac{(\psi_{max} - \gamma\,\psi_D)\;\left[\phi_{\psi_{max}} + SF\;\left(\phi_{\psi_{max}} - \phi_D\right) - \phi\right]^2}{\left[\phi_{\psi_{max}} + SF\;\left(\phi_{\psi_{max}} - \psi_D\right) - \psi_D\right]^2} \tag{4.30}$$

where the best fitting has to be obtained only by varying SF (Shape Factor). In the case considered in this study, the value of SF that guarantees the best fit is 0.5. The generalized map obtained can be then reconverted in the compressor performance map by only applying the reverse scaling process.

As can be noted, a parameter γ is present in the formulation. This is a degradation coefficient that corrects the maps in response to compressor fouling. A clean engine corresponds to gamma equals 1, while a value of gamma less than one stands for a fouled engine. The global compressor maps obtained by applying this procedure is depicted in Fig. 4.8, where Π is the pressure ratio, and Γ is the corrected mass flow rate. The figure reports both the clean ($\gamma = 1$) and an example of fouled ($\gamma = 0.9$) maps.

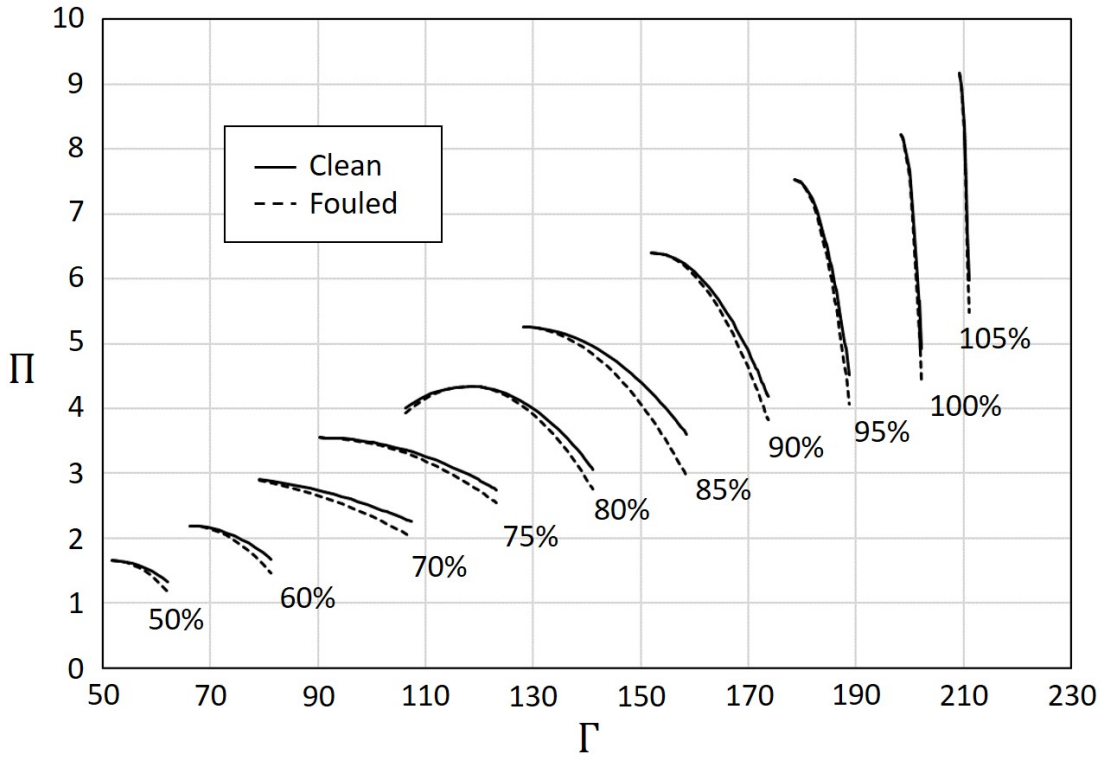

Figure 4.8: High-pressure compressor maps in clean (solid) and fouled (dashed) conditions.

4.3.2 Engine Module

The engine is modelled with a 0D gas path code developed by the authors and already explained in Sec. 4.2. As done for the airframe geometry, since no specific gas turbine was chosen, also for the engine a summary of the design parameters is reported (Tab. 4.3). These values represent the default engine in the software GasTurb9, where only the mass flow rate and the TIT were varied to meet the aircraft thrust needed.

4.3.3 Compressor Fouling Cases and Effects

The algorithm results are obviously dependent on the choice of the degradation coefficients, which describe the effects of fouling on the high-pressure compressor. These coefficients are a function of several parameters, such as the type of contaminant ingested, the ambient conditions during the ingestion (relative humidity), the mass of contaminants ingested, etc. (Suman et al. 2017). In this work, the degradation coefficients are set by using the experimental results reported in Casari et al. (2021). In their study, they built the test rig reported in Fig. 4.9 with the purpose of conducting fouling tests on real turbomachinery. Specifically, in the cited work, they investigated the fouling effects on the multistage compressor unit aboard the Allison 250 C18 (see Fig. 4.9, bottom left). The tests were conducted in different engine operating conditions, and by using the Arizona road dust nominal $(0 - 3)\ \mu m$ as a contaminant. Uncertainty bars cannot be visualized since they are contained inside each marker. For a more detailed description of the test rig, the reader is referred to Casari et al. (2021). The Authors are aware that the compressor taken as reference is scaled with respect to an actual compressor unit of a turbofan engine. The bases of our investigation are listed as follows:

- the reference compressor (Allison 250 C18) has characteristic curves in line with an actual unit (Aldi, Morini, Pinelli, Spina & Suman 2014). Therefore, the shape of the

Table 4.3: Design engine parameters

Parameter	**Value**	**Unit**
By-pass ratio	6	-
TIT	1700	K
Core nozzle angle	10	°
By-pass nozzle angle	12	°
HP spool speed	44000	rpm
LP spool speed	13500	rpm
Thrust	177	kN

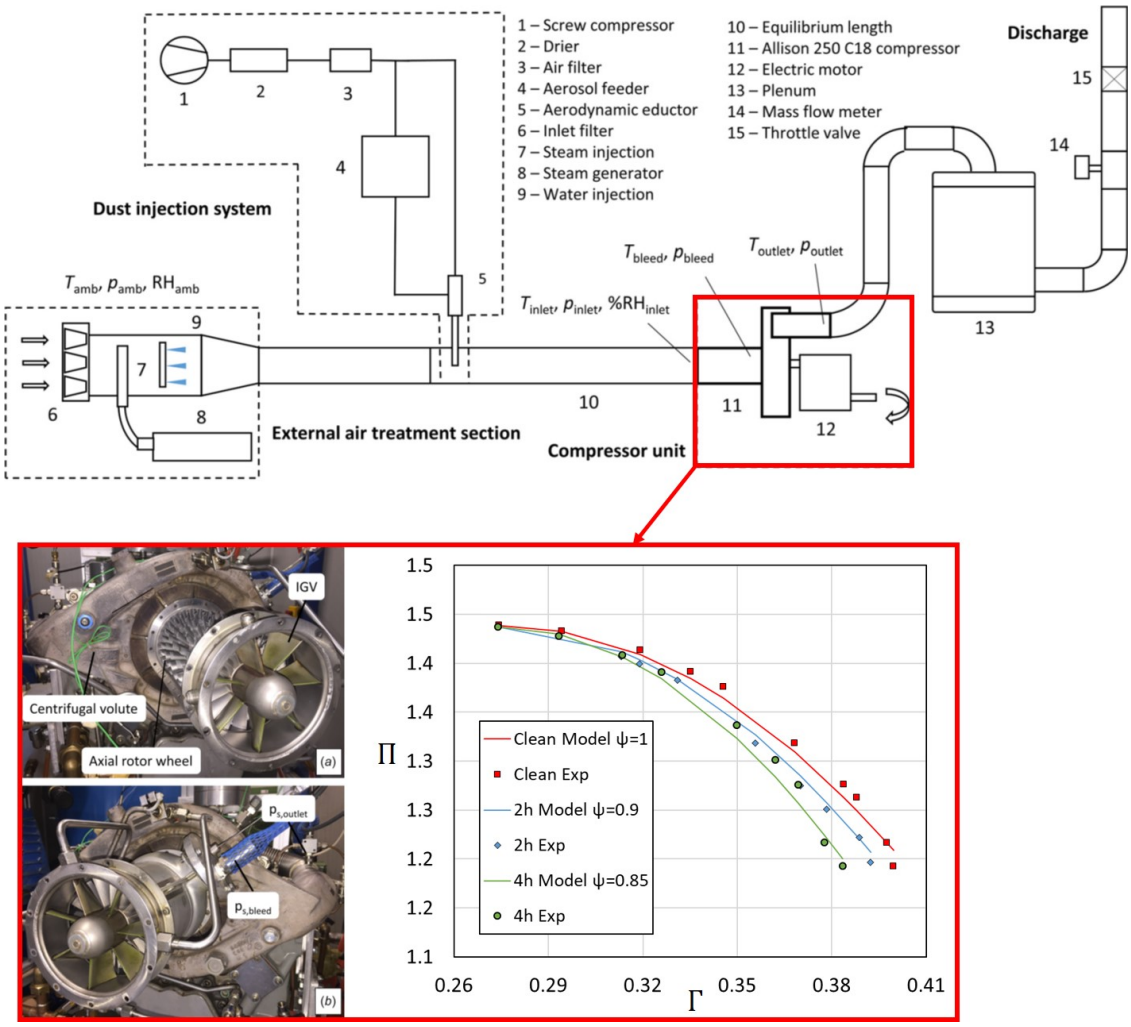

Figure 4.9: Schematic layout of the test rig (Casari et al. 2021), and fitting model results for degrading compressor maps.

performance curve (and its modification due to the degradation) could be assumed to be representative of a real unit;

- The coefficients of the degraded unit come from an experimental campaign conducted under controlled conditions. This allows the accurate determination of the deposit effects by monitoring the contaminant concentration, type, and operating conditions (temperature and humidity).

- The modification (shape and magnitude) of the performance curves depends on the engine sensibility and susceptibility to compressor fouling (Meher-Homji et al. 2009). Therefore, each engine experiences different behaviour when it operates under contaminated conditions. The results reported in this paper must be intended relative to the clean conditions. The modifications of the curves have to be believed as an example to show the potential application of the methodology. Each engine (or compressor) shows a specific modification according to the experienced contamination.

It is obvious that to obtain more realistic results, experimental deposition studies have to be conducted with the same engine modeled here. Nonetheless, since the present work is mainly focused on the methodology proposed, only the physical soundness of the results was assessed rather than their absolute values.

The result of the fitting is reported in Fig. 4.9, bottom right. Specifically, the performance after 2 (mild fouling) and 4 (severe fouling) hours of contaminant exposition are considered, corresponding to the degradation coefficients equals 0.9 and 0.85 respectively.

In this work, the effects of compressor fouling in a single and in three repeated airline missions are analyzed. For this purpose, the cases reported in Tab. 4.4 are considered. For the single mission, the fuel consumption is computed in the case of a clean (C), mild fouled (MF), and severe fouled engine (SF). For the three repeated missions, the fuel consumption is estimated considering three different engine conditions:

- clean in all the three missions;
- clean in the first mission and mild fouled in the other twos;
- clean in the first mission, mild fouled in the second mission, and severe fouled in the third mission.

The results in terms of TIT (Turbine Inlet Temperature), SFC and fuel consumption during the single mission are presented in Fig. 4.10, Fig. 4.11 and 4.12 respectively, where also the altitude is reported (red solid line). A change in both TIT and SFC is observed throughout the mission with the increase in the fouling level, which results in higher fuel consumption. This can be better appreciated by focusing on Fig. 4.12. With the increase in the compressor fouling level (decrease of the degradation coefficient), the fuel consumption found after completing the mission increases by 4.6% in mild fouling conditions, and by 5.1% in severe fouling conditions. These values are in line with the ones found in the work of Igie *et al.* (Igie et al. 2016), where *a priori* mass flow rate reduction has been imposed at the engine inlet to account for fouling effects.

Table 4.4: High-pressure compressor degradation cases

Mission	**Cases**	**Degradation Factor**
Single	Clean	1
	Mild fouled	0.9
	Severe fouled	0.85
3 Repeted	C-C-C	1-1-1
	C-MF-MF	1-0.9-0.9
	C-MF-SF	1-0.9-0.85

Table 4.5: High-pressure compressor degradation cases

Mission	Cases	Degradation Factor	Δm_{fuel}
Single	Clean	1	-
	Mild fouled	0.9	+4.60%
	Severe fouled	0.85	+5.10%
3 Repeated	C-C-C	1-1-1	-
	C-MF-MF	1-0.9-0.9	+4.67%
	C-MF-SF	1-0.9-0.85	+10.00%

For what concerns the repeated missions, the results are presented only in terms of fuel consumption in Fig. 4.13. The study is carried out by considering three equal missions, that are a repetition of the single one previously analyzed. As it can be noted, as the fouling level increase, the fuel consumed after a set of missions grows. Specifically, extra consumption of 4.67% is found with the C-MF-MF case, and of 10.00% in the C-MF-SF case. A summary of the results found is reported in Tab. 4.5.

Now that the whole digital twin strategy has been presented, one can immediately realize that its use is conditioned to the resolution of two big problems: finding a method to adequately evaluate degradation (or Melino's) coefficients and, in this track, a procedure to estimate the correct contaminant concentration the aircraft encounters during the mission. It is obvious that the former is a function of the latter. In the following two sections, two strategies will be reported to face these issues. In the first one, a program that is capable to read the CALIPSO data and giving the atmospheric contaminant concentration as the output

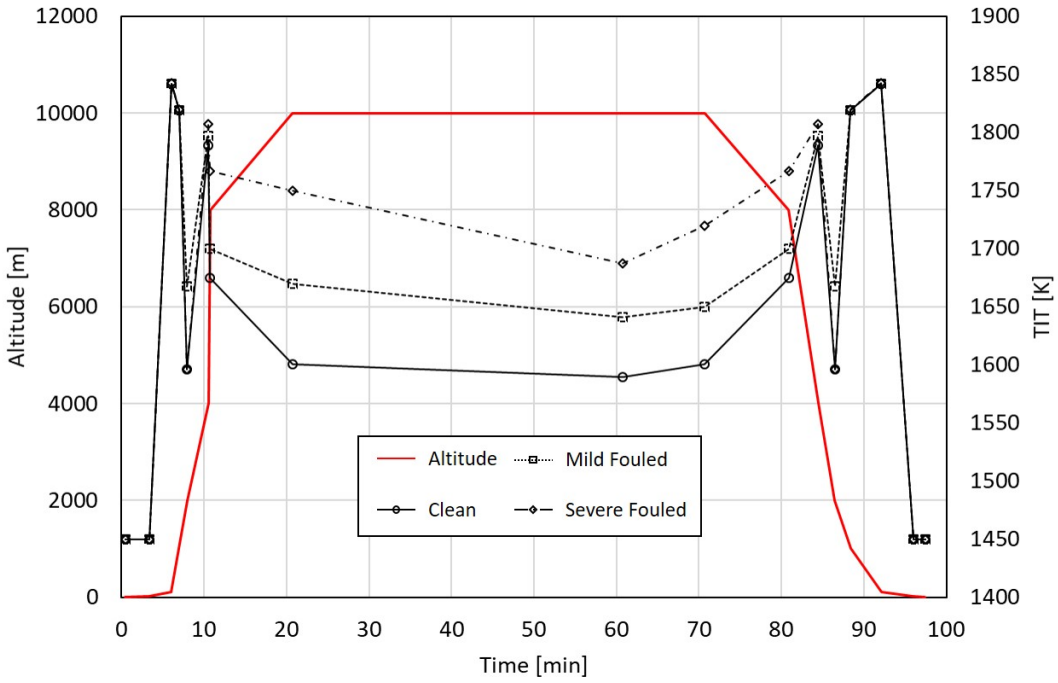

Figure 4.10: Change in TIT due to fouling during a mission.

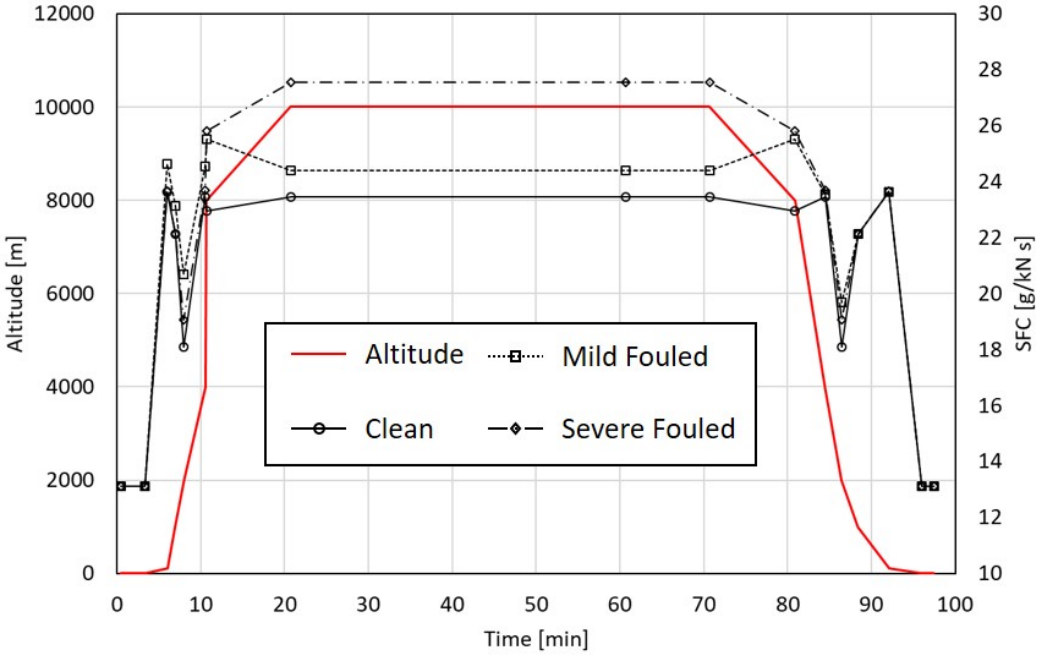

Figure 4.11: Change in SFC due to fouling during a mission.

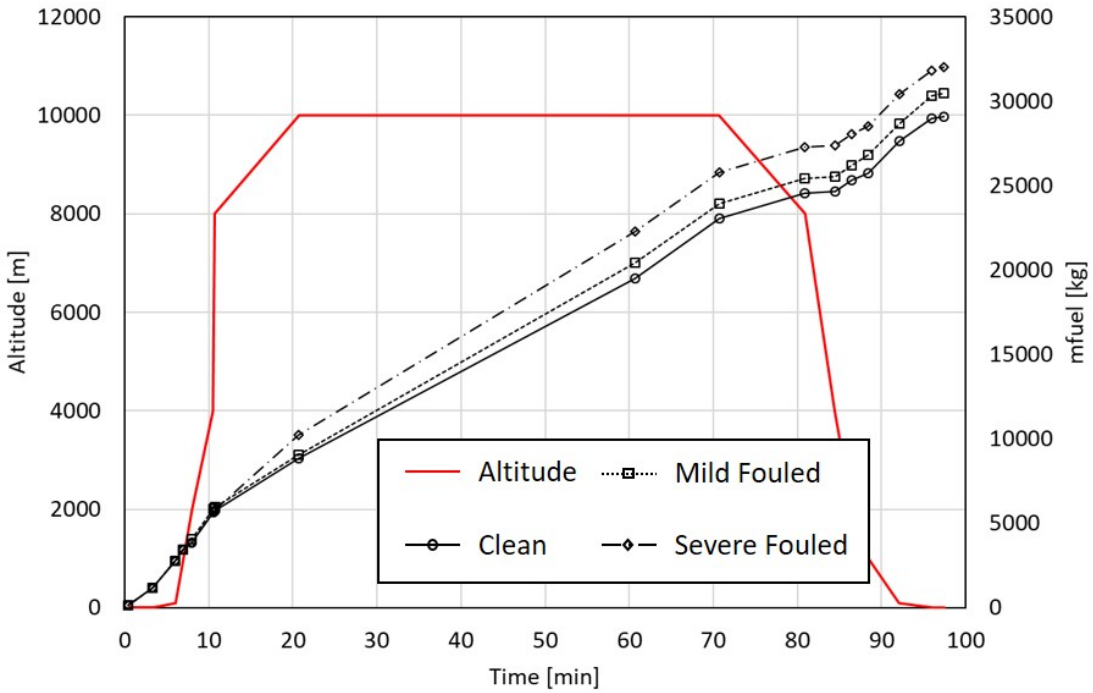

Figure 4.12: Change in cumulative fuel consumption due to fouling during a mission.

will be presented. In the second one, a methodology for estimating Melino's coefficients for turbomachinery will be proposed.

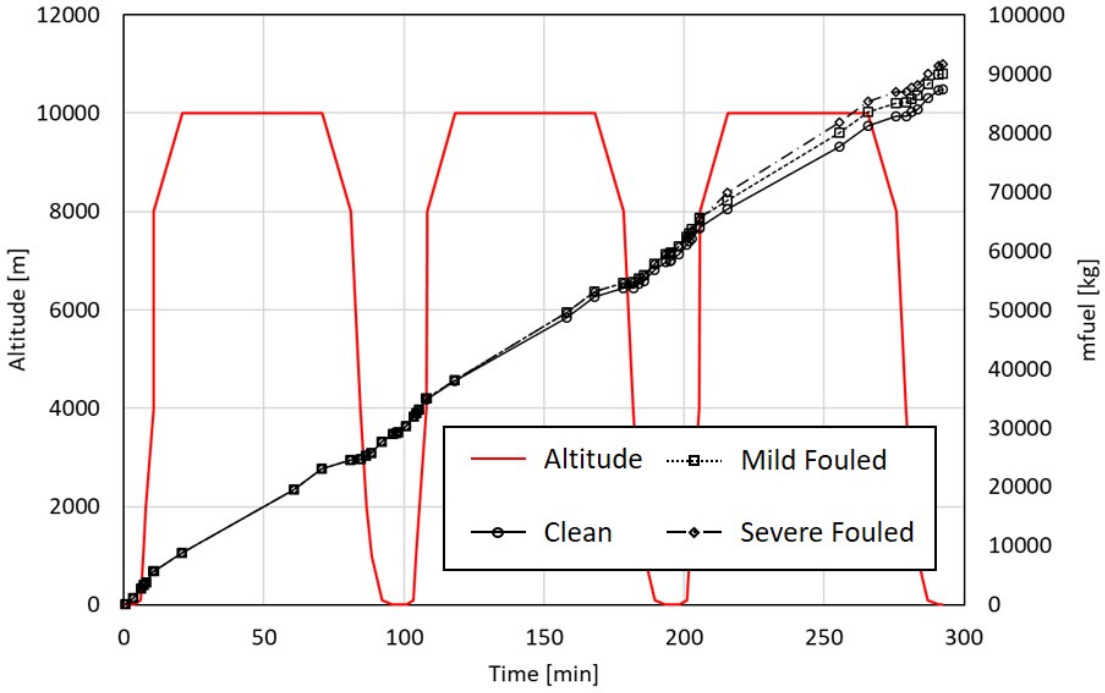

Figure 4.13: Change in cumulative fuel consumption due to fouling during three repeated mission.

4.4 A CALIPSO-based model to Derive Atmospheric Particle Concentration

To monitor the airborne dispersion and characteristics of the contaminants, a range of satellites in the last decades was launched and used to gather data from the Earth's atmosphere. The satellite Cloud-Aerosol Lidar and Infrared Pathfinder Satellite Observation CALIPSO is part of the "A-Train", flying in formation with several other satellites (Aqua, Aura, and CloudSat) launched in 2006 to measure Earth and climate quantities. In particular, the Cloud-Aerosol Lidar with Orthogonal Polarization (CALIOP) device, based on the light detection and ranging – LIDAR device, is able to detect the backscattering coming from the airborne particles. In addition, this measurement system also provides the vertical distribution of the aerosols generating three-dimensional data, which comprises spatial information (latitude, longitude, and altitude), the detected backscatter signal, and the contaminant type definition. Using a proper calibration data set reported in the literature, backscatter data could be reorganized to obtain the particle concentration according to a three-dimensional map.

In this section, a methodology to calculate the contaminant type and concentration encountered by an aircraft has been set up. With reference to open source databases provided by the CALIPSO satellite, a calculation strategy to determine the contaminant concentration starting from the backscattering values has been proposed. A set of reference values of particle density according to the contaminant type are also defined. Two flight routes have

been selected to demonstrate the applicability of this methodology. According to the flight data recorder (coming from an open-source database), an estimation of the contaminant encountered by the aero-engine has been done, demonstrating the reliability of the calculation tool based on open-source data.

4.4.1 Methodology

The aerosol optical properties are commonly involved in measurements of the air quality by means of the scattering and absorption of the light emitted by a LIDAR. These two effects are commonly quantified through the backscatter and the absorption coefficients. The first quantifies the ability of the aerosol matter to scatter light back into the source direction, while the second quantifies the reduction of returning light due to the particle matter absorption. Coupling these data with specific parameters of the technology employed, it is possible to estimate the aerosol type and the aerosol concentration distribution along the emitted light ray.

Here, the methodology developed to estimate the aerosol encountered by an aircraft during a mission is proposed. At first, the flight coordinates of the aircraft (latitude, longitude, and altitude) coupled with the flight date and time are considered. Next, the CALIPSO satellite open data available in the Atmospheric Science Data Center (https://asdc.larc.nasa.gov/) are taken into account. Only the vertical profile measurements closest to the geographical and temporal flight coordinates are considered. The entire mission data log is analyzed and only the discrete points that match the coordinates of satellite measurements are evaluated.

For this purpose, the dust mass concentration estimation based on LIDAR measurements proposed by Mamouri et al. (2016) is taken into account. The authors employed Eq. 4.31 to compute the vertical distribution of the dust concentration during sand storms near Cyprus. Here, their method was extended to all the aerosol types detected by CALIPSO.

$$M_{aerosol} = \rho c_v \beta S \tag{4.31}$$

ρ is particles density, c_v is the volume-to-extinction conversion factor, here assumed constant and equal to 0.64×10^{-9} km according to Mamouri et al. (2016), β is the total attenuated backscatter coefficient $[km^{-1}sr^{-1}]$, and S is the aerosol lidar ratio $[sr]$. The measurements obtained from CALIPSO are collected into data clusters and then divided into different levels depending on the degree of processing and maturity (Winker et al. 2009). The total attenuated backscatter coefficient profiles are contained in level 1 cluster data, while the aerosol type profiles are stored in data of level 2 named *vertical feature mask* (VFM). While the backscatter coefficient is related to the physical and optical properties of the encountered object (aerosol, clouds, etc...), particle density and the lidar ratios are defined for a specific

type of aerosol. Six aerosol models representative of the aerosol mixtures most frequently detected in previous experimental observations (Lee et al. 2010) can be discriminated by CALIPSO. The selection algorithm is reported by Omar et al. (2009) and an analysis over the reliability of the aerosol classification was carried out by Burton et al. (2013). For sake of completeness, the parameters for each aerosol type are reported in Tab. 4.6.

The aerosol model named *dust* comprises the characteristics of African and Asian desert dust (Sahara, Gobi, and Arabian Deserts). The *polluted continental* refers to the contaminant generated in urban-industrial areas, and it is commonly recognized as representative of black carbon emission. The *polluted dust* aerosol model accounts for episodes of dust mixed with biomass burning smoke typical of African and Asian regions. This type of dust is representative of coarser particles (desert sand) and finer particles (biomass smoke). The aerosol model called *smoke* refers to the biomass burning process while the *clean continental* is representative of the northern hemisphere aerosol, but the microphysical properties are likely to have significant uncertainties. Finally, the last aerosol model, called *clean marine*, refers to the detection of marine aerosol but is not completely free from terrestrial and anthropogenic influences. According to Syverud & Bakken (2007), the salt ingested by axial compressors operating in near-shore plants can deposit onto the blades. This leads to the modification of the blade surface roughness. For these reasons, the density value for the *clean marine* aerosol model is assumed equal to 2160 $\mathrm{kg/m^3}$, which is the density of salt.

Once the density and the lidar ratio for each aerosol class are assigned, utilizing the satellite measurements of total attenuated backscatter 532 nm and aerosol type in Eq. 4.31, the vertical aerosol concentration profile along the satellite orbit is computed. The flight mission is divided into discrete points each of which is characterized by three geographical coordinates (latitude, longitude, altitude). A selection algorithm arranges the aerosol concentration with the mission discrete points by matching the local satellite coordinates and the altitude of the aerosol layer. In Fig. 4.14a) a schematization of the intersection of the aircraft and satellite routes is reported and in Fig. 4.14b) the altitude for each considered

Table 4.6: Aerosol densities and lidar ratios

	Clean marine	Dust	Polluted continental	Clean continental	Polluted dust	Smoke
Type	1	2	3	4	5	6
S [sr]	20	40	70	35	65	70
ρ $[kg/m^3]$	2160 (Syverud & Bakken 2007)	2650 (Kok et al. 2012)	1800 (DeCarlo et al. 2004)	1000 (Rocha-Lima et al. 2018)	2173 (Hu et al. 2021)	1695 (Hu et al. 2021)

discrete point is extrapolated from the mission data. The matching process is divided into three phases: first of all, a proximity threshold value both for latitudinal and longitudinal coordinates is set to determine which discrete points of the mission should be considered matched with the satellite readings. Among these, the nearest satellite data are considered by computing the minimum geographical distance between satellite and aircraft. Finally, the aerosol type and concentration are known by looking at which satellite data layer is closest to the aircraft altitude for the considered discrete point. The main steps of the methodology proposed in this work are summarized in Fig. 4.15.

Brandes et al. (2021) carrying out an aircraft mission severity evaluation of a civil flight, pinpointed that take-off and landing operations were the most detrimental phases of the flight due to the highest values of contaminants encountered. To better seize the aerosols faced by the aircraft, the number of discrete points was doubled during these relevant phases. In light of this, it is important to underline that a preliminary analysis of the aerosol vertical profile near the take-off and landing regions could be useful to determine the appropriate size of the discrete steps.

4.4.2 Model application

To test the feasibility of the method described in the previous section, two civil scheduled flight missions (medium and long haul) were analyzed, and the encountered particulate was evaluated using the data provided by CALIPSO. The aerosol type and its relative mass concentration were estimated through Eq. 4.31 employing the total attenuated backscatter 532 nm vertical profiles. The routes considered are the *Sharjah - Mumbai* (medium haul) and the *Hong Kong - Frankfurt* (long haul). With these routes, it is possible to examine different

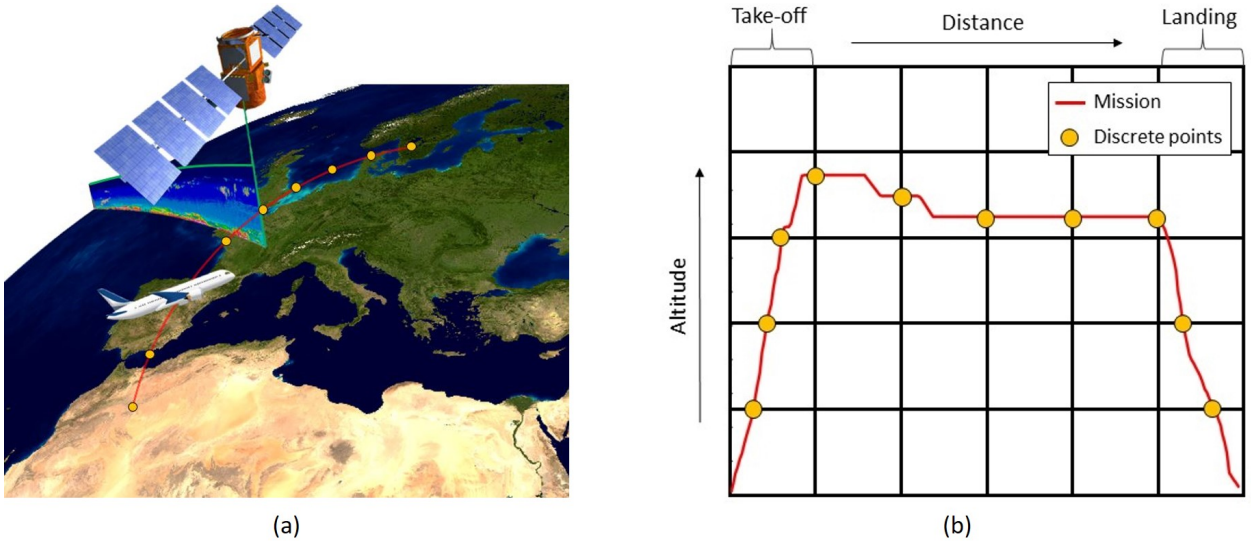

Figure 4.14: Conceptualization of crossing aircraft and satellite coordinates.

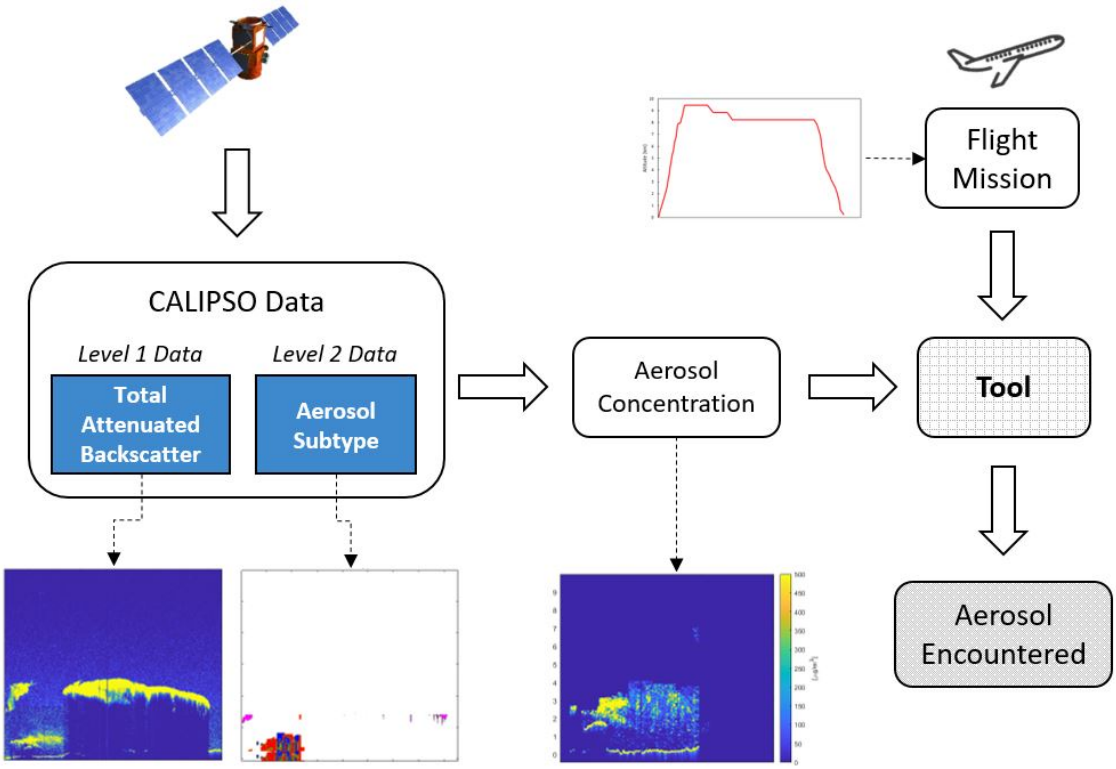

Figure 4.15: Scheme of calculation for the aerosol encountered during an aircraft mission.

environmental conditions during flight missions. In the first case, the take-off occurs in a typical sandy environment; then, after a cruise mostly across the Arabic sea, the landing operation faces high-polluted and near-shore conditions. In the second case, starting from a polluted and high-density populated environment, the mission crosses both Asia and Europe. In both the test cases, remarkable aerosol concentrations were encountered during the take-off and landing operations while few aerosols were detected for altitudes higher than 8000 m (26 300 feet). Since the cruise phase generally develops for higher altitudes, the encountered aerosol during this phase was neglected and the result just for the take-off and landing operations are provided as results.

Sharjah - Mumbai

The estimation of the aerosol encountered by the flight from the international airport of Sharjah (SHJ) to Mumbai (BOM) operated by Air Arabia 405 on May 26, 2022, is reported in this section. A medium entity sand storm was ongoing during the take-off. The aircraft is an Airbus A320, which is commonly employed for short-medium range civil flights. The covered distance is about 2410 km (1300 miles) with a flight time of three hours. A depiction of the mission trace is reported in Fig. 4.16.

During the take-off, the satellite data (Fig. 4.17) pinpointed the presence of aerosols above the Sharjah International Airport from the ground level to almost 5000 m (16 400 feet).

Figure 4.16: *Sharjah-Mumbai* mission trace.

Dust is the main component of these clusters of aerosols as expected for a typical Arabic desert environment Nelli et al. (2021) but also remarkable amounts of also *Smoke*, *Clean continental* and *Polluted continental* were also found. The higher aerosol concentrations are experienced near the ground level reaching values around 1000 µg/m^3, which are in agreement with the findings of previous experimental investigations Draxler et al. (2001) where concentrations in the range 100-1000 µg/m^3 were detected during a two-month test campaign.

As mentioned before, no considerable amount of aerosols was detected along the route during the cruise. On the other hand, landing in Mumbai leads to facing different types of contaminants (Fig.4.18). *Dust* is still the prevalent type of aerosol dispersed in the atmosphere and traces of *Smoke*, *Polluted dust* and *Clear marine* are located. Almost all the detected aerosols can be found at altitudes lower than 6000 m (19 700 feet).

Finally, in Fig.4.19 the aerosol concentration for each type of contaminant encountered during the mission is reported. High-severity flight regions were detected both for the take-

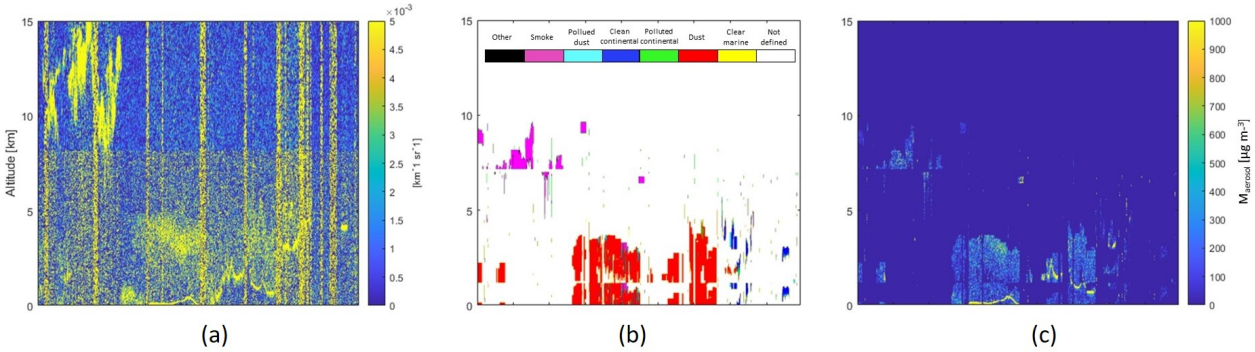

Figure 4.17: Aerosol detection from satellite data during the take-off in Sharjah - (a) Total attenuated backscatter 532 nm; (b) Aerosol type; (c) Aerosol mass concentration.

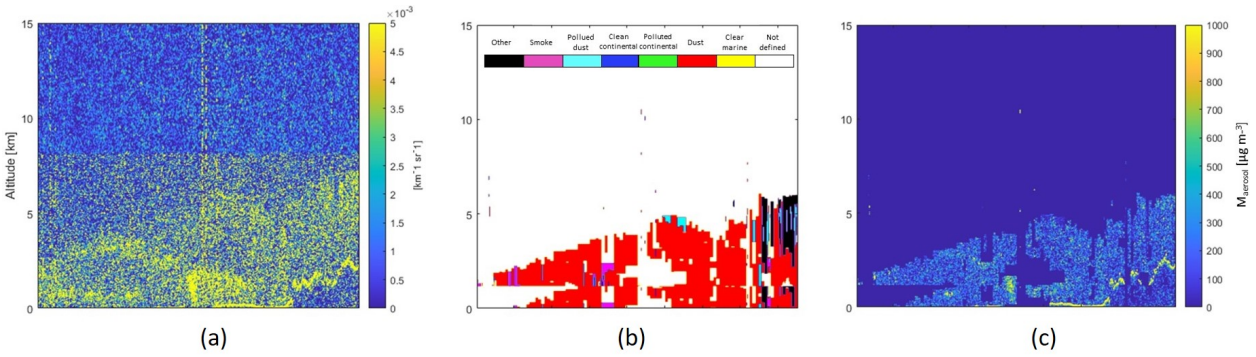

Figure 4.18: Aerosol detection from satellite data during the landing in Mumbai - (a) Total attenuated backscatter 532 nm; (b) Aerosol type; (c) Aerosol mass concentration.

off and landing. In the first phase, the aircraft faced negligible amounts of *smoke* and huge quantities of *dust* and *polluted dust*, reaching a concentration of almost 1000 µg/m^3. For the second, only *dust* was detected but for a longer exposure time and with a concentration up to 700 µg/m^3.

Hong Kong - Frankfurt

For what concern the long-haul mission, the flight between the international airports of Hong Kong (HKG) and Frankfurt (FRA) was considered to test the model proposed in this work. For the mission of May 22, 2022, operated by Cathay Pacific, a BOEING 777-300ER was employed. The covered distance is about 3510 km (6500 miles) for a flight time of about thirteen hours. A depiction of the entire mission is reported in Fig. 4.20. After

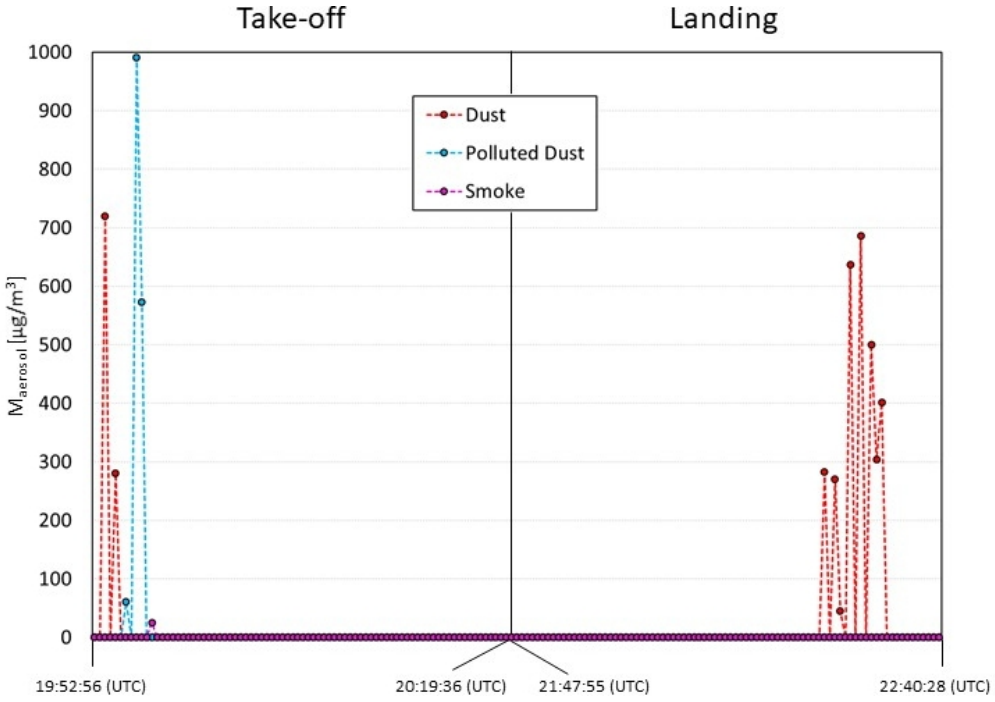

Figure 4.19: Aerosol encountered during the flight from *Sharjah* to *Mumbai*.

Figure 4.20: *Hong Kong - Frankfurt* mission trace.

having crossed China and several Asian countries, the aircraft passed the Caspian Sea and then arrived at Frankfurt flying over middle-east Europe. The proposed long-haul mission can help to study the influence of different environmental conditions on the quality of air elaborated by the aero-engines.

The mission begins at the Hong Kong International Airport where thick aerosol layers were found from 4000 to 10 000 m (13 000 to 32 800 feet) (13,000 to 32,800 feet) altitude as reported in Fig. 4.21. Among these, much of the PM belongs to the *smoke* and *clean continental* aerosol types, which corresponds to a huge industrial and high-density populated environment as reported by Wong et al. (2013). Previous investigations from literature reported the vertical distribution and concentration of the PM in Hong Kong (Chan & Kwok 2000, Chan et al. 2001, Ho et al. 2002). Chan & Kwok (2000), Chan et al. (2001) found particles concentrations between 100-300 µg/m^3 near the ground level during an extensive experimental campaign in an urban area of Hong Kong, while Ho *et al.* reported values up to 120 µg/m^3 collecting particles across the same region. As reported in Fig. 4.21, good agreement was found with the estimations presented in this work. Also *polluted dust* and

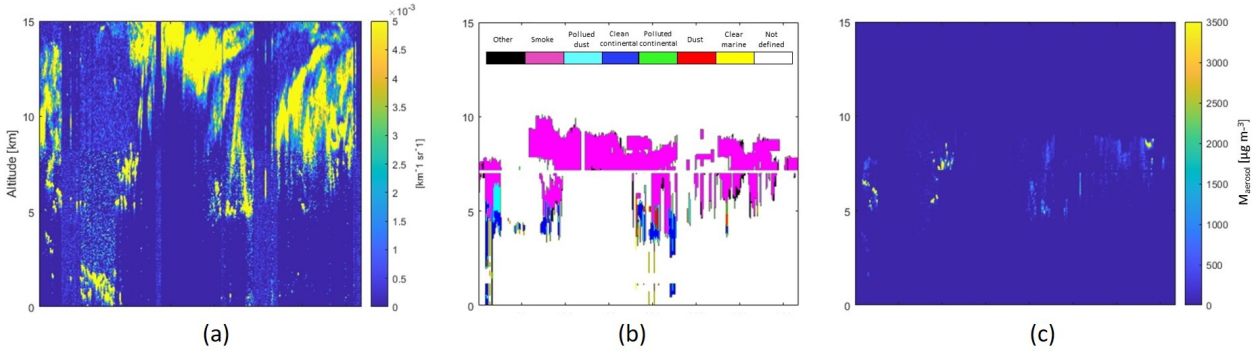

Figure 4.21: Aerosol detection from satellite data during the take-off in Hong Kong - (a) Total attenuated backscatter 532 nm; (b) Aerosol type; (c) Aerosol mass concentration.

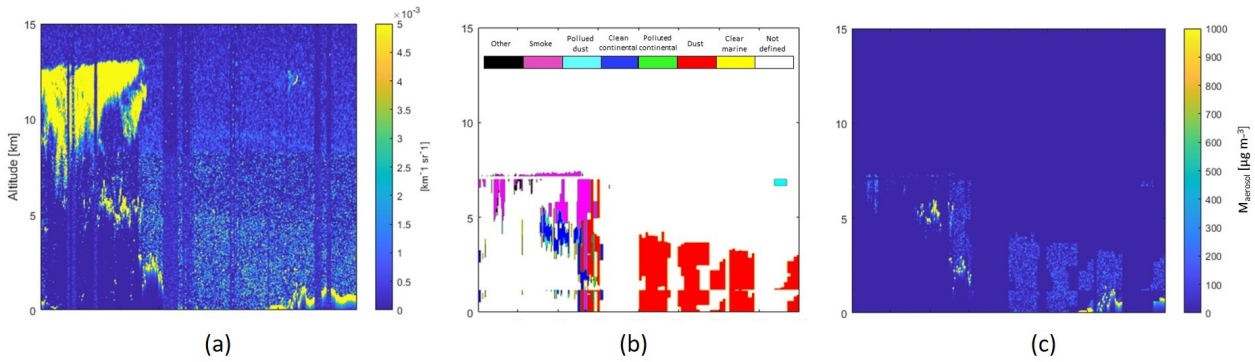

Figure 4.22: Aerosol detection from satellite data during the landing in Frankfurt - (a) Total attenuated backscatter 532 nm; (b) Aerosol type; (c) Aerosol mass concentration.

clear marine aerosol type were detected in few zones. The higher aerosol concentrations are experienced at altitudes of about 7500 m (24 600 feet), reaching values around 3500 µg/m^3.

Although the long haul of the mission, as found for the *Sharjah-Mumbai* in Sec. 4.4.2, no relevant amount of aerosol was detected during the cruise phase due to the lack of notable particle concentrations at the altitudes where the cruise typically takes place. However, different aerosols were found during the landing in Frankfurt, as reported in Fig. 4.22. Most of them are classified as *dust*, with also considerable amounts of *smoke* and *clean continental*. The estimated mass concentration reaches 1000 µg/m^3 at middle altitudes, i.e. around 5000 m (16 400 feet). According to Brand et al. (1992), values of mass concentration from 50 µg/m^3 up to 200 µg/m^3 can be found typically at the ground level near Frankfurt.

Through the intersection of satellite and flight data, the aerosol concentration for each type of contaminant encountered during the mission can be calculated. The results are reported in Fig. 4.23. The most detrimental flight conditions were detected during the take-off in Hong Kong where *smoke* concentrations of about 3400 µg/m^3 were encountered (Fig.

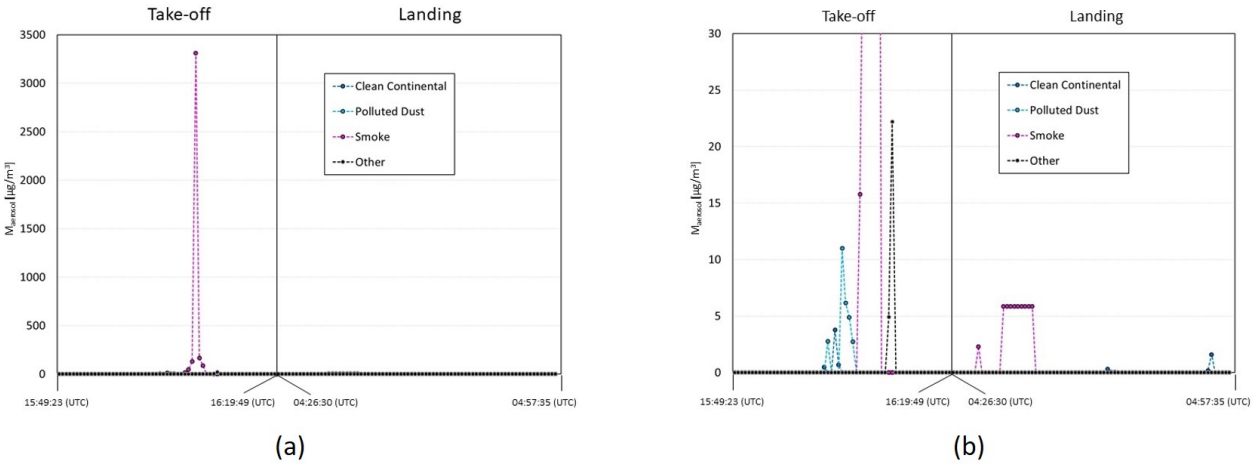

Figure 4.23: (a) Aerosol encountered during the flight from *Hong Kong* to *Frankfurt*; (b) magnification of the 4.23(a) in the range 0-30 $\mu g/m^3$.

4.23a). In addition, *clean continental polluted dust* aerosol types were faced in concentrations up to 25 µg/m^3 (Fig. 4.23b). On the other hand, the landing in Frankfurt leads to the ingestion of a restrained amount of *smoke* and *clean continental* with concentrations not over 6 µg/m^3. As a result, the aircraft encounters aerosols of different natures both during the take-off and landing.

4.5 Degradation Coefficients Derivation Strategies

As said in Sec. 4.3, besides the derivation of the atmospheric contaminant concentration, one of the big problems that must be faced to build a predictive maintenance tool is the estimation of adequate degradation coefficients, since they are the parameters that describe the component deterioration. In this context, the strategy proposed in the present work wants to be the solution to this problem. In particular, a multi-fidelity machine learning-based methodology that can be trained with experimental and numerical data is presented. The procedures to obtain the dataset will be deeply presented, whilst the machine learning algorithm will be only introduced since the reader is free to choose the multi-fidelity method it likes.

4.5.1 Experimental Strategy

The experimental campaign has been conducted on the rotating test facility located in the Fluid Machinery Laboratory of the University of Ferrara, Italy. The test rig (Bettocchi et al. 2003) mounts the multistage compressor of the Allison 250 C18 (Suman et al. 2021) engine shown in Fig. 4.24. A schematic layout of the system used for this work is reported in Fig. 4.25 and is divided into four parts, which are described in detail in this section. Looking at Fig. 4.25, the pressure values are taken in the suction section and at the bleed valve installation (the bleed valve is positioned in correspondence with the fifth axial stage). Two ceramic absolute pressure transducers (MEAS U5200) have been used at the inlet and bleed sections with a measuring range of 345 000 Pa. The measurement taps were checked to ascertain the absence of burrs or slag and, thus, avoid their contributions to the total error of pressure measurements, which can be significant. During the tests, a volumetric flow rate was measured at the inlet duct in order to check the operating conditions of the compressor and to ensure the particle concentration at the inlet section. Due to the operating conditions, the volumetric flow rate is not taken as a reference for evaluating the performance losses due to fouling. All acquired signals are transmitted to a desktop by a National Instrument devices and acquisition rack. The voltage signals provided by the pressure transducers are elaborated by the National Instruments acquisition module NI 9201. These devices are comprised in the uncertainty assessment.

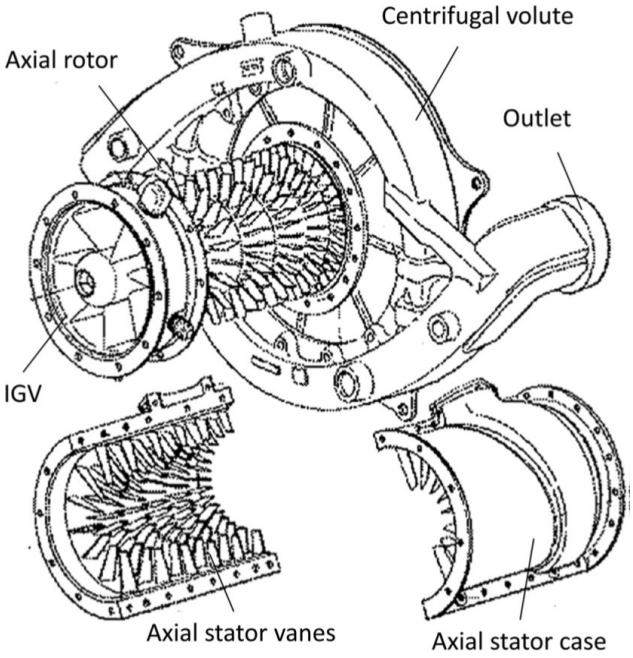

Figure 4.24: Sketch of the Allison 250 C18 compressor unit: IGV, stator, and rotor axial wheels. From Suman et al. (2021).

Dust Injection System

The system is designed to inject a constant amount of contaminants toward the inlet of the compressor. The air required to drive the system is supplied by a screw compressor. A heat exchanger downstream of the compressor provides the removal of humidity from the shop air and a set of filters ensures the total removal of the impurity, such as dust and oil droplets. The clean and dry shop air follows three paths: two of them enter the particle feeder and

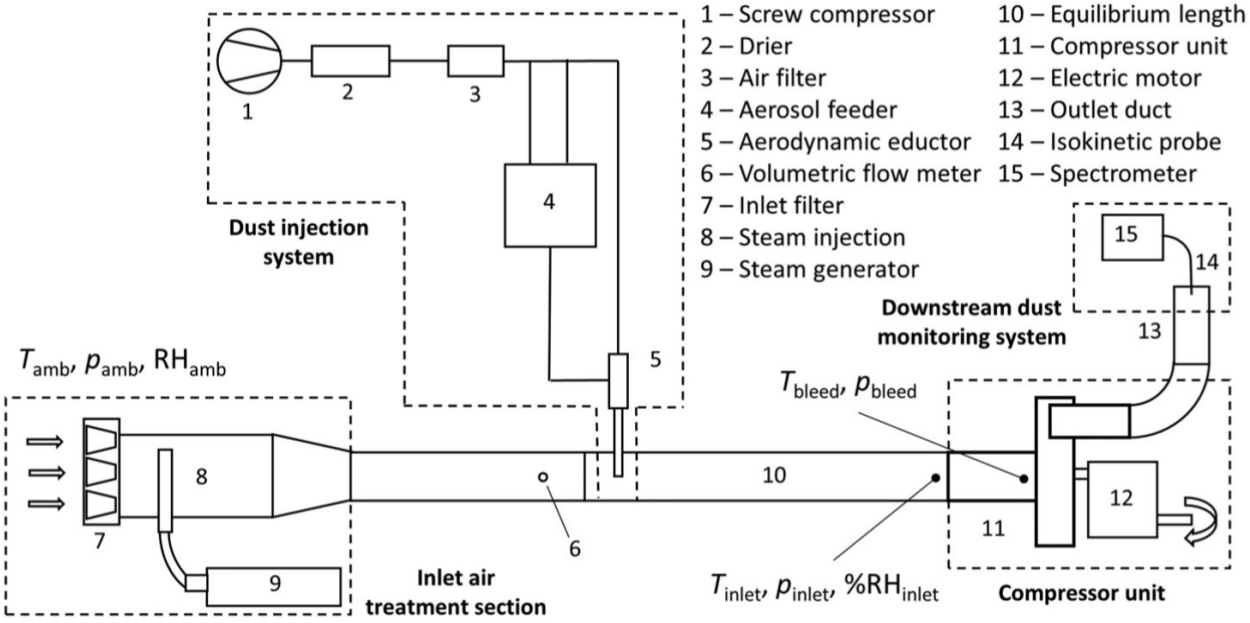

Figure 4.25: Schematic layout of the multistage compressor test facility.

one goes to an aerodynamic eductor. The particle feeder is the SAG 410 Ultralow Flow model made by TOPAS GMBH. This device provides the dosage of the injected powder. A rotating ring is charged with the powder in a drizzling manner. The powder on the ring is carried at a constant speed from the charging site to the sucking dispersing nozzle that de-agglomerates and disperses the powder. The rotation speed of the dosing ring can be freely selected, changing the mass flow rate of the injected powder. One of the paths of the supplied air is used to drive the dispersing nozzle and the other one provides the purge air to maintain the feeder clean. The aerodynamic eductor is driven by the third line of the supplied shop air. The eductor disperses the dust, that has been previously dosed by the feeder, into the upstream compressor pipeline after de-agglomeration of the powder thanks to the shear stress applied by the Venturi nozzle (Yoshiyuki Endo et al. 1997, Calvert et al. 2009). The injection system has been calibrated in an external circuit with the use of the Particle Spectrometer OPS 3330 made by TSI. Thereupon, the particle mass flow injected into the compressor pipeline is always known. Before entering the compressor, an equilibrium length of 2 m has been used to ensure the achievement of the kinetic and thermal equilibrium between particles and air. This distance permits the proper mixing process and allows a uniform particle concentration at the compressor inlet.

External Air Treatment Section

The test facility is located in a closed room where the air is maintained at the almost constant condition of 22 °C and 50 %RH. The values of pressure, temperature, and humidity are always monitored for the entire duration of the test. To avoid the ingestion of external dust without introducing high-pressure losses, a compact filter EPA F9 class has been placed at the inlet of the circuit. A steam nozzle is placed afterward the filter in order to increase the relative humidity of the air. The use of steam humidification is crucial to avoid the temperature modification of the inlet air. The nozzle is linked to a steam generator and the steam mass flow rate can be selected in order to achieve the desired relative humidity value at the inlet of the compressor. Before entering the steam generator, the supplied water is treated by an osmotic system.

Compressor Unit

The test rig was built to test the Allison 250 C18 compressor (Suman et al. 2021). The machine is characterized by an inlet diameter of 0.104 m with an inlet guide vane. The compressor has six axial stages and one centrifugal stage. The centrifugal stage has two semivolutes, each with a circular exit duct with a diameter of 0.056 m. Two flexible tubes link the outlet ducts to an exhaust outlet with a diameter of 0.100 m. At its nominal operative conditions, the compressor achieves a pressure ratio of 6.2, with a rotational speed

of 51 600 rpm rpm and a mass flow rate of 1.36 kg/s.

Test Conditions

The long time required for the deposition phenomena to occur in real operative conditions makes its faithful reproduction in the laboratory practically unachievable. The strategy adopted by researchers, in the literature and also in this study, is to increase the concentration of dust by several orders of magnitude with respect to the ambient condition (Syverud & Bakken 2007, Döring et al. 2017*b*, Jensen et al. 2004), in order to accelerate the phenomena and realize the test in a laboratory time scale. In such tests, the reinforcement of the deposited layer due to the bridges generated by the presence of water and the oxidation process is neglected. However, in common applications, these phenomena are considered higher-order effects. The contaminants selected to study the deposition on the Allison 250 C18 are micrometric powders of Arizona road dust. The ARD is a silica-based standard powder for filter testing and it is widely used in literature to study deposition mechanisms (Yu & Tafti 2016, Whitaker et al. 2016).

Three particle size distributions of ARD have been tested: Nominal 0-3 µm (ARD N), ISO 12103—1 Ultra-Fine (ARD UF) and ISO 12103—1 Medium (ARD M). The powder samples were provided by Powder Technology, Inc. (Arden Hills, MN), and they are obtained in agreement with ISO 12103-1:2016. The characteristics related to the particle size are reported in Tab. 4.7 and the frequency curves of the number distribution are reported in Fig. 4.26.

The layout of the test rig allows changing the relative humidity at the inlet of the compressor. The role of relative humidity is crucial in the adhesion mechanisms between particles and compressor internal surfaces. For this reason, the experimental campaign has been performed considering three values of the relative humidity: 15 %RH, 50 %RH. and 80 %RH. The value of 15 %RH was the lower limit reachable during the test campaign days. Whereas, the value of 80 %RH was the upper limit to avoid the formation of drops of condensation at the inlet of the compressor that could have washed away the deposited dust.

The tests have been conducted only at the rotational speed of 20 000 rpm. This constraint was due to the capability of the test rig. The mass flow rate was 0.36 kg/s. Summing up, the experimental campaign concerned the following variables: three values of relative humidity (15 %RH, 50 %RH. and 80 %RH), and three types of contaminants (three grades of ARD).

Table 4.7: Contaminant diameter distributions

Powder type	$d_{mean}(\mu m)$	$d_{10}(\mu m)$	$d_{50}(\mu m)$	$d_{90}(\mu m)$
ARD N	1.3	0.9	1.1	1.9
ARD UF	4.8	1.1	4.3	8.5
ARD M	25.5	2.5	14.0	60.3

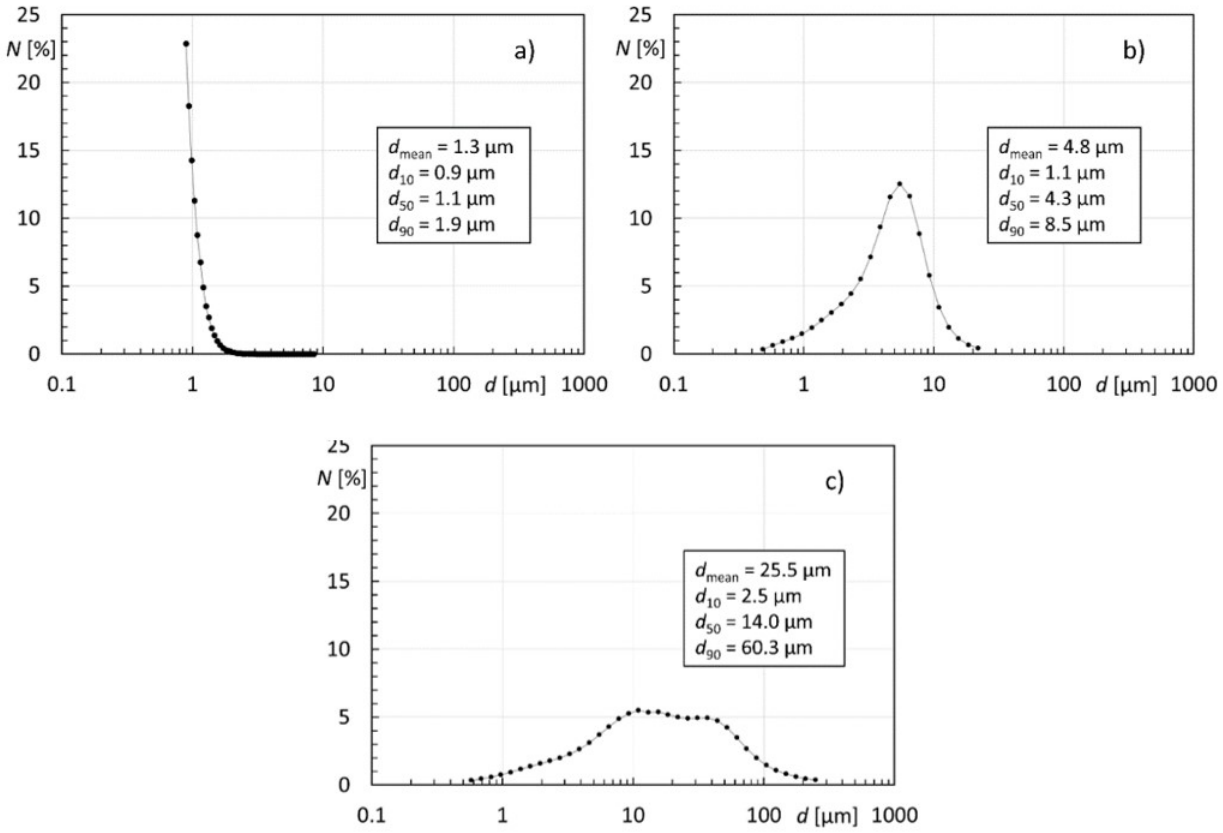

Figure 4.26: Frequency curves of number distribution of a) ARD N, b) ARD UF, and c) ARD M.

Before being injected, the powders have been baked for twelve hours at 15 %RH, 50 %RH. and 70 °C in order to eliminate their water content. The matrix of the tests conducted is reported for the sake of clarity in Fig. 4.27.

Test Procedure

Starting from the number of variables introduced in the previous section "Test Conditions," a total number of five tests have been performed. At the beginning of each test, the compressor was deeply cleaned. The offline cleaning has been carried out by disassembling the stator axial part to allow easy access to the rear stages of the compressor. The stator and rotor blades, the shroud and the hub were cleaned with demineralized water, a cleaner product and brushes to restore the initial condition of cleanliness. Due to the inaccessibility of the Allison 250 C18 compressor to the centrifugal impeller and volute, the cleaning of these parts has been carried out using demineralized water and a cleaner product from the outside. The cleaning effectiveness has been assessed with borescope observations. After the conclusion of the cleaning operation, pictures of the IGV, axial rotor and axial stator are taken. After the compressor startup, the achievement of the desired operating point and the assessment of the thermal equilibrium, the injection of the contaminant is carried out. The duration of the tests was 4 hours. For the duration of the test, the particle flow rate injected is kept

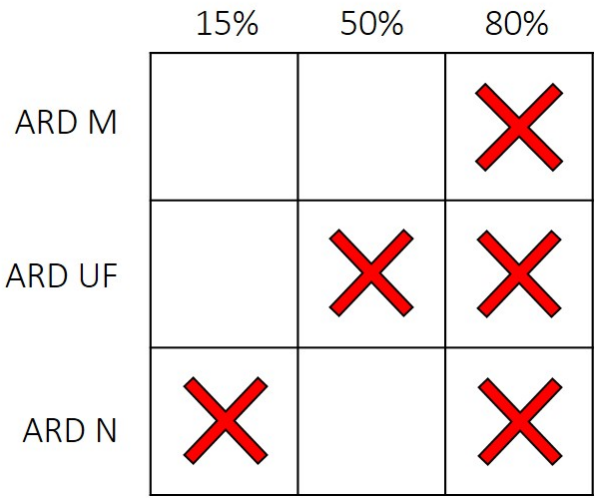

Figure 4.27: Test matrix.

constant. For every test, the injection of contaminants was stopped after 2 hours, and the characteristic curve of the machine was acquired. The latter was obtained also after the 4 hours of exposure. At the end of each test, the axial part is disassembled and pictures of the fouled parts (IGV, axial stator and rotor) are taken. As stated before, the centrifugal impeller and volute are inaccessible, and for this reason, representative pictures of deposited dust on those parts are not provided in this work.

Uncertainty Assessment

The present investigation is based on the timewise monitoring of the compressor performance to detect the losses due to the fouling phenomenon. Since the operating conditions (subidle and quasi-idle) and the sensor position adopted in this work (shown in Fig. 4.25) impose an accurate assessment of the pressure values, a detailed analysis of the uncertainty value associated with the pressure measurement has been carried out. The uncertainty calculation is performed in order to estimate the uncertainty of the pressure measurement and the compression ratio β provided by the machine by means of the uncertainty propagation. The uncertainty calculation is based on the procedure reported in the standard ISO/IEC Guide 98-3:2008 and EA-4/ 02M. The propagation of the uncertainty is realized by employing the classic procedure based on propagation rules. The definition of the pressure ratio is

$$\beta = \frac{p_{s,bleed}}{p_{s,inlet}} \tag{4.32}$$

and its associated uncertainty can be expressed as

$$\delta\beta = \sqrt{\left(\frac{\partial\beta}{\partial p_{s,bleed}}\right)^2 \delta p_{s,bleed}^2 + \left(\frac{\partial\beta}{\partial p_{s,inlet}}\right)^2 \delta p_{s,inlet}^2 + 2r\left(\frac{\partial\beta}{\partial p_{s,bleed}}\right)\left(\frac{\partial\beta}{\partial p_{s,inlet}}\right)\delta p_{s,bleed}\delta p_{s,inlet}} \tag{4.33}$$

where the uncertainty of pressure values measured at the suction ($\delta p_{s,inlet}$) and bleed ($\delta p_{s,bleed}$) sections are evaluated according to the procedure reported in the following description. Eq. 4.33 shows the propagation equation including the part of the uncertainty due to the correlated terms. In the present investigation, pressure transducers are calibrated against the same prime laboratory standard and share the same acquisition signal chain. For this reason, the uncertainty of the pressure ratio will include the correlated terms with a correlation coefficient r equal to 1 (one). The uncertainties of pressure values are estimated according to the data collected during the calibration process.

The standard procedure consists of the definition of the first-order (linear) calibration curve realized using several pairs of measured pressure and reference pressure values. The best straight line was obtained by considering twenty-five (25) independent points and it is used during the tests to correct the measured pressure values. During the calibration process, the evaluation of the sensor hysteresis has been carried out by means of a two-way calibration process (from lower to higher pressure values, and vice versa). Besides, since the calibration process was carried out in the same conditions as the usual measurement system operation, the temperature effects on the pressure measurement were considered intrinsically in the calibration process. The two pressure transducers (mounted at the compressor inlet and outlet sections) and the correspondent measurement chain have been calibrated at the same time, using a three-way manifold connected to the pressure calibrator Micro-Cal PM200þ, representing the in-house laboratory secondary standard which, in turn, is calibrated toward a primary laboratory standard certified in agreement with the Italian Accreditation Body (Accredia). This methodology is the base for the assumption of a coefficient of correlation equal to 1 (one). The type B uncertainty is obtained by considering the uncertainty of the primary laboratory standard (that represents the reference uncertainty of the certified laboratory standard) UPLS (considered as a Gaussian distribution, and for this reason, it is divided by 2 for calculating the standard deviation equivalents) and the residual uncertainty value of the pressure measurement chain E_R. The latter value is estimated considering the difference between the reference value (also called true value because is the value provided by the primary laboratory standard) and the average value of the signal provided by the measurement chain reordered for 2 s under a constant pressure input (generated and controlled by the Micro-Cal PM200þ). This term is considered to have a rectangular probability distribution and for this reason, it is divided by $3^{1/2}$. Finally, this procedure also allows the evaluation of the type A uncertainty by estimating the standard deviation (considered as

Table 4.8: Extended uncertainty values for the pressure measurement chains for the inlet and the bleed sections 2σ.

	$p_{s,inlet}$	$p_{s,bleed}$
(rpm)	20000	20000
U_{PLS} [Pa]	38	284
E_R [Pa]	49	33
U_σ [Pa]	2	2

a Gaussian distribution, and for this reason, it is divided by 2 for calculating the standard deviation equivalents) of the set of data U_σ. The size of the sample (about 2000 pressure measurements) ensures the proper application of the statistical methodology. The final assessment of the pressure measurements uncertainty is

$$\delta p = \sqrt{\left(\frac{U_{PLS}}{2}\right)^2 + \left(\frac{E_R}{\sqrt{3}}\right)^2 + \left(\frac{U_\sigma}{2}\right)^2} \tag{4.34}$$

while Tab. 4.8 reports all the extended uncertainty data with a level of confidence of 2r (coverage factor $k = 2$). Based on these data, the uncertainty of the compressor pressure ratio has been assessed. After the uncertainty propagation, the uncertainty of pressure ratio is 0.038 % for the tests at 20 000 rpm.

Correction Factors

Since during the tests, the corrected rotational velocity changed as a consequence of fouling, in order to compare results from different fouled conditions a correction in the rotational speed was necessary. For this purpose, the correction strategy reported in the ASME PTC 10 was used.

The corrections were performed for both the mass flow rate and the pressure ratio. The first was done by applying Eq. 4.35.

$$\dot{m}_{corr} = \dot{m}\,\frac{\omega}{\omega_{corr}}\,Re_{m_{\dot{m}}} \tag{4.35}$$

where ω_{corr} is the corrected rotational speed, and $Re_{m_{\dot{m}}}$ is the machine Reynolds nomber computed as

$$Re_{m_{\dot{m}}} = \frac{l_{p,rif}}{l_p} \tag{4.36}$$

where l_p is the polytropic efficiency, which, assuming air as perfect gas and neglecting the compressibility effects, can be calculated as

$$l_p = \left(\frac{n}{n-1}\right)\,R\,T_{0,asp}\,\left[\beta^{\frac{n-1}{n}} - 1\right] \tag{4.37}$$

On the other hand, the correction of the pressure ratio has to be preceded by the correction of the polytropic efficiency as

$$l_{p,corr} = l_p \left(\frac{\omega}{\omega_{corr}} \right)^2 Re_{m_{\dot{m}}} \tag{4.38}$$

Once corrected the efficiency, also the pressure ratio can be corrected as

$$\beta_{corr} = \left(\frac{l_{p,corr}}{R\, T_{0,asp}} \frac{n}{n-1} + 1 \right)^{\frac{n}{n-1}} \tag{4.39}$$

Performance Degradation

The evaluation of compressor performance has been assessed according to the pressure ratio and mass flow rate over the axial stages. Among the tests that have been carried out, only the ones with ARD N and ARD UF lead to appreciable results, whereas the ones with ARD M did not show particular effects on the performance of the compressor. For this reason, only the results obtained with the ARD N and ARD UF will be shown here. Fig. 4.28, and 4.29 shown the timewise performance modification and the characteristic curve found respectively.

For what concern Fig. 4.28, it can be noted that the only configuration that leads to a degradation of the performance is the ARD UF at 50 %RH. The other configurations reported seem to conduct a change in the operating point rather than a degradation of the performance. In particular, both ARDN at 15 %RH and 80 %RH lead to a shift of the operating point towards the surge conditions (rise in the pressure ratio and drop in the mass flow rate). On the other hand, AR UF at 80 %RH shows the opposite behaviour, since the pressure ratio tends to decrease and the mass flow rate increases. Besides that, a note can be made in the trend of the ARD N at 80 %RH. It seems that the pressure ratio tends to reach an asymptotic behaviour with the increase in the contaminant injected. This leads the Author to consider that, in this particular circumstance, the equilibrium between adhesion and detachment has been achieved.

The results reported in terms of trends over time are also reported in terms of performance curves in Fig. 4.29. As it can be noted, all the considerations reported previously can be transported here. The most important thing to highlight in these results is that they can be perfectly used to estimate Melino's coefficients for a specific machine. This procedure can be repeated for other turbomachinery, with the purpose of creating a database that can be employed to train a machine learning algorithm to give the degradation coefficients.

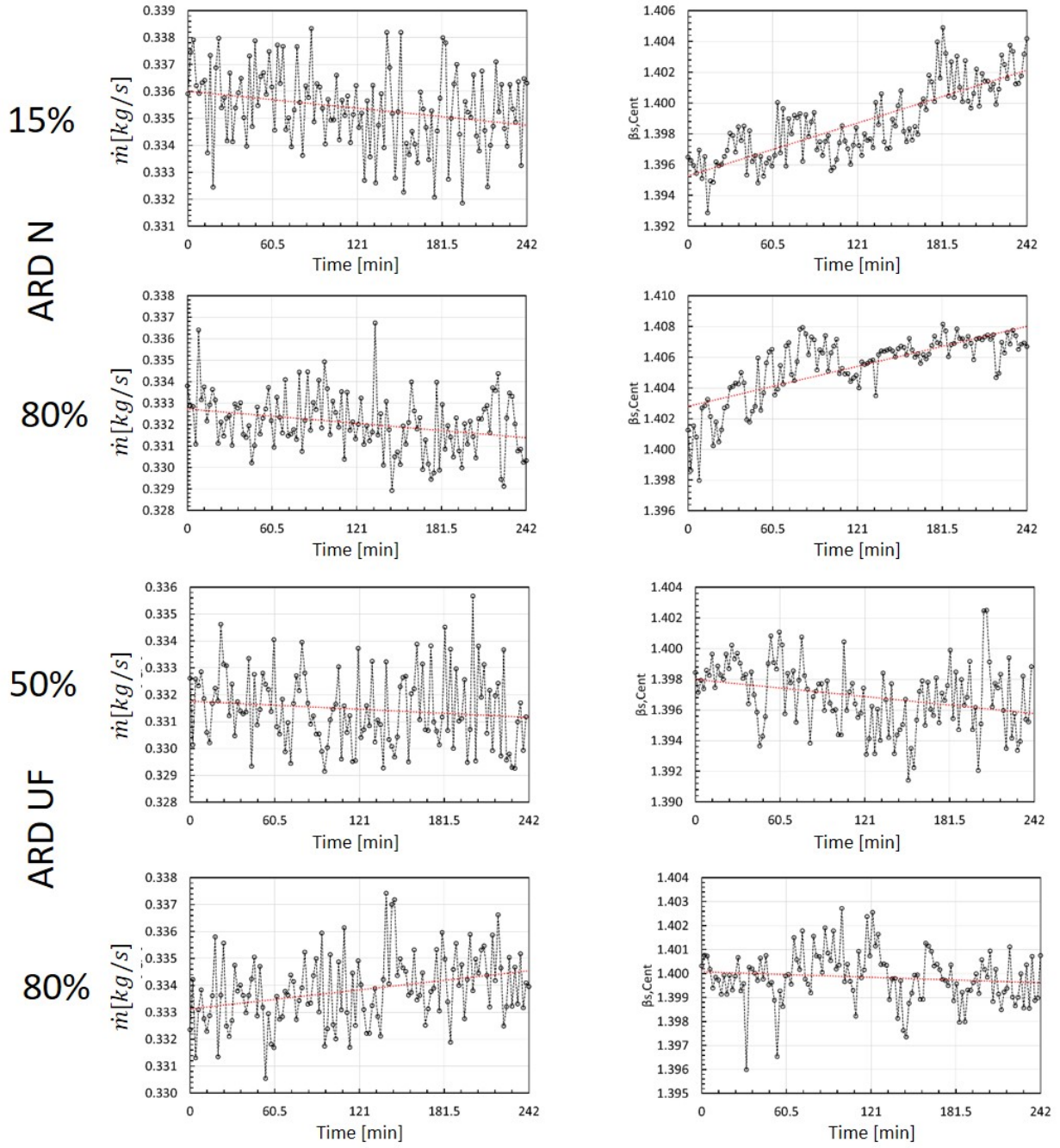

Figure 4.28: Performance trends over time at 20 000 rpm as a function of contaminant and relative humidity values. The trend of the clean condition is equipped with error bars referring to the extended uncertainty of the pressure ratio and the mass flow rate.

4.5.2 Computational Strategy

As reported earlier, the dataset for the estimation of Melino's coefficients can be built with both experimental and numerical results. In this section, the second method is explored. For this purpose, some consideration has to be pointed out. First of all, it is obvious that in order to obtain a more accurate result, the whole turbomachinery should be simulated. This, however, would result in tremendous computational costs, often unattainable. For this

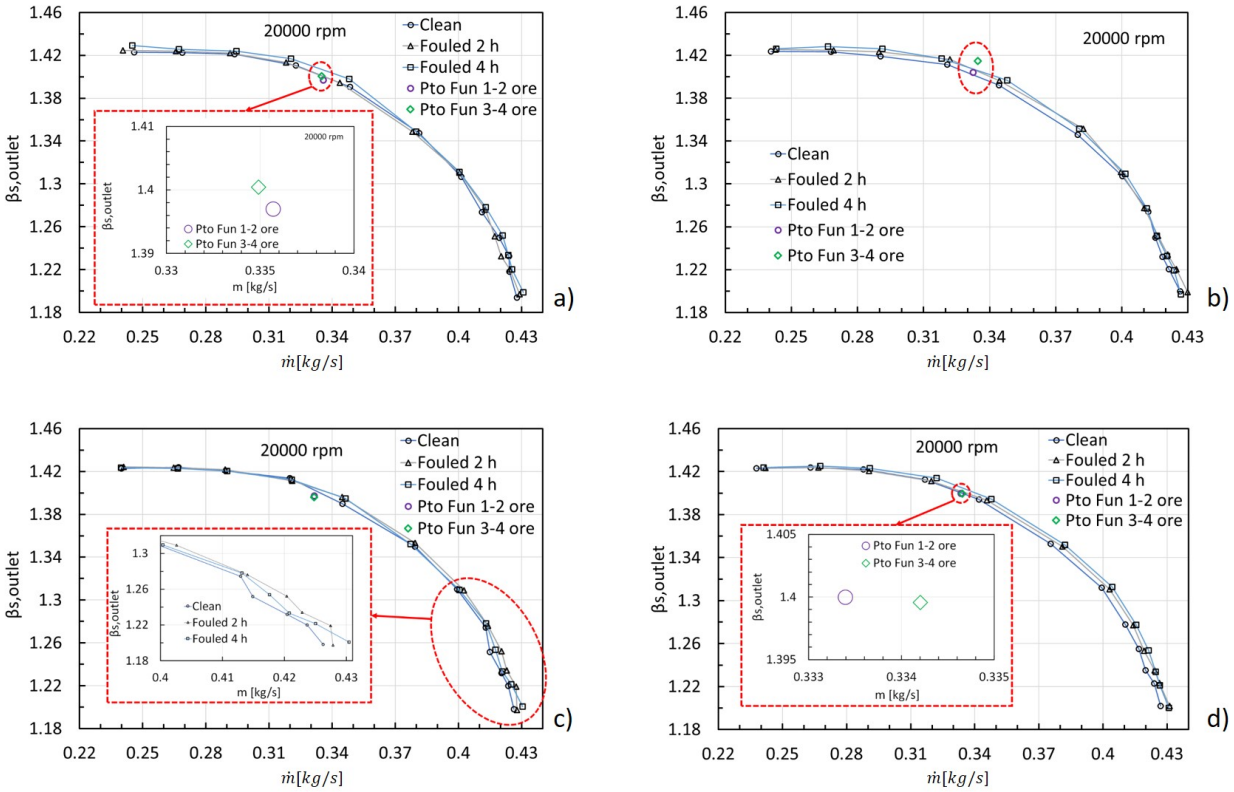

Figure 4.29: Performance curves at 20 000 rpm as a function of contaminant and relative humidity values: a) ARD N - 15 %RH, b) ARD N - 80 %RH, c) ARD UF - 50 %RH, and d) ARD UF - 80 %RH .

reason, in this work, the stage-stacking strategy is proposed in order to avoid the simulation of the entire machine, and then focus the efforts only on its first stage. This is because the stage-stacking allows the estimation of the engine performance by only knowing the ones of its first stage. With the use of this technique, a problem arises when the open-source software OpenFOAM is employed, since it lacks the mixing-plane algorithm, that is useful for multistage turbomachinery simulations. To face this problem, foamExtend-v4.1 instead of OpenFOAM was utilised, since the mixing plane was already implemented in it. Nonetheless, efforts have been done to adapt the algorithm to interact with particle tracking. Finally, the whole procedure, constituted by the new cold deposition model (Sec. 2.2.3), the mixing plane strategy, and the microscale model (Sec. 2.2.3), was applied to a real turbomachinery, that is the axial compressor used for the experimental campaign introduced in the previous section.

The Stage Stacking Technique

The stage-stacking technique here exposed was firstly introduced by Spina (2002). The procedure to obtain the performance maps of a multistage compressor, which link together overall pressure ratio (β_C), efficiency (η_C), corrected mass flow (μ_C) and corrected rotational

speed (ν_C), is based on the fact that the overall performance of a multistage compressor depends on the performance of its stages. Therefore, by starting from stage characteristics, which link together pressure coefficient (ψ), stage efficiency (η) and flow coefficient (ϕ), the stage-by-stage evaluation of the outlet conditions from the knowledge of those at the inlet is possible. At this point, the use of a "stage-stacking" procedure allows the evaluation of the overall multistage compressor performance.

In order to model each compressor stage, generalized relationships between $\psi^*=\psi/\psi_r$, $\eta^*=\eta/\eta_r$ and $\phi^*=\phi/\phi_r$ were used. These relationships allow the complete evaluation of stage characteristics once the stage reference point (ψ_r, η_r, phi_r) is known or estimated.

The first generalized relationship, $\psi^* = F_\psi(\phi)$, was set up based on the work of Muir et al. (1989), who obtained a generalized curve by fitting experimental data points of a number of compressor stages. First, the curve of Muir et al. (1989) was approximated using the following relationship:

$$\psi^* = \psi^*_{max} - \frac{\psi^* - 1}{\left(\phi^*_{\psi_{max}} - 1\right)^2} \left(\phi^*_{\psi_{max}} - \phi^*\right)^2 \tag{4.40}$$

Secondly, in order to account for different stage characteristics based on different stage types, a number of generalized $\psi^* = F_\psi(\phi^*)$ curves covering all experimental data points reported by Muir et al. (1989) were used. These curves were obtained by substituting, for each ψ^* value calculated by means of the Eq. 4.40, the respective abscissa ϕ^* with $(\phi^* + (\phi^* - 1)\,SF)$, where SF is the "Shape Factor" introduced by Cerri et al. (1993). This allows the representation of different types of compressor stages, including transonic and supersonic stages (negative SF values). In Fig. 4.30 three curves $\psi^* = F_\psi(\phi^*, SF)$ obtained using $SF \in [-0.5, 1]$ are shown, together with the experimental data points and the curve reported by Muir et al. (1989).

The second generalized relationship, $\eta^* = F_\eta(\psi^*/\phi^*)$, was set up by substituting the abscissa ξ^*/ϕ^* of the generalized stage efficiency curve $\eta^* = F_\eta(\xi^*/\phi^*)$ proposed by Howell & Bonham (1950) with $\psi^*/\phi^* = \eta^*\,(\xi^*/\phi^*)$. The obtained curve was then approximated using the following relationships:

$$\eta^* = 1 - \frac{1 - \eta^*_{(\psi/\phi)_{min}}}{\left[1 - \left(\frac{\psi^*}{\phi^*}\right)_{min}\right]^{3.5}} \left(1 - \frac{\psi^*}{\phi^*}\right)^{3.5}, \quad \frac{\psi^*}{\phi^*} \in \left[\left(\frac{\psi^*}{\phi^*}\right)_{min}, 1\right] \tag{4.41}$$

$$\eta^* = 1 - \frac{1 - \eta^*_{(\psi/\phi)_{max}}}{\left[\left(\frac{\psi^*}{\phi^*}\right)_{max} - 1\right]^2} \left(\frac{\psi^*}{\phi^*} - 1\right)^2, \quad \frac{\psi^*}{\phi^*} \in \left[\left(1, \frac{\psi^*}{\phi^*}\right)_{max}\right] \tag{4.42}$$

Fig. 4.31 shows the generalized stage efficiency curve obtained by using Eqs. 4.41 and 4.42 compared to data obtained from the curve proposed by Howell and Bonham (1950).

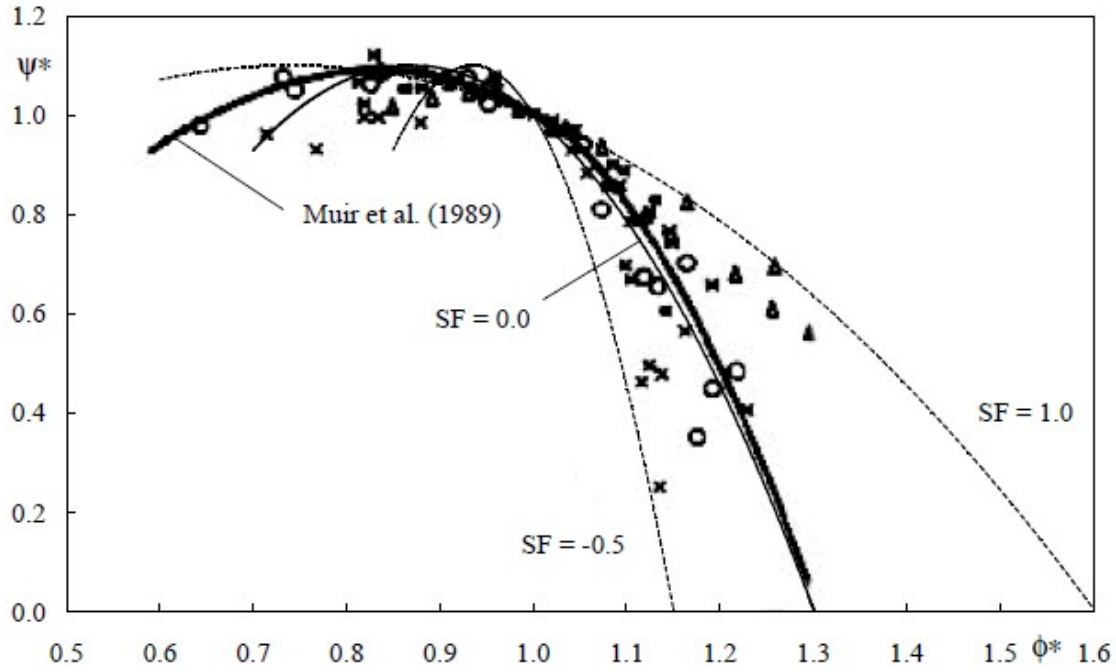

Figure 4.30: Generalized stage characteristics $\psi^* = F_\psi(\phi^*, SF)$ and experimental data points (Muir et al. 1989).

This single curve, together with the curves $\psi^* = F_\psi(\phi^*, SF)$, allows the obtainment of relationships $\eta^* = F_\eta(\psi^*, SF)$ for all types of compressor stages.

Once the generalized stage characteristics are known, the following relationships are used for the stage-by-stage evaluation of the outlet conditions starting from the inlet ones:

$$h(T_{0(i+1)s}) = h(T_{0i}) + U_i^2\,\psi_i = h(T_{0i}) + U_i^2\,F_\psi(\phi_i) \tag{4.43}$$

$$h(T_{0(i+1)}) = h(T_{0i}) + \frac{U_i^2\,\psi_i}{\eta_i} = h(T_{0i}) + \frac{U_i^2\,F_\psi(\phi_i)}{F_\eta(\phi_i)} \tag{4.44}$$

$$\frac{p_{0(i+1)}}{p_{0i}} = e^{[\Phi(T_{0(i+1)s}) - \Psi(T_{0i})]} \tag{4.45}$$

$$\phi_{i+1} = \phi_i\,\frac{U_i}{U_{i+1}}\,\frac{A_i}{A_{i+1}}\,\frac{p_{0i}}{p_{0(i+1)}}\,\frac{T_{0(i+1)}}{T_{0i}} \tag{4.46}$$

By stacking all the "n" stages it is then possible to evaluate: the overall pressure ratio, the overall enthalpy variation, and the compressor efficiency.

Particle-Mixing plane interaction

To date, a number of multistage simulations including discrete-phase presence has been performed. For example, Ghenaiet (2014) studied particle ingestion in a two-stage gas turbine for erosion analysis using a frozen rotor, multiple reference frame model. On the other hand, Yang & Boulanger (2012), Suzuki et al. (2006) tracked particles in frozen flow fields obtained

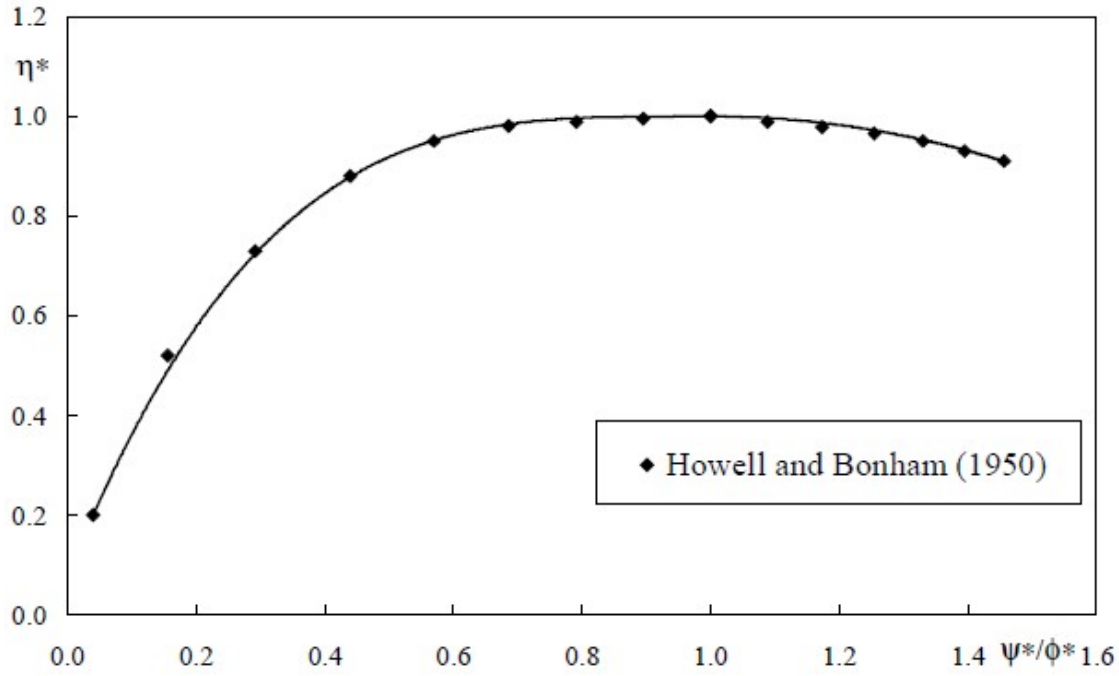

Figure 4.31: Generalized stage efficiency curve (Spina 2002).

from unsteady simulations with a consequent large computational time. In consideration of this issue, Zagnoli et al. (2015) used a mixing-plane interface and studied two different particle averaging techniques: averaged and preserved. The first method broke up the vane exit into radial bands, averaging all the particle properties in each of them and assigning those averaged values to each particle within the respective band. The second method preserved each particle's properties but randomly assigned a new circumferential coordinate. They found that no significant differences are yielded between the two methods.

In the present section, the authors tried to push the investigation forward. Three particle-interface interaction methods have been proposed, comparing their prediction capabilities to a high-fidelity transient simulation based on the sliding mesh approach. The first stage of the high-pressure turbine of the General Electric Energy Efficient Engine (EEE) analysed by Thulin et al. (1982) is considered as the reference geometry. All the simulations have been performed with the open-source software foam-extend-4.1, and efforts have been done to implement an extended interface treatment for Eulerian-Lagrangian simulations. To be more general as possible, the results are presented in terms of particle impact efficiencies on the vane and rotor blade. The aim of this work is to find a particle-mixing plane interaction method suitable to capture the time-averaged behaviour of particle impacts on blade surfaces. This is of crucial importance in particle-laden flows since unsteady calculations typically need a considerable computational effort, and one has often to resort to steady-state simulations to obtain results in an acceptable turnaround time.

The techniques for particle tracking through mixing plane interfaces were implemented

from scratch in the foam-extend software and are readily applicable to any kind of turbomachinery flow.

Geometry and Computational Domain In this study, the first stage of the EEE high-pressure turbine is considered as reference geometry for GT applications. The whole annulus 3D configuration has been modified for exploiting periodicity properties. The actual number of vanes and rotor blades in the experiment (24 and 54, respectively) has been changed to obtain a 1 : 2 ratio (25 and 50). In this way, the simulations could be carried out in a one-vane/two-blade domain. The cooling system was not taken into consideration, so as not to introduce further complexity in the numerical analysis. The computational domain extends one vane chord upstream of the inlet section and one blade chord downstream from the stage exit (see Fig. 3.15). A fully structured hexahedral grid of nearly 3.3 million cells was generated using ANSYS TurboGrid. Furthermore, cell refinement close to the walls has been introduced to resolve the near-wall region according to the selected turbulence model (see below). The growth rate of the prism layers was set in such a way as to provide an average wall $y^+ \approx 1$ and everywhere lower than 5.

Solution methods The numerical resolution of the particle-laden flow starts with the computation of the continuous phase, which is clean airflow without solid particles. This phase was modelled by the Favre-averaged Navier-Stokes equations. The explicit density-based solver *transonicMRFDyMFoam* developed by Borm et al. (2011) was used for the numerical solution. It adopts the *hllc* approximate Riemann solver to compute inviscid fluxes, while the viscous term is treated with a central difference approximation. Second-order accuracy in space is obtained by reconstructing the variables according to the MUSCL approach, with the Van Albada slope limiter. The solver was implemented in the open-source software foam-extend-4.1. For the steady simulations, a *pseudo* time stepping approach combined with a 4-step Runge-Kutta integration was used, while a *dual time stepping* method

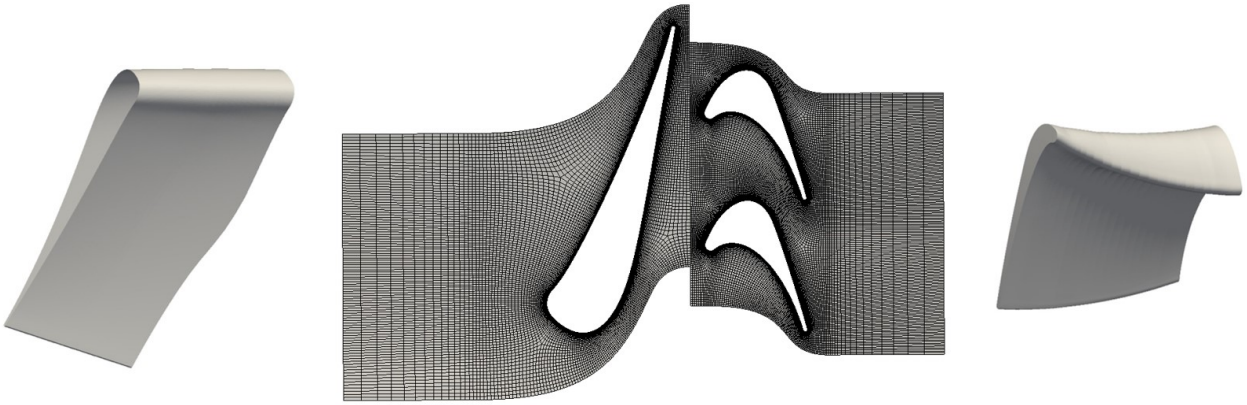

Figure 4.32: Computational domain.

was exploited to solve the unsteady problem. In the unsteady case, second-order accuracy in time was also achieved using three-time levels backwards Euler scheme.

The operating conditions considered for the study reproduce the design point described by the technical report by Thulin et al. (1982). At the inlet of the domain, uniform total pressure and temperature equal to $p_0 = 13.25\,\text{bar}$ and $T_0 = 1633\,\text{K}$ respectively have been imposed. Besides, the turbulence intensity at the inlet of the vane passage has been set to 5 %. The effects of turbulence were computed by the *shear stress transport k-ω* (SST) model, either for the steady (RANS) or unsteady (URANS) framework. A temperature of $T_{wall} = 1100\,\text{K}$ has been imposed at the domain walls to approximate the coolant injection effect. Finally, the static pressure of $p = 2.75\,\text{bar}$ has been set at the outlet of the domain, in order to guarantee an absolute isentropic exit Mach number of 0.52 as reported in the technical report. For steady calculations, the mixing-plane approach has been used. This has been implemented in foam-extend software by Jasak & Beaudoin (2011) as an evolution of the Generic Grid Interface (GGI). Since the purpose of the paper is to compare several types of treatments of solid particles at the mixing-plane interface, the authors have chosen a transient simulation as a high-fidelity reference for the comparison. The sliding-mesh approach makes use of an overlapGGI interface to preserve fluxes between the two rows. In this way, the transient interaction between the stationary and rotational domains is accounted for.

Once the flow field was solved, particles were seeded from the inlet of the domain with a uniform distribution. Aware of the large variety of solid particles that can enter the engine, the authors have chosen the Arizona Road Dust (ARD), which is one of the most common and tested in the literature, see Reagle et al. (2014). The choice was guided by considering the possible reproducibility of the results in experimental test rigs and maximizing the generalization of the outcomes. The particle size distribution has been divided into 8 discrete sub-diameters starting from 1 μm and growing with a power of two until 128 μm. The amount of particles injected is derived with the aim of obtaining a statistically meaningful representation of the impacts. A number of 100,000 particles for each diameter has been chosen by the authors. Particle trajectories were computed by integrating the Basset-Boussinesq-Oseen (BBO) equation for each of them. The only relevant force to be kept into account is the drag since other forces are at least one order of magnitude smaller, as suggested by Rispoli et al. (2015). For steady-state simulations, particles are tracked in a relative reference of frame and centrifugal and Coriolis non-inertial forces are added to the equation of motion. The magnitude of these forces is set to zero in the statoric domain, while in the rotating part they are respectively defined as

$$\mathbf{F_{centr}} = -m_p \boldsymbol{\Omega} \times \boldsymbol{\Omega} \times \mathbf{r_p} \tag{4.47}$$

$$\mathbf{F_{Cor}} = -2m_p \boldsymbol{\Omega} \times \mathbf{v_p} \tag{4.48}$$

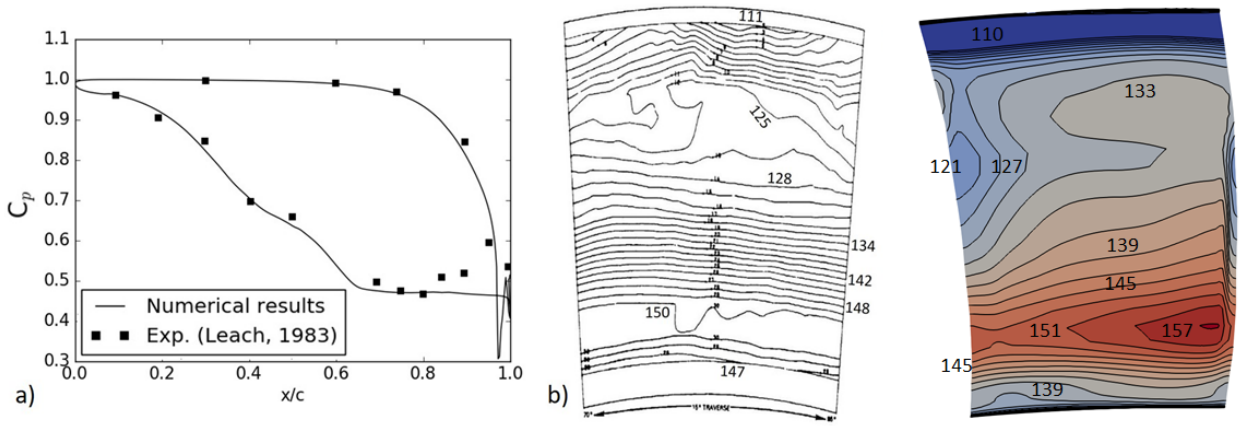

Figure 4.33: Numerical validation results: C_p evolution along the mid-span a) and rotor exit flow angles b).

where $\mathbf{\Omega}$ is the angular velocity of the rotating frame. The maximum particle volume fraction is small enough to model the interaction between particles and fluid flow with the one-way coupling, according to Elghobashi (1994). Particles are tracked through the domain until they escape from the outlet. The impact behaviour was modelled using the rebound model proposed by Reagle et al. (2014), where normal velocity and impact angle are used to compute the restitution coefficients. Finally, to account for the effect of turbulent dispersion on particles, the Discrete Random Walk Model of Gosman & loannides (1983) has been used.

Flow Field Validation The technical report by Leach (1983) was taken as a reference for either vane or rotor validation. Concerning the vane, the pressure coefficient C_p has been adopted to compare the numerical results to the experimental ones. The outcome of the comparison is reported in Fig. 4.33 a). In this figure, the C_p profile along the vane mid-span from the steady mixing plane simulation is depicted. As can be seen, good matching has been reached for this section, even if some difference is present at the trailing edge. Regarding the rotor, no blade pressure measurements are available in the test report. To overcome this issue, the validation of the blade was conducted by comparing the exit flow angles at the outlet of the domain. The results are reported in Fig. 4.33 b), where labels have been added to the original experimental contours to ease comprehension. As can be noted, the general spanwise trend and contour shapes of the experimental measures are captured by the steady-state simulation. Moreover, the same solver *transonicMRFDyMFoam* was also validated elsewhere (see Borm et al. (2011)) and has been used to perform both steady as well as transient computations. For this reason, the solution is considered validated also for the unsteady case.

Discrete-Phase Treatment at the Interface The main purpose of this work is to compare three particle-mixing plane interaction models to a high-fidelity transient simulation.

Novel particle-interface support has been implemented in foam-extend, allowing the passage of particles through different kinds of coupled interfaces such as mixing planes and GGIs. The particle passage through interfaces hinges upon the face addressing between the two coupled sides. Therefore, there is no preferential crossing direction of the interface, making the algorithm robust with respect to separation bubbles and reverse flows between the blade rows. Besides, three types of discrete-phase treatments at the interface have been introduced in the computational routine, as will now be shown. The chosen techniques are based on different easiness of implementation and physical soundness:

- no redistribution (noRed): no particle redistribution and no particle velocity changes through the mixing plane interface (frozen rotor-like model);
- circumferential redistribution (crcRed): particles are circumferentially redistributed along the interface, but no particle velocity changes occur through the mixing plane. Here, the particles approaching the interface will be redistributed randomly inside each of the stripes created by the mixing plane algorithm;
- circumferential redistribution with new velocity value assigned (crcVelRed): particles are circumferentially redistributed after the mixing plane (like in the crcRed), and the velocity of each particle is set equal to the mixed-out fluid velocity in the rotating frame of reference of the correspondent stripe;

noRed and crcRed have already been used in the previous frozen rotor and mixing plane simulations, while crcVelRed is a new type of model, aiming to simulate a full mixed-out state, where particles are at the equilibrium with the surrounding fluid. Once they cross the interface, particles are tracked into the relative frame of reference of the blade domain using the relative velocity. Since for GTs deposition and erosion are the most dangerous consequences of particle ingestion, the distribution of the impacts on the wall surfaces was chosen as the reference parameter for the comparison.

Regarding the unsteady simulation, a sliding mesh approach is used and particle trajectories are tracked in a continuous manner across the interface. The complete transient particle-laden flow through the entire stage has been computed with a pretty fine time step of 10×10^{-7} s. This was necessary to provide accurate particle trajectory all the way through the domain, due to the importance of mesh motion effects.

Impact efficiency Results The first parameter the authors considered is the impact efficiency (η_{imp}), that is the number of impacted particles over the total particles injected for each diameter. Impact efficiencies for the three explored methods against the particle diameter have been reported in Figure 4.34 for either the vane or the blade. As can be seen, in both cases there are efficiencies greater than one. This is due to particles that

impact walls more than once, leading to a total count of impacts greater than the total amount of particles injected. Concerning the vane surface, Figure 4.34a) shows extremely good agreement between the various types of redistribution. This is expected since the only difference in vane impacts is due to the larger particles that rebound from the blade row back to the statoric row. These particles interact twice with the mixing plane: once when they cross the interface forward and once backwards. This effect causes slightly different impacts for very large particles, as can be noticed for 64 µm and 128 µm diameters in Fig. 4.34a). The authors noted that the trend shown in this figure is similar to the one reported in the experiments of Liu & Agarwal (1974*b*), where turbulent deposition in a straight pipe was caught. As in the experiments, also here three different regimes such as diffusion ($d_p <$ 2 µm), diffusion-impaction (2 µm $< d_p <$ 8 µm) and inertia-moderated ($d_p >$ 8 µm) can be highlighted (Forsyth et al. (2016)). These three regimes distinguish three different physical mechanisms of impact, which hinge upon particles' inertial characteristics (the larger the inertia greater the impact efficiency). On the other hand, the rotating component presents a more complex behaviour compared to the stationary one. As can be noted in Fig. 4.34 b), the rotor is very sensitive to the specific technique used for the interface treatment. Analyzing the different effects of redistribution and mixed-out fluid velocity assignment, the authors found a sort of threshold point (see Figure 4.34 b)): when the particle diameter is less or equal to 8 µm (diffusion regime), crcVelRed, crcRed and noRed lead to similar impact efficiencies; When particles diameter is greater than 8 µm (inertia-moderated regimes), the results of the crcRed and noRed tend to follow the same trend, while the crcVelRed shows significant differences as the diameter increase. Therefore, from a global-impacts count

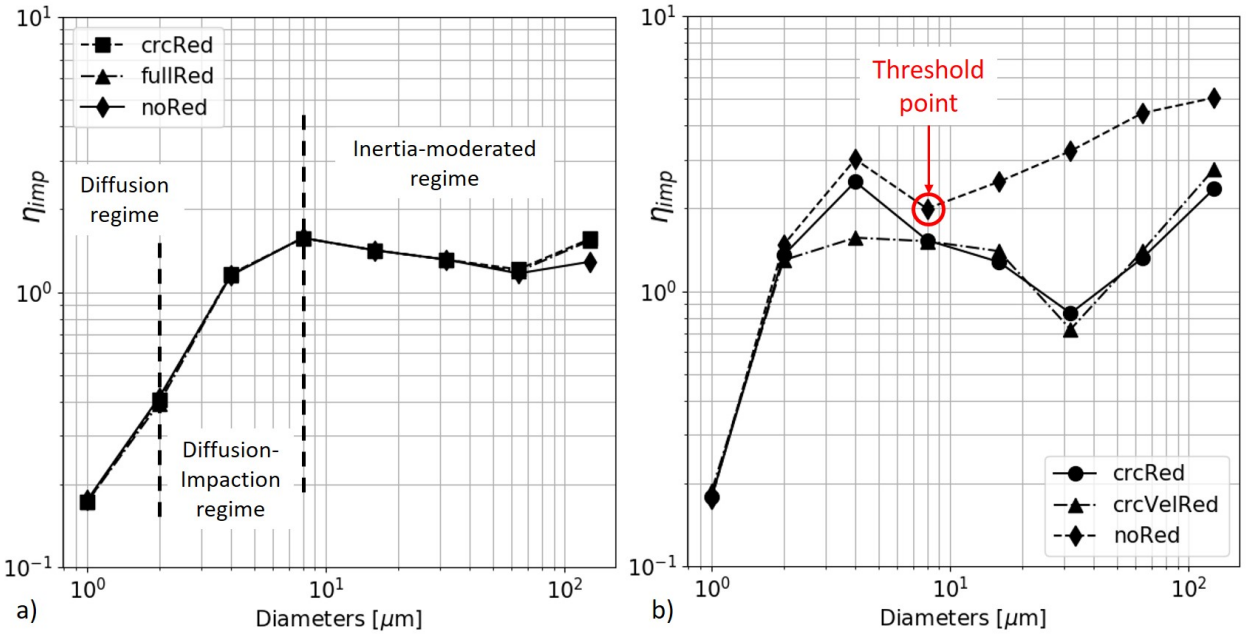

Figure 4.34: Impact efficiency evolution along vane a) and rotor b) varying the particle diameter.

perspective, the velocity of the particles downstream of the mixing plane becomes the most important factor affecting their behaviour when inertial properties become important. On the other hand, very small particles will rapidly settle to fluid velocity, and therefore the preservation or not of their velocity across the interface has not a major effect.

Impact areas Since the impacts on stationary components were not appreciably influenced by the interface treatment, major attention has been paid to the rotating component for the analysis of impact areas.

In Fig. 4.35 the comparison of the three different discrete-phase treatments at the interface has been reported. Particles diameters have been grouped into three ranges: 1-4 µm, 8-32 µm and 64-128 µm. In the figure, pictures laying in the same column have been subjected to the same treatment, and pictures laying in the same row pertain to the same particle diameter range. It is worth noting that particle impacts with the noRed technique will necessarily show a dependency on the vane-blade clocking. For this reason, both blades are reported in the corresponding column. When redistribution is applied, this dependence vanishes leading to the same impact areas for the two blades. As can be seen, when small particles are injected, impacts count and areas do not change significantly (first row). Naturally, this consideration holds true for the average impacts between the two blades in the

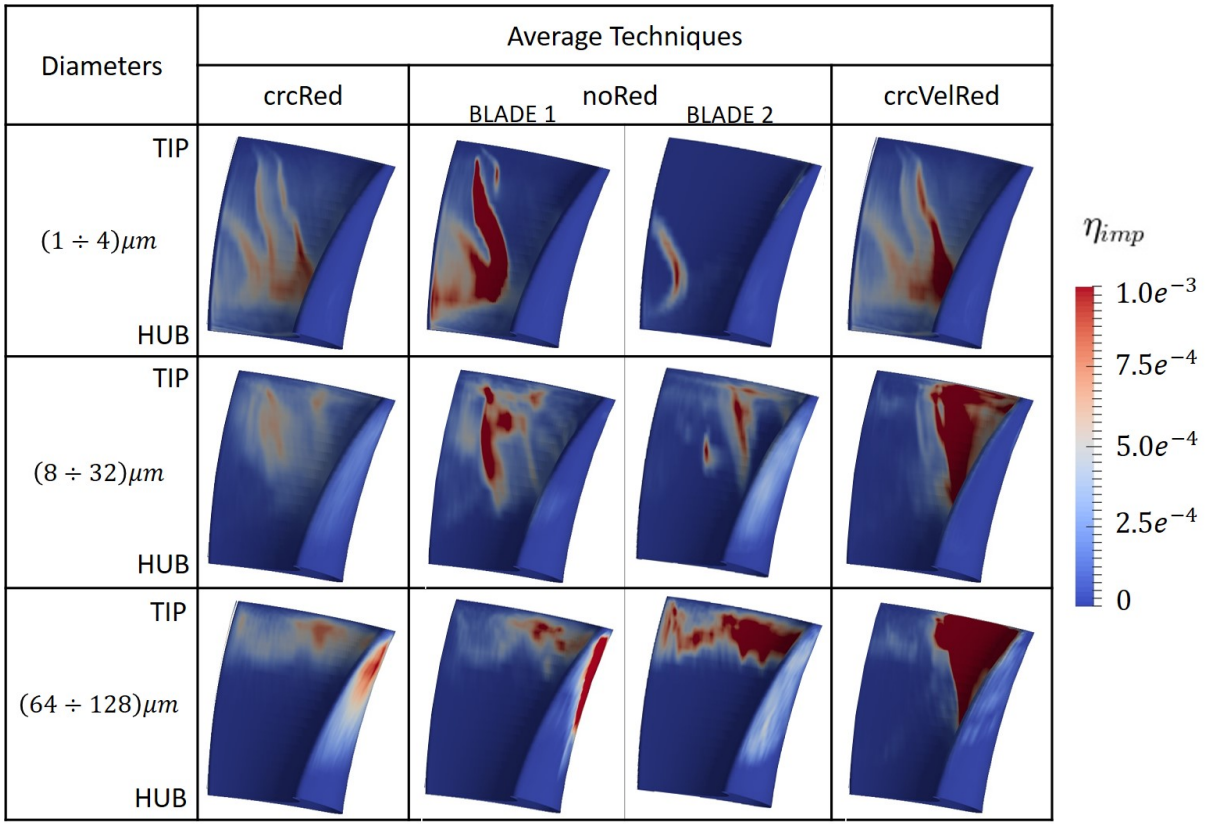

Figure 4.35: Impact areas on blade surface. View downstream; LE and suction surface shown on right hand side in lighter shade.

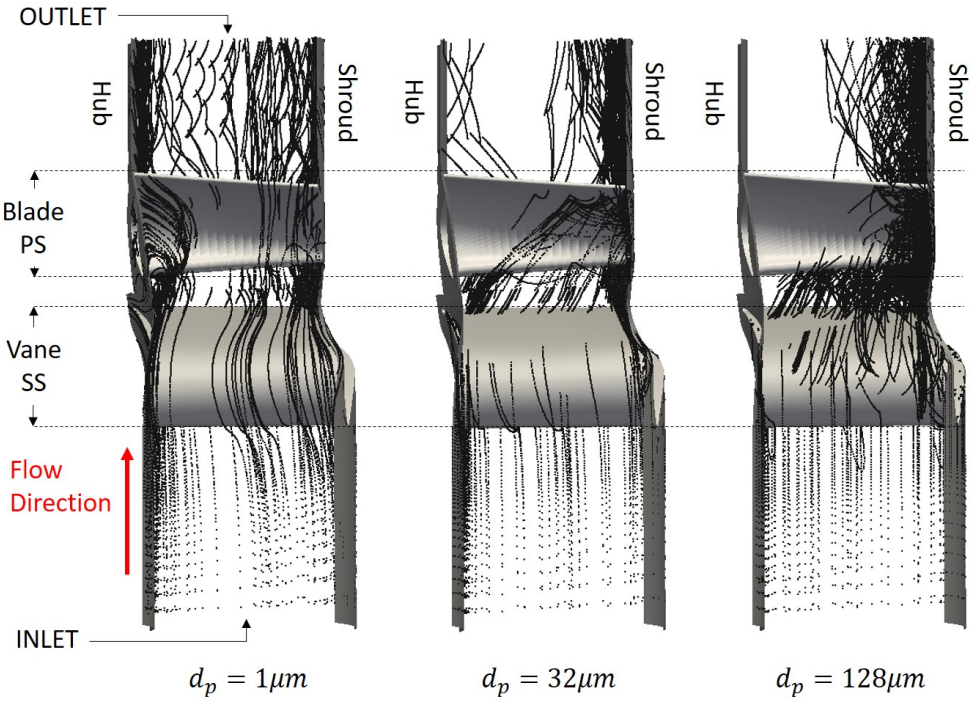

Figure 4.36: Particles trajectories through the domain varying particles diameter.

noRed case. On the other hand, when diameter increases, impact efficiency magnitudes and areas change between the different methods. Specifically, while crcRed and noRed find agreement in terms of impact efficiency and patterns, crcVelRed seems to over-predict both the characteristics (larger areas and impacts). Again, this difference between the proposed techniques is mainly due to the velocity of particles downstream of the interfaces. When the crcVelRed method is used, all the particles lying on the same strip are given the same velocity (the corresponding mixed-out fluid velocity in the strip) and their trajectory is significantly modified. Indeed, when the velocity is maintained across the interface, larger particles will have a negative incidence angle relative to the rotor blade. As noticed also by Tabakoff et al. (1991), this is due to the fact that the acceleration of bigger particles in the stator is not as high as for the smallest ones, thus strongly reducing the incidence direction of particles approaching the blade row. This effect is wiped out when crcVelRed is applied because particle velocity at the inlet of the rotating component is forced to be equal to fluid velocity. Besides, it can be noted also that as the particle diameter increases, the impact zones shift toward the tip area of the blade due to the centrifugal effect. This result has been also found by Tabakoff et al. (1991), where the effects of particle size on a turbine stage have been studied. As in the present work, they noticed that larger particles undergo a greater amount of impacts with the blade surface. Moreover, large particles centrifuge faster after they impact the rotor blade suction surface near the leading edge, as shown in Fig. 4.36 where the trajectories along the domain in the noRed case have been reported as an example.

Consider now the influence of the vane wake on the particle distribution at the interface. Since the flow is far from being uniform at that area, the redistribution forces the particles to spread uniformly in the circumferential direction. To illustrate this effect, the distribution at the vane interface for the noRed case is reported in Fig. 4.37, where dashed lines are introduced to highlight the wake region. As can be seen, smaller particles (1 µm) have a more span-wise uniform distribution, while medium-sized (16 µm) and larger particles (128 µm) tend to gravitate towards the wake, heavily influencing their position on the interface. These results are useful to understand how strong the hypothesis behind particles redistribution at the mixing-plane is. Anyway, this doesn't mean that such a technique is not able to capture the average effect over one blade passing period.

Steady and transient comparison In this section, the comparison between the transient simulation and steady-state results has been reported. Similarly to the previous section, the trend of the global impact efficiency function of particle diameters has been firstly analyzed. Since no significant difference has been found for the impacts on the vane due to the low degree of unsteadiness in the statoric row, the results are here reported only for the rotating cascade. In Fig. 4.38 the outcomes are presented by means of the percentage difference in the impact number on the blades between each of the steady-state simulations and the transient results. Of the three techniques proposed, the crcRed is the one that best describes the average behaviour of the particles through the interface between the stationary and the rotating component, thus representing the analogue of the mixing-plane theory of continuous flows applied to the discrete phases. As can be noted, the impact efficiencies of the crcRed are within a 20% difference relative to the transient ones everywhere except for the smallest particles ($1\mu m$). For this diameter, the impact number is more than doubled with respect to the steady simulation. This discrepancy is also present for the other two methods (noRed

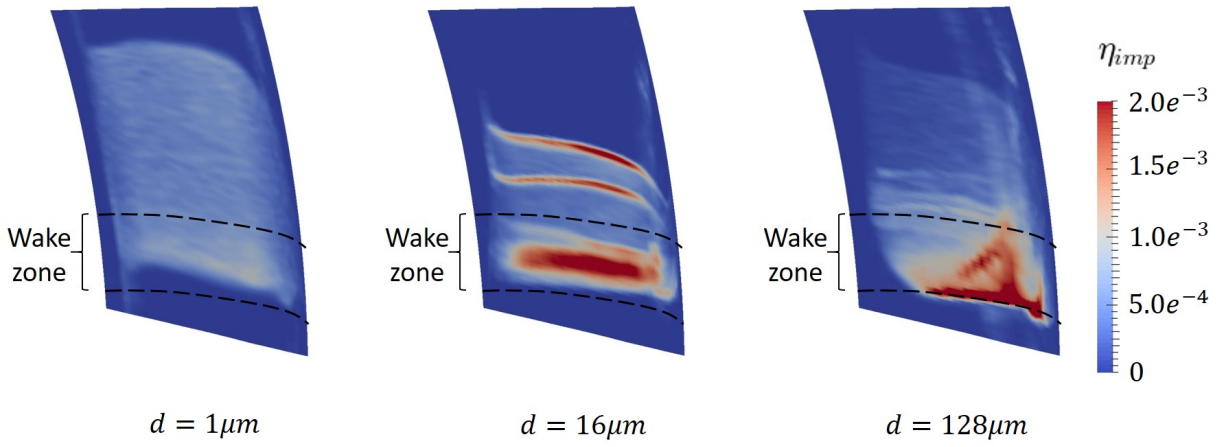

Figure 4.37: Impact efficiency on the interface for small (1 µm), medium (16 µm), and large (128 µm) diameters.

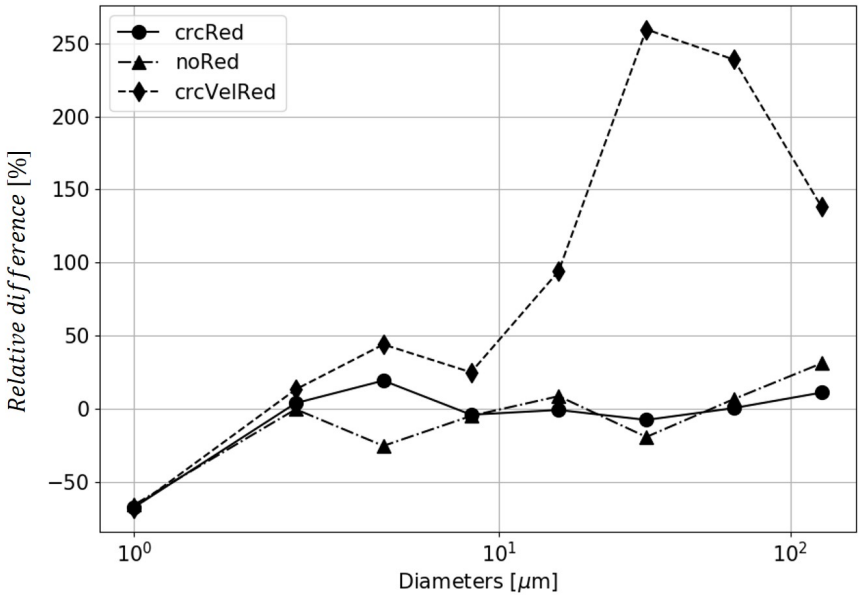

Figure 4.38: Relative difference between transient and stationary impact efficiencies

and crcVelRed), which are less accurate in reproducing transient results. This result is somewhat in contrast with the findings of Prenter et al. (2017), who stated that impact efficiency for smaller diameters is better captured with the crcRed. This disagreement can be due to the different geometry and operating conditions of the component considered as a reference. Furthermore, this pattern is attributed to the unsteady effects of the wakes and rows interactions, which are propagated in transient simulations and cancelled in the steady ones. Indeed, the trajectory of the smallest particles that gravitate in the wake and low-velocity regions is significantly affected by the unsteady transport operated by the continuous phase. On the other hand, larger particles are less influenced by the fluid drag, and their time-averaged behaviour is well captured by the evening-out effect pertaining to

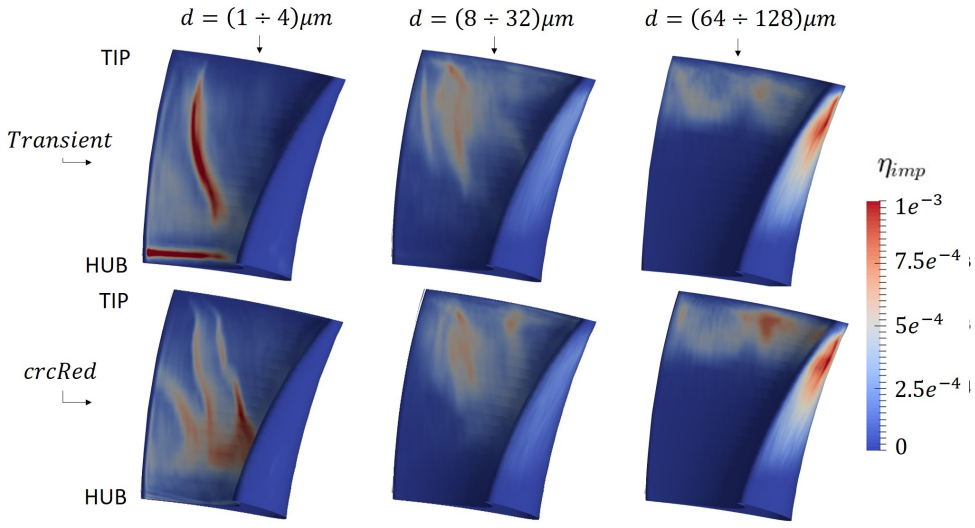

Figure 4.39: Comparison between impact areas on the blade of transient and crcRed simulations

the circumferential redistribution (crcRed). To have also local results from the comparison, impact areas of transient and crcRed simulations have been analyzed. For this purpose, the same diameter intervals used for the comparison in the previous section have been kept. The outcomes are reported in Fig. 4.39. As can be seen from the figure, the impact pattern is closely related for the two frameworks, although some remarkable differences are present for lower diameters. In the transient computation, highly localized impact zones appear in proximity of the blade hub, which are not captured by the crcRed computation. The authors impute these discrepancies to the capability of the transient simulation to capture complex unsteady interactions between vane and blade wakes and secondary flows. Such a feature reflects on low-inertia particles, whose impacts are governed by diffusive effects in proximity of solid walls. Indeed, an accumulation of these particles in the rotor hub region was found in the unsteady simulation causing the greater number of impacts.

Application to a Real Turbomachinery

With the ingredients exposed, it is possible to estimate numerically the Melino's coefficients in order to obtain the computational results to enrich the dataset to train the machine learning algorithm. Specifically, with the use of the mixing plane with particle tracking integration, the deposition/detachment model, and the microscale model, one can obtain the deterioration curve of the first stage. With this, by using the stage-stacking strategy, the degraded performance of the whole compressor can be obtained.

In this final section, the application of the first part of the methodology (mixing plane, deposition/detachment model, and microscale model) to the Allison 250 C18 is shown. In particular, the analysis will be focused on the comparison between the experimental and computational deposit areas.

Geometry and Computational Domain The compressor geometry is reconstructed through a reverse engineering procedure. The geometry reconstruction of the real components is performed by means of a laser scanner. At first, a three-dimensional (3D) polygonal geometry of the actual geometry is obtained by interpolating the point cloud derived from the laser scanner by means of POLYWORKS V12 software. A 3D model is then obtained and exported to the solid modeller SOLIDWORKS 2015 through an interchange file format (Aldi et al. 2018). A sketch of the computational domain for the compressor is shown in Fig. 4.40. As can be seen, the computational domain consists of eighteen fluid domains: ten stationary domains (inlet duct, stators, and outlet duct) and eight rotating domains (rotors).

The grid used in the calculations is a hexahedral grid with a total number of 1116895 elements. The grid is realized by employing an O-grid around both the rotor blade and the stator vane, with local refinements near the hub and shroud regions. Rotor tip and stator

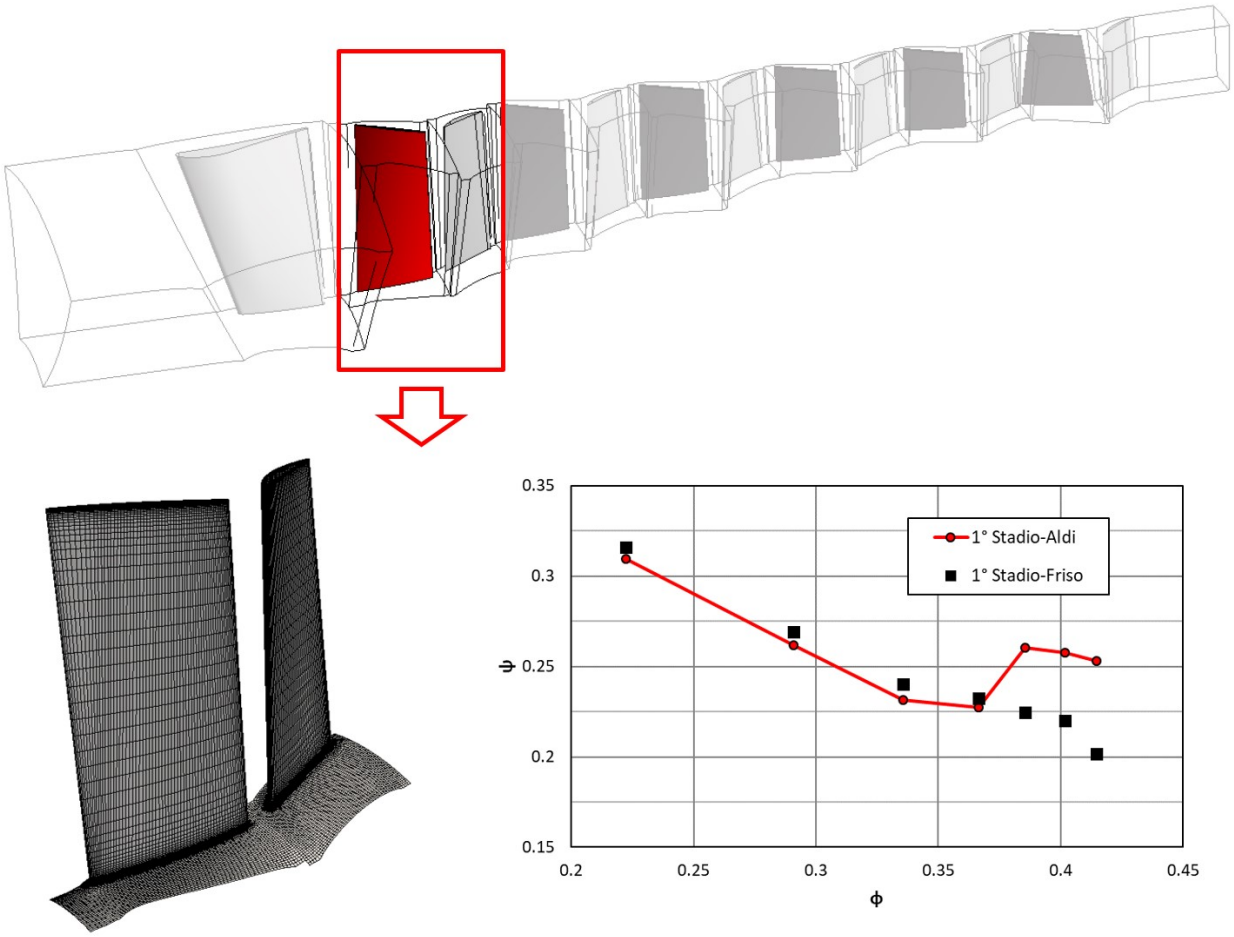

Figure 4.40: Computational domain (top), first stage mesh (bottom left), and flow field validation (bottom right) for the axial sections of the Allison 250 C-18 compressor.

hub clearances are resolved with 4 nodes across the gap span. The meshes on the rotor blade and the stator vane are shown in Fig. 4.40. The first grid points on the rotor blade, stator vane, and end walls are positioned in such a way that the y^+ values range from 1 to 8.

Solution methods The numerical simulations are carried out by means of the open-source CFD code foam-extend-4.1. The explicit density-based solver *transonicMRFDyMFoam* developed by Borm et al. (2011) was used for the numerical solution. The operating conditions considered for the flow field validation reproduce the design curve of the Allison 250 C18, that is the one at 6054 rpm. The validation was performed against the numerical results obtained by Aldi, Morini, Pinelli, Spina, Suman & Venturini (2014), who validated the CFD of the whole compressor against experimental results. To validate the first stage only, in this work the data resulting from the simulations of Aldi, Morini, Pinelli, Spina, Suman & Venturini (2014) for the first rotor/stator was considered as the reference. The outcomes obtained in terms of ψ versus ϕ are reposted in Fig. 4.40. As can be seen, a really good agreement can be recognized, especially at the lower mass flow rates. Nonetheless, when the simulation approaches the choking area, a discrepancy occurs. The author assigns these

dissimilarities to the fact that, in the simulations conducted here, the IGV was not modelled, hence the inflow conditions were not exactly the same as in the reference work. Moreover, only the first stage was simulated, hence the influence of the subsequent stages was not taken into consideration, which was instead considered in the reference work. Besides the discrepancies, the author considers the flow field, hence the numerical setup, satisfactorily validated.

For the simulations conducted to analyze the deposition, the idle conditions tested during the deposition tests were considered instead of the design conditions. This means that the rotational speed of 20 000 rpm was imposed in the numerical setup. Uniform total pressure of $p_0 = 101\,325$ Pa and uniform total temperature of $T_0 = 298.15$ K have been assumed at the inlet, whereas a mass flow rate has been set at the outlet of the domain. The latter was varied in order to span the operative range of the compressor, in order to create the performance curve. Ones the flow field reached convergence, particles were seeded from the inlet of the domain, with the diameter distribution reported in Fig. 4.26a), that is for the ARD N contaminant.

Rotor/Stator Interaction Model The simulations are performed in steady multiple frames of reference, taking into account the contemporary presence of moving and stationary domains. In particular, a mixing plane approach is imposed at the rotor/stator interface (which is located halfway between the two components) and used for all the simulations. In this approach, a single-pass steady-state solution is calculated, exchanging the flow field variables at the interface. Flow field data are averaged circumferentially for both frames at the interface and passed to the adjacent zone as boundary conditions. This spatial averaging at the interface removes any unsteadiness generated in the zone-to-zone flow field, but the resulting solutions are often reasonable approximations of the time-averaged flow field. The particles through the interface were modelled by means of the *crcRed* explained in the previous section.

Comparison against the Experimental Results The new deposition/detachment model, the microscale model, and the mixing plane integration already introduced in this thesis are now together used with the purpose of replicating one of the experimental outcomes reported in Sec. 4.5.1. Specifically, the ARD N at 80 %RH was the configuration selected, since it was recognized to be the one that most fouled the compressor used. As already reported, at the end of each experimental test, the axial part was disassembled and pictures of the fouled parts (IGV, axial stator and rotor) are taken. The ones related to the configuration chosen are reported in Fig. 4.41.

Based on that, the simulations conducted had the purpose of replicating the experimentally found fouled areas. The results obtained are reported in Fig. 4.42, where the deposit

patterns found after 4 hours of test on the stators and the rotors are depicted in yellow.

From the figure, it can be recognized an extraordinary agreement between the deposition patterns, especially considering that only the first stage of the machine was simulated. In particular, a strong agreement can be identified for both the pressure side and the suction side of the rotor. Only the deposit towards the tip was not well replicated for this component. Besides, also the pressure side of the stator was moderately well predicted by the numerical model. The only part that was badly reproduced is the suction side of the stator. The authors think that the latter is mainly guided by the non-accurate prediction of the corner separation in the vane. This was also found in other works (Casari et al. 2020) and also in a previous study of the author (Friso et al. 2022).

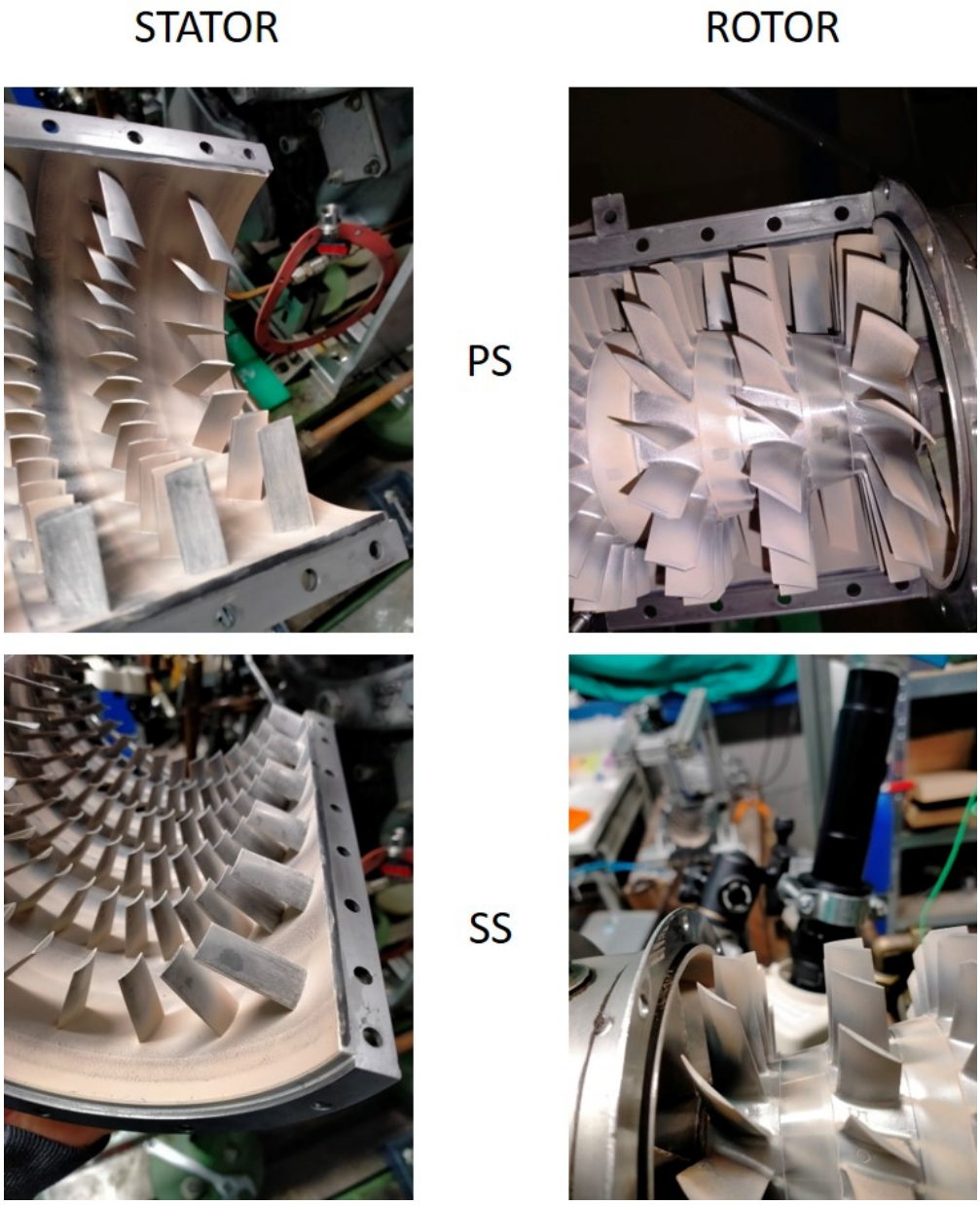

Figure 4.41: Picture of the compressor after 4 hours to ARD N exposition.

4.6 Conclusion and Remarks

In this chapter, a strategy to predict the compressor fouling impact on an aircraft mission has been proposed. A mission analysis model integrated with a gas path is used for this purpose. The main problems that have to be faced in order to obtain an applicable tool for predictive maintenance have been faced, and two different strategies were proposed. Specifically, a multi-fidelity machine learning algorithm trained by both experimental and numerical outcomes was suggested. The procedure for conducting the experimental tests was exposed, and all the ingredients to perform the numerical simulations were reported. The computational strategy was also applied to the compressor used for the experimental tests, finding a really good agreement between the predicted and the experimental outcomes.

Besides that, many steps have to be made to reach a good predictive maintenance tool.

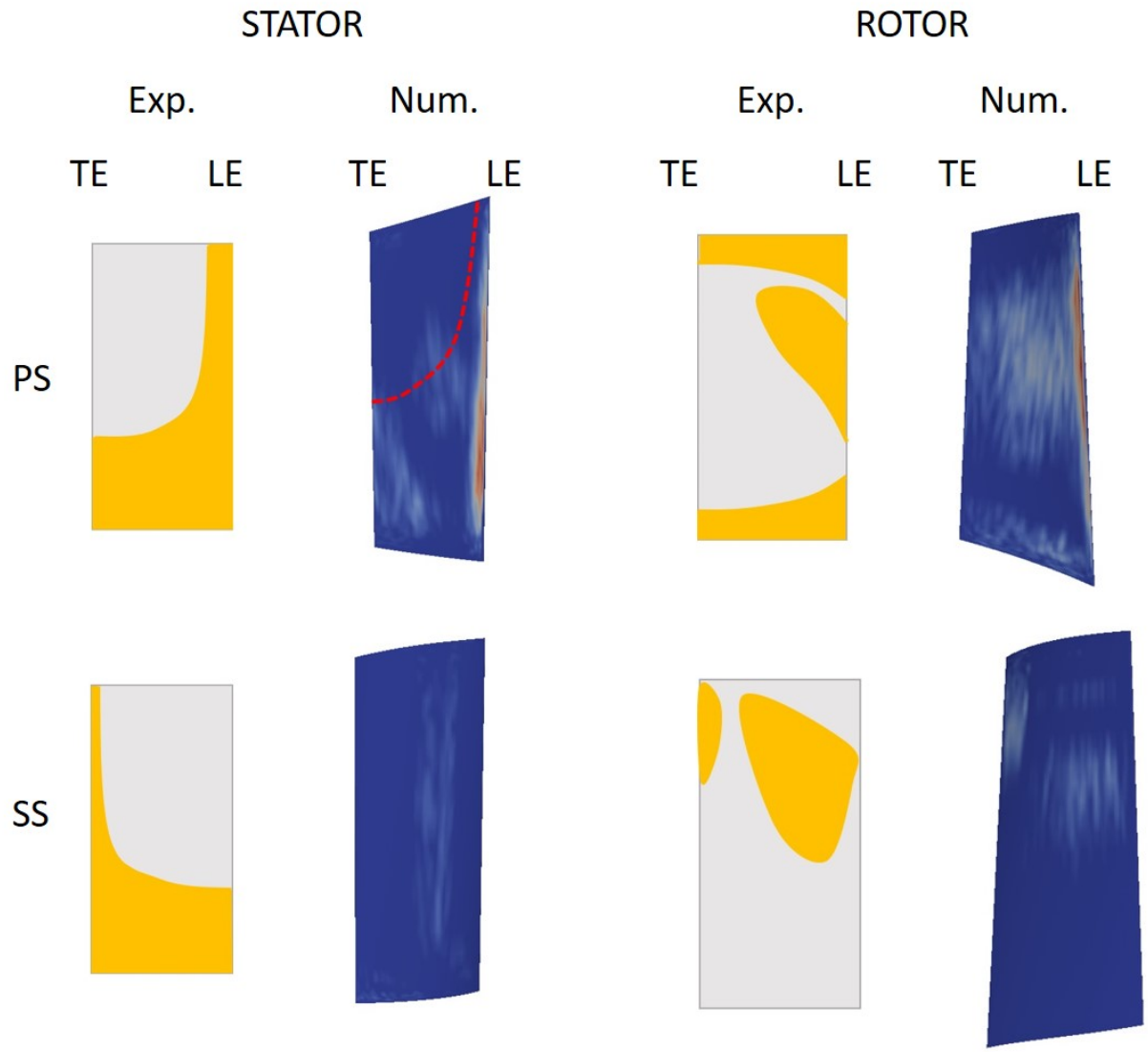

Figure 4.42: Comparison between experimental and numerical deposition pattern on the Allison 250 C18 after 4 hours of exposure to ARD N at 80 %RH.

One of them consists of the finding of the best multi-fidelity machine learning technique capable to fuse both experimental and numerical results and giving adequate degradation coefficients. Another limitation is related to the contaminant characteristics. In this study, only ARD was considered as the contaminant, but many others have to be taken into consideration, such as the carbon black or the soot for example. A method to incorporate the contaminant properties in the proposed strategy is of main importance to make it more general and applicable.

Chapter 5

Fouling Induced Emissions Prediction

In this chapter, the author wants to suggest an application in the field of emission prediction, that nowadays is considered a very big deal, of the digital twin proposed in the previous chapter. Only a first step towards this kind of application was conducted, hence several hints will be proposed in order to deeply face the problem. Firstly, a review of the emission policies present in the present days will be presented. After that, a strategy to forecast the carbon price will be shown. In the second step of the research, which the author will leave to future researchers to develop, several methodologies to model the combustor of a gas turbine will be exposed. The purpose is the integration of one of them into the already conceived digital twin, and then use it to estimate the emissions of a whole aircraft mission, thus its costs.

5.1 Aviation and the EU ETS: an overview and a data-driven approach

Mitigating the environmental impacts of civil aviation is undeniably one of the most difficult challenges for sustainable transportation researchers. The sector accounts for roughly 2.5% of global CO_2 emissions plus non-CO_2 effects, which may amount to 2/3 of the total net radiative forcing (Lee et al. 2021). The reasons behind the complexity of this issue are many: the difficulties related to restraining aviation activity due to its importance in connecting nations in a globalized world; technical barriers, industry structure, and its lobbying capacity (Efthymiou & Papatheodorou 2019); the fact that the connection between aviation and climate change has been de facto ignored by media and institutions for a long time (Gössling 2020); the issue of replacing kerosene with SAFs (Sustainable Alternative Fuels) which is an extremely challenging process, as some of these alternative fuels may actually generate worse impacts than traditional fossil fuels (O'Connell et al. 2019) whereas other sustainable alternatives have production costs that are up to ten times higher than traditional jet A-1 kerosene and require substantial policy measures to stimulate market uptake and bring down

production costs.

In order to tackle aviation's CO_2 emissions, the European Union adopted in July 2008 Directive 2008/101/EC that included the aviation sector under the umbrella of the European Union Emission Trading System (EU ETS). The EU ETS is a transboundary cap and trade scheme established in 2005 designed to fight climate change in a way that is both economically efficient and legally rigorous (Borghesi et al. 2016). The system entitles the EU Commission to set a yearly EU-wide cap of emission allowances that correspond to equivalents of CO_2 metric tons. Allowances are allocated within the EU and the economic actors subject to the scheme's application have to monitor and report their greenhouse gases (GHG) annual emissions in order to surrender every year a number of allowances equal to their emissions produced in the previous year. These economic actors may comply with this obligation by improving their environmental performance (i.e. cutting their GHG emissions) or by buying the allowances on the related auctioning and trading market. Currently, two types of emission allowances are used, EUAs (European Union Allowances), and EUAA (European Union Aviation Allowances). Until 2020, aviation was allowed to submit both types of allowances to comply with the regulations, whereas stationary sources were bound to EUAs.

Aviation was effectively incorporated in the EU ETS on the 1st of January 2012 and required all airlines departing or arriving at an EU airport to surrender allowances covering the emissions of all EU flights they had operated in a given year. Until at least 2020, all flights from or to European airports were envisaged to be included in the scheme, apart from a few exemptions. However, following an international outcry and in order to ease ongoing negotiations at the International Civil Aviation Organization (ICAO) where carriers were negotiating a global mitigation mechanism, the European Union decided to limit the coverage of the EU ETS to emissions from internal flights within the European Economic Area (EEA) (i.e. flights departing and arriving at an airport in the EEA) for the period from 2013 to 2016 (the so-called "stop-the-clock" decision - Decision no. 377/2013/EU). When minimal progress was made at ICAO's 38th assembly in October 2013, the clock was stopped again. In 2016, ICAO managed to agree on a global measure, CORSIA (the Carbon Offsetting and Reduction Scheme for International Aviation), and the Commission proposed to extend the exemption indefinitely, pending a review of the effectiveness of the scheme. The co-legislative process eventually settled on an extension until 2024, when further details about CORSIA and its alleged efficacy will be known. CORSIA's structure and functioning will not be discussed in this paper; for our purpose, it is sufficient to note that there are serious questions about the scheme's effectiveness in terms of emission reduction (Gössling 2020, Scheelhaase et al. 2018, Larsson et al. 2019).

The capability of the EU ETS to reduce CO_2 emissions depends greatly on the number of allowances issued every year. For the aviation sector, from 2013 until 2020, the total quantity

of allowances allocated to aircraft operators is limited to 95 percent of the average historical aviation emissions of the years 2004–2006 (so-called overall "cap"). Aircraft operators have the option to use up to 15% of the auctioned allowances from the greater pool of EUAs; from those traded by other aircraft operators (European Union Aviation Allowances, EUAAs); and from other eligible international projects (limited to a maximum of 1.5% of the annual verified emissions). Regarding the allocation method, the Directive states that 82% of allowances are allocated for free to aircraft operators while 15% is allocated through the auctioning system (the remaining 3% go to a special reserve for later distribution to new entrants and fast-growing airlines). The actual allocation of allowances is scaled down from 2013 to 2023, to take account of the temporary reduction of the scope of the EU ETS to flights between airports in the European Economic Area ("stop-the-clock"). The fact that the majority of allowances are freely allocated to the aviation sector is one of the main reasons for the so far negligible economic and environmental impacts of the scheme that will be highlighted in the subsequent literature review.

The second fundamental variable for the scheme's effectiveness is the allowances' price level. This price is determined at primary auctions based on relative demand and supply. After an initial period of low prices (around 5€ from 2012 to 2017) allowance prices have constantly increased. This rising trend is the result of several policy measures introduced to stabilize allowance prices and create greater market tightness, such as delaying auctions (the so-called "back-loading"), and introducing mechanisms designed to avoid a surplus of allowances and improve the system's resilience to shocks (market stability reserve). Moreover, since 2020, prices have risen exponentially mainly because of the introduction of increasingly stringent climate change policies in the EU and globally alongside various changes in ETS market design. As of July 2022, the price of an EU ETS allowance has risen to around 85€. Nevertheless, in order to bring the sector in line with the goals of the Paris Agreement much more action by regulators is required, inside and outside of the EU ETS.

In July 2021, the European Commission presented a legislative package designed to meet its medium-term environmental objectives (a 55% reduction of GHG emissions by 2030 compared to 1990 levels) known as "Fit for 55". Aviation is directly involved in three of these legislative proposals: the revision of the Energy Taxation Directive with the introduction of a jet fuel tax for intra-EU flights; the ReFuelEU Aviation initiative, introducing a blending mandate for SAFs; and the revision of the EU ETS for aviation. For reasons of space and clarity, this paper will focus only on the third legislative proposal.

The European Commission proposed a strengthened EU ETS for aviation, with a progressive phase-out of the free allowances allocated to aircraft operators from 2024 to 2026 by respectively 25%, 50%, and 75%, and a complete phase-out from 2027 onwards (with full auctioning); in addition, the annual linear reduction factor of EUAAs will be almost doubled,

moving from 2.2% to 4.4%. Regarding the coexistence of the scheme with CORSIA, the EU ETS would continue to apply to intra-EEA flights as well as flights to the UK and Switzerland, exempting those flights from CORSIA. For other international flights, EU airlines would be obliged to apply ICAO's scheme. On the 8th of June 2022, the European Parliament adopted an even stronger position on the matter, proposing a full phase-out of free allowances as early as 2025 and a return to a "full-scope" ETS (covering all flights departing from EU airports regardless of their destination). The European Parliament, Council, and Commission will now enter "trilogue" negotiations hoping to conclude the political process by the end of 2022.

Given all this, the importance of the EU ETS for aviation and, more specifically, the level of the carbon price is thus becoming more and more significant for the sector, both from an economic and an environmental point of view. Moving from this assumption, in the second section of this paper, a selected literature review composed of studies analyzing this peculiar subject will be developed. It will be divided into two streams, from early literature to the latest studies. Subsequently, in the third section, a brief literature review on carbon price forecasting will be presented. In the fourth section, a simple data-driven methodology for the prediction of the carbon price will be carried out, using the Hankel alternative view of Koopman (HAVOK) algorithm. Finally, in the fifth section results and conclusions will be presented, together with some considerations on the next possible steps for this study and this line of research.

5.1.1 Literature review on the EU ETS and aviation

Given the aforementioned motivations, our selected literature review will be focused on studies investigating specifically aviation and the EU ETS. The review will be divided into two streams. The first one is composed of a number of early studies investigating the possible impacts of the inclusion of the aviation sector in the EU ETS from different points of view, mainly its economic and environmental impacts inside and outside the European Union and its potential for induced airline network reconfiguration. The motivations, specifications, and model designs behind all these studies stem from the July 2008 European Union's directive on the inclusion of aviation in the EU ETS (Directive 2008/101/EC) and they are all antecedent to the "stop-the-clock" decision (Decision no. 377/2013/EU) which, as explained in the introduction, completely changed the scope of aviation's inclusion in the trading scheme. For these reasons, we decided to group these studies together. In fact, even if the final assessments of these studies have been surpassed by the consequent policy developments, they remain meaningful as they contributed greatly to the creation of a modeling framework for future studies. Moreover, it is interesting to analyze the findings of these studies in a counter-factual perspective in order to understand what could have been the impacts of the

original directive if the "stop-the-clock" decision would have not been taken.

The second stream of literature is composed of studies which were published after the "stop-the-clock" decision. These studies built on the foundation of the previous stream and revised the model assumptions in accordance with the new policy environment. Moreover, after 2016, some of the revised studies investigated the links and policy implications between the EU ETS and ICAO's global carbon mitigation scheme, CORSIA. Finally, the most recent study included in our literature review was published after the proposed July 2021 revision of the scheme in the context of the "fit-for-55" legislative package. The analysis of this study and its policy recommendations will conclude our literature review.

First stream (2009-2013)

As was already noted, the foundation of these studies is mainly the July 2008 directive on the inclusion of the aviation sector in the EU ETS. The first study under our scrutiny is a meta-study by Anger & Köhler (2010). The decision to start our review in 2009 was not in fact taken because no studies on the subject existed before this date. On the contrary, Anger & Köhler (2010) analyze nine different studies published between 2005 and 2009, as the political discussion around the inclusion of aviation under the umbrella of the EU ETS was going on for several years before the July 2008 Directive. There are three main reasons why these studies are not included in our literature review which are made explicit by the meta-study itself. First of all, the majority of these studies belong to the grey literature, which are consultancy reports that are not peer-reviewed. Secondly, some of these studies are based on assumptions that differ from the final legislation, regarding for example the auctioning rate of allowances. Finally, the authors note an over-simplification of the models and calculations used in these studies, often accompanied by the omission of important variables. In any case, all the reviewed studies forecast limited effects of aviation's inclusion in the scheme, both from an environmental and economic viewpoint: CO_2 emissions are projected to decline by a maximum of 3.8% and GDP to decline by a maximum of -0,0002% by 2020.

Following the criticism highlighted above, Anger (2010) develops her own model to investigate the impacts of the EU ETS on air transport. Using a hybrid post-Keynesian macroeconomic dynamic simulation model, the author develops three allowance price scenarios and compares them with a reference scenario, forecasting impacts on industry activity and carbon emissions. In terms of demand reduction, a slight decrease in demand is projected by 2020 (0.04% for an allowance price of €5, 0.54% for an allowance price of €20, and 0.98% for an allowance price of €40, compared with the reference scenario); regarding carbon emissions by the industry, the study forecasts a decrease of respectively 0.3%, 3.4% and 7.4% in the three scenarios. Finally, changes in real GDP in the EU are found to be

either nonexistent or very small (0.02% in the high price scenario). It is worth noting that while demand reduction effects are found to be smaller than in the previous literature, CO_2 emission reductions are greater than previously estimated.

Another study investigating these effects is Vespermann & Wald (2011). These authors build a simulation model in order to investigate the impacts of the scheme on the sector until 2020. Regarding the economic effects, they foresee the industry burden to rise from € 2.25 billion after the introduction of the ETS system to about € 3.67 billion in 2020, which translates into a cost base increase of about 1.25%. Regarding the demand side, passenger growth in 2013 is estimated to be reduced by 0.7% compared to the unrestricted base scenario, and this reduction is expected to rise to about 6% by 2020. However, the authors note that these impacts are highly dependent on external settings, such as allowance prices and demand growth. Regarding the emission reduction effects, the model shows that even if in the first years after the introduction of the ETS scheme emissions reductions will be comparably low (<3%) the system will unfold its impact in the mid- and long-term, generating a CO_2 emission reduction of 7.7% in 2020. The authors also make an observation on possible competition distortion arising from the scheme but find those impacts to be rather low.

The impact on competition between European and non-European network airlines is the subject of another study analyzed in this section carried out by Scheelhaase et al. (2010). Their model-based analysis focuses on the competitive impacts of the EU ETS on EU- and US-based network carriers, drawing a comparison between two exemplary airlines, namely Lufthansa and Continental Airlines. In contrast with Vespermann and Wald (2011), their model shows how under the carbon mitigation scheme Continental would gain a significant competitive advantage compared to Lufthansa on the market for long-haul air services. This result could in turn be extended to all European network carriers competing with non-EU network carriers on markets for long-haul air services. Their opinion is that the EU should address this systematic problem by introducing separate benchmarks for different types of routes, separating at least long-haul from short-haul flights to avoid or at least reduce this competitive distortion.

Malina et al. (2012) also indirectly investigate competition effects by estimating the economic impacts of the directive on US airlines from 2012 to 2020. These authors link an economy-wide computable general equilibrium model with a partial equilibrium model focused on the aviation industry. Their results are quite striking, in the fact that not only they forecast a relatively small impact on aggregate traffic and carbon emissions (3% CO2 emission reduction compared to the reference scenario) but in their full cost pass-through scenario the model shows a potential for windfall gains amounting to $2.6 billion associated with the opportunity cost pass-through that arises from the grandfathering allocation

procedure (i.e. free allocation) of the emission allowances.

The last two studies reviewed in this section are Albers et al. (2009) and Derigs & Illing (2013). Both studies estimate possible airline network reconfigurations following the adoption of the Directive. The first study models potential policy-induced cost increases for individual passenger routes and concludes that the magnitude of the induced effects is too small (between €9 and €27 per route) to instigate major route reconfigurations among European airlines. Derigs & Illing (2013) focus on the air cargo network and come to the same conclusion, stating that the EU ETS rules planned for the first years will result in insignificant or only marginal impacts on emissions and cost increases as well. It is worth noting their conclusion on the whole matter: "Only aggressive rules by which cost per allowance is raised significantly and free allowances are skipped lead to the intended reduction of CO_2 emissions".

Second stream (2016-2022)

As was mentioned in the introductory section, in 2013 two impactful events occurred in the context of aviation, sustainability and mitigation market-based measures. At the European level, with the "stop-the-clock" decision, the scope of the EU ETS for aviation was restricted to only intra-EEA flights. At the global level, the 2013 ICAO Assembly agreed on the development of a global market-based scheme designed to mitigate aviation's carbon emissions. The proposed scheme would later become known as CORSIA (Carbon Offsetting and Mitigation Scheme for Aviation) and would be officially adopted in the 39th ICAO Assembly in October 2016. These two decisions inevitably affected the subsequent literature on the subject: in this section, we will first review two studies analyzing the economic effects of the EU ETS on Italian airlines before moving on to a number of papers investigating the new regulatory environment and the coexistence perspectives of the two mitigation schemes.

Meleo et al. (2016) add their contribution to the previously analyzed line of research of cost evaluation as they focus on Italian airlines. These authors develop a cost calculation for the period 2012-2014 plus a forecast of future costs for the years 2015-2016, referring to three scenarios related to different hypotheses on allowance price (low, medium, and high scenarios). Their results show that direct costs linked to the scheme are quite limited but are expected to slightly increase from 2016 in reaction to the reduction of surplus allowances and rising carbon prices. Expanding the analysis from this model, Nava et al. (2018) find that two main factors influence airline profits when the EU ETS is enforced: the share of freely granted allowances and the airlines abatement effort cost, with a higher share of free allowances being associated to lower incentives for airlines to reduce emissions.

A different but still meaningful approach to this subject comes from Efthymiou & Papatheodorou (2019). These authors examine policy issues related to the implementation of

the EU ETS in the aviation sector through a two-round Delphi study based on a sample of 31 expert stakeholders. The answers given to the questionnaire confirm the relevance of three main elements affecting the efficiency and the design of the mitigation scheme: the allocation of emission allowances, the policy influences on the market, and the linking of the EU ETS with other schemes. It is worth noting that even if stakeholders working for airlines or IATA (International Air Transport Association) expressed similar views on the relaxation of environmental regulations whereas academics and government representatives pushed for stricter allocation methods, all stakeholders agreed on the fact that lobbying influences the EU ETS and more generally environmental policy design as a whole. As the authors clearly state, "in the area of EU ETS in aviation, the most influential players are the airlines and the governmental institutions with conflicting interests regarding environment."

Moving to the analysis of the studies comparing CORSIA and the EU ETS, Scheelhaase et al. (2018) weigh up the two aforementioned mitigation schemes in terms of functioning and future perspectives, focusing on their differences (CORSIA is an offsetting scheme, while the EU ETS is a cap-and-trade scheme) and outlining political options for the EU to adjust its own scheme in light of CORSIA's introduction. The authors list several coexistence policy options and conclude by stating that a continuance of the EU "reduced scope" regime beyond 2020 and a parallel coverage of international flights by CORSIA would be the best option as a compromise between political feasibility and environmental effectiveness. It is worth noting that as was reported in the introduction this option was in fact the one proposed by the EU Commission in the context of the reform of the EU ETS for the aviation sector included in the "fit-for-55" legislative package (the European Parliament, however, proposed a return to a "full-scope" EU ETS).

A similar conclusion is reached by Maertens et al. (2019) in a study that focuses on the options to continue for the EU ETS in a CORSIA-world. The authors stress again the difficulties in directly comparing the two mitigation schemes, given their structural differences, and pose questions on the environmental effectiveness of CORSIA's CERs (Certified Emission Reductions). The analysis carried out concludes by stating that keeping the intra-European EU ETS in addition to the introduction of CORSIA on other international routes would have far greater mitigation effects than CORSIA alone, even if this would likely create political tensions between ICAO and the European Union.

Another study worth mentioning is Larsson et al. (2019). This paper analyzes both national and international emissions mitigation policies for aviation and forecasts the effects of the EU ETS and CORSIA on the expected development of air travel emissions from 2017 to 2030 for the sample country Sweden, finding these impacts to be far too limited to achieve the 2°C target contained in the Paris Agreement. Alternatively, these authors cite three legally feasible national policy options which could, in their opinion, greatly help in

the undertaking of limiting aviation's carbon emissions. These are the introduction of a tax for jet fuel, a distance-based air passenger tax, and a quota obligation for biofuels.

The last study reviewed in this section is a very recent paper by Scheelhaase et al. (2021) that followed the Commission proposal to reform the EU ETS for aviation in the "fit-for-55" package. Here, the authors extensively discuss possible options for coexistence between the two schemes in light of the July 2021 legislative proposal. They highlight a number of key challenges to be addressed in the final legislation, including the geographical scope of the EU ETS for aviation, the level of auctioning of the allowances, and the level of the CO_2 emission cap. They also present some selected quantitative results illustrating potential effects on airfares of the proposed revision, under a full auctioning assumption (which is currently envisaged to be enforced by 2025 or 2027 according to the proposed reform) and a full cost pass-through to passengers. Their calculations result in a 2.6%, 5.9%, and 9% airfare increase for an allowance cost of respectively €45, €83, and €120. The authors conclude their study with a recommendation for policy makers to tackle some critical issues, such as the linkage between the two schemes, the need to strengthen CORSIA offsetting effectiveness, and to deal with potential carbon leakage and competitive distortion.

5.1.2 Literature review on carbon price forecasting

The preceding literature review has shown how the level of the carbon price is one of the fundamental variables in the investigation of the climate and economic impacts of all ETS-related activities and policies. In fact, many of the scrutinized studies adopted a scenario strategy where different carbon price levels were hypothesized in order to estimate projected costs and impacts. This approach is a consequence of the intrinsic uncertainty of the carbon price in the EU ETS which is, as we have seen in the introduction, dependant on several interrelated factors such as demand and supply dynamics, policy measures, international cooperation, and financial markets. However, a different approach to this uncertainty issue exists and it is embodied by studies developing carbon price forecasting models. In the next sections these techniques will be briefly mentioned and an original model will be presented, followed by some conclusions on the model's results and its applicability to our object of study.

As was already mentioned before, the inherent nonlinearity of the carbon price in EU ETS is the most challenging issue that has to be faced to accurately predict its behaviour over time. Several studies tried to tackle this problem by using univariate or multivariate linear models, including ARIMA, Factor-Augmented VAR, VARMA, and MIDAS (Chevallier 2010, García-Martos et al. 2013, Guobrandsdóttir & Óskar Haraldsson 2011, Zhao et al. 2018). Despite the good results, the volatility of the carbon price in EU ETS does not allow to reach accurate results from these techniques. In this regard, with the increase in

computational resources, the use of machine learning techniques became more and more extensive in the price prediction community (Atsalakis 2016, Zhu 2012, Fan et al. 2015, Xu et al. 2020). In particular, their coupling with the linear models above mentioned showed marked improvement in the predictive capability (Huang et al. 2021).

Nonetheless, these methodologies are complex and difficult to be implemented. For this reason, in this work, a simple data-driven technique is proposed for the prediction of the carbon price in EU ETS.

5.1.3 Data-driven carbon price prediction model

This section presents a different methodology to predict the carbon price over time. After a brief introduction of the Koopman theory, the modelisation strategy is discussed and assessed. The CO_2 price dataset is directly used to feed the algorithm in order to evaluate its forecasting capability.

Koopman operator theory

Koopman spectral analysis was introduced in 1931 by B. O. Koopman (Koopman 1931) to provide an operator-theoretic perspective on dynamical systems. The theory was then generalized in 1932 by Koopman and von Neumann to systems with continuous spectra (Koopman & v. Neumann 1932).

Throughout the paper, we will consider continuous-time dynamical systems of the form:

$$\frac{d\boldsymbol{x}(t)}{dt} = \boldsymbol{f}(\boldsymbol{x}(t)) \tag{5.1}$$

where $\boldsymbol{x} \in \boldsymbol{M}$ is an n-dimensional state on a smooth manifold $\boldsymbol{M}$, and t is the time. We will also consider the induced discrete-time dynamical system:

$$\boldsymbol{x}_{k+1} = \boldsymbol{F}(\boldsymbol{x}_k) \tag{5.2}$$

where $\boldsymbol{x}_k = \boldsymbol{x}(kt)$ may be obtained by sampling the trajectory in Eq. 5.1.

The Koopman operator K is an infinite-dimensional linear operator that advances measurement functions g of the state $\boldsymbol{x}$ forward in time according to the dynamics in Eq. 5.2:

$$K\, g = g \otimes \boldsymbol{F} \Rightarrow K\, g(\boldsymbol{x}_k) = g(\boldsymbol{x}_{k+1}) \tag{5.3}$$

Because this is true for all measurement functions g, K is infinite-dimensional and acts on the Hilbert space of state functions. For a more detailed discussion on the Koopman operator, the reader is referred to Brunton et al. (2016).

Consider a measurement subspace spanned by measurement functions $\{g_1, g_2, ..., g_p\}$ so that for any measurement g in this subspace

$$g = \alpha_1\, g_1 + \alpha_2\, g_2 + ... + \alpha_p\, g_p \tag{5.4}$$

In this case, we may confine the Koopman operator to this p-dimensional measurement subspace and obtain a p×p matrix representation K. If such matrix representation exists, it is possible to define a linear system that advances the measurement functions, restricted to the subspace in Eq. 5.4, as follows:

$$\boldsymbol{y}_{k+1} = \boldsymbol{K}\, \boldsymbol{y}_k \tag{5.5}$$

where $\boldsymbol{y}_k = [g_1(\boldsymbol{x}_k) \quad g_2(\boldsymbol{x}_k) \quad ... \quad g_p(\boldsymbol{x}_k)]^T$ is a vector of measurements in the invariant subspace, evaluated at $\boldsymbol{x}_k$.

In practice, obtaining such a representation in terms of a Koopman invariant subspace is extremely challenging. Because of this, the perspective of a data-driven linear approximation to a dynamical system is still valuable. In the following, we will show the application of the data-driven method proposed by Brunton et al. (2017) to estimate the Koopman operator as best as possible, to forecast the CO2 price during time.

Hankel alternative view of Koopman (HAVOK) method

This section formulates the HAVOK method for univariate time series analysis. The algorithm consists of three stages: (1) Time delay embedding, (2) dynamic mode decomposition, and (3) reconstruction and forecasting. Each step is explained in more detail in the following subsections.

Time delay embedding The HAVOK modelisation tries to reconstruct a dynamical system from a sequence of observations of the system's state. The first step of the algorithm consists of the generation of a so-called Hankel matrix by rearranging the dataset. In particular, the time delay embedding strategy proposed by Takens (1981).

The strategy can be thought of as a mapping that converts a univariate time series $\boldsymbol{x}_k = [x_1, x_2, ...x_T]$ into a multidimensional series $\boldsymbol{H} = [\overline{\boldsymbol{x}}_1, \overline{\boldsymbol{x}}_2, ...\overline{\boldsymbol{x}}_p]$, where $\overline{\boldsymbol{x}}_n = [x_n, x_{n+1}, ...x_K]$. Thus, the time series is decomposed into $K = n + T - p$ overlapping segments of length p.

The structure of the matrix $\boldsymbol{H}$ is the following:

$$\begin{bmatrix} x_1 & x_2 & \dots & x_p \\ x_2 & x_3 & \dots & x_{p+1} \\ \vdots & \vdots & \ddots & \vdots \\ x_K & x_{K+1} & \dots & x_{K+p-1} \end{bmatrix} \tag{5.6}$$

Dynamic Mode Decomposition (DMD) The Dynamic Mode Decomposition (DMD) was firstly introduced by P. J. Schmid in 2010 (Schmid 2010). Shortly after, the work of ROWLEY et al. (2009) showed a strong connection between the DMD and the Koopman spectral analysis. In particular, the DMD provides a practical framework to approximate the Koopman operator.

The DMD algorithm aims to find the best-fit linear model to relate the following two data matrices:

$$\boldsymbol{X} = \begin{bmatrix} | & | & \dots & | \\ x_1 & x_2 & \dots & x_{m-1} \\ | & | & \dots & | \end{bmatrix} \quad \boldsymbol{X'} = \begin{bmatrix} | & | & \dots & | \\ x_2 & x_3 & \dots & x_m \\ | & | & \dots & | \end{bmatrix} \tag{5.7}$$

where the matrix $\boldsymbol{X}$ contains snapshots of the system in time, and $\boldsymbol{X'}$ is a matrix of the same snapshots advanced a single step forward in time. These matrices may be related by a best-fit linear operator $\boldsymbol{A}$ given by

$$\boldsymbol{X'} = \boldsymbol{A}\,\boldsymbol{X} \Rightarrow \boldsymbol{X'}\,\boldsymbol{X^*} \tag{5.8}$$

where $\boldsymbol{X^*}$ is the pseudo-inverse, obtained via the singular value decomposition (SVD). In this way, we can obtain a linear operator $\boldsymbol{A}$ capable to advance a matrix $\boldsymbol{X}$ in time.

HAVOK HAVOK analysis (Brunton et al. 2016) provides linear representations for the dynamics of the dynamical systems ($\boldsymbol{f}$ in Eq. 5.1 and $\boldsymbol{F}$ in Eq. 5.2). The first step of the algorithm consists of the finding of the eigen-time-delay coordinates by taking the singular value decomposition (SVD) of the Henkel matrix:

$$\boldsymbol{H} = \begin{bmatrix} x_1 & x_2 & \dots & x_p \\ x_2 & x_3 & \dots & x_{p+1} \\ \vdots & \vdots & \ddots & \vdots \\ x_K & xK+1 & \dots & x_{K+p-1} \end{bmatrix} = \boldsymbol{U}\,\boldsymbol{\Sigma}\,\boldsymbol{V}^T. \tag{5.9}$$

The columns of $\boldsymbol{U}$ and $\boldsymbol{V}$ from the SVD are arranged hierarchically by their ability to model the columns and rows of $\boldsymbol{H}$, respectively. $\boldsymbol{H}$ can be well approximated by the first r columns

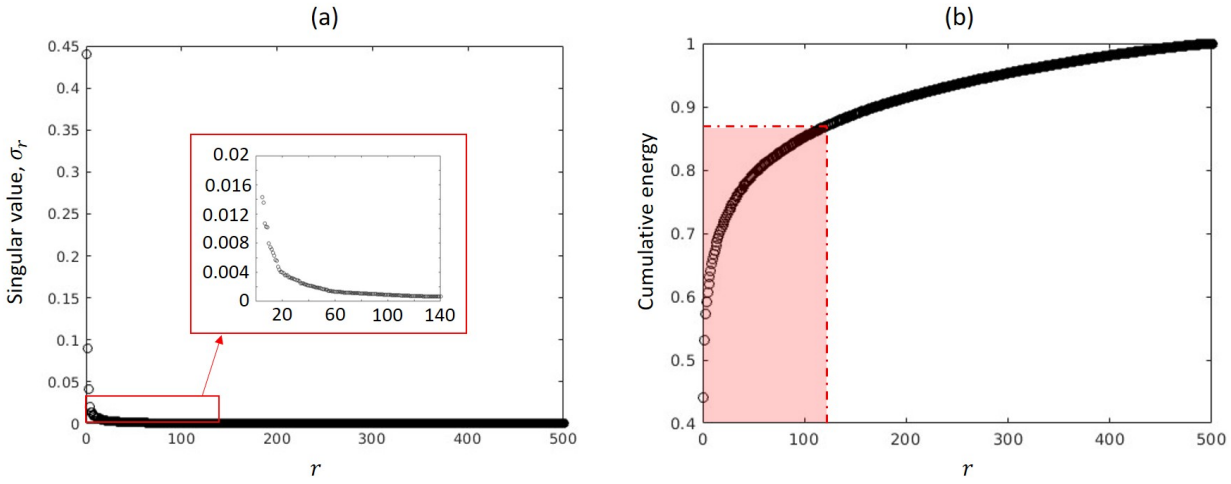

Figure 5.1: Singular values σ_r (a) and cumulative energy in the first r modes (b).

of $\boldsymbol{U}$, $\boldsymbol{V}$. According to the HAVOK analysis (Brunton et al. 2016), the first r-1 variables in V can be built as a linear model:

$$\boldsymbol{v}(t+dt) = \boldsymbol{A}\,\boldsymbol{v}(t) \tag{5.10}$$

where $\boldsymbol{v} = [v_1 \quad v_2, \quad \ldots \quad v_{r-1}]^T$ is a vector of the first $r-1$ eigen-time-delay coordinates. The linear system in Eq. 5.10, specifically the matrix $\boldsymbol{A}$, was derived by applying the DMD.

Model assessment

After building the time-delay embedded data matrices, we have to find the value of the best-rank approximation (r) as introduced in the previous paragraph before applying the DMD algorithm. This is done by analysing the singular values of the matrix $\boldsymbol{\Sigma}$ coming from the application of the SVD to the main matrix. The results in terms of $\sigma_r = diag(\Sigma)/sum(diag(\Sigma))$ and $\sigma_r = cumsum(diag(\Sigma)/sum(diag(\Sigma)))$, where $cumsum()$ is the function "cumulative sum", are shown in Fig. 5.1. From Fig. 5.1(b), it can be noted that to achieve the 90% of the total information, a rank equal to roughly 150 has to be chosen. Nonetheless, it can be noted from Fig. 5.1(a) that for rank values above 140, the eigenvalues become so small to be considered negligible. In view of this, a rank of 140 has been chosen for the present study, leading to roughly the 87% of the total information.

To demonstrate the capability of HAVOK for CO_2 price forecasting, data from 01-Jan-2005 to 11-Mar-2022 have been used as the training set, leaving the remaining data, from 11-Mar-2022 to 31-Mar-2022, as the test set. The results of the assessment are shown in Fig. 5.2, where is reported the training data with the black line, the reconstructed trend with the yellow line, the test data with the blue line, and the predicted trend with the red line.

First of all, a good agreement between the training data and the reconstructed trend can

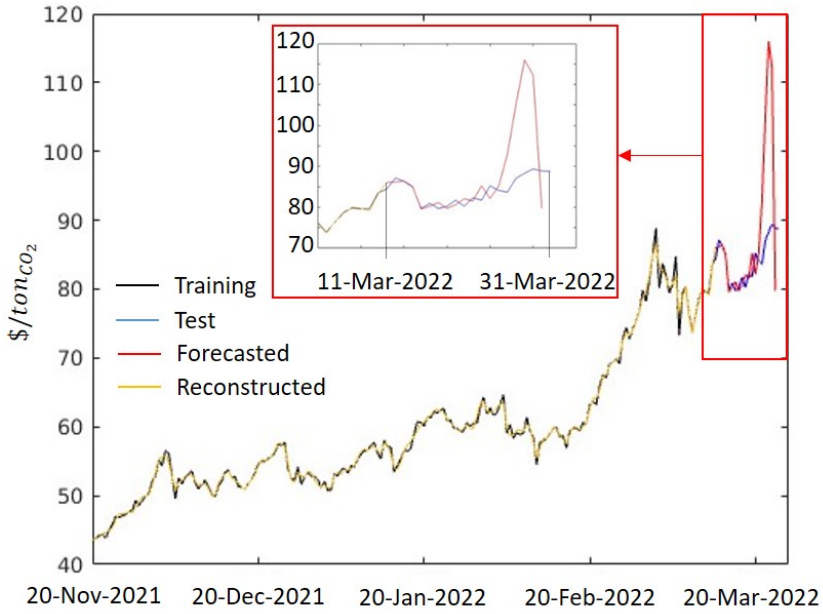

Figure 5.2: CO_2 price forecasting assessment.

be observed. This confirms that the rank value chosen is correct, hence the capability of describing the entire behaviour with a reduced order model. What concerns the predictive capability assessment, can be adequately discussed by observing the zoom in Fig. 5.2. In particular, it can be recognized that HAVOK can well capture the trend for the first 12 days, but began to be unstable beyond this value. Although the prediction is considered acceptable only for 12 days beyond the training data, the authors want to stress that this is the first attempt to find a data-decomposition predictive model for the EU ETS CO2 forecasting. Moreover, a daily resolution as the time discretization has been considered, hence the 12 days could be 12 months if the time resolution had been monthly. The latter consideration, that is the sensibility of the predictive algorithm to the time resolution, will be the focus of the next steps of the research. Concerning the instability behaviour, this is due to the fact that the eigenvalues of the linear operator are for the most part outside the unit circle on the Argand-Gauss plane. A possible cause of this problem may be the time resolution chosen for the present study (daily).

5.2 Gas Turbine Combustor Modeling for Emission Prediction

Interest in environmental problems has grown considerably during the last few years since emission regulations are becoming more and more stringent, as can be also gathered from the previous section. In particular, whenever a new plant for power production is designed or an existing one has to be updated or modified to meet the required emission levels,

the environmental impact of the system must be accurately investigated, especially when the plant is located within or near human settlements. For this reason, it is important to achieve knowledge of the combustion process which is as accurate as possible, in order to inform the design of the system and to have comprehensive information on the pollutant emissions along the whole operating range of the system (Bettocchi et al. 2002).

For these reasons, in addition to experimental campaigns, the development of numerical codes for combustion analysis and evaluation of pollutant emissions has received great attention. In fact, both experimental and numerical studies are necessary to gain a clear internal view of the combustion process. The experimental approach can give the most reliable information, but it can usually be carried out only in a few operating conditions, while the numerical analyses, though their predictive capability is still limited but can extend the information to a wider range of working points (Bettocchi et al. 2002).

In recent years, three-dimensional approaches based on CFD analysis have been widely used, allowing, with reasonably good accuracy, the determination of flow field and temperature distribution inside combustion systems (such as for instance, gas turbine combustors, furnaces, boilers, etc.).

In contrast, due to the incomplete understanding of various combustion mechanisms and to unsolved numerical deficiencies, numerical prediction of combustion performance and emissions is still not very accurate. To overcome the problems outlined and improve the predictive capability of the models, the CFD calculation is often combined and/or supported with calculations performed using simplified model approaches, for both thermal and chemical analysis of the system (Rizk & Mongia 1993, 1995, Nicol et al. 1999, Boysan et al. 1982).

The numerical study of combustion processes using Chemical Reactors (CR) analysis based on Perfectly Stirred Reactor (PSR) and/or Plug-Flow Reactor (PFR) approaches is still widely used. In fact, these simplified zero- or one-dimensional analyses can give significant information to both designer and user, while being quite easy to implement, flexible to use and not requiring a relevant computational effort, compared to that required by three-dimensional codes. In addition, using these models, it is possible to take into consideration detailed chemical kinetics mechanisms, through analytical, semi-analytical or empirical expressions, to obtain more complete information on emissions. In brief, these approaches can be useful since:

- it is possible to obtain qualitative information about pollutant emission trends with respect to combustor operating conditions and geometry;
- they can represent a starting point for subsequent three-dimensional analysis;
- they can be used to have rapid responses in analysing many real devices and to orient

experimental tests.

Combined cycle power plants with supplementary firing have been widely studied from a thermodynamic and economic point of view, and also many examples of field applications can be found. The main advantage of this plant is the presence of supplementary combustion in a duct burner at the gas turbine exit that permits higher flexibility in managing the electric-to-thermal power ratio and, in some cases, an improvement of the overall efficiency.

In these plants, two kinds of combustion systems are present: (i) the Gas Turbine (GT) combustor and (ii) the Supplementary Fired Burner (SFB) at the turbine outlet, which allows an increase of the exhaust gas temperature before they enter the Heat Recovery Steam Generator.

Researchers have thoroughly investigated gas turbine combustion chambers, both numerically and experimentally. An exhaustive state-of-the-art review can be found in Correa (1998). On the contrary, the SFB has not yet been so extensively investigated as GT combustors. These combustion chambers are located at the GT turbine exit and use the exhaust gases, which usually still contain a significant amount of oxygen, as oxidants. The SFB is supplied by a fuel different from that of the GT and, if necessary, by a different air mass flow rate.

In this section, a one-dimensional technique to model a gas turbine combustor is presented, with the purpose of suggesting its integration in the digital twin model exposed in the previous chapter, in order to estimate the emissions after a whole aircraft mission.

5.2.1 Emissions Evaluation

In a Perfectly Stirred Reactors formulation, the domain to be studied is considered as a single or as a series of elemental reactors in which a given geometry can be divided. The choice of the reactor number and combination permits the approximation of complex combustion systems. The selection of reactors has to be chosen with respect to the particular problem under investigation, considering both the geometry and the physics of the problem, and it can be based on field experience or on CFD calculations (Turns 1996). Many authors have dealt with gas turbine combustors through PSR and PFR modelling. The original works of Hammond and Mellor (Hammond & Mellor 1970, 1973) are still very interesting and used by many authors. This is the reason why also in this work, the author suggests using it for the emission evaluation.

Reactor model

In this formulation, the PSR model (Hammond & Mellor 1970) is proposed. The combustion zone of can-type gas turbine combustors has been shown to be extremely turbulent. The

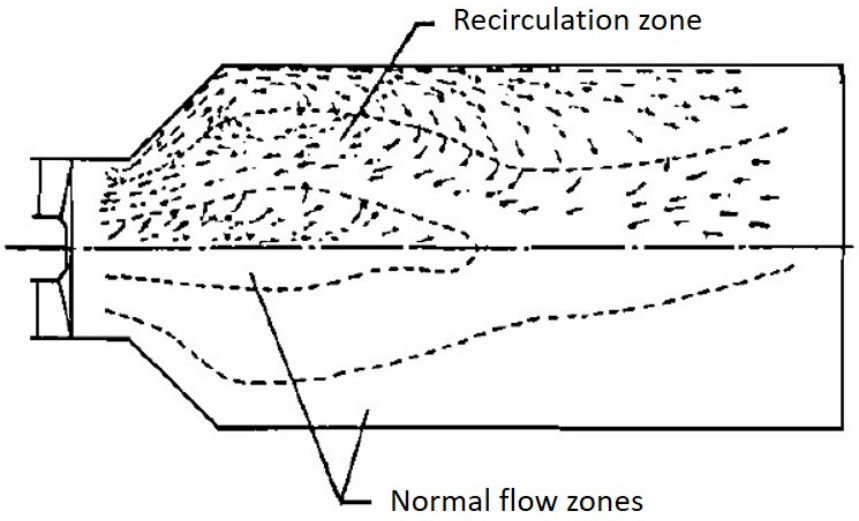

Figure 5.3: Experimental combustor flow pattern. From Hiett & Powell (1962).

airflow patterns inside the combustor liner have been studied using three-dimensional velocity probes by Hiett & Powell (1962), and a typical flow pattern is shown in Fig. 5.3. In the forward end of the liner, a strong flow reversal or recirculation zone is present. Throughout the liner, considerable turbulence is produced from the interaction of the airflow through the liner and the secondary air jets. The important features to note are:

- the reverse flow zone established by the fuel injector-swirler assembly;
- the high degree of turbulence present inside the liner, giving a correspondingly high mixing rate;
- the staged addition of air to the combustion zone.

The swirler and air addition scheme are used to induce turbulence inside the liner. The success of this method is evident in the flow pattern shown, and the high degree of turbulence present indicates that the combustion zones inside the liner are very well mixed. If the rate of mixing is rapid compared to the rate of chemical reaction, mixing may be neglected entirely, and the system will be controlled by chemical kinetics alone. This argument is particularly applicable when considering gaseous fuels.

Chemical rate-limited systems represent the maximum performance to be attained by improving mixing. Since designs are directed toward inducing a high mixing rate, and a high turbulence level has been observed experimentally, it is reasonable to assume that portions of can-type gas turbine combustors can approach the perfectly stirred reactor, in which chemical kinetics are rate-controlling and mixing times are considered infinitesimal. Thus, with this assumption, stirred reactor theory can be applied to make analytical predictions of performance.

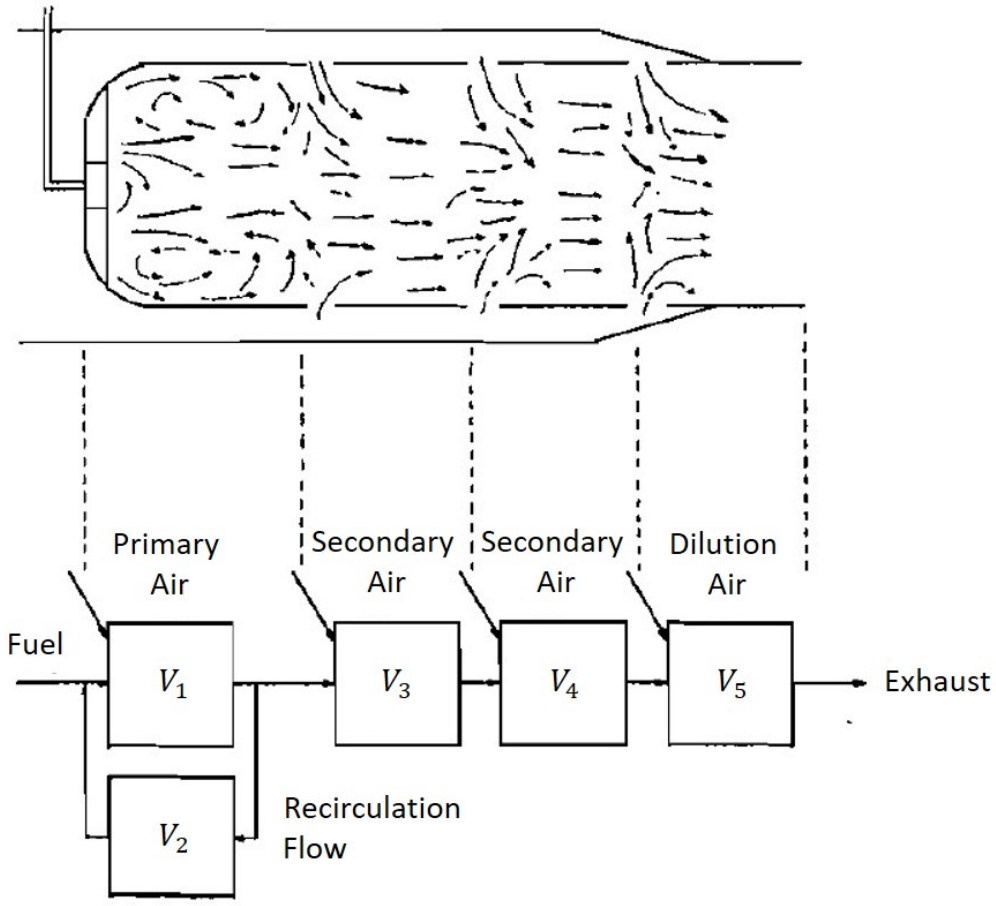

Figure 5.4: Hammond combustor model compared with a typical combustor configuration. From Hammond & Mellor (1970).

In formulating any combustor model, many physical factors must be neglected to make solutions possible by analytical methods (in this case mixing is neglected). One would expect that model corresponding most closely to the physical system to predict actual performance with the best accuracy. The model shown in Fig. 5.4 has been constructed by Hammond & Mellor (1970) to include many of the characteristics of an actual combustor. V_1 and V_2 are stirred reactors arranged as in the model of Hottel et al. (1958). V_3, V_4, and V_5 are plug flow reactors, which can be approximated by a series of small stirred reactors.

The initial fuel-air mixture will be determined by the air flow through the swirl vanes of the combustor (primary air flow, Fig. 5.5) and the total fuel flow. In general, this mixture will be close to stoichiometric. The air entering V_3 and V_4 (and additional reactors if desired) corresponds to the flow through the two (or more) rows of secondary air holes, and the air entering V_5 corresponds to the flow through the dilution air holes. It is hoped that the $V_1 - V_2$. coupling, will predict stability phenomena, as observed by Hottel et al. (1958), while the remaining volumes will predict downstream burning.

This model differs from that of Hottel et al. (1958) in that some attempt is made to model secondary combustion by the inclusion of a series of plug flow reactors. Their recir-

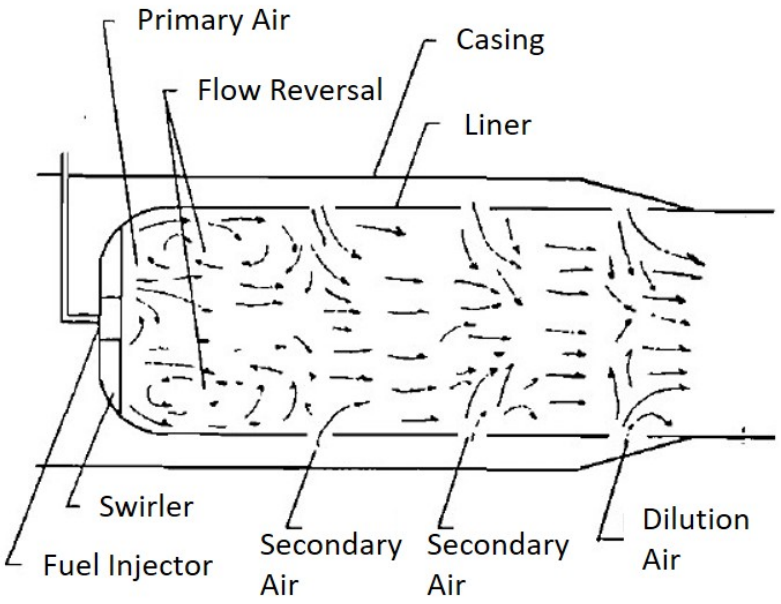

Figure 5.5: Can-type combustor. From Hammond & Mellor (1970).

culation scheme is incorporated as the best available model considering combustion with a flow reversal. The model of Thring and Masdin also considers recirculation, but in their case, all six reactors are involved in the recirculation path; as a result, the reverse flow is more completely burned. In the proposed model the reverse flow is less completely burned since only two reactors are included in the recirculation path.

Plug flow reactors rather than stirred reactors were chosen to model the downstream burning volumes by considering an actual combustor. In the secondary air entry zones, turbulence is still high but no large-scale flow reversals exist; therefore, at each cross-section, the gases are well mixed, but little mixing occurs in the axial direction. Thus the reactant concentrations and reaction rate should decrease monotonically with an axial position as in a plug flow reactor.

Application of the model will require knowledge of the volume of each reactor. These values can be determined by analyzing either experimental (Hiett & Powell 1962) or theoretical flow patterns. V_1 will be the portion of the liner volume (ahead of the first row of secondary air holes) in which the flow is in the normal downstream direction and V_2 the reverse flow portion. The other volumes can initially be taken as the volume contained between adjacent rows of liner air holes. The recirculation ratio for V_1 and V_2 must also be determined from flow studies. Hopefully, these values would remain constant with flow variations, but their variation could possibly be considered.

Liner cooling must be a major consideration in designing an airflow pattern. Sufficient secondary cooling air must flow in the annulus between the liner and casing to maintain the liner temperature below its failure point under all conditions. To determine the cooling

flow required, the heat transfer from the combustion zone to the liner must be known. As the cooling air flows down the liner, its temperature will rise; by allowing variable injection temperatures to V_3, V_4, and V_5, this effect can be considered. However, lacking a valid heat transfer analysis the assumption of adiabatic combustion is made for the present effort.

Admittedly this model neglects many factors which may be important. Even with gaseous fuels, homogeneity is not assured. If the mixing rate is not extremely rapid, the use of stirred and plug flow reactors will introduce considerable error. Since liquid fuels are used in gas turbine combustors, the model's neglect of fuel vaporization and droplet burning may be a serious limitation. Such factors may necessitate revision of the model in light of new experimental evidence. Using the proposed model will produce the smallest combustor for a given situation since only kinetics are considered. As mixing is improved in an actual combustor, its performance will approach (in the limit) the performance predicted by the model. In the model, mixing is grossly approximated using the variable recirculation flow between V_1 and V_2.

Residence Time

The residence time τ_{res} inside each reactor is one of the parameters that greatly affects the production of the main pollutant emissions. The residence time in each reactor is usually calculated as the ratio between the reactor volume and the volume flow rate:

$$\tau_{res} = \frac{V}{\dot{V}} \tag{5.11}$$

This equation can be considered correct only for gaseous fuel. For liquid fuels, in fact, it is to be considered that not all the interval [0, τ_{res}] is available for the combustion reaction since chemical reaction has to be preceded by liquid fuel atomisation, fuel spray evaporation, mixing of vaporised fuel with air and ignition delay (Sturgess et al. 1993).

Thus, in the program, the residence time has to be modified to consider these effects, except for liquid fuel atomisation which can be neglected. Thus, the final equation for the residence time is then:

$$\tau_{res} = \frac{V}{\dot{V}} - [(\tau_{ev} + \tau_{mix} + \tau_{del}) - \tau_{over}] \tag{5.12}$$

where τ_{over} accounts for any kind of overlapping among the other characteristic times ($\tau_{ev}, \tau_{mix}, \tau_{del}$) due to concurrency of elemental processes. The expressions of each term on the right hand side of Eq. 5.12 are fully described in Sturgess et al. (1993).

Emission Model

The semi-analytical emission model adapted from the original model of Rizk & Mongia (1995), that originally developed their model to simulate different typologies of GT combustors, is the one suggested by the author. In their work, the authors considered the combustion reaction to proceed through a four-step based scheme involving seven elemental species (a parent fuel $C_X H_Y$, an intermediate fuel $C_i H_j$, H_2, CO, O_2, CO_2, H_2O) and added an equation to simulate NO_x production via the Zeldovich mechanism (Toof 1986). Then, they obtained a number of reaction rate expressions that simulate the results obtained with a detailed chemical kinetics scheme, based on a multi-step combustion model and which uses an extended number of reactions.

In this chapter, the carbon monoxide CO and thermal NO expressions obtained by Rizk & Mongia (1995) are as follows:

$$\begin{aligned}\frac{d(CO)}{dt} &= C_1(p)\, e^{-E_1/T}\, [C_X H_Y]^b\, [O_2]^c\, [C_i H_j]^d\, [CO]^e\, [H_2O]^f\, f_1(\psi) \\ &\quad - C_2(p)\, e^{-E_2/T}\, [O_2]^g\, [C_i H_j]^h\, [CO]^i\, [CO_2]^l\, f_2(\psi)\end{aligned} \tag{5.13}$$

and

$$\begin{aligned}\frac{d(NO_x)}{dt} &= C_3(p)\, e^{-29000/T}\, [O_2]^{0.9}\, [CO]^{0.8}\, f_3(\psi) \\ &\quad - C_4(p)\, e^{-60000/T}\, [O_2]^{0.8}\, [C_i H_j]^{0.7}\, [NO]^{0.3}\, [CO]^{2.5}\, f_4(\psi)\end{aligned} \tag{5.14}$$

where ϕ is the equivalence ratio. The dependence on combustor pressure is taken into consideration through the functions C_i, i=1,...,4. Both the CO and thermal NO reaction rate expressions can be integrated through an explicit time scheme.

For prompt and fuel NO contribution to NO_x emission level evaluation, two integral empirical expressions can be used. The prompt NO are evaluated through an expression based on Toof (1986), which correlates the concentration of prompt NO to the equilibrium concentration of nitric oxide calculated at the adiabatic flame temperature

$$[NO]_{prompt} = \chi_{HC}\, f(\phi)\, p^{0.5}\, [NO]_{eq,T_{ad}} \tag{5.15}$$

where $f(\psi)$ is an empirical expression depending on the equivalence ratio and χ_{HC} accounts for the presence of hydrocarbons in fuel.

The fuel NO are calculated by making use of an empirical relation once again obtained by Toof (1986). This relation is based on a conversion factor Y, which links the fraction of fuel nitrogen converted to NO to the equilibrium concentration of fuel nitrogen itself. In the model implemented the simplifying hypothesis that all the fuel nitrogen is converted to

ammonia (NH_3) and then to fuel NO has been adopted. The final equation is then

$$[NO]_{fuel} = Y\,[NO]_{(NH_3),eq} \tag{5.16}$$

Heat Transfer Model

The emission levels, in particular the thermal NO_x, strictly depend on temperature. To improve the accuracy of the emission evaluation a heat transfer model has been implemented within the program to take into consideration any kind of external cooling. The model accounts for the heat exchange between hot gases and reactor walls, and between walls and the external environment. The external environment can be either the presence of a cooling medium (water, air) or the surroundings. Both convective and radiative heat transfer mechanisms are considered.

The convective contribution to heat transfer is calculated through the definition of a heat transfer coefficient h, calculated as a function of the combustor geometry and by introducing hypotheses on the flow regime.

For radiative heat transfer, a simplified model developed by Hottel et al. (1958) has been implemented. This model considers the hot gases and the wall as two grey surfaces separated by a non-participating medium. With these hypotheses, the radiative heat transfer can be expressed by the equation

$$q_{rad} = \zeta_{gw}\,\sigma\,(T_g^4 - T_w^4) \tag{5.17}$$

where the factor ζ_{gw} is a function of the wall and hot gas emissivity (ϵ_w and ϵ_g), of the gas-wall view factor and of the wall area.

The solution of Eq. 5.17 requires the determination of the hot gases emissivity ϵ_g, which enters in the definition of the factor ζ_{gw}. In this section, the main hypothesis introduced is that only CO_2 and H_2O determine the total emissivity of the hot gases. The hot gases' total emissivity ϵ_g is then

$$\epsilon_g = \epsilon_{CO_2}\,C_{CO_2} + \epsilon_{H_2O}\,C_{H_2O} - \Delta\epsilon_i \tag{5.18}$$

where the C_i terms are correction factors which account for pressurized combustion chambers, and $\Delta\epsilon_i$ is a correction on ϵ_g for superimposed radiation from CO_2 and H_2O.

Each component emissivity, following data originating from total emissivity measurements at ambient pressure reported in (Hottel et al. 1958), is calculated as a function of the partial pressure of the component of the gas temperature and of the mean beam length. The latter parameter, in particular, was introduced to correlate, in terms of a single parameter, the dependence of hot gas emissivity on both the size and shape of the flame geometry.

5.3 Conclusions and Remarks

This chapter is the first step towards a general fouling-induced emission prediction tool, that should be integrated with the one proposed in Ch. 4. In the first part, a CO2 price forecasting algorithm has been introduced, in order to accompany the physic-based emission model in the prediction of the mission (emissions) costs. In this context, the nowadays critical climate emergency is introduced, and a review of the consequent EU policies have been performed to face it is reported.

Besides that, also a physics-based technique to predict gas turbine emissions is proposed. This technique should be integrated into the already presented digital twin, in order to obtain the emission of an engineer during a whole aircraft mission.

Chapter 6

Conclusions and Limitations

This chapter summarises the results presented in this thesis, assessing the suitability of the methods developed in addressing the defined aims and objectives of the work. Also, the limitations of the proposed strategy are commented on, with the purpose of highlighting the steps that should be undertaken to advance the research in this field.

6.1 Conclusions

This thesis proposes different methodologies capable to mitigate the effects of fouling or predicting the performance degradation that it generates. For this purpose, both hot and cold engine sections are considered.

In particular, concerning the turbine section, new design guidelines are presented. This is because, for this specific component, the time scales of failure events due to hot deposition can be of the order of minutes, which makes any predictive model inapplicable. In this respect, design optimization techniques were applied to find the best HPT vane geometry that is less sensitive to the fouling phenomena. After that, machine learning methods were adopted to obtain a design map that can be useful in the first steps of the design phase. Moreover, after a numerical uncertainty quantification analysis, it was demonstrated that a deterministic optimization is not sufficient to face highly aleatory phenomena such as fouling. This suggests the use of robust or aggressive design techniques to front this issue. The research branch that tries to face this problem has been called Design for Fouling (DoF) by the author since represents the first attempt to optimize a gas turbine geometry against deposition in the literature.

On the other hand, with respect to the compressor section, the research was mainly focused on the building of a predictive maintenance tool. This is because the time scales of failure events due to cold deposition are longer than the ones for the hot section, hence the main challenge for this component is the optimization of the washing schedule. As reported

in the previous sections, there are several studies in the literature focused on this issue, but almost all of them are data-based instead of physics-based. The innovative strategy proposed here is a mixture between physics-based and data-based methodologies. In particular, a reduced-order model has been developed to predict the behaviour of the whole engine as the degradation proceeds. For this purpose, a gas path code that uses the components' characteristic maps has been created to simulate the gas turbine. A map variation technique has been used to take into account the fouling effects on each engine component. Particularly, fouling coefficients as a function of the engine architecture, its operating conditions, and the contaminant characteristics have been created. For this purpose, both experimental and computational results have been used. Specifically for the latter, efforts have been done to develop a new numerical deposition/detachment model, that shows really strong accordance with the deposit pattern found experimentally.

6.2 Limitations

The strategies proposed are affected by some limitations, that for clarity are summarized as follows:

- The deposition/detachment model proposed in this work shows a strong agreement with the experimental results. Nonetheless, there are areas of the vanes and the blades that are not well reproduced. In particular, the deposition on the suction side of the vane is the one that is predicted in the worst way by the model. The problem is that this area is also the most important in terms of performance since it is the most sensitive to flow separation.

- The effects of the deposition on the flow field have been modelled by the microscale model. This shows a good forecasting capacity when the deposition process begins, but the predictive error rises as the deposit grows since also the effect of the geometric variations start to be important.

- The design map proposed in chapter 3 is a really good tool for the design procedure of gas turbine components. The main problem is that a deterministic map is demonstrated to be not sufficient for mitigating the fouling issue. Moreover, only a simple HPT vane geometry was considered here, without cooling holes and 3D effects, which can markedly affect the deposition process and the results here presented.

- In chapter 4 a digital twin strategy has been proposed to predict the fouling impact in a whole aircraft mission. One of the main problems in this methodology is that the components' characteristic maps are often difficult to find. In this context, several strategies are present in the literature to reproduce them from some geometrical

data but are a strong approximation of the real curves. Moreover, only a simple aircraft modelisation has been presented here, without considering a lot of geometric and aerodynamic features that are often not known. Last but not least, there is the problem of finding the best multi-fidelity machine learning technique capable to fuse both experimental and numerical results and giving adequate degradation coefficients.

6.3 Future Prospective

The understanding of fouling mechanisms in compressors and turbines is still a challenge for manufacturers and users. Through the results reported in this thesis, it is possible to mitigate or predict the fouling effects in gas turbines. In particular, the design map generation could be of main help for the designers, in case they need a geometry less sensitive to deposition. On the other hand, if washing scheduling or mission costs are of interest, the digital twin strategy proposed could be useful.

In the future, these approaches could be the standard methods to face the fouling issue, hence all the limitations reported in the previous section should be tackled.

Bibliography

Adams, R. M., Dunn, M. G. & Padova, C. (1987), Operation of gas turbine engines in dust laden environments, Technical report, AGARD-CP-421, AGARD.

Aguet, E. & Von Salis, J. (1960), Three Years' Operating Experience With 1500-kw Gas-Turbine Plants in Belgian Steelworks, *in* 'ASME Turbo Expo, Paper No. 60-GTP-3.'.

Albers, S., Bühne, J.-A. & Peters, H. (2009), 'Will the eu-ets instigate airline network reconfigurations?', *Journal of Air Transport Management* **15**(1), 1–6.

Aldi, N., Casari, N., Dainese, D., Morini, M., Pinelli, M., Spina, P. R. & Suman, A. (2017), Quantitative CFD Analyses of Particle Deposition in a Heavy-Duty Subsonic Axial Compressor, Vol. Volume 9: Oil and Gas Applications; Supercritical CO2 Power Cycles; Wind Energy of *Turbo Expo: Power for Land, Sea, and Air*.

Aldi, N., Casari, N., Dainese, D., Morini, M., Pinelli, M., Spina, P. R. & Suman, A. (2018), 'Quantitative Computational Fluid Dynamics Analyses of Particle Deposition in a Heavy-Duty Subsonic Axial Compressor', *Journal of Engineering for Gas Turbines and Power* **140**(8).

Aldi, N., Morini, M., Pinelli, M., Spina, P. R. & Suman, A. (2014), Cross Validation of Multistage Compressor Map Generation by Means of Computational Fluid Dynamics and Stage-Stacking Techniques, Vol. Volume 3B: Oil and Gas Applications; Organic Rankine Cycle Power Systems; Supercritical CO2 Power Cycles; Wind Energy of *Turbo Expo: Power for Land, Sea, and Air*.

Aldi, N., Morini, M., Pinelli, M., Spina, P. R., Suman, A. & Venturini, M. (2013), Performance Evaluation of Non-Uniformly Fouled Axial Compressor Stages by Means of Computational Fluid Dynamic Analyses, Vol. Volume 5B: Oil and Gas Applications; Steam Turbines of *Turbo Expo: Power for Land, Sea, and Air*.

Aldi, N., Morini, M., Pinelli, M., Spina, P. R., Suman, A. & Venturini, M. (2014), 'Numerical analysis of the effects of surface roughness localization on the performance of an axial compressor stage', *Energy Procedia* **45**, 1057–1066. ATI 2013 - 68th Conference of the Italian Thermal Machines Engineering Association.

Allen, C., Holcomb, C. & Oliviera, M. (2018), 'Estimating recoverable performance degradation rates and optimizing maintenance scheduling', *Journal of Engineering for Gas Turbines and Power* **141**.

Ames, F. & Moffat, R. (1990), 'Effects of simulated combustor turbulence on boundary layer heat transfer', *Proceeding of AIAA/ASME Joint Thermophysics and Heat Transfer Conference, Turbulent Flow Session* .

Anger, A. & Köhler, J. (2010), 'Including aviation emissions in the eu ets: Much ado about nothing? a review', *Transport Policy* **17**(1), 38–46.

Armenio, V. & Fiorotto, V. (2001), 'The importance of the forces acting on particles in turbulent flows', *Physics of Fluids* **13**(8), 2437–2440.

Arts, T. & Lambert de Rouvroit, M. (1992), 'Aero-Thermal Performance of a Two-Dimensional Highly Loaded Transonic Turbine Nozzle Guide Vane: A Test Case for Inviscid and Viscous Flow Computations', *Journal of Turbomachinery* **114**(1), 147–154.

Asan, U. & Ercan, S. (2012), *An Introduction to Self-Organizing Maps*, pp. 299–319.

Atsalakis, G. S. (2016), 'Using computational intelligence to forecast carbon prices', *Applied Soft Computing* **43**, 107–116.

Basendwah, A. A., Pilidis, P. & Li, Y. G. (2006), Turbine Off-Line Water Wash Optimization Approach for Power Generation, Vol. Volume 4: Cycle Innovations; Electric Power; Industrial and Cogeneration; Manufacturing Materials and Metallurgy of *Turbo Expo: Power for Land, Sea, and Air*, pp. 65–76.

Bettocchi, R., Pinelli, M. & Spina, P. R. (2002), A Program for the Evaluation of Pollutant Emissions in Combined Cycle Power Plants With Supplementary Firing, Vol. Volume 4: Turbo Expo 2002, Parts A and B of *Turbo Expo: Power for Land, Sea, and Air*, pp. 327–334.

Bettocchi, R., Pinelli, M. & Spina, P. R. (2003), A Multi-Stage Compressor Test Facility: Uncertainty Analysis and Preliminary Test Results, Vol. Volume 4: Turbo Expo 2003 of *Turbo Expo: Power for Land, Sea, and Air*, pp. 53–61.

Bitter, J. (1963), 'A study of erosion phenomena part i', *Wear* **6**(1), 5–21.

Bojdo, N. & Filippone, A. (2019), 'A simple model to assess the role of dust composition and size on deposition in rotorcraft engines', *Aerospace* **6**(4).

Bojdo, N. M. (2012), ROTORCRAFT ENGINE AIR PARTICLE SEPARATION, PhD thesis, University of Manchester.

Bons, J. P. (2002), 'St and cf augmentation for real turbine roughness with elevated freestream turbulence', *J. Turbomach.* **124**(4), 632–644.

Bons, J. P. (2010), 'A Review of Surface Roughness Effects in Gas Turbines', *Journal of Turbomachinery* **132**(2).

Bons, J. P., Blunt, R. & Whitaker, S. (2015), A Comparison of Techniques for Particle Rebound Measurement in Gas Turbine Applications, Vol. Volume 1: Aircraft Engine; Fans and Blowers; Marine of *Turbo Expo: Power for Land, Sea, and Air*.

Bons, J. P., McClain, S. T., Wang, Z. J., Chi, X. & Shih, T. I. (2008), 'A comparison of approximate versus exact geometrical representations of roughness for cfd calculations of cf and st', *Journal of Turbomachinery* **130**(2).

Bons, J. P., Prenter, R. & Whitaker, S. (2017), 'A Simple Physics-Based Model for Particle Rebound and Deposition in Turbomachinery', *Journal of Turbomachinery* **139**(8).

Booker, A., Dennis, J., Frank, P., Serafini, D. B., Torczon, V. & Trosset, M. (1998), 'A rigorous framework for optimization of expensive functions by surrogates', *Structural optimization* **17**, 1–13.

Borello, D., D'Angeli, L., Salvagni, A., Venturini, P. & Risopli, F. (2014), 'Study of particles deposition in gas turbine blades in presence of film cooling', *Proceeding of ASME Turbo Expo 2014* .

Borghesi, S., Montini, M. & Barreca, A. (2016), *The European emission trading system and its followers: Comparative analysis and linking perspectives*, Switzerland: Springer.

Borm, O., Jemcov, A. & Kau, H. (2011), Density based navier stokes solver for transonic flows, *in* '6th OpenFOAM workshop', pp. 1–30.

Boyce, M. P. & Gonzalez, F. (2005), 'A Study of On-Line and Off-Line Turbine Washing to Optimize the Operation of a Gas Turbine', *Journal of Engineering for Gas Turbines and Power* **129**(1), 114–122.

Boysan, F., Ayers, W. H., Pan, Z. & Swithenbank, J. (1982), 'Three-dimensional model of spray combustion in gas turbine combustors', **6**.

Bradley, R. (1932), 'LXXIX. The cohesive force between solid surfaces and the surface energy of solids', *The London, Edinburgh, and Dublin Philosophical Magazine and Journal of Science* **13**(86), 853–862.

Brand, P., Ruoß, K. & Gebhart, J. (1992), 'Performance of a mobile aerosol spectrometer for an in situ characterization of environmental aerosols in frankfurt city', *Atmospheric Environment. Part A. General Topics* **26**(13), 2451–2457.

Brandes, T., Koch, C. & Staudacher, S. (2021), 'Estimation of Aircraft Engine Flight Mission Severity Caused by Erosion', *Journal of Turbomachinery* **143**(11), 111001.

Brooke, J. W., Kontomaris, K., Hanratty, T. J. & McLaughlin, J. B. (1992), 'Turbulent deposition and trapping of aerosols at a wall', *Physics of Fluids A* **4**(4), 825–834.

Brunton, S. L., Brunton, B. W., Proctor, J. L., Kaiser, E. & Kutz, J. N. (2017), 'Chaos as an intermittently forced linear system', *Nature Communications* **8**(1).

Brunton, S. L., Brunton, B. W., Proctor, J. L. & Kutz, J. N. (2016), 'Koopman invariant subspaces and finite linear representations of nonlinear dynamical systems for control', *PLOS ONE* **11**(2), 1–19.

Bukar, A. A., Oumarou, M. B., Tela, B. M. & Eljummah, A. M. (2019), 'Assessment of biomass gasification: A review of basic design considerations', *American Journal of Energy Research* **7**(1), 1–14.

Bultzo, C. (1980), Some Unique Gas Turbine Problems, *in* 'ASME Turbo Expo, Paper No. 80-GT-179.'.

Burton, S., Ferrare, R., Vaughan, M., Omar, A., Rogers, R., Hostetler, C. & Hair, J. (2013), 'Aerosol classification from airborne hsrl and comparisons with the calipso vertical feature mask', *Atmospheric Measurement Techniques* **6**(5), 1397–1412.

Calvert, G., Ghadiri, M. & Tweedie, R. (2009), 'Aerodynamic dispersion of cohesive powders: A review of understanding and technology', *Advanced Powder Technology* **20**(1), 4–16.

Casari, N., Altmeppen, J., Koch, C., Pinelli, M., Staudacher, S., Suman, A. & Vulpio, A. (2020), Numerical Analysis of Particle Deposition in an Aircraft Engine Compressor Cascade, Vol. Volume 2B: Turbomachinery of *Turbo Expo: Power for Land, Sea, and Air*.

Casari, N., Fortini, A., Pinelli, M., Suman, A., Vulpio, A. & Zanini, N. (2022), 'Measurement approaches for the analysis of soil layer by microparticle adhesion', *Measurement* **187**, 110185.

Casari, N., Pinelli, M., Spina, P. R., Suman, A. & Vulpio, A. (2021), 'Performance Degradation Due to Fouling and Recovery After Washing in a Multistage Test Compressor', *Journal of Engineering for Gas Turbines and Power* **143**(3).

Casari, N., Pinelli, M. & Suman, A. (2018*a*), An Innovative Approach Towards Fouling Modeling: Microscale Deposition Pattern and its Effect on the Flow Field, Vol. Volume 2D: Turbomachinery of *Turbo Expo: Power for Land, Sea, and Air*.

Casari, N., Pinelli, M. & Suman, A. (2018*b*), On deposition and build-up detachment in compressor fouling, *in* 'Turbo Expo: Power for Land, Sea, and Air'.

Casari, N., Pinelli, M., Suman, A., di Mare, L. & Montomoli., F. (2017), 'Gas turbine blade geometry variation due to fouling', *Proceedings of 12th European Conference on Turbomachinery Fluid dynamics and Thermodynamics - ETC2017-353* .

Casari, N., Pinelli, M., Suman, A., di Mare, L. & Montomoli, F. (2018), 'Ebfog: Deposition, erosion, and detachment on high-pressure turbine vanes', *Journal of Turbomachinery* **140**(6).

Cerri, G., Salvini, C., Procacci, R. & Rispoli, F. (1993), Fouling and Air Bleed Extracted Flow Influence on Compressor Performance, Vol. Volume 3C: General of *Turbo Expo: Power for Land, Sea, and Air*.

Ceze, M., Hayashi, M. & Volpe, E. (2009), A study of the cst parameterization characteristics, Collection of Technical Papers - AIAA Applied Aerodynamics Conference.

Chan, L. & Kwok, W. (2000), 'Vertical dispersion of suspended particulates in urban area of hong kong', *Atmospheric Environment* **34**(26), 4403–4412.

Chan, L., Kwok, W., Lee, S. & Chan, C. (2001), 'Spatial variation of mass concentration of roadside suspended particulate matter in metropolitan hong kong', *Atmospheric Environment* **35**(18), 3167–3176.

Chevallier, J. (2010), 'Volatility forecasting of carbon prices using factor models', *Economics Bulletin* **30**(2), 1642–1660.

Cicic, T., Gjessing, S. & Kure, Ø. (2002), 'Tree recovery in pim sparse mode', *Telecommunication Systems* **19**, 443–460.

Clarkson, R. J., Majewicz, E. J. & Mack, P. (2016), 'A re-evaluation of the 2010 quantitative understanding of the effects volcanic ash has on gas turbine engines', *Proceedings of the Institution of Mechanical Engineers, Part G: Journal of Aerospace Engineering* **230**(12), 2274–2291.

Clarkson, R. & Simpson, H. (2017), 'Maximising airspace use during volcanic eruptions: Matching engine durability against ash cloud occurrence', *Proceedings of the Science and Technology Organisation Meeting STO-MP-AVT-272* .

Coats, C. M. (1986), 'Thrust and drag: Its prediction and verification. progress in astronautics and aeronautics', *The Aeronautical Journal (1968)* **90**(894), 152–152.

Connolly, B., Lotha, E. & Smith, C. F. (2020), 'Shape and drag of irregular angular particles and test dust', *Powder Technology* **363**, 275–285.

Corey, A. T. (1949), 'Influence of shape on the fall velocity of sand grains'. M.S. Colorado Agricultural and Mechanical College Thesis dissertation.

Correa, S. M. (1998), 'Power generation and aeropropulsion gas turbines: From combustion science to combustion technology', *Symposium (International) on Combustion* **27**(2), 1793–1807.

Crowe, C. T., Troutt, T. R. & Chung, J. N. (1996), 'Numerical models for two-phase turbulent flows', *Annual Review of Fluid Mechanics* **28**(1), 11–43.

de Boer, J. H. (1936), 'The influence of van der waals' forces and primary bonds on binding energy, strength and orientation, with special reference to some artificial resins', *Trans. Faraday Soc.* **32**, 10–37.

DeCarlo, P. F., Slowik, J. G., Worsnop, D. R., Davidovits, P. & Jimenez, J. L. (2004), 'Particle morphology and density characterization by combined mobility and aerodynamic diameter measurements. part 1: Theory', *Aerosol Science and Technology* **38**(12), 1185–1205.

Derigs, U. & Illing, S. (2013), 'Does eu ets instigate air cargo network reconfiguration? a model-based analysis', *European Journal of Operational Research* **225**(3), 518–527.

Derjaguin, B., Muller, V. & Toporov, Y. (1975), 'Effect of contact deformations on the adhesion of particles', *Journal of Colloid and Interface Science* **53**(2), 314–326.

Diakunchak, I. S. (1992), 'Performance Deterioration in Industrial Gas Turbines', *Journal of Engineering for Gas Turbines and Power* **114**(2), 161–168.

Draxler, R. R., Gillette, D. A., Kirkpatrick, J. S. & Heller, J. (2001), 'Estimating pm10 air concentrations from dust storms in iraq, kuwait and saudi arabia', *Atmospheric Environment* **35**(25), 4315–4330.

Dunn, M. G. (2012*a*), 'Operation of Gas Turbine Engines in an Environment Contaminated With Volcanic Ash', *Journal of Turbomachinery* **134**(5).

Dunn, M. G. (2012*b*), 'Operation of gas turbine engines in an environment contaminated with volcanic ash', *Journal of Turbomachinery* **134**(5).

Durst, F., Jovanović, J. & Sender, J. (1995), 'Lda measurements in the near-wall region of a turbulent pipe flow', *Journal of Fluid Mechanics* **295**, 305–335.

Döring, F., Staudacher, S., Koch, C. & Weißschuh, M. (2017*a*), 'Modeling Particle Deposition Effects in Aircraft Engine Compressors', *Journal of Turbomachinery* **139**(5).

Döring, F., Staudacher, S., Koch, C. & Weißschuh, M. (2017*b*), 'Modeling particle deposition effects in aircraft engine compressors', *Journal of Turbomachinery* **139**(5).

Efthymiou, M. & Papatheodorou, A. (2019), 'Eu emissions trading scheme in aviation: Policy analysis and suggestions', *Journal of Cleaner Production* **237**, 117734.

El-Batsh, H. (2001), Modeling Particle Deposition on Compressor and Turbine Blade Surfaces, PhD thesis, Vienna University of Technology.

Eldered, M. & Burkardt, J. (2009), 'Comparison of non-intrusive polynomial chaos and stochastic collocation methods for uncertainty quantification', *AIAA Proceeding* pp. 05–08.

Eldred, M. S. (1998), 'Optimization strategies for complex engineering applications', *Sandia National Labs., Albuquerque, NM (United States)* .

Elghobashi, S. E. (1994), 'On predicting particle-laden turbulent flows', *Flow Turbulence and Combustion* **52**, 309–329.

Ellis, M. J. (2021), Predicting Dust Damage in Aero-Engines, PhD thesis, The University of Manchester.

Fan, X., Li, S. & Tian, L. (2015), 'Chaotic characteristic identification for carbon price and an multi-layer perceptron network prediction model', *Expert Systems with Applications* **42**(8), 3945–3952.

Filippone, A. (2012), *Advanced Aircraft Flight Performance*, Cambridge Aerospace Series, 1st edn, Cambridge University Press, United Kingdom.

Flack, K. A. & Schultz, M. P. (2010), 'Review of hydraulic roughness scales in the fully rough regime', *Journal of Fluids Engineering* **132**(4).

Flack, K., Schultz, M. & Barros, J. (2020), 'Skin friction measurements of systematically-varied roughness: probing the role of roughness amplitude and skewness', *Flow, Turbulence and Combustion* **104**(2), 317–329.

Fletcher, P. & Walsh, P. (2008), *Gas Turbine Performance*, Wiley.
URL: *https://books.google.it/books?id=DtFml9BQkEIC*

Forsyth, P., Gillespie, D. R. H., McGilvray, M. & Galoul, V. (2016), Validation and Assessment of the Continuous Random Walk Model for Particle Deposition in Gas Turbine Engines, Vol. Volume 1: Aircraft Engine; Fans and Blowers; Marine of *Turbo Expo: Power for Land, Sea, and Air*.

Friso, R., Casari, N., Suman, A., Pinelli, M. & Montomoli, F. (2019), A Design for Fouling Oriented Optimization of an HPT Nozzle, Vol. Volume 2D: Turbomachinery of *Turbo Expo: Power for Land, Sea, and Air*.

Friso, R., Zanini, N., Suman, A. & Pinelli (2022), A Microscale-based Methodology to Predict the Performance Degradation in Turbomachinery due to Particle Deposition, Vol. Volume 2D: Turbomachinery of *Turbo Expo: Power for Land, Sea, and Air*.

García-Martos, C., Rodríguez, J. & Sánchez, M. J. (2013), 'Modelling and forecasting fossil fuels, co2 and electricity prices and their volatilities', *Applied Energy* **101**, 363–375. Sustainable Development of Energy, Water and Environment Systems.

Gbadebo, S. A., Hynes, T. P. & Cumpsty, N. A. (2004), 'Influence of Surface Roughness on Three-Dimensional Separation in Axial Compressors ', *Journal of Turbomachinery* **126**(4), 455–463.

Ghanem, R. & Spanos, P. D. (2003), *Stochastic finite elements: a spectral approach*, Dover Pubns.

Ghenaiet, A. (2014), Study of Particle Ingestion Through Two-Stage Gas Turbine, *in* 'Proceedings of the ASME Turbo Expo 2014: Turbomachinery Technical Conference and Exposition, GT2014-25759'.

Ghosal, S. & Self, S. (1995*a*), 'Particle size-density relation and cenosphere content of coal fly ash', *Fuel* **74**, 522–529.

Ghosal, S. & Self, S. A. (1995*b*), 'Particle size-density relation and cenosphere content of coal fly ash', *Fuel* **74**(4), 522–529.

Giunta, A. A., Dudley, J. M., Narducci, R., Grossman, B., Haftka, R. T., Mason, W. H. & Watson, L. T. (1994), Noisy aerodynamic response and smooth approximations in hsct design, *in* 'Proc. 5-th AIAA/USAF/NASA/ISSMO Symp. on Multidisciplinary and Structural Optimization', pp. 1117–1128.

Giunta, A. & Watson, L. (1998), A comparison of approximation modeling techniques-polynomial versus interpolating models, *in* '7th AIAA/USAF/NASA/ISSMO Symposium on Multidisciplinary Analysis and Optimization', p. 4758.

Goldberg, D. E. (1989), *Genetic Algorithms in Search, Optimization and Machine Learning*, 1st edn, Addison-Wesley Longman Publishing Co., Inc., USA.

Gosman, A. D. & loannides, E. (1983), 'Aspects of computer simulation of liquid-fueled combustors', *Journal of Energy* **7**(6), 482–490.

Granovskiy, A., Manev, I., Vassiliev, V. & Kissel, H. (2013), Effects of blade degradation on turbine performance, Vol. ASME 2013 Turbine Blade Tip Symposium.

Grant, G. & Tabakoff, W. (1975), 'Erosion prediction in turbomachinery resulting from environmental solid particles', *Journal of Aircraft* **12**(5), 471–478.

Granville, P. S. (1987), 'Three indirect methods for the drag characterization of arbitrarily rough surfaces on flat plates', *Journal of Ship Research* **31**(1).

Guffanti, M., Mayberry, G., Casadevall, T. & Wunderman, R. (2008), 'Volcanic hazards to airports', *Natural Hazards* **51**, 287–302.

Guha, A. (2008), 'Transport and deposition of particles in turbulent and laminar flow', *Annual Review of Fluid Mechanics* **40**(1), 311–341.

Guobrandsdóttir, H. N. & Óskar Haraldsson, H. (2011), 'Predicting the price of eu ets carbon credits', *Systems Engineering Procedia* **1**, 481–489. Engineering and Risk Management.

Gössling, S. (2020), 'Risks, resilience, and pathways to sustainable aviation: A covid-19 perspective', *Journal of Air Transport Management* **89**, 101933.

Hamaker, H. C. (1937), 'The london—van der waals attraction between spherical particles', *Physica* **4**(10), 1058–1072.

Hamed, A. & Kuhn, T. P. (1995), 'Effects of Variational Particle Restitution Characteristics on Turbomachinery Erosion', *Journal of Engineering for Gas Turbines and Power* **117**(3), 432–440.

Hamed, A., Tabakoff, W. C. & Wenglarz, R. (2006), 'Erosion and deposition in turbomachinery', *Journal of Propulsion and Power* **22**(2), 350–360.

Hammond, D. C. & Mellor, A. M. (1970), 'A preliminary investigation of gas turbine combustor modelling', *Combustion Science and Technology* **2**(2-3), 67–80.

Hammond, D. C. & Mellor, A. M. (1973), 'Analytical predictions of emissions from and within an allison j-33 combustor', *Combustion Science and Technology* **6**(5), 279–286.

Hanachi, H., Liu, J., Banerjee, A. & Chen, Y. (2015), Effects of the intake air humidity on the gas turbine performance monitoring, *in* 'Turbo Expo: Power for Land, Sea, and Air', Vol. 56758, American Society of Mechanical Engineers, p. V006T05A018.

Hanachi, H., Liu, J., Ding, P., Yong Kim, I. & Mechefske, C. K. (2018), 'Predictive Compressor Wash Optimization for Economic Operation of Gas Turbine', *Journal of Engineering for Gas Turbines and Power* **140**(12).

Helton, J. C., Johnson, J. D., Sallaberry, C. J. & Storlie, C. B. (2006), 'Survey of sampling-based methods for uncertainty and sensitivity analysis', *Reliability Engineering & System Safety* **91**(10-11), 1175–1209.

Henning, C., Brodbeck, M., Koch, C., Staudacher, S. & Ricken, T. (2021), 'Phase-field model for erosion processes', *PAMM* **20**(1), e202000282.

Hepperle, N., Therkorn, D., Schneider, E. & Staudacher, S. (2011), Assessment of Gas Turbine and Combined Cycle Power Plant Performance Degradation, *in* 'Volume 4: Cycle Innovations; Fans and Blowers; Industrial and Cogeneration; Manufacturing Materials and Metallurgy; Marine; Oil and Gas Applications', Turbo Expo: Power for Land, Sea, and Air, pp. 569–577.

Hicks, R. M. & Henne, P. A. (1978), 'Wing design by numerical optimization', *Journal of Aircraft* **15**(7), 407–412.

Hicks, R., Murman, E. & Vanderplaats, G. (1974), 'An assessment of airfoil design by numerical optimization', *NASA technical report, Document ID: 19740020369* p. Document ID: 19740020369.

Hiett, G. & Powell, G. (1962), 'Three-dimensional probe for investigation of flow patterns', *The Engineer* **213**(1), 165.

Hill, R. C., Hubbell, R. H. & Krapp, M. L. (1960), Operation and Maintenance of Remotely Controlled Gas-Turbine Units, *in* 'ASME 1960 Gas Turbine Power and Hydraulic Divisions Conference and Exhibit', Turbo Expo: Power for Land, Sea, and Air.

Ho, K., Lee, S., Jimmy, C. Y., Zou, S. & Fung, K. (2002), 'Carbonaceous characteristics of atmospheric particulate matter in hong kong', *Science of the Total Environment* **300**(1-3), 59–67.

Hosder, S., Walters, R. & Perez, R. (2006), 'A non-intrusive polynomial chaos method for uncertainty propagation in cfd simulations', *Proceeding of the 44th AIAA aerospace science meeting* **14**, 10649–10667.

Hottel, H., Williams, G. & Bonnell, A. (1958), 'Application of well-stirred reactor theory to the prediction of combustor performance', *Combustion and Flame* **2**(1), 13–34.

Howe, D. (2000), *Aircraft conceptual design synthesis*, Professional Engineering Publishing, London.

Howell, A. R. & Bonham, R. P. (1950), 'Overall and stage characteristics of axial-flow compressors', *Proceedings of the Institution of Mechanical Engineers* **163**(1), 235–248.

Hu, D., Alfarra, M. R., Szpek, K., Langridge, J., Cotterell, M., Belcher, C., Rule, I., Liu, Z., Yu, C., Shao, Y. et al. (2021), 'Physical and chemical properties of black carbon and organic matter from different sources using aerodynamic aerosol classification', *Atmos. Chem. Phys* **21**(21), 1–50.

Huang, Y., Dai, X., Wang, Q. & Zhou, D. (2021), 'A hybrid model for carbon price forecastingusing garch and long short-term memory network', *Applied Energy* **285**, 116485.

Igie, U. (2017), 'Gas Turbine Compressor Fouling and Washing in Power and Aerospace Propulsion', *Journal of Engineering for Gas Turbines and Power* **139**(12).

Igie, U., Goiricelaya, M., Nalianda, D. & Minervino, O. (2016), Aero engine compressor fouling effects for short- and long-haul missions, Vol. 230, pp. 1312–1324.

Igie, U., Pilidis, P., Fouflias, D., Ramsden, K. & Laskaridis, P. (2014), 'Industrial gas turbine performance: compressor fouling and on-line washing', *Journal of turbomachinery* **136**(10).

I.Lee, Ryou, H., Lee, S. & Chae, S. (2002), 'Comparison of two- equation model and reynolds stress models with experimental data for the three-dimensional turbulent boundary layer in a 30 degree bend', *KSME International Journal* **14**(10), 93–102.

Israelachvili, J. (2011), *Intermolecular and Surface Forces*, Academic Press.

Jasak, H. & Beaudoin, M. (2011), Openfoam turbo tools: from general purpose cfd to turbomachinery simulations, *in* 'Proceedings of the ASME-JSME-KSME 2011 Joint Fluids Engineering Conference, AJK2011-05015'.

Jensen, J. W., Squire, S. W., Bons, J. P. & Fletcher, T. H. (2004), 'Simulated Land-Based Turbine Deposits Generated in an Accelerated Deposition Facility', *Journal of Turbomachinery* **127**(3), 462–470.

Jeong, S., Chiba, K. & Obayashi, S. (2005), 'Data mining for aerodynamic design space', *Journal of aerospace computing, information, and communication* **2**(11), 452–469.

Jin, R., Chen, W. & Simpson, T. W. (2001), 'Comparative studies of metamodelling techniques under multiple modelling criteria', *Structural and multidisciplinary optimization* **23**(1), 1–13.

Johnson, K. L., Kendall, K. & Roberts, A. D. (1971), 'Surface Energy and the Contact of Elastic Solids', *Proceedings of the Royal Society of London Series A* **324**(1558), 301–313.

Kellersmann, A., Weiler, S., Bode, C., Friedrichs, J., Städing, J. & Ramm, G. (2018), 'Surface Roughness Impact on Low-Pressure Turbine Performance Due to Operational Deterioration', *Journal of Engineering for Gas Turbines and Power* **140**(6).

Kendall, K. (1969), PhD thesis, Cambridge University.

Kim, J., Dunn, M. G., Baran, A. J., Wade, D. P. & Tremba, E. L. (1993), 'Deposition of Volcanic Materials in the Hot Sections of Two Gas Turbine Engines', *Journal of Engineering for Gas Turbines and Power* **115**(3), 641–651.

Kim, T. W. & Bhushan, B. (2007), 'The adhesion model considering capillarity for gecko attachment system', *Journal of the Royal Society, Interface* **5**(20), 319–327.

Kok, J. F., Parteli, E. J., Michaels, T. I. & Karam, D. B. (2012), 'The physics of wind-blown sand and dust', *Reports on progress in Physics* **75**(10), 106901.

Konstandopoulos, A. G. (2006), 'Particle sticking/rebound criteria at oblique impact', *Journal of Aerosol Science* **37**(3), 292–305.

Koopman, B. O. (1931), 'Hamiltonian systems and transformation in hilbert space', *Proceedings of the National Academy of Sciences* **17**(5), 315–318.

Koopman, B. O. & v. Neumann, J. (1932), 'Dynamical systems of continuous spectra', *Proceedings of the National Academy of Sciences* **18**(3), 255–263.

Kulfan, B. & Bussoletti, J. (2006), " fundamental" parameteric geometry representations for aircraft component shapes, *in* '11th AIAA/ISSMO multidisciplinary analysis and optimization conference', p. 6948.

Kurz, R. & Brun, K. (2000), 'Degradation in Gas Turbine Systems ', *Journal of Engineering for Gas Turbines and Power* **123**(1), 70–77.

Kurz, R., Brun, K., Meher-Homji, C. & Moore, J. (2012), Gas Turbine Performance and Maintenance, *in* 'Proceedings of the Forty-First Turbomachinery Symposium', pp. 24–27.

Kurz, R., Brun, K. & Wollie, M. (2009), 'Degradation effects on industrial gas turbines', *Journal of Engineering for Gaas Turbines and Power* **131**, 062401.

Kurz, R., Musgrove, G. & Brun, K. (2016), 'Experimental Evaluation of Compressor Blade Fouling', *Journal of Engineering for Gas Turbines and Power* **139**(3).

Kurzke, J. (1996), How to Get Component Maps for Aircraft Gas Turbine Performance Calculations, Vol. Volume 5: Manufacturing Materials and Metallurgy; Ceramics; Structures and Dynamics; Controls, Diagnostics and Instrumentation; Education; General of *Turbo Expo: Power for Land, Sea, and Air*.

Kyprianidis, K. G. (2011), Future aero engine designs: An evolving vision, *in* E. Benini, ed., 'Advances in Gas Turbine Technology', IntechOpen, Rijeka, chapter 1.
URL: *https://doi.org/10.5772/19689*

Lanzillotta, F., Sciacchitano, A. & Rao, A. G. (2017), 'Effect of film cooling on the aerodynamic performance of an airfoil', *International Journal of Heat and Fluid Flow* **66**, 108–120.

Larson, F. & Miller, J. (1952), 'A time-temperature relationship for rupture and creep stresses', *Transactions of ASME* **74**, 765–775.

Larsson, J., Elofsson, A., Sterner, T. & Åkerman, J. (2019), 'International and national climate policies for aviation: a review', *Climate Policy* **19**(6), 787–799.

Leach, K. P. (1983), Energy efficient engine high-pressure turbine component rig performance test report, Technical Report CR-160189, NASA Report.

Lee, D., Fahey, D., Skowron, A., Allen, M., Burkhardt, U., Chen, Q., Doherty, S., Freeman, S., Forster, P., Fuglestvedt, J., Gettelman, A., De León, R., Lim, L., Lund, M., Millar, R., Owen, B., Penner, J., Pitari, G., Prather, M., Sausen, R. & Wilcox, L. (2021), 'The contribution of global aviation to anthropogenic climate forcing for 2000 to 2018', *Atmospheric Environment* **244**, 117834.

Lee, J., Kim, J., Song, C., Kim, S., Chun, Y., Sohn, B. & Holben, B. (2010), 'Characteristics of aerosol types from aeronet sunphotometer measurements', *Atmospheric Environment* **44**(26), 3110–3117.

Li, Z. & Zheng, X. (2017), 'Progress in aerospace sciences review of design optimization methods for turbomachinery aerodynamics', *Progress Aerospace Science* **93**, 1–23.

Liu, B. Y. & Agarwal, J. K. (1974*a*), 'Experimental observation of aerosol deposition in turbulent flow', *Journal of Aerosol Science* **5**(2), 145–155.

Liu, B. Y. H. & Agarwal, J. K. (1974*b*), 'Experimental observation of aerosol deposition in turbulent flows', *Journal of Aerosol Sciences* **5**(2), 145–148.

Liu, Y., Song, C., Lv, G., Chen, N., Zhou, H. & Jing, X. (2018), 'Determination of the attractive force, adhesive force, adhesion energy and hamaker constant of soot particles generated from a premixed methane/oxygen flame by afm', *Applied Surface Science* **433**, 450–457.

Livingstone, D. (2009), *Artificial Neural Networks*, Springer - Humana Press.

London, F. (1930), 'Zur theorie und systematik der molekularkrafte', *Z. Physik* **63**, 245–279.

L.P.Timko (1990), ENERGY EFFICIENT ENGINE High Pressure Turbine Component Test Performance Report, Technical report NASA CR-168289, NASA Lewis Research Center.

Maertens, S., Grimme, W., Scheelhaase, J. & Jung, M. (2019), 'Options to continue the eu ets for aviation in a corsia-world', *Sustainability* **11**(20).

Malina, R., McConnachie, D., Winchester, N., Wollersheim, C., Paltsev, S. & Waitz, I. A. (2012), 'The impact of the european union emissions trading scheme on us aviation', *Journal of Air Transport Management* **19**, 36–41.

Mamouri, R.-E., Ansmann, A., Nisantzi, A., Solomos, S., Kallos, G. & Hadjimitsis, D. G. (2016), 'Extreme dust storm over the eastern mediterranean in september 2015: satellite, lidar, and surface observations in the cyprus region', *Atmospheric Chemistry and Physics* **16**(21), 13711–13724.

Marti, A., Folch, A., Jorba, O. & Janjic, Z. (2017), 'Volcanic ash modeling with the online nmmb-monarch-ash v1.0 model: model description, case simulation, and evaluation', *Atmospheric Chemistry and Physics* **17**(6), 4005–4030.

Martins, J. & Hwang, J. (2013), 'Review and unification of methods for computing derivatives of multidisciplinary computational models', *AIAA Journal* **51**, 2582–2599.

Meher-Homji, C. B., Chaker, M. & Bromley, A. F. (2009), The Fouling of Axial Flow Compressors: Causes, Effects, Susceptibility, and Sensitivity, Vol. Volume 4: Cycle Innovations; Industrial and Cogeneration; Manufacturing Materials and Metallurgy; Marine of *Turbo Expo: Power for Land, Sea, and Air*, pp. 571–590.

Meher-Homji, C. & Bromley, A. (2004), Gas Turbine Axial Compressor Fouling And Washing, *in* 'Turbomachinery and Pump Symposia', pp. 163–192.

Meireles, M. R., Almeida, P. E. & Simões, M. G. (2003), 'A comprehensive review for industrial applicability of artificial neural networks', *IEEE transactions on industrial electronics* **50**(3), 585–601.

Meleo, L., Nava, C. R. & Pozzi, C. (2016), 'Aviation and the costs of the european emission trading scheme: The case of italy', *Energy Policy* **88**, 138–147.

Melino, F., Peretto, A. & Spina, P. R. (2010), Development and validation of a model for axial compressor fouling simulation, Vol. Volume 5: Industrial and Cogeneration; Microturbines and Small Turbomachinery; Oil and Gas Applications; Wind Turbine Technology of *Turbo Expo: Power for Land, Sea, and Air*, pp. 87–98.

Menter, F., Kuntz, M. & Langtry, R. B. (2003), Ten years of industrial experience with the sst turbulence model, *in* 'Turbulence, Heat and Mass Transfer', Vol. 4.

Mittal, K. & Jaiswal, R. (2015), *Particle Adhesion and Removal*, Adhesion and Adhesives: Fundamental and Applied Aspects, Wiley.
URL: *https://books.google.it/books?id=sAl9BgAAQBAJ*

Montgomery, D. C. (2017), *Design and Analysis of Experiments*, John Wiley & Sons, Inc., Hoboken, NJ, USA.

Montomoli, F. (2019), *Uncertainty Quantification in computational fluid dynamics and aircraft engine - Second edition*, Springer.

Montomoli, F., Amirante, D., Hills, N., Shahpar, S. & Massini, M. (2014), 'Uncertainty quantification, rare events and mission optimization: stochastic variations of metal temperature during a transient', *Proceeding of ASME Turbo Expo 2014, GT2014-25398* .

Montomoli, F., D'Ammaro, A. & Uchida, S. (2013), 'Uncertainty quantification and conjugate heat transfer: a stochastic analysis', *Journal of Turbomachinery* .

Moody, L. (1944), 'Friction factors for pipe flow', *Trans. American Society of Mechanical Engineers* **66**, 671–684.

Morini, M., Pinelli, M., Spina, P. R. & Venturini, M. (2009), 'Influence of Blade Deterioration on Compressor and Turbine Performance', *Journal of Engineering for Gas Turbines and Power* **132**(3).

Morini, M., Pinelli, M., Spina, P. R. & Venturini, M. (2011), 'Numerical analysis of the effects of nonuniform surface roughness on compressor stage performance', *Journal of Engineering for Gas Turbines and Power* **133**(7).

Muir, D. E., Saravanamuttoo, H. I. H. & Marshall, D. J. (1989), 'Health Monitoring of Variable Geometry Gas Turbines for the Canadian Navy', *Journal of Engineering for Gas Turbines and Power* **111**(2), 244–250.

Muller, V., Yushchenko, V. & Derjaguin, B. (1980), 'On the influence of molecular forces on the deformation of an elastic sphere and its sticking to a rigid plane', *Journal of Colloid and Interface Science* **77**(1), 91–101.

Mund, F. C. & Pilidis, P. (2005), 'Gas Turbine Compressor Washing: Historical Developments, Trends and Main Design Parameters for Online Systems', *Journal of Engineering for Gas Turbines and Power* **128**(2), 344–353.

Myhre, G., Shindell, D., Bréon, F.-M., Collins, W., Fuglestvedt, J., Huang, J., Koch, D., Lamarque, J.-F., Lee, D., Mendoza, B., Nakajima, T., Robock, A., Stephens, G., Takemura, T. & Zhang, H. (2013), *Anthropogenic and natural radiative forcing*, Cambridge University Press, Cambridge, UK, pp. 659–740.

Nasr, B., Ahmadi, G., Ferro, A. R. & Dhaniyala, S. (2019), 'Overview of mechanistic particle resuspension models: comparison with compilation of experimental data', *Journal of Adhesion Science and Technology* **33**(24), 2631–2660.

Nasr, B., Dhaniyala, S. & Ahmadi, G. (2017), Chapter 2 - particle resuspension from surfaces: Overview of theoretical models and experimental data, *in* R. Kohli & K. L. Mitta, eds, 'Developments in Surface Contamination and Cleaning: Types of Contamination and Contamination Resources', William Andrew Publishing, pp. 55–84.

Nava, C. R., Meleo, L., Cassetta, E. & Morelli, G. (2018), 'The impact of the eu-ets on the aviation sector: Competitive effects of abatement efforts by airlines', *Transportation Research Part A: Policy and Practice* **113**, 20–34.

Nelli, N., Fissehaye, S., Francis, D., Fonseca, R., Temimi, M., Weston, M., Abida, R. & Nesterov, O. (2021), 'Characteristics of atmospheric aerosols over the uae inferred from calipso and sun photometer aerosol optical depth', *Earth and Space Science* **8**(6), e2020EA001360.

Nicol, D. G., Malte, P. C., Hamer, A. J., Roby, R. J. & Steele, R. C. (1999), 'Development of a Five-Step Global Methane Oxidation-NO Formation Mechanism for Lean-Premixed Gas Turbine Combustion', *Journal of Engineering for Gas Turbines and Power* **121**(2), 272–280.

Nikuradse, J. (1933), *Strömungsgesetze in rauhen Rohren*, Forschungsheft auf dem Gebiete des Ingenieurwesens, VDI-Verlag.

Ogiriki, E. A., Li, Y. G., Nikolaidis, T., Isaiah, T. E. & Sule, G. (2015), 'Effect of fouling, thermal barrier coating degradation and film cooling holes blockage on gas turbine engine creep life', *Procedia Cirp* **38**, 228–233.

Omar, A. H., Winker, D. M., Vaughan, M. A., Hu, Y., Trepte, C. R., Ferrare, R. A., Lee, K.-P., Hostetler, C. A., Kittaka, C., Rogers, R. R. et al. (2009), 'The calipso automated aerosol classification and lidar ratio selection algorithm', *Journal of Atmospheric and Oceanic Technology* **26**(10), 1994–2014.

Orr, F. M., Scriven, L. E. & Rivas, A. P. (1975), 'Pendular rings between solids: meniscus properties and capillary force', *Journal of Fluid Mechanics* **67**(4), 723–742.

O'Connell, A., Kousoulidou, M., Lonza, L. & Weindorf, W. (2019), 'Considerations on ghg emissions and energy balances of promising aviation biofuel pathways', *Renewable and Sustainable Energy Reviews* **101**, 504–515.

Papavergos, P. G. & Hedley, A. B. (1984), 'particle deposition behaviour from turbulent flows', *Chemical Engineering Research & Design* **62**, 275–295.

Parker, S., Foat, T. & Preston, S. (2008), 'Towards quantitative prediction of aerosol deposition from turbulent flows', *Journal of Aerosol Science* **39**(2), 99–112.

Perullo, C. A., Barron, J., Grace, D., Angello, L. & Lieuwen, T. (2015), Evaluation of Air Filtration Options for an Industrial Gas Turbine, Vol. Volume 3: Coal, Biomass and Alternative Fuels; Cycle Innovations; Electric Power; Industrial and Cogeneration of *Turbo Expo: Power for Land, Sea, and Air*.

Peter, J. & Marcelet, M. (2008), 'Comparison of surrogate models for turbomachinery design', *Wseas transactions on fluid mechanics* **3**(1), 10–17.

Poppe, T., Blum, J. & Henning, T. (2000), 'Analogous experiments on the stickiness of micron-sized preplanetary dust', *The Astrophysical Journal* **533**(1), 454–471.

Préndez, M., Araya, M., Criollo, C., Egas, C., Farías, I., Fuentealba, R. & González, E. (2019), *Urban Trees and Their Relationship with Air Pollution by Particulate Matter and Ozone in Santiago, Chile*, Springer International Publishing, pp. 167–206.

Prenter, R., Ameri, A. & Bons, J. P. (2017), 'Computational simulation of deposition in a cooled high-pressure turbine stage with hot streaks', *Journal of Turbomachinery* **139**(9), 091005.

Rai, M. & Madavan, N. (2000), 'Aerodynamic design using neural networks', *AIAA Journal* **38**, 173–182.

Rao, P. N. S. & Naikan, V. N. A. (2008), 'An Optimal Maintenance Policy for Compressor of a Gas Turbine Power Plant', *Journal of Engineering for Gas Turbines and Power* **130**(2).

Reagle, C. J., Delimont, J. M., Ng, W. F. & Ekkad, S. V. (2014), 'Study of microparticle rebound characteristics under high temperature conditions', *J. Eng. Gas Turbines Power* **1360**(1), 011501.

Rispoli, F., Delibra, G., Venturini, P., Corsini, A., Saavedra, R. & Tezduyar, T. (2015), 'Particle tracking and particle–shock interaction in compressible-flow computations with the v-sgs stabilization and yzb shock-capturing', *Computational Mechanics* **55**, 1201–1209.

Rizk, N. K. & Mongia, H. C. (1993), 'Three-Dimensional Gas Turbine Combustor Emissions Modeling', *Journal of Engineering for Gas Turbines and Power* **115**(3), 603–611.

Rizk, N. K. & Mongia, H. C. (1995), 'A Semi-Analytical Emission Model for Diffusion Flame, Rich/Lean and Premixed Lean Combustors', *Journal of Engineering for Gas Turbines and Power* **117**(2), 290–301.

Roberts, A. (1968), PhD thesis, Cambridge University.

Rocha-Lima, A., Martins, J. V., Remer, L. A., Todd, M., Marsham, J. H., Engelstaedter, S., Ryder, C. L., Cavazos-Guerra, C., Artaxo, P., Colarco, P. et al. (2018), 'A detailed characterization of the saharan dust collected during the fennec campaign in 2011: in situ ground-based and laboratory measurements', *Atmospheric Chemistry and Physics* **18**(2), 1023–1043.

Rogers, L. N. & Reed, J. (1984), 'The adhesion of particles undergoing an elastic-plastic impact with a surface', *Journal of Physics D: Applied Physics* **17**(4), 677–689.

ROWLEY, C. W., MEZIC, I., BAGHERI, S., SCHLATTER, P. & HENNINGSON, D. S. (2009), 'Spectral analysis of nonlinear flows', *Journal of Fluid Mechanics* **641**, 115–127.

Salvadori, S., Montomoli, F., Martelli, F., Adami, P., Chana, K. & Castillon, L. (2011), 'Aero-thermal study of unsteady flow field in a transonic gas turbine with inlet temperature distortions', *Journal of Turbomachinery* **133**, 031030.

Saravanamuttoo, H., Rogers, G. & Cohen, H. (2009), *Gas Turbine Theory*, Pearson Prentice Hall.
URL: *https://books.google.it/books?id=Ir1DE5_8TQwC*

Scheelhaase, J., Grimme, W. & Schaefer, M. (2010), 'The inclusion of aviation into the eu emission trading scheme – impacts on competition between european and non-european network airlines', *Transportation Research Part D: Transport and Environment* **15**(1), 14–25. Air Transport, Global Warming and the Environment.

Scheelhaase, J., Maertens, S. & Grimme, W. (2021), 'Options for improving the eu emissions trading scheme (eu ets) for aviation', *Transportation Research Procedia* **59**, 193–202. 10th International Conference on Air Transport – INAIR 2021, TOWARDS AVIATION REVIVAL.

Scheelhaase, J., Maertens, S., Grimme, W. & Jung, M. (2018), 'Eu ets versus corsia – a critical assessment of two approaches to limit air transport's co2 emissions by market-based measures', *Journal of Air Transport Management* **67**, 55–62.

Schlichting, H. (1937), *Experimental investigation of the problem of surface roughness*, number 823, National Advisory Commitee for Aeronautics.

Schmid, P. J. (2010), 'Dynamic mode decomposition of numerical and experimental data', *Journal of Fluid Mechanics* **656**, 5 – 28.

Schultz, M. & Flack, K. (2007), 'The rough-wall turbulent boundary layer from the hydraulically smooth to the fully rough regime', *Journal of Fluid Mechanics* **580**, 381–405.

Schultz, M. P. & Flack, K. A. (2013), 'Reynolds-number scaling of turbulent channel flow', *Physics of Fluids* **25**(2), 025104.

Schurovsky, V. & Levikin, A. (1986), Fouling and cleaning of gas turbine axial compressor flow path, *in* 'Moscow, series Transport and Gas Conservation'.

Sigal, A. & Danberg, J. E. (1990), 'New correlation of roughness density effect on the turbulent boundary layer', *AIAA journal* **28**(3), 554–556.

Soltani, M. & Ahmadi, G. (1994), 'On particle adhesion and removal mechanisms in turbulent flows', *Journal of Adhesion Science and Technology* **8**(7), 763–785.

Speziale, C., Sarkar, S. & Gatski, T. (1990), *Journal of Fluid Mechanics* **227**, 245–272.

Spina, P. R. (2002), Gas Turbine Performance Prediction by Using Generalized Performance Curves of Compressor and Turbine Stages, Vol. Volume 2: Turbo Expo 2002, Parts A and B of *Turbo Expo: Power for Land, Sea, and Air*, pp. 1073–1082.

Sripawadkul, V., Padulo, M. & Guenov, M. (2010), A comparison of airfoil shape parameterization techniques for early design optimization, *in* '13th AIAA/ISSMO multidisciplinary analysis optimization conference', p. 9050.

Stalder, J.-P. (2000), 'Gas Turbine Compressor Washing State of the Art: Field Experiences1', *Journal of Engineering for Gas Turbines and Power* **123**(2), 363–370.

Sturgess, G. J., McKinney, R. G. & Morford, S. A. (1993), 'Modification of Combustor Stoichiometry Distribution for Reduced NOx Emission From Aircraft Engines', *Journal of Engineering for Gas Turbines and Power* **115**(3), 570–580.

Suder, K. L., Chima, R. V., Strazisar, A. J. & Roberts, W. B. (1995), 'The Effect of Adding Roughness and Thickness to a Transonic Axial Compressor Rotor', *Journal of Turbomachinery* **117**(4), 491–505.

Suman, A., Morini, M., Aldi, N., Casari, N., Pinelli, M. & Spina, P. R. (2017), 'A Compressor Fouling Review Based on an Historical Survey of ASME Turbo Expo Papers', *Journal of Turbomachinery* **139**(4).

Suman, A., Vulpio, A., Casari, N. & Pinelli, M. (2021-22), 'Outstretching population growth theory towards surface contamination', *Powder Technology* **394**, 597–607.

Suman, A., Vulpio, A., Casari, N., Pinelli, M., di Lillo, F. & D'Amico, L. (2021-3), 'Analysis of soil and soot deposits by x-ray computed microtomography', *Powder Technology* **394**, 608–621.

Suman, A., Vulpio, A., Casari, N., Pinelli, M., Kurz, R. & Brun, K. (2021), 'Deposition Pattern Analysis on a Fouled Multistage Test Compressor', *Journal of Engineering for Gas Turbines and Power* **143**(8).

Suman, A., Vulpio, A., Fortini, A., Fabbri, E., Casari, N., Merlin, M. & Pinelli, M. (2021-23), 'Experimental analysis of micro-sized particles time-wise adhesion: the influence of impact velocity and surface roughness', *International Journal of Heat and Mass Transfer* **165**, 120632.

Suman, A., Vulpio, A., Pinelli, M. & D'amico, L. (2022), Microtomography of soil and soot deposits: Analysis of three-dimensional structures and surface morphology, *in* 'Proceedings of the ASME Turbo Expo 2022, GT2022-83070'.

Sun, H. (2011), 'Wind turbine airfoil design using response surface method', *Journal of Mechanical Science and Technology* **25**, 1335–1340.

Sun, X., Jafari, S., Miran Fashandi, S. A. & Nikolaidis, T. (2021), 'Compressor degradation management strategies for gas turbine aero-engine controller design', *Energies* **14**(18).

Suzuki, M., Inaba, K. & Yamamoto, M. (2006), 'Numerical simulation of sand erosion phenomena in rotor/stator interaction of compressor', *Journal of Thermal Science* **17**, 125–133.

Syverud, E. & Bakken, L. E. (2007), 'Online Water Wash Tests of GE J85-13', *Journal of Turbomachinery* **129**(1), 136–142.

Sánchez, D., Chacartegui, R., Becerra, J. A. & Sánchez, T. (2009), 'Determining compressor wash programmes for fouled gas turbines', *Proceedings of the Institution of Mechanical Engineers, Part A: Journal of Power and Energy* **223**(4), 467–476.

Tabakoff, W., Hamed, A. & Metwally, M. (1991), 'Effect of Particle Size Distribution on Particle Dynamics and Blade Erosion in Axial Flow Turbines', *Journal of Engineering for Gas Turbines and Power* **113**(4), 607–615.

Tabakoff, W. & Malak, M. F. (1987), 'Laser measurements of fly ash rebound parameters for use in trajectory calculations'.

Taiwo, A. M., Beddows, D. C., Shi, Z. & Harrison, R. M. (2014), 'Mass and number size distributions of particulate matter components: Comparison of an industrial site and an urban background site', *Science of The Total Environment* **475**, 29–38.

Takens, F. (1981), Detecting strange attractors in turbulence.

Taltavull, B., Dean, J. & Clyne, T. (2015), 'Adhesion of volcanic ash particles under controlled conditions and implications for their deposition in gas turbines', *Advanced engineering material* **218**(5).

Tang, G., Iaccarino, G. & Eldred, M. (2010), 'Global sensitivity analysis for stochastic collocation', *AIAA Structures, structural dynamics, and materials conference, AIAA 2010-2922* .

Tang, Y., Guo, B. & Ranjan, D. (2015), 'Numerical simulation of aerosol deposition from turbulent flows using three-dimensional rans and les turbulence models', *Engineering Applications of Computational Fluid Mechanics* **9**(1), 174–186.

Tarabrin, A. P., Schurovsky, V. A., Bodrov, A. I. & Stalder, J.-P. (1998*a*), 'An Analysis of Axial Compressor Fouling and a Blade Cleaning Method', *Journal of Turbomachinery* **120**(2), 256–261.

Tarabrin, A. P., Schurovsky, V. A., Bodrov, A. I. & Stalder, J.-P. (1998*b*), Influence of Axial Compressor Fouling on Gas Turbine Unit Perfomance Based on Different Schemes and With Different Initial Parameters, *in* 'Turbo Expo: Power for Land, Sea, and Air', Vol. Volume 4: Heat Transfer; Electric Power; Industrial and Cogeneration.

Tatarko, J. & Presley, D. (2009), 'Principles of wind erosion and its control', *K-State Research and Extension Publication* **MF-2860**.

Tatsukawa, T., Oyama, A. & Fujii, K. (2008), Comparative study of data mining methods for aerodynamic multiobjective optimizations, 8th World Congress on Computational Mechanics (WCCM8)/5th European Congress on Computational Methods in Applied Sciences and Engineering (ECCOMAS2008).

Thulin, R. D., Howe, D. C. & Singer, I. D. (1982), High-pressure turbine detailed design report, Technical Report CR-165608, NASA Report.

Toof, J. L. (1986), 'A Model for the Prediction of Thermal, Prompt, and Fuel NOx Emissions From Combustion Turbines', *Journal of Engineering for Gas Turbines and Power* **108**(2), 340–347.

Torenbeek, E. (1982), *Synthesis of Subsonic Airplane Design*, Delft University Press, Delft.

Turns, S. (1996), *An Introduction to Combustion*, McGraw-Hill, New York.

UNEP, WMO & UNCCD (2016), Global assessment of sand and dust storms, Technical report, United Nations Environment Programme, Nairobi.

Van Beek, M. (2001), Gas-side fouling of heat recovery boilers, PhD thesis, Technische Universiteit Eindhoven.

Van Rij, J. A., Belnap, B. J. & Ligrani, P. M. (2002), 'Analysis and experiments on three-dimensional, irregular surface roughness', *Journal of Fluids Engineering* **124**(3), 671–677.

Venturini, P. (2009), Modelling of particle wall-deposition in two phase gas-solid flows, PhD thesis, Sapienza University of Rome.

Vespermann, J. & Wald, A. (2011), 'Much ado about nothing? – an analysis of economic impacts and ecologic effects of the eu-emission trading scheme in the aviation industry', *Transportation Research Part A: Policy and Practice* **45**(10), 1066–1076. A Collection of Papers:Transportation in a World of Climate Change.

Visser, J. (1972), 'On hamaker constants: A comparison between hamaker constants and lifshitz-van der waals constants', *Advances in Colloid and Interface Science* **3**(4), 331–363.

Vogel, A., Durant, A. J., Cassiani, M., Clarkson, R. J., Slaby, M., Diplas, S., Krüger, K. & Stohl, A. (2018), 'Simulation of Volcanic Ash Ingestion Into a Large Aero Engine: Particle–Fan Interactions', *Journal of Turbomachinery* **141**(1).

Vulpio, A., Suman, A., Casari, N. & Pinelli, M. (2021), 'Dust ingestion in a rotorcraft engine compressor: Experimental and numerical study of the fouling rate', *Aerospace* **8**(3).

Vulpio, A., Suman, A., Casari, N., Pinelli, M., Kurz, R. & Brun, K. (2021-22), 'Analysis of timewise compressor fouling phenomenon on a multistage test compressor: Performance losses and particle adhesion', *Journal of Engineering for Gas Turbines and Power* **143**(8).

Wang, M., Hu, M., Zheng, R., Lianhui, G. & Di, Y. (2018), 'Quantitative detection of mass concentration of sand-dust storms via wind-profiling radar and analysis of z-m relationship', *Theoretical and Applied Climatology* **131**.

Whitaker, S. M., Peterson, B., Miller, A. F. & Bons, J. P. (2016), The Effect of Particle Loading, Size, and Temperature on Deposition in a Vane Leading Edge Impingement Cooling Geometry, Vol. Volume 5B: Heat Transfer of *Turbo Expo: Power for Land, Sea, and Air*.

Wiener, N. (1938), 'The homogeneus chaos', *Am. J. Math* **60**, 897–936.

Wilcox, M., Baldwin, R., Garcia-Hernandez, Augusto & Brun, K. (2010), 'Guideline for gas turbine inlet air filtration systems', *Gas Machinery Research Council, Dallas, TX* .

Wilson, D. & Korakianitis, T. (2014), *The Design of High-Efficiency Turbomachinery and Gas Turbines*, The MIT Press, MIT Press.
URL: *https://books.google.it/books?id=QwGZBAAAQBAJ*

Winker, D. M., Vaughan, M. A., Omar, A., Hu, Y., Powell, K. A., Liu, Z., Hunt, W. H. & Young, S. A. (2009), 'Overview of the calipso mission and caliop data processing algorithms', *Journal of Atmospheric and Oceanic Technology* **26**(11), 2310–2323.

Wong, M. S., Nichol, J. E. & Lee, K. H. (2013), 'Estimation of aerosol sources and aerosol transport pathways using aeronet clustering and backward trajectories: a case study of hong kong', *International Journal of Remote Sensing* **34**(3), 938–955.

Xu, H., Wang, M., Jiang, S. & Yang, W. (2020), 'Carbon price forecasting with complex network and extreme learning machine', *Physica A: Statistical Mechanics and its Applications* **545**, 122830.

Yamamoto, S., Araki, K., Moriguchi, S., Miyazawa, H., Furusawa, T., Yonezawa, K., Umezawa, S., Ohmori, S. & Suzuki, T. (2021), 'Effects of wetness and humidity on transonic compressor of gas turbine', *International Journal of Heat and Mass Transfer* **178**, 121649.

Yang, H. & Boulanger, J. (2012), 'The Whole Annulus Computations of Particulate Flow and Erosion in an Axial Fan', *Journal of Turbomachinery* **135**(1), 011040.

Yondo, R., Andrés, E. & Valero, E. (2018), 'A review on design of experiments and surrogate models in aircraft real-time and many-query aerodynamic analyses', *Progress in aerospace sciences* **96**, 23–61.

Yoshiyuki Endo, Shinji Hasebe & Yasuo Kousaka (1997), 'Dispersion of aggregates of fine powder by acceleration in an air stream and its application to the evaluation of adhesion between particles', *Powder Technology* **91**(1), 25–30.

Yu, K. & Tafti, D. (2016), 'Impact model for micrometer-sized sand particles', *Powder Technology* **294**, 11–21.

Zaba, T. (1980), 'Losses in gas turbines due to deposits on the blading', *Brown Boveri Review* **67**(4), 715–722.

Zagnoli, D., Prenter, R., Ameri, A. & Bons, J. P. (2015), Numerical study of deposition in a full turbine stage using steady and unsteady methods, *in* 'Proceedings of the ASME Turbo Expo 2015, GT2015-43613'.

Zender, C. S., Bian, H. & Newman, D. (2003), 'Mineral dust entrainment and deposition (dead) model: Description and 1990s dust climatology', *Journal of Geophysical Research: Atmospheres* **108**.

Zhao, X., Han, M., Ding, L. & Kang, W. (2018), 'Usefulness of economic and energy data at different frequencies for carbon price forecasting in the eu ets', *Applied Energy* **216**, 132–141.

Zhu, B. (2012), 'A novel multiscale ensemble carbon price prediction model integrating empirical mode decomposition, genetic algorithm and artificial neural network', *Energies* **5**(2), 355–370.

Zimmermann, D. C. (1996), Genetic algorithms for navigating expensive and complex design spaces, *in* 'Report for Sandia National Laboratories contract AO-7736 CA 02', Sandia National Laboratories.